VOLUME 75 MARCH 4, 1971 NUMBER 5

JPCHAx

THE JOURNAL OF PHYSICAL CHEMISTRY

PUBLISHED BIWEEKLY BY THE AMERICAN CHEMICAL SOCIETY

Reprints from Chemical & Engineering News

Keeping broadly informed challenges every person today. If you missed these features from recent issues of C&EN, you can still get copies by filling in the coupon below.

Reinforced Plastics

Gilbert R. Parker, C&EN

January 26, 1970 **50¢**

In the 1970-75 period reinforced plastics will enjoy many successes—in terms of sales, production, and earnings growth, product value, and acceptance. The industry, the products, and the consumers are examined in this article. **12670**

The Paint Industry

David M. Kiefer, C&EN

December 22, 1969 **50¢**

The article takes an extended look at this industry—an old business now facing challenges of new technology. The industry is a solid and dependable one, however, with steady gains in sales ahead. **12229**

Career Opportunities Corelator 1970

March 9, 1970 **25¢**

C&EN's annual career guide for chemists and chemical engineers; a separate issue. Overall manpower needs; salaries; and two directories—an Employers Directory and a Job Specialty Directory. **03970**

Public Policy and the Environment

February 9, 1970 **50¢**

Speaking at the 158th ACS National Meeting, Lee DuBridge, Herbert Doan, and Barry Commoner urged cooperation among government, industry, and university in tackling environmental improvement. **02970**

Computers in Chemical Education

Dr. Frederick D. Tabbutt
Reed College
Portland, Oregon

January 19, 1970 **50¢**

A number of experiments with computers in education have been undertaken in the past few years. Some of the approaches to computer-assisted education now show promise as useful adjuncts as surrogate teachers. **11970**

Heterocycles

Alan R. Katritzky
University of East Anglia
England

April 13, 1970 **50¢**

The article examines some of the recent advances in heterocyclic chemistry—a field important to understanding biochemical mechanisms, natural-product chemistry, dyes, pharmaceuticals, and polymers. **41370**

Chemical Frontiers in Biology

William F. Fallwell, C&EN

April 6, 1970 **50¢**

A review of the 58th annual meeting of the Federation of American Societies for Experimental Biology, Atlantic City, April 12-17, 1970, which explored molecular-level science from blood to brain chemistry, as well as other aspects of biology and biochemistry. **04670**

Rubber in the 70's

Ernest L. Carpenter, C&EN

April 27, 1970 **50¢**

More than ever before, costs will likely become a bigger influence in the direction taken by the rubber industry's research and development during the 1970's. The means by which the industry will attempt to overcome its performance-cost dilemma will likely wed polymer technology with that of instruments, computers, and processing chemicals. **42770**

Textiles in the 70's

Walter S. Fedor
Technomic Publishing Co.
Stamford, Conn.

April 20, 1970 **50¢**

The once sluggish textile industry now enjoys an unprecedented demand for its products. This demand is created by a rapidly growing population with more money available for textile purchases than a decade or so ago, as well as a growing consumer desire for the many man-made fibers that offer improved performance, durability, or aesthetic values. **42070**

Chaos in Science Teaching

Dr. Conrad E. Ronneberg
Professor Emeritus, Denison University

June 1, 1970 **50¢**

To many people familiar with the situation in teaching introductory science courses, both in high school and college, the situation is utter chaos. To place attempts to improve science teaching in proper perspective requires a brief review of the progress of science teaching since World II. **06170**

Allergy

Howard J. Sanders, C&EN

May 11, 1970 **50¢**

Although hay fever, bronchial asthma, and other allergies will not be conquered, they will be better understood and better treated. The expanding study of these diseases in fundamental scientific terms, using the latest research techniques, allergic disorders will yield more and more of their secrets that only a few years ago seemed almost unfathomable. **5117C**

Arthritis

A 3-part feature
Howard J. Sanders, C&EN

July 22, 29, & Aug. 12, 1968 **75¢**

Causes of arthritis are still a mystery, although more and more evidence points to infection as a possible trigger. Mr. Sanders discusses and examines the possible causes and the past, present, and future of treatment. **07228**

Population

A 2-part feature
David M. Kiefer, C&EN

Oct. 7 & 14, 1968 **75¢**

Mr. Kiefer finds that population is growing unchecked in much of the world, and that U.S. population will expand 50% in the next 30 years or so. Social as well as technological innovation is needed to thwart this advance. **10148**

Infrared Spectroscopy

Dr. Kermit Whetsel
Tennessee Eastman Co.

Feb. 5, 1968 **50¢**

The usefulness of ir spectroscopy is widening. Dr. Whetsel examines the developments in instrumentation, data handling, technique, and applications, that promise greater utility in the future. **02058**

1 to 49 copies—single copy price 50 to 299 copies—20% discount

Prices for larger quantities available on request

☐ 12670 ☐ 12229 ☐ 03970

☐ 02970 ☐ 11970 ☐ 41370

☐ 04670 ☐ 42770 ☐ 42070 ☐ 06170

☐ 51170 ☐ 07228 ☐ 10148 ☐ 02058

TO: REPRINT DEPARTMENT

ACS Publications
1155 Sixteenth St., N.W.
Washington, D.C. 20036

FROM:

Name _____

Street _____

City _____

State _____ Zip Code _____

Amount enclosed $_____

THE JOURNAL OF

PHYSICAL CHEMISTRY

AMERICAN CHEMICAL SOCIETY, PUBLICATIONS DIVISION,
1155 Sixteenth St., N.W., Washington, D. C. 20036
RICHARD L. KENYON, *Director*
JOSEPH H. KUNEY, *Director of Business Operations and Director of Publications Research*
DAVID E. GUSHEE, *Publication Manager, Journals*

 Published biweekly by the American Chemical Society at 20th and Northampton Sts., Easton, Pa. 18042. Second-class postage paid at Easton, Pa.

All manuscripts should be sent to *The Journal of Physical Chemistry,* Department of Chemistry, University of Minnesota, Minneapolis, Minn. 55455.

Additions and Corrections are published once yearly in the final issue. See Volume 74, Number 26 for the proper form.

Extensive or unusual alterations in an article after it has been set in type are made at the author's expense, and it is understood that by requesting such alterations the author agrees to defray the cost thereof.

The American Chemical Society and the Editor of *The Journal of Physical Chemistry* assume no responsibility for the statements and opinions advanced by contributors.

Correspondence regarding accepted copy, proofs, and reprints should be directed to Editorial Production Office, American Chemical Society, 20th and Northampton Sts., Easton, Pa. 18042. Manager: CHARLES R. BERTSCH. Assistant Editor: EDWARD A. BORGER. Editorial Assistant: EVELYN J. UHLER.

Advertising Office: Century Communications Corporation, 142 East Avenue, Norwalk, Conn. 06851.

Business and Subscription Information

Remittances and orders for subscriptions and for single copies, notices of changes of address and new professional connections, and claims for missing numbers should be sent to the Subscription Service Department, American Chemical Society, 1155 Sixteenth St., N.W., Washington, D. C. 20036. Allow 4 weeks for changes of address. Please include an old address label with the notification.

Claims for missing numbers will not be allowed (1) if received more than sixty days from date of issue, (2) if loss was due to failure of notice of change of address to be received before the date specified in the preceding paragraph, or (3) if the reason for the claim is "missing from files."

Subscription rates (1971): members of the American Chemical Society, $20.00 for 1 year; to nonmembers, $40.00 for 1 year. Those interested in becoming members should write to the Admissions Department, American Chemical Society, 1155 Sixteenth St., N.W., Washington, D. C. 20036. Postage to Canada and countries in the Pan-American Union, $4.00; all other countries, $5.00. Single copies for current year: $2.00. Rates for back issues from Volume 56 to date are available from the Special Issues Sales Department, 1155 Sixteenth St., N.W., Washington, D. C. 20036.

This publication and the other ACS periodical publications are now available on microfilm. For information write to: MICROFILM, Special Issues Sales Department, 1155 Sixteenth St., N.W., Washington, D. C. 20036.

Notice to Authors last printed in the issue of December 24, 1970

ISOTOPE EFFECTS IN CHEMICAL PROCESSES
ADVANCES IN CHEMISTRY SERIES NO. 89

Thirteen papers from a symposium by the Division of Nuclear Chemistry and Technology of the American Chemical Society, chaired by William Spindel. Includes:

- Separating isotopes by chemical exchange, distillation, gas chromatography, electromigration, and photochemical processes
- Methods for fractionating isotopes of hydrogen, lithium, boron, carbon, and nitrogen
- Thermotransport in monatomic and ionic liquids
- Statistical-mechanical theory determining isotope effects

278 pages with index Clothbound (1969) $13.00

Set of L.C. cards free with library orders upon request

Other books in the ADVANCES IN CHEMISTRY SERIES in physical and colloid chemistry include:

No. 87 Interaction of Liquids at Solid Substrates. Twelve papers survey recent research on solid/liquid interaction, including work on "coupling agents," adhesion of polymers, organic/inorganic interfaces, ultrasonic impedometry. Four more papers are concerned with heparinized surfaces at the blood/material interface. 212 pages
Cloth (1968) $9.50

No. 84 Molecular Association in Biological and Related Systems. Nineteen articles survey and report new work on molecular association in fat digestion, in soap systems, in membrane constituents, and in mixed monolayers. Other topics include bile salt micelles, lipid monolayers and membranes, and a definitive review of biological membrane structure. 308 pages
Cloth (1968) $10.50

No. 82 Radiation Chemistry—II. Thirty-six papers and 17 abstracts on radiation chemistry in gases, solids, and organic liquids. Includes three plenary lectures. 558 pages
Cloth (1968) $16.00

No. 81 Radiation Chemistry—I. Forty-one papers and 17 abstracts on radiation chemistry in aqueous media, biology, and dosimetry. From the international conference at Argonne National Laboratory. 616 pages
Cloth (1968) $16.00
No. 81 and No. 82 ordered together $30.00.

No. 79 Adsorption from Aqueous Solution. Fifteen papers discuss thermodynamic and kinetic aspects of adsorption phenomena and the results of studies on a variety of adsorbate-adsorbent systems. 212 pages
Cloth (1968) $10.00

No. 68 Mössbauer Effect and its Application in Chemistry. Ten papers that will familiarize chemists with Mössbauer spectroscopy as an analytical tool, for studying chemical bonding, crystal structure, electron density, magnetism, and other properties. 178 pages
Cloth (1967) $8.00

No. 67 Equilibrium Concepts in Natural Water Systems. Sixteen papers represent the collaboration of aquatic chemists, analytical chemists, geologists, oceanographers, limnologists, and sanitary engineers, working with simplified models to produce fruitful generalizations and valuable insights into the factors that control the chemistry of natural systems. 344 pages
Cloth (1967) $11.00

No. 64 Regenerative EMF Cells. Seventeen papers survey current progress and research on regenerative systems for converting and storing electrical energy. Principal emphasis is on thermally regenerative systems, but chemical and photochemical systems are considered. 309 pages
Cloth (1967) $11.00

No. 63 Ordered Fluids and Liquid Crystals. Twenty-two studies on characterization, properties, and occurrence of these phenomena in many substances such as tristearin, p-azoxyanisole, mono-and di-hydric alcohols, phospholipids and polypeptides. 332 pages
Cloth (1967) $11.50

No. 58 Ion-Molecule Reactions in the Gas Phase. Eighteen papers survey spectrometric and other methods for producing and studying ion-molecule reactions, such as pulsed sources for studying thermal ions, reactions in flames and electrical discharges. 336 pages
Cloth (1966) $10.50

No. 54 Advanced Propellant Chemistry. Primarily directed to the search for new oxidizers; 26 papers survey oxygen-containing oxidizers, fuels and binders, fluorine systems including oxygen difluoride and difluoramines and liquid systems. 290 pages
Cloth (1966) $10.50

No. 50 Solvated Electron. Reviews of theory, structure, reactions of solvated and hydrated electrons; detailed papers on electrical transport properties, photochemistry, theory of electron transfer reactions, structure of solvated electrons, hydrated electron research. 304 pages
Cloth (1965) $10.50

No. 47 Fuel Cell Systems. Developments in theory, performance, construction, and new systems for the energy converter that is proving itself in military and space uses. 360 pages
Cloth (1965) $10.50

No. 43 Contact Angle, Wettability, and Adhesion. Twenty-six papers on theoretical and practical approaches to wettability and adhesion; with summary of the surface chemical studies of W. A. Zisman, the 1963 Kendall Award winner. 389 pages
Cloth (1964) $10.50

No. 40 Mass Spectral Correlations. By Fred W. McLafferty. Over 4000 spectra listed by mass/charge ratios of fragment ions with the most probable original structures for each. 117 pages
Paper (1963) $6.00

No. 33 Solid Surfaces and the Gas-Solid Interface. Thirty-seven papers from the Kendall Award Symposium honoring Stephen Brunauer. Theory and techniques for studying surface phenomena.
Cloth (1961) $12.00

No. 31 Critical Solution Temperatures. By Alfred W. Francis. CST answers the question, "Do two liquids mix?" and is widely used for screening solvents. Over 6000 systems are included, 70% with a hydrocarbon as one component; nearly 1100 non-hydrocarbon solvents are listed. 246 pages
Cloth (1961) $8.00

All books postpaid in U.S. and Canada; plus 20 cents in PUAS and elsewhere.

Order from: SPECIAL ISSUES SALES
AMERICAN CHEMICAL SOCIETY
1155 SIXTEENTH ST., N.W.
WASHINGTON, D.C. 20036

THE JOURNAL OF

PHYSICAL CHEMISTRY

Volume 75, Number 5 March 4, 1971

NOTES

COMMUNICATIONS TO THE EDITOR

AUTHOR INDEX

THE JOURNAL OF
PHYSICAL CHEMISTRY

VOLUME 75, NUMBER 5 MARCH 4, 1971

Reactions of Deuterated Methyl Radicals with Methylfluorosilanes. Polar Effects in Hydrogen Abstraction

by T. N. Bell* and A. E. Platt

Department of Chemistry, Simon Fraser University, Burnaby 2, B. C., Canada *(Received July 8, 1970)*

Publication costs borne completely by The Journal of Physical Chemistry

The abstraction of hydrogen by CD_3 radicals (source, photolysis of Ac-d_6) from the methylfluorosilanes CH_3SiF_3, $(CH_3)_2SiF_2$, $(CH_3)_3SiF$, and $(CH_3)_4Si$ was studied over the temperature range 150–300° in the gas phase. The following Arrhenius parameters were obtained: log k (ml mol^{-1} sec^{-1}) = 12.1 − (12,560/2.3RT), $MeSiF_3$; log k (ml mol^{-1} sec^{-1}) = 12.0 − (12,110/2.3RT), Me_2SiF_2; log k (ml mol^{-1} sec^{-1}) = 12.0 − (11,530/2.3RT), Me_3SiF; log k (ml mol^{-1} sec^{-1}) = 12.0 − (10,790/2.3RT), Me_4Si. The increase in reactivity with successive replacement of fluorine atoms by methyl groups we suggest is due to a decrease in the C–H bond strength. The importance of polar effects in the comparative reaction of CF_3 radicals is estimated and discussed.

Introduction

The present study continues our previous work concerned with the interaction of CF_3 radicals with halogen substituted silanes[1,2] and organometallic compounds[3] and was designed to determine the Arrhenius parameters for H abstraction by methyl radicals. The overall study is aimed at determining the factors controlling the reactivity of molecules to free-radical attack. The presence of an atom other than carbon, in the present case silicon, can lead to sufficient modification of the molecule that differences in reactivity can be enhanced, and this in turn linked to various molecular properties.

We expect that polar effects will be minimal in the reactions of CH_3 radicals with various substrates, and thus a comparison with the corresponding CF_3 reactions, where large differences in reactivity are observed, should lead to a better understanding of the importance of the extent of polar effects.

Experimental Section

Materials. A. Hexadeuterioacetone was obtained from Stohler Isotope Chemicals, and shown to contain none other than isotopic impurities, $(CD_3)_2CO$ (95%) and CD_3CHD_2CO (5%) (Hitachi Perkin-Elmer mass spectrometer RMU 6E). The acetone was thoroughly degassed and bulb-to-bulb distilled; then it was stored in a blackened bulb.

B. Methylfluorosilanes (Peninsula Chemical Research) were repeatedly fractioned with rejection of large head and tail fractions. CH_3SiF_3 was retained at −112°, $(CH_3)_2SiF_2$ at −99°, $(CH_3)_3SiF$ at −116°, and $(CH_3)_4Si$ at −90°.

Apparatus. This was described previously.[1] Ethane and methane were fractionated at −160° and transferred by Toepler pump to glass ampoules. They were subsequently analyzed by gas chromatography. Isolation of methane alone from the reaction mixture was carried out by fractionation at −196°. Analysis was by mass spectrometry (Hitachi RMU 6E).

Results

Photolysis of Acetone-d_6. The photolysis of hexadeuterioacetone was used as a source of CD_3 radicals; under

(1) T. N. Bell and U. F. Zucker, *J. Phys. Chem.*, **74**, 979 (1970).
(2) T. N. Bell and U. F. Zucker, *Can. J. Chem.*, **48**, 1209 (1970).
(3) T. N. Bell and A. E. Platt, *Int. J. Chem. Kinet.*, **2**, 299 (1970).

our experimental conditions the photolysis is adequately described by reaction 1. Secondary reactions of the

$$CD_3COCD_3 \xrightarrow{h\nu} 2CD_3 + CO \quad (1)$$

CD_3 radicals give rise to CD_4, CD_3H (from isotopic impurity), and C_2D_6, through reactions 2, 3, and 4.

$$CD_3 + (CD_3)_2CO \longrightarrow CD_4 + CD_2COCD_3 \quad (2)$$

$$CD_3 + CD_3COCHD_2 \longrightarrow CD_3H + CD_3COCD_2 \quad (3)$$

$$2CD_3 \longrightarrow C_2D_6 \quad (4)$$

From (2) and (4)

$$R_{CD_4}/R_{C_2D_6}^{1/2} = k_2[HDA]/k_4^{1/2} \quad (5)$$

A series of experiments were carried out between 150 and 300° to determine R_{CD_4} and $R_{C_2D_6}$ for acetone pressures of 30 mm, and hence by application of eq 5 to determine $k_2/k_4^{1/2}$. An Arrhenius plot of the data treated by the method of least squares, and using a value[4] for $k_4 = 10^{13.34}$ ml mol^{-1} sec^{-1} yielded the following Arrhenius parameters for reaction 2: $\log A_2 = 12.0 \pm 0.04$, $E_2 = 11.97 \pm 0.08$ kcal/mol. The error limits here and elsewhere are standard deviations. These results are in reasonable agreement with previous workers for D abstraction from HDA by CD_3 radicals. The most recent data on this reaction yield $\log A_2 = 11.6$, $E_2 = 11.5$[5] and $\log A_2 = 11.7$, $E_2 = 11.4$.[6]

Photolysis of Acetone-d_6 + Silanes. In the presence of the silanes $Si(Me)_4$, $FSi(Me)_3$, $F_2Si(Me)_2$, $F_3Si(Me)$, an additional source of methane arises through reaction 6. We assume the reaction between $CD_3 + CH_2Si<$

$$CD_3 + CH_3Si< \longrightarrow CD_3H + CH_2Si< \quad (6)$$

does not give rise to significant amounts of CD_3H.

Two methods are available to determine k_6. Method A is by direct comparison of the methane produced in (6) to the methane produced in (2), yielding k_6 relative to k_2. This method requires mass spectrometric analysis in all experiments. Method B, whereby the total methane is measured, is corrected for that expected from reactions 2 and 3 (determined from the photolysis of HDA alone), and k_6 determined relative to k_4. This method does not require mass spectrometric analysis in all experiments.

Method B has been criticized by Pritchard and Pritchard[7] because of the possible error due to "nonzero extinction coefficients." Owing to limited mass spectrometric analytical capability we preferred method B. To determine whether method B involved significant error under our experimental conditions, $k_{6(SiMe_4)}$ was determined by both method A and method B. The results obtained show that no significant corrections need be made for nonzero extinction coefficients under our experimental conditions (see below).

$Si(Me)_4 + CD_3$ (Method A). In a series of experiments between 150 and 300°, the ratio CD_4/CD_3H was determined and corrected for any CD_3H resulting from reaction 2. From reactions 2 and 6 we have

$$\frac{R_{CD_4}[\text{silane}]}{R_{CD_3H}[\text{Ac-}d_6]} = \frac{k_2}{k_6} \quad (7)$$

$k_6/k_4^{1/2}$ was determined by application of eq 7 and 5 to the experimental results. Least-squares treatment of the Arrhenius plot of $\log k_6/k_4^{1/2}$ yields, using the values obtained above for $k_2/k_4^{1/2}$, the following Arrhenius parameters for k_6: $\log A_6 = 12.0 \pm 0.12$, $E_6 = 10.82 \pm 0.26$ kcal/mol.

$Si(Me)_4 + CD_3$ (Method B). From the methane producing reactions 2, 3, and 6, we define R_1(methane) = methane produced from (2) and (3), and R_2(methane) = methane produced from (6), and R_3(methane) = total methane produced. Thus

$$\frac{R_1(\text{methane})}{R_1^{1/2}C_2D_6} = \frac{k_2[\text{Ac-}d_6] + k_3[\text{Ac-}d_5]}{k_4^{1/2}} \quad (8)$$

$$\frac{R_2(\text{methane})}{R_2^{1/2}C_2D_6} = \frac{k_6[\text{silane}]}{k_4^{1/2}} \quad (9)$$

$$\frac{R_3(\text{methane})}{R_3^{1/2}C_2D_6} = \frac{R_1(\text{methane})}{R_1^{1/2}C_2D_6} + \frac{R_2(\text{methane})}{R_2^{1/2}C_2D_6} \quad (10)$$

Hence

$$\frac{R_3(\text{methane})}{R_3^{1/2}C_2D_6} - \frac{R_1(\text{methane})}{R_1^{1/2}C_2D_6} = \frac{R_2(\text{methane})}{R_2^{1/2}C_2D_6} = \frac{k_6[\text{silane}]}{k_4^{1/2}} \quad (11)$$

In a series of experiments at 150° in the presence and absence of silane and using a constant pressure of acetone, $R_3(\text{methane})/R_3^{1/2}C_2D_6$ and $R_1(\text{methane})/R_1^{1/2}C_2D_6$ were determined for various pressures of silane. The straight line relationship predicted by eq 11 was verified from the experimental results which are plotted in Figure 1.

In a second series of experiments at differing temperatures, $k_6/k_4^{1/2}$ was determined through application of eq 11 to the experimental results. The results tabulated in Table I are plotted in Arrhenius form, Figure 2. From a least-squares evaluation of the data, and using a value[4] for $k_4 = 10^{13.34}$ ml mol^{-1} sec^{-1}, the following Arrhenius parameters were obtained for k_6: $\log A_6 = 12.0 \pm 0.10$, $E_6 = 10.79 \pm 0.22$ kcal/mol. Excellent agreement is seen between the Arrhenius parameters for reaction 6, using either method A or method B; accordingly, method B was used for all other evaluations of k_6 involving the methylfluorosilanes.

(4) A. Shepp, *J. Chem. Phys.*, **24**, 939 (1956).
(5) P. Gray and A. A. Herod, *Trans. Faraday Soc.*, **62**, 1568 (1968).
(6) R. Shaw and J. C. J. Thynne, *ibid.*, **62**, 104 (1966).
(7) H. O. Pritchard and G. O. Pritchard, *Can. J. Chem.*, **41**, 3042 (1963).

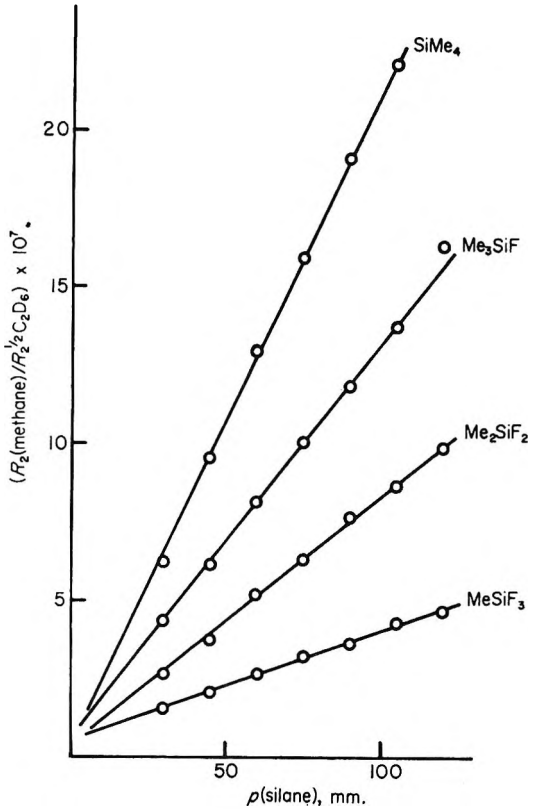

Figure 1. Variation of $R_2(\text{methane})/R_2^{1/2}C_2D_6$ *vs.* p(silane), temp 150°.

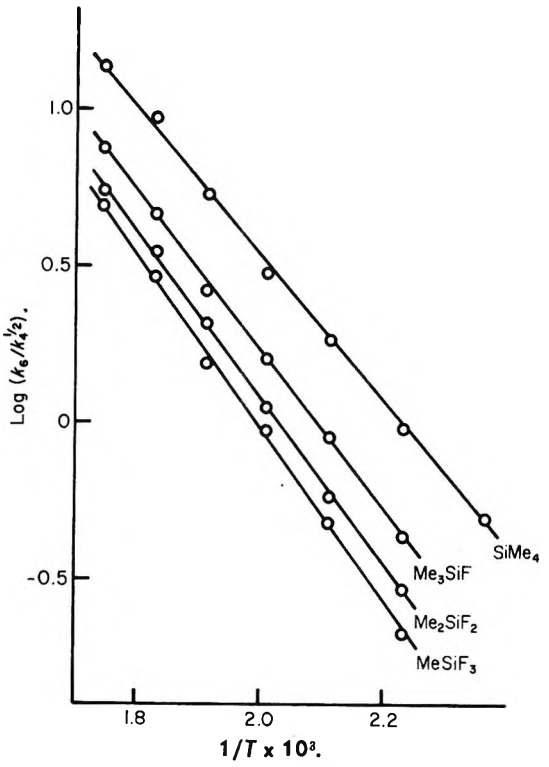

Figure 2. Arrhenius plot, log $k_6/k_4^{1/2}$ *vs.* $1/T$.

Table I: Values Obtained for $k_6/k_4^{1/2}$ ($ml^{1/2}$ $mol^{-1/2}$ $sec^{-1/2}$) for CD_3 + $CH_3Si<$ Obtained by Method B[a]

Temp, °C	$SiMe_4$	$FSiMe_3$	F_2SiMe_2	F_3SiMe
150	0.63			
175	0.97	0.436	0.293	0.213
200	1.86	0.90	0.581	0.479
225	3.01	1.60	1.12	0.944
250	5.35	2.64	2.07	1.55
275	9.42	4.66	3.49	2.93
300	13.80	7.57	5.48	4.92

[a] p(acetone), 30 mm; p(silane), 30 mm in all cases.

Previously reported values for $k_{6(SiMe_4)}$ yields log A_6 11.8, E_6 = 10.4 kcal/mol,[8] log A_6 11.5, E_6 = 10.3 kcal/mol.[9]

CD_3 + $FSiMe_3$, F_2SiMe_2, F_3SiMe (Method B). A series of experiments similar to the above were carried out at 150° to check the validity of eq 11 for each of the silanes. The results plotted in Figure 1 accord with the predicted linear relationship, $R_2(\text{methane})/R_2^{1/2}$-$C_2D_6$ *vs.* [silane].

From the application of eq 11 to a series of experimental results obtained over the temperature range 150 to 300°, the values of $k_6/k_4^{1/2}$ shown in Table I were derived. An Arrhenius plot of the results is shown, Figure 2. $k_6/k_4^{1/2}$ was determined by the method of least squares, and hence using a value[4] for $k_4 = 10^{13.34}$ ml mol^{-1} sec^{-1}, a value for k_6 and the associated Arrhenius parameters was obtained. The parameters are tabulated in Table II.

Table II: Arrhenius Parameters for H Abstraction by CD_3 and CF_3

	CD_3		CF_3[a]	
Substrate	log A	E, kcal/mol	log A	E, kcal/mol
$(CH_3)_4Si$	12.0 ± 0.1	10.79 ± 0.22	11.9	7.3
$(CH_3)_3SiF$	12.0 ± 0.12	11.53 ± 0.21	12.4	9.5
$(CH_3)_2SiF_2$	12.0 ± 0.05	12.11 ± 0.12	12.3	10.5
$(CH_3)SiF_3$	12.1 ± 0.12	12.56 ± 0.25	12.0	11.7

[a] See ref 1.

Discussion

The reactivity of methylhalosilanes towards free-radical attack has been the subject of a recent discussion. It has been observed that A factors in these and similar systems[1,2,8-11] fall in the range $10^{11.5}$–$10^{12.5}$. The A

(8) J. A. Kerr, A. Stephens, and J. C. Young, *Int. J. Chem. Kinet.*, **1**, 339 (1969).

(9) E. R. Morris and J. C. J. Thynne, *J. Phys. Chem.*, **73**, 3294 (1969).

(10) O. P. Strausz, E. Jakubowski, H. S. Sandhu, and H. E. Gunning, *J. Chem. Phys.*, **51**, 552 (1969).

(11) O. P. Strausz, E. Jakubowski, H. S. Sandhu, and H. E. Gunning, *ibid.*, in press.

factors obtained in the present work fall into this normal range. From the measured Arrhenius parameters it is very clear that variations in reactivity of the various substrates in this work, namely the methylfluorosilanes, are a function of activation energy differences. The present results are collected in Table II where the analogous reactions involving CF_3 radicals are also included. Both sets of results are discussed below.

In interpreting the CD_3–silane reactivities, we make a basic assumption that polar effects are minimal or nonexistent in hydrogen abstraction reactions by methyl radicals. Thus we consider that the variation in activation energy observed along the series of substrates is purely due to differences in the heats of reaction, brought about by differences in the C–H bond energies among the compounds studied.

An estimate of these C–H bond energies can be made from the application of the Polanyi equation, $E = 0.49.(D_{C-H} - 74.3)$, recently tested by Trotman-Dickenson.[12] Thus from the experimental results involving methyl radicals we obtain the following estimates for the C–H bond strengths, D_{C-H}; $SiMe_4$ = 96.3; $FSiMe_3$ = 97.8; F_2SiMe_2 = 99.0; F_3SiMe_3 = 99.9 kcal/mol.

Our estimate for D_{C-H} in $SiMe_4$ compares extremely well with the estimate 97 kcal/mol made by Kerr, Stephens, and Young.[8]

The reactivity of neopentane[13] is less than that of tetramethylsilane with respect to hydrogen abstraction by methyl radicals. This is to be expected when the bond strengths are considered: $D_{C-H}(CMe_4) \simeq 99$ kcal,[14] $D_{C-H}(SiMe_4) \simeq 97$ kcal. The corresponding difference in activation energy is 1.2 kcal using E_{CMe_4} = 12.0 kcal,[13] E_{SiMe_4} = 10.8 kcal (this work), and 1.6 kcal using[8] E_{SiMe_4} = 10.4 kcal.

For the purpose of further discussion, we will assume a contribution of 1.5 kcal (average of above) to the activation energy, for a 2-kcal difference in heat of reaction for systems having overall exothermicities similar to those in the above two cases.

In comparing the difference in activation energy for attack by CF_3 and CD_3 radicals on a given substrate, an added effect is through possible polar effects involving the electrophilic CF_3 radical. The difference in heats of reaction for attack on a given compound will be due to the difference $D_{CF_3-H} - D_{CH_3-H} \simeq 106–104 \simeq 2$ kcal.[14,15] For the compounds under study here, the overall exothermicities are in the same range as for the CMe_4 and $SiMe_4$ systems, and using the arguments above, we ascribe a ball park value of ~1.5 kcal as the difference $E_{CD_3} - E_{CF_3}$ expected, due to heat of reaction differences.

The magnitude of the observed difference $E_{CD_3} - E_{CF_3}$, Table III, is very variable along the series $Si(Me)_4$ to F_3SiMe. In a previous paper Bell and Zucker[1] correlated the activation energy for CF_3 attack with the proton chemical shift and suggested that the large differences for E_{CF_3} compound to compound were in part due to polar effects. By using the data now obtained for the corresponding CD_3–silane systems, we can now attempt to estimate the magnitude of the polar interaction.

Table III: Estimated Bond Dissociation Energies C–H and Polar Term δ for CF_3 Attack

	D_{C-H}	$E_{CD_3} - E_{CF_3}$, kcal mol^{-1}	δ, kcal mol^{-1}
$(CH_3)_4Si$	96	3.5	+2.0
$(CH_3)_3SiF$	98	2.0	+0.6
$(CH_3)_2SiF_2$	99	1.6	+0.1
$(CH_3)SiF_3$	100	0.8	−0.7

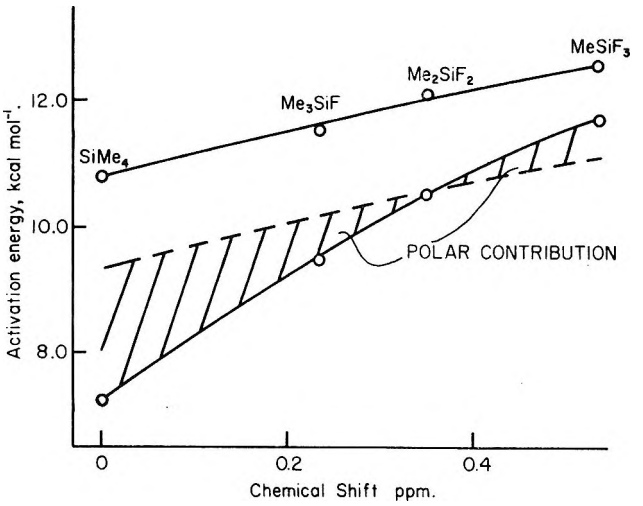

Figure 3. Correlation of activation energy for H abstraction by CF_3 and CD_3 with proton chemical shift. The circles on the upper curve designate CD_3 attack; those on the lower curve, CF_3 attack.

In Figure 3 is plotted the activation energy for CH_3 and CF_3 attack on each silane against the proton chemical shift. The dotted line is set parallel to the methyl reactivity line, some 1.5 kcal below; we suggest this should represent the activation energy difference due to ΔH effects as discussed above.

An additional lowering of the activation energy thus occurs for CF_3 attack in the case of $Si(Me)_4$, Me_3SiF, and Me_2SiF_2 of 2.0, 0.6, and 0.1 kcal, respectively. In the case of $MeSiF_3$, the activation energy difference is less than expected from ΔH considerations by some 0.7 kcal.

If the chemical shift values parallel changes in the electron density on the H atom, then the greatest difference $E_{CD_3} - E_{CF_3}$ is observed with that system having the greatest electron density on the hydrogen atom,

(12) A. F. Trotman-Dickenson, *Chem. Ind. (London)*, 379 (1965).
(13) J. A. Kerr and D. Timlin, *J. Chem. Soc. A*, 1241 (1969).
(14) J. A. Kerr, *Chem. Rev.*, **66**, 465 (1966).
(15) J. C. Amphlett, J. W. Coomber, and E. Whittle, *J. Phys. Chem.*, **70**, 593 (1966).

namely $Si(Me)_4$. As the electron density decreases, so do the observed activation energy differences $E_{CD_3} - E_{CF_3}$.

Further evidence that the H-atom electron density decreases $SiMe_4 \rightarrow MeSiF_3$ is obtained from the quenching cross sections of these compounds with respect to triplet Hg, if this is regarded as an electrophile.[16]

Qualitatively this pattern would be expected from electronegativity considerations (C 2.5, Si 1.8, F 4.0). The inductive effect of fluorine should lessen the drift towards the methyl group and reduce the hydrogen electron density.

Regarding the CF_3 radical as electrophilic in nature, we suggest there is a polar effect operative which lowers the activation energy for H abstraction in the case of $SiMe_4$, $FSiMe_3$, and F_2SiMe_2. Bell and Zucker suggested that this could be incorporated in a Polanyi-type relationship of the form

$$E \propto (\text{constant} - \Delta H) - \delta$$

where δ represents a polar effect and ΔH the heat of reaction.

We note that $E_{CD_3} - E_{CF_3}$ is less than expected on ΔH considerations in the case of $MeSiF_3$. In some cases of H abstraction it has been noticed that $E_{CF_3} > E_{CH_3}$ notably in the cases of HCl,[17] HBr,[18] H_2S,[19,20] $SiHCl_3$.[21] In these cases the hydrogen atom is protonic in nature and forms the positive end of a dipole. It has been suggested that polar effects may be responsible for increasing E_{CF_3} in these cases. On the other hand, in the case[9-11] of SiH_4, $E_{CF_3} < E_{CH_3} \simeq 2$ kcal. In this case the H atom should be much more hydridic than in $SiHCl_3$, and any polar effect should tend to lower E_{CF_3}.

Thus we conclude that if the hydrogen electron density is reduced sufficiently, repulsion occurs between the electrophilic CF_3 radical and the hydrogen atom, and the activation energy increases. In the compounds under investigation we suggest that the crossover between the attractive and repulsive polar effects is between H-atom electron densities corresponding to F_2SiMe_2 and F_3SiMe.

The activation energy for CF_3 attack is thus a complex function of heat of reaction and polar effects, the latter increasing or decreasing E depending on whether the H atom is protonic or hydridic in nature.

$F_3C^{\delta+}$	$H^{\delta-}$–X	attractive polar effect
$F_3C^{\delta+}$	$H^{\delta+}$–X	repulsive polar effect

Estimates of the polar contribution, *i.e.*, δ terms, are collected in Table III. Whether δ can be calculated *a priori* for a given system remains to be seen. That this interaction, which would appear to be electrostatic in nature, can have a large effect on the energy of activation is very clear from the results obtained in many systems.

Acknowledgment. We are grateful to the National Research Council for financial support.

(16) M. A. Nay, G. N. C. Woodall, O. P. Strausz, and H. E. Gunning, *J. Amer. Chem. Soc.*, **87**, 179 (1965).

(17) J. C. Amphlett and E. Whittle, *Trans. Faraday Soc.*, **62**, 1662 (1966).

(18) B. G. Tucker and E. Whittle, *ibid.*, **61**, 866 (1965).

(19) N. L. Arthur and T. N. Bell, *Can. J. Chem.*, **44**, 1445 (1966).

(20) P. Gray, A. A. Herod, and L. J. Leyshon, *ibid.*, **47**, 689 (1969).

(21) J. A. Kerr, A. Stephens, and J. C. Young, *Int. J. Chem. Kinet.*, **1**, 371 (1969).

Pulse Radiolysis of Aqueous Cyanogen Solution[1a]

by I. G. Draganić,[1b] Z. D. Draganić,[1b] and R. A. Holroyd*

Chemistry Department, Brookhaven National Laboratory, Upton, L. I., New York 11973 *(Received September 10, 1970)*

Publication costs assisted by the U. S. Atomic Energy Commission

Pulse radiolysis has been used to study directly radiation-induced chemical changes in aqueous solutions of cyanogen. Reaction with the hydrated electron is fast, $k(e_{aq}^- + (CN)_2) = (2.1 \pm 0.2) \times 10^{10}\ M^{-1}\ sec^{-1}$. The absorption spectrum of the cyanogen ion-radical $(CN)_2^-$ shows two maxima at 290 and 440 nm, with respective molar extinction coefficients of 2100 and 360 $M^{-1}\ cm^{-1}$. The decay kinetics of the electron-adduct show a pseudo-first-order and a second-order process as two consecutive processes; probable reactions are discussed. The reactions of H and OH with cyanogen are slow in dilute solutions, and the rate constants were estimated as $<10^7\ M^{-1}\ sec^{-1}$. The formation of iminoacetonitrile radical N–ĊCNH and oxime radical NC–ĊNOH was considered.

Introduction

The importance of the carbon–nitrogen triple bond in chemical evolution during the prebiological era[2,3] may explain the increasing interest in the chemistry and radiation chemistry of cyanogen compounds. The present paper describes our experiments with cyanogen, N≡C—C≡N. Gaseous $(CN)_2$ has been studied by flash photolysis,[4,5] but there are no published data on the radiation chemistry of aqueous solutions of cyanogen.

There is very little information on the chemistry of cyanogen dissolved in water.[6] Like other cyanogen compounds it hydrolyzes and polymerizes in aqueous solution,[7,8] but by application of fast reaction techniques the precursors of molecular products formed in irradiated aqueous solutions can be studied. Cyanogen is also very poisonous and pulsed beam experiments, with short irradiation and the possibility for direct observation of short-lived intermediates, minimizes the amount of sample handling required.

Experimental Section

The pulse radiolysis was carried out using a Febetron 705 system which provides a single pulse of 2-MeV electrons in a total time interval of less than 0.1 μsec. Some irradiations were also performed with a Van de Graaff machine, 1.9-MeV electron pulses of about 60-μsec duration. Dosimetry was carried out using two systems: (a) N_2O-saturated 0.1 M thiocyanate solutions and measuring the $(CNS)_2^-$ radical-ion at 500 nm, for which ϵ_{500} is 7600 $M^{-1}\ cm^{-1}$;[9] (b) N_2O-saturated solutions of 0.001 M ferrocyanide containing a small amount of air. The ferricyanide formed was followed at 420 nm and ϵ_{420} is 1000 $M^{-1}\ cm^{-1}$.[10] Both systems measure the free-radical yield and the value 5.4 was used for $G_{OH} + G_{e_{aq}^-}$ in the dose calculation. Absorbed doses varied from about 1 to 40 krads per pulse. The analysing light source was a 450-W xenon lamp. For Febetron irradiations its output was increased with an arc booster which provided a square pulse of 200 A for 2.5-msec duration. This increased the lamp intensity by approximately 60-fold in the ultraviolet. The optical arrangement allowed light path lengths through the cell of 4.0 and 6.1 cm in Febetron and Van de Graaff, respectively. High-intensity Bausch and Lomb gratings monochromators were used, and the light was detected by a photomultiplier (Amperex XP 1003) and oscilloscope (Tektronix 454) combination. The Febetron pulse and oscilloscope trace were delayed separately by 1.2 msec after the start of the light pulse. At this time the light pulse was flat for ~0.2 msec. Scattered light was reduced by suitable orientation of a quartz prism placed in the front of the monochromator. Cyanogen gas (Matheson) was used without additional purification. Triply distilled water was deaerated by bubbling with helium. The syringe technique[11] was used to prepare samples with various cyanogen concentrations; a saturated solution was diluted and the cyanogen content calculated from the solubility data[12,13] and the

(1) (a) Research performed under the auspices of the U. S. Atomic Energy Commission; (b) on leave from Boris Kidrič Institute of Nuclear Sciences, Vinča, Yugoslavia.

(2) (a) G. W. Fox, Ed., "The Origins of Prebiological Systems," Academic Press, New York, N. Y., 1965; (b) M. Calvin, "Chemical Evolution," Oxford University Press, London, 1969.

(3) R. M. Lemon, *Chem. Rev.*, **70**, 95 (1970).

(4) D. E. Paul and F. W. Dalby, *J. Chem. Phys.*, **37**, 592 (1962).

(5) N. Basco and K. K. Yee, *Chem. Commun.*, 150 (1968).

(6) T. K. Brotherton and J. W. Lynn, *Chem. Rev.*, **59**, 841 (1959).

(7) R. Nauman, *Z. Elektrochem.*, **18**, 772 (1910).

(8) R. L. Webb, "Hydrogen Cyanide and Cyanogen Polymers," in "Encyclopedia of Polymer Science and Technology," Vol. 7, Wiley, New York, N. Y., 1967, p 571.

(9) J. H. Baxendale, P. L. T. Bevan, and D. A. Scott, *Trans. Faraday Soc.*, **64**, 2389 (1968).

(10) P. Pagsberg, H. Christensen, J. Rabani, G. Nilsson, J. Fenger, and S. O. Nielsen, *J. Phys. Chem.*, **73**, 1029 (1969).

(11) E. J. Hart, "The Hydrated Electron," in "Actions Chimiques et Biologiques des Radiations," Vol. 10, M. Haissinsky, Ed., Masson, Paris, 1966, p 11.

(12) A. Seidel, "Solubilities of Inorganic and Metal Organic Compounds," Van Nostrand, Princeton, N. J., 1940, p 216.

dilution factor. The solutions studied were at a natural pH of about 6. Since added substances accelerated chemical changes (see below), no buffer could be used.

Some irradiations (1–2-min durations) were made with a laboratory ^{60}Co source. In such cases the optical densities were measured in a Cary 16 spectrophotometer at various time intervals after irradiation.

Nonirradiated Aqueous Solutions of Cyanogen. It is known[6,7] that concentrated cyanogen solutions change chemically on standing for a few hours. The first visible result is the appearance of a yellow color in the solution followed by a brownish precipitate. We have examined the optical density changes of dilute solutions in time conditions currently used in our irradiation experiments. Cyanogen was introduced directly into the optical cell, and the measurements were performed various times after the end of bubbling. Dilute cyanogen solutions do not absorb appreciably above 230 nm; below 230 nm the absorption increases with decreasing wavelength. Absorbancy increases with time and with the initial concentration of $(CN)_2$. The increase is especially pronounced in the far-uv (<230 nm). However, as confirmed in irradiation experiments, these changes do not present an obstacle if the measurements are performed 1 to 2 hr after the solution preparation. Most of the measurements were made at wavelength > 240 nm, where the nonirradiated solution does not absorb appreciably. This is not the case if some other substances are present in the solution. Depending on the nature and concentration, they often cause such an increase in absorbancy that the use of scavengers is extremely delicate if not impossible. The chemistry that takes place in such cases is not well understood. It is even more complex in the presence of radiation, as shown by the analysis of kinetic data. We have studied the following solutes known to be good free-radical scavengers: CH_3OH, H_2O_2, KCNS, HCOONa, KCN, KNO_3, and N_2O. The conclusion reached was that they are, with the exception of N_2O, unsuitable for competition experiments in the presence of cyanogen. The effect of pH variations could not be studied since the presence of acids or bases in the aqueous solutions of cyanogen accelerates the hydrolysis and other chemical changes.

Results and Discussion

Figure 1 shows the absorption spectrum of transients observed in a helium-purged cyanogen solution (1.92×10^{-3} *M*) 0.2 μsec after the beginning of the Febetron pulse (9.9 krads). The shape of the spectrum is independent of cyanogen concentration (0.37×10^{-3} to 38.4×10^{-3} *M*) and independent of the dose in the pulse (4.7–37.3 krads). The maximum absorption is at 290 nm initially but shifts to shorter wavelengths following the pulse.

Our experiments have shown that cyanogen reacts

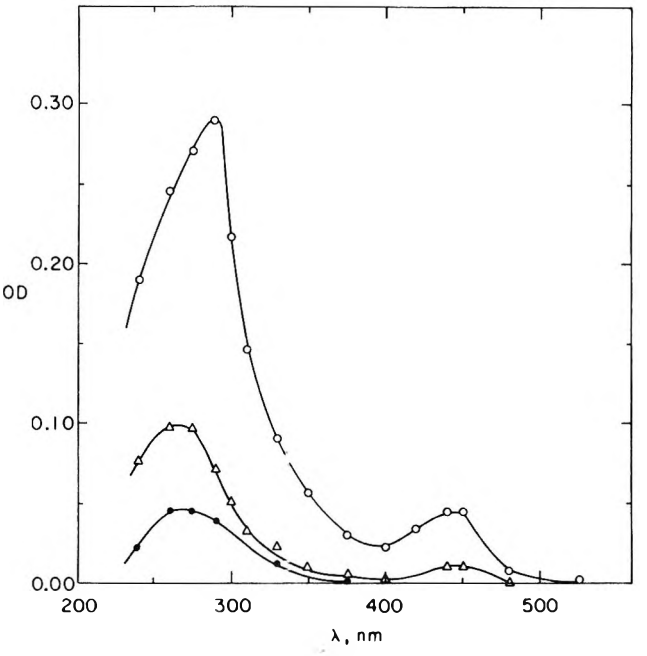

Figure 1. Absorption spectrum of transients observed in helium-purged aqueous solutions of cyanogen (1.92×10^{-3} *M*): ○, 0.2 μsec after the beginning of the Febetron pulse; △, 6 μsec after; ●, 40 μsec after; absorbed dose 9.9 krads/pulse.

very efficiently with hydrated electrons. The rate constant for this reaction was derived from the first-order decay of e_{aq}^- in dilute solutions of cyanogen (5×10^{-5} to 1×10^{-4} *M*). Appropriate corrections for decay in the absence of solute were applied. The value calculated from the experimental data is $(2.1 \pm 0.2) \times 10^{10}$ M^{-1} sec^{-1}. This value was confirmed by also following the buildup in absorption by the electron adduct in the uv range.

The presence of nitrous oxide in the solutions causes a decrease in absorbancy and the disappearance of absorption maxima. In these solutions the reaction of the

$$(CN_2) + e_{aq}^- \longrightarrow (CN)_2^- \qquad k_1 = 2.1 \times 10^{10}\ M^{-1}\ sec^{-1} \quad (1)$$

hydrated electron with cyanogen is in competition with its reaction with N_2O. The effect observed can be seen

$$N_2O + e_{aq}^- \longrightarrow OH + N_2 + OH^- \qquad k_2 = 8.67 \times 10^9\ M^{-1}\ sec^{-1}\ [14] \quad (2)$$

in Figure 2. The top curve gives the absorption spectrum in the uv range of a helium-purged dilute cyanogen solution (3.7×10^{-4} *M*). The dashed curve represents the same solution saturated with nitrous oxide (2.4×10^{-2} *M* N_2O), while the lower curve concerns helium-purged water saturated with N_2O (2.4×10^{-2} *M*). The doses in the pulse were the same within experi-

(13) "Handbook of Chemistry and Physics," Chemical Rubber Publishing Co., Cleveland, Ohio, 1960.

(14) S. Gordon, E. J. Hart, M. S. Matheson, J. Rabani, and J. K. Thomas, *Discussions Faraday Soc.*, **36**, 193 (1963).

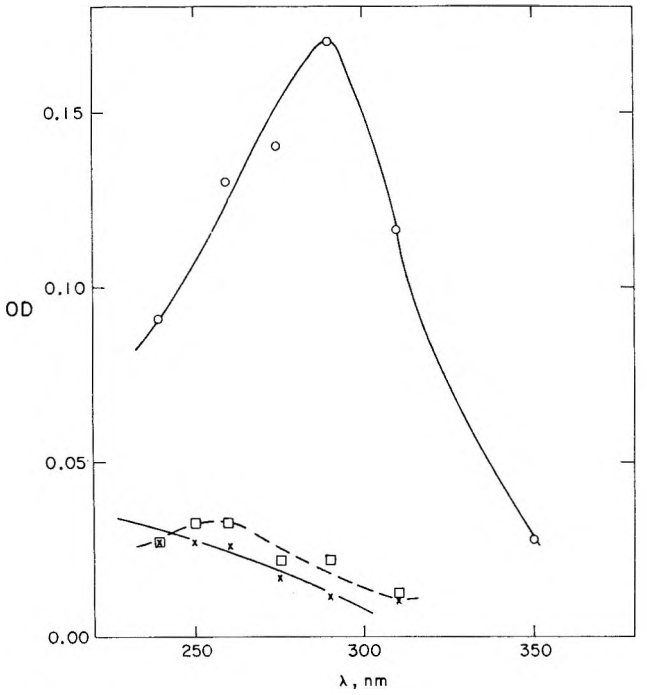

Figure 2. Absorption spectra of transients observed in 3.7×10^{-4} M cyanogen solutions: O, top curve, helium-purged solutions; □, dashed curve, 2.4×10^{-2} M N_2O present; X, lower curve, 2.4×10^{-2} M N_2O in helium-purged water. Lower solid line through the experimental data was calculated assuming $G_{OH} = 2.7$ and using molar extinction coefficients for OH radical according to Pagsberg, *et al.*[10] Absorbed dose, 4.72 krads/pulse; For lower curves OD = $0.5OD_{measured}$.

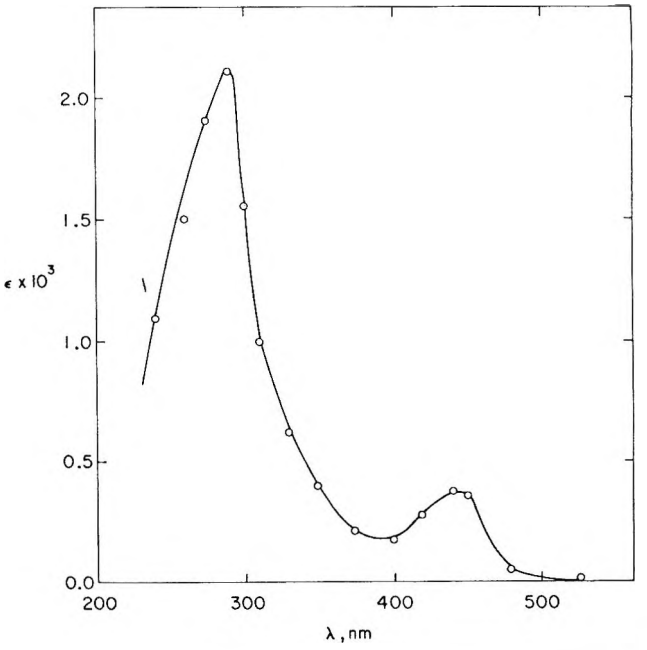

Figure 3. Absorption spectrum of cyanogen ion-radical $(CN)_2^-$ calculated as molar extinction coefficients.

mental error. It is significant that the lower curves differ very little. The solid line through the experimental data in Figure 2 was calculated assuming $G_{OH} = 2.7$ and using published molar extinction coefficients for the OH radical.[10] The difference between the two lower curves can be attributed to the incomplete conversion of the hydrated electron into OH in reaction 2 and to the presence of small amounts of the electron-adduct. The species giving rise to upper absorption curve could only be the electron-adduct $(CN)_2^-$ plus either the hydroxyl radical-adduct or, if the reaction 3 is

$$(CN)_2 + OH \longrightarrow \begin{matrix} \dot{C}NOH \\ | \\ CN \end{matrix} \qquad (3)$$

slow, the hydroxyl radicals themselves. Analysis of the experimental data excludes the oxime radical, which is the eventual product of reaction 3, as the possible contributor in the above conditions. As seen in Figure 2, the experimental data agree fairly well with the generally accepted trend for the hydroxyl radical.[10] Also kinetic analysis of the data indicates the presence of OH; a second-order decay is observed with a $2k \simeq 1 \times 10^{10}$ M^{-1} sec^{-1}.

Similar observations were made in nitrous oxide saturated solutions containing larger cyanogen concentrations (9.2×10^{-4} and 1.92×10^{-3} M). The conclusion was that the reaction of cyanogen with OH is slow in dilute solution ($k_3 \leqslant 10^7$ M^{-1} sec^{-1}), and the species contributing to the absorption shown in Figure 2 (top curve) are OH and $(CN)_2^-$ only. The presence of oxime radicals and reaction 3 would require investigations with larger concentrations of cyanogen.

Figure 3 shows the absorption spectrum of the electron-adduct, derived from the experimental data corrected for hydroxyl-radical contributions. The data in Figure 2 and the corresponding doses in pulse were used for correction calculations. The accuracy of such correction was considered sufficient as the OH contributions were low ($\leqslant 10\%$); only at 260 and 240 nm were they somewhat more important, up to about 20%.

The decay of the absorbancy shown in Figure 1 is fairly fast; about 40 μsec after a 9.9-krad pulse it is reduced to 20% of the initial value. Kinetic analysis of the experimental data was carried out at wavelengths where the OH contribution could be neglected (λ 440 and 450 nm), or the correction was low $\leqslant 10\%$ ($\geqslant 290$ nm) and the experimentally obtained corrections were considered as satisfactory. The two bands exhibit similar decay kinetics. The corrected decay can be resolved into two consecutive processes (Figure 4). At the beginning a fast first-order process which could be observed for only less than two half-lives ($\tau_{1/2} \simeq 2$ μsec); this process is followed with a second-order reaction.

The first-order process may be attributed to the reaction of cyanogen ion-radical with water. The

$$(CN)_2^- + H_2O \longrightarrow \begin{matrix} \dot{C}NH \\ | \\ CN \end{matrix} + OH^- \qquad (4)$$

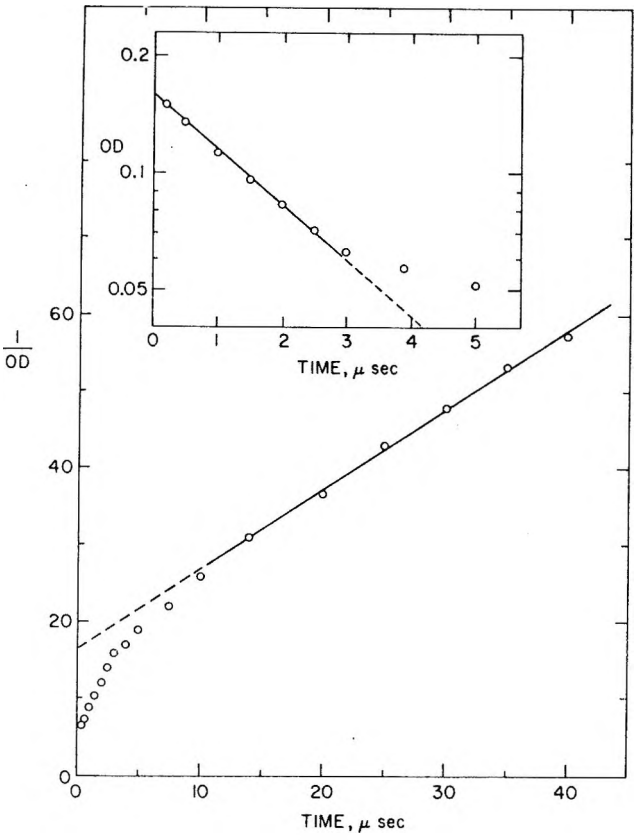

Figure 4. Second-order plot of the decay of transients in 3.7 × 10^{-4} M cyanogen solution. Insert: first-order plot of the data registered in the first 5 μsec; λ 290 nm; absorbed dose, 4.72 krads/pulse.

observed second-order decay could be the disappearance of the iminoacetonitrile radical formed in reaction 4. From the experimental data given in Figure 4 and

$$2\,\dot{C}NH(CN) \longrightarrow \left(\begin{matrix}CNH\\|\\CN\end{matrix}\right)_2 \xrightarrow{nH_2O} \text{products} \qquad (5)$$

also from similar observations at other wavelengths (275, 310, 440, 450 nm), we calculated $k_4 = (6 \pm 2) \times 10^3\ M^{-1}\ \text{sec}^{-1}$. The error is quite large as the first-order process could be observed for only less than two half-lives. For the second-order reaction the value $2k/\epsilon = 4 \times 10^6\ \text{sec}^{-1}$ was calculated from measurements at 290 nm. The molar extinction coefficient of the iminoacetonitrile was calculated assuming that no significant decay occurs during reaction 4. As seen in Figure 4, this assumption leads to a 25% higher value for the radical concentration and its real value should be somewhat lower. We therefore estimated $\epsilon_{290} = 900 \pm 150\ M^{-1}\ \text{cm}^{-1}$; hence, $2k_5 = 3.6 \pm 0.5 \times 10^9\ M^{-1}\ \text{sec}^{-1}$.

Some measurements were performed at various dose rates at λ 310 nm. They confirm the above assumptions. We found the half-life dependence characteristic of a second-order process and, for about 3 μsec, the first part of the kinetic curves follows a fast first-order process. However, one cannot completely exclude the possibility that reaction 4 is an artifact and that the first part of the curve is mixed kinetics involving a competition between reaction 6 and reaction 7. Since the

$$(CN)_2^- + OH \longrightarrow (CN)_2 + OH^- \qquad (6)$$

$$2(CN)_2^- \xrightarrow{2H_2O} \left(\begin{matrix}CNH\\|\\CN\end{matrix}\right)_2 + 2OH^- \qquad (7)$$

reaction of OH radicals with cyanogen is slow, reaction 6 should occur during the first few microseconds after the pulse, when most of the OH radicals are recombining. The use of an OH scavenger would help in establishing reaction 6 but, as mentioned in the Introduction, the high chemical reactivity of cyanogen in aqueous solutions excludes such experiments. However, it is important to note that both reaction paths, eq 4, 5 and 6, 7, are expected to lead to the same products. The difference is that in one case the cyanogen ion-radical disappears through the iminoacetonitrile radical.

We do not have evidence concerning the reaction of H atoms with cyanogen. It probably results in the same product as reaction 4. The data in Figure 2,

$$(CN)_2 + H \longrightarrow \dot{C}NH(CN) \qquad (8)$$

dashed curve, show that the contribution of hydrogen atom adduct produced in the above reaction can be neglected in the dilute cyanogen solutions (3.7×10^{-4} M) and at pH ~6. The value of k_8 was estimated to be $<10^7\ M^{-1}\ \text{sec}^{-1}$.

We have also considered the possibility that the fate of the cyanogen ion-radical is not in the pseudo-first-order reaction represented by eq 4 but is the dissociation

$$(CN)_2^- \longrightarrow CN + CN^- \qquad (9)$$

and that the consecutive second-order process concerns CN radicals instead of NC–ĊNH or $(CN)_2^-$ species

$$2CN \longrightarrow (CN)_2 \qquad (10)$$

A test of this mechanism was attempted by adding larger amounts of cyanide ions to influence the reaction sequence 9, 10. This was not feasible, however, since added salts of cyanide accelerate the polymerization of cyanogen in the solutions studied, complicate the decay of transients formed, and make the test impossible. However, an indirect, but reliable, argument supporting reactions 4, 5 or 7 is the fact that the trend of radiation-induced chemical changes is the formation of larger molecules. Irradiated solutions change visibly after irradiation. Like concentrated cyanogen solutions on longer standing, they become yellow and the formation of a brownish precipitate known as azulmic acid is accelerated. This could hardly be explained if the second-order

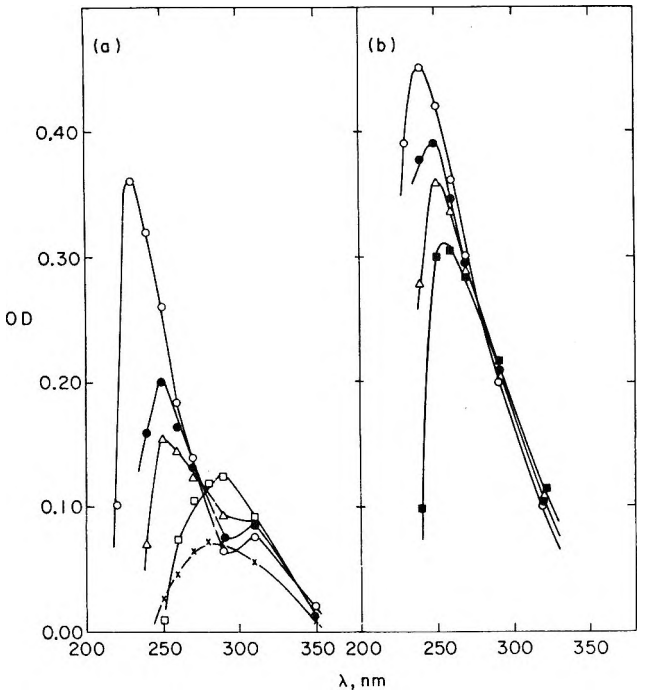

Figure 5. Optical density changes in helium-purged cyanogen solutions (1.92×10^{-2} *M*) taken various times after the end of irradiation; absorbed dose, 19 krads. Part a, Van de Graaff irradiation, 60-μsec pulse; part b, 1.5-min ^{60}Co irradiation. Measurements after the irradiation: 200 μsec, ×; 5 min, ○; 30 min, ●; 60 min, △; 120 min, □; 240 min, ■.

process observed in pulsed beam experiments is reaction 10. The same is true for the fast and complex chemical changes that take place in the solution after irradiation. Figure 5 illustrates such changes in a solution irradiated with a 60-μsec Van de Graaff pulse (a) and after 1.5-min ^{60}Co irradiation (b). The initial products are subjected to further chemical changes, hydrolysis and polymerization. The result is very likely the formation of C_4 molecules like HCN tetramer (diaminomaleonitrile, λ_{max} 290 nm; diaminofumaronitrole, λ_{max} 305 nm; 4-aminoimidazole-5-carbonitrile, λ_{max} = 245 nm) or adenine (λ_{max} 261 nm). Also some of these products could be, similar to the finding in the radiolysis of aqueous solutions of HCN,[15,16] polymers containing up to C_{16} atoms. It is also known that iminoacetonitrile is an important step in the formation of HCN tetramer from hydrogen cyanide.[15,17]

Concluding Remarks

The results obtained in this work show that the most important reaction in irradiated aqueous solutions of cyanogen is the reaction with hydrated electrons (eq 1) and the formation of the ion-radical $(CN)_2^-$ (Figure 3). The supporting evidence for this species comes also from esr studies of γ-ray irradiated solid sodium and potassium cyanide.[18] Reactions with H and OH radicals (eq 8 and 3) are slow in dilute solutions. It is not clear whether the fast second-order decay, observed in irradiated dilute cyanogen solutions, concerns NC–ĊNH radical (eq 5) or $(CN)_2^-$ (eq 7). Molecular products should be the same in both cases.

This study was limited to the precursors of molecular products and not to the molecular products themselves. Evidence obtained in this work shows that such a study should take into account not only the expected influence of the absorbed dose and the solute concentration but some other facts. Figure 5 shows that the molecular products in the radiolysis of aqueous cyanogen solutions depend also on the way in which the energy is deposited and the time after irradiation when the chemical identification is carried out.

Acknowledgments. The authors are indebted to Dr. A. O. Allen for his interest in this work, to Dr. H. Schwarz for his advice and assistance, and to Mr. L. C. Rogers for building the xenon arc booster.

(15) D. Hummel and O. Janssen, *Z. Phys. Chem.* (*Frankfurt am Main*), **31**, 111 (1962).
(16) H. Ogura, *Bull. Chem. Soc. Jap.*, **41**, 2871 (1968).
(17) Th. Völker, *Angew. Chem.*, **72**, 379 (1960).
(18) K. D. J. Root and M. C. R. Symons, *J. Chem. Soc. A*, 21 (1968).

The Radiation-Induced Oxidation of Trichloroethylene[1]

by Armen R. Kazanjian* and David R. Horrell

The Dow Chemical Company, Rocky Flats Division, Golden, Colorado 80401 *(Received July 6, 1970)*

Publication costs assisted by The Dow Chemical Company

The radiation-induced oxidation of trichloroethylene was investigated. It was found that a chain reaction is operable, producing extremely high radiation yields. The three major products are dichloroacetyl chloride, phosgene, and trichloroethylene oxide. The effects of dose rate, temperature, and inhibitor on the overall reaction were examined. The reaction was found to continue after the irradiation was stopped. A mechanism is postulated to account for these effects.

Introduction

The radiation-induced oxidation of unsaturated organic compounds has not received much attention. In particular, the study of chlorinated hydrocarbons would be of interest because of the extremely high yields and the postirradiation effect that has been experienced in this investigation. No previous investigations had been made on trichloroethylene (TCE). There are two previous reports on the radiation-induced oxidation of tetrachloroethylene, which would be expected to be very similar to that of trichloroethylene. One of these reports[2a] does not mention a postirradiation effect, while the other[2b] explains the effect as a delayed reaction of the products with water. The present work does not indicate this to be true for trichloroethylene. The postirradiation effect is real and has to be included in the mechanism.

Experimental Section

Materials. The trichloroethylene used was unstabilized Baker reagent grade. Chromatographic analysis showed that batches of this reagent usualy contain 0.1–0.2% impurities. Most of these impurities can be removed by allowing the solvent to remain in contact with Linde molecular sieve. However, some batches contained less than 0.01% impurities and were used to obtain the quantitative results presented here. The less pure TCE was used for qualitative work. The purity of the material appeared to be very critical, as discussed later. Oxygen was used as received, and its purity was greater than 99.6%.

Irradiation. Irradiations were carried out in a Gammacell-220, a commercial source containing about 3200 Ci of cobalt-60. All irradiations were carried out at the source temperature of 28–30°, unless otherwise stated. Energy absorption was measured with a Fricke dosimeter and corrections for material differences were made on the basis of electron fraction. The usual unshielded dose rate was 2.70×10^{17} eV/(ml min) (2.53×10^5 rads/hr) and could be attenuated more than tenfold by the use of lead shields.

Since the radiation yields were very sensitive to irradiation conditions, a uniform procedure was adopted and followed throughout. The liquid was always irradiated in a particular Pyrex flask under an oxygen pressure of 500 Torr. Other conditions, which would vary the amount of oxygen available to the TCE during irradiations, would change the total yields. As long as there is more than ample oxygen for the complete oxidation, one would obtain yields similar to those reported here.

Method of Analysis. Analysis was difficult because of the reactivity of the radiolysis products. However, satisfactory results were obtained using a variety of analytical methods. One commonly used measure of the product yield was the total water-extractible acid. This was determined by shaking the irradiated solvent with H_2O and titrating the mixture with a base. Chloride ion was also analyzed in some solutions.

Attempts to analyze the radiolysis products directly by gas chromatography were unsuccessful. Product peaks were observed occasionally, but they were not reproducible, probably due to the reactivity on the columns. Nevertheless, this method was used to analyze dichloroacetyl chloride indirectly. Quantitative yields were obtained by adding methyl alcohol to produce the methyl ester before injection into a silicone oil (DC-200) column.

Although mass spectrometry and nuclear magnetic resonance spectroscopy were used to obtain some information, infrared spectrometry proved to be the most valuable method of analysis. A typical spectrum from the Perkin-Elmer 137 instrument is shown in Figure 1. Quantitative measurements were made on the basis of peak heights. A standard curve was made up for the quantitative determination of dichloroacetyl chloride by ir spectrometry. A single solution of phosgene in tri-

(1) Work performed under the auspices of the U. S. Atomic Energy Commission Contract AT(29-1)-1106.

(2) (a) V. A. Poluektov, I. V. Dobrov, and S. A. Lyapina, *High Energy Chem.*, **2**, (6) 461 (1968); (b) J. W. Sutherland and J. W. T. Spinks, *Can. J. Chem.*, **37**, 79 (1959).

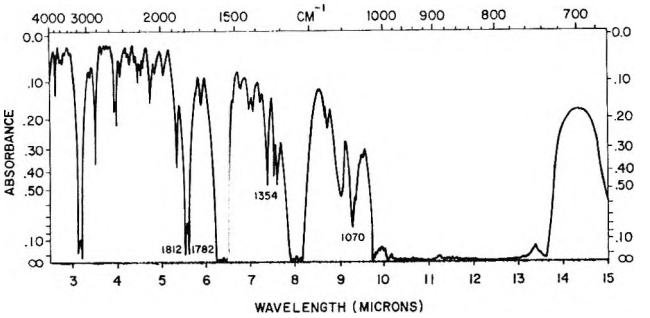

Figure 1. Infrared spectrum of trichloroethylene irradiated in the presence of oxygen.

chloroethylene was also prepared to verify the above procedure for the quantitative determination of phosgene.

Results and Discussion

Product Identification. The three major radiolysis products are dichloroacetyl chloride (DCAC), phosgene, and trichloroethylene oxide (TCE oxide). There was no HCl or Cl_2 formed, as determined by specific spot tests and mass spectrometry.

Dichloroacetyl chloride was positively identified by forming the *p*-toluidide derivative. The unknown had the same melting point (156°) and the same infrared spectrum as the known compound. Phosgene was identified by forming the anilide derivative (diphenylurea, mp 246°). Phosgene could also be detected by its odor.

Dichloroacetyl chloride was also analyzed qualitatively and quantitatively by adding methyl alcohol to irradiated TCE to form the methyl ester and then using gas chromatography to separate and identify the ester. Mass spectrometry could also detect DCAC, but quantitative analysis was very poor.

Infrared analysis was used most successfully for the three products. A spectrum is shown in Figure 1. The 1070-cm^{-1} peak (a C–H bending frequency) was used to analyze dichloroacetyl chloride quantitatively. The doublet (C=O stretch) at 1782 and 1812 cm^{-1} could also be used since it followed Beer's law. However, phosgene also has a C=O peak at this frequency. This contribution from phosgene could be accounted for by making use of the constant ratio between the 1070 and 1782–1812-cm^{-1} peaks of DCAC. The use of a standard solution of phosgene in TCE showed this procedure to be a valid analytical method for phosgene.

A strong infrared absorption at 1354 cm^{-1} also emerged when the purer batches of TCE were used. The fact that this peak was either absent or small during the earlier irradiations was attributed to an impurity. The 1354-cm^{-1} peak has been assigned to trichloroethylene oxide by Derkosch, *et al.*,[3] who attribute this peak to a symmetrical ring pulsation and find that there is an accompanying peak at 962 cm^{-1} due to a symmetrical ring deformation. This peak was highly evident in those spectra where matched cells were used to eliminate the strong TCE absorptions below 1000 cm^{-1}.

Nuclear magnetic resonance spectroscopy was of limited value because of the scarcity of H atoms. The simple spectra of three singlets at 6.48, 6.13, and 5.26 ppm were ascribed to TCE, DCAC, and TCE oxide, respectively. The peak at 5.26 ppm was deductively assumed to be TCE oxide. Some of the possible compounds in the mechanism were eliminated because they contained more than one hydrogen. Such compounds would have generated more than the one peak that was available for assignment.

Trichloroethylene oxide could not be determined directly because of the lack of the pure compound to use as a standard. Trichloroethylene oxide is not commercially available, and the many attempts to isolate the compound were unsuccessful. This compound was referred to (as trichloroethylene epoxide) in a report by Bertrand, *et al.*,[4] but the preparational details were not included. However, the TCE oxide yield could be determined by difference, using the total acidity produced by reacting the three products with water. Dichloroacetyl chloride and phosgene each produce 2 mol of acid (reactions 1 and 2), whereas TCE oxide can produce either 2 mol of acid (reaction 3a) or 3 mol of acid (*via* reaction 3b—according to the work of Frankel, *et al.*,[5] on tetrachloroethylene oxide). Using 2 mol as the basis of calculation, the total yield is made up of 56% TCE oxide, 31% DCAC, and 13% $COCl_2$. These values were obtained from a number of runs using our purest TCE. Since the TCE oxide yields were much higher using relatively more pure TCE, there is the possibility that a larger fraction or even all of the radiation yield could consist of TCE oxide. Trichloroethylene oxide may isomerize to DCAC under certain conditions[5] and sometimes did so when irradiated samples were kept at elevated temperatures.

Product yields from the irradiation of trichloroethylene under vacuum were relatively small. The two major products were hydrogen chloride and chloroacetylene, each with a G value of about 0.25. This work under vacuum was not extended.

Acid Yields. Irradiation of trichloroethylene in the presence of oxygen produces very large amounts of acidic products. Figure 2 shows that the $G(H^+)$ values are in the thousands, indicating a chain reaction. These are the total water-extractible acid yields that are produced by the following reactions

$$CHCl_2COCl + H_2O \longrightarrow CHCl_2COOH + HCl \quad (1)$$

(3) J. Derkosch, E. Ernstbrunner, E. G. Hoffman, F. Osterreicher, and E. Ziegler, *Monatsh. Chem.*, 98, 956 (1967).

(4) L. Bertrand, J. A. Franklin, P. Goldfinger, and G. Huybrechts, *J. Phys. Chem.*, 72, 3926 (1968).

(5) G. M. Frankel, C. E. Johnson, and H. M. Pitt, *J. Org. Chem.*, 22, 1119 (1957).

$$COCl_2 + H_2O \longrightarrow 2HCl + CO_2 \quad (2)$$

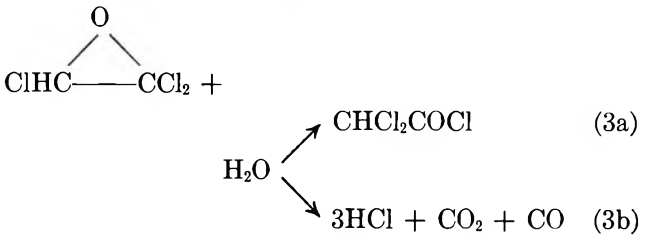

$$ClHC\text{——}CCl_2 + H_2O \rightarrow CHCl_2COCl \quad (3a)$$

$$H_2O \rightarrow 3HCl + CO_2 + CO \quad (3b)$$

Equation 3 is not balanced. The trichloroethylene oxide may partially isomerize and partially decompose to HCl, CO_2, and CO.[4]

The first two reactions were found to be rapid, whereas the third reaction occurs over a period of hours. In those samples in which both Cl^- and H^+ were analyzed after a short H_2O shakeout (*i.e.*, only reactions 1 and 2 occurring) the H^+/Cl^- ratio was about 1.5:1. This ratio would be obtained from a dichloroacetyl chloride to phosgene yield ratio of 2:1, in general accord with later findings. It should be noted that the acid titration using phenolphthalein indicator did not include the CO_2. It was shown that the CO_2 was removed in our procedure of shaking an acidic solution.

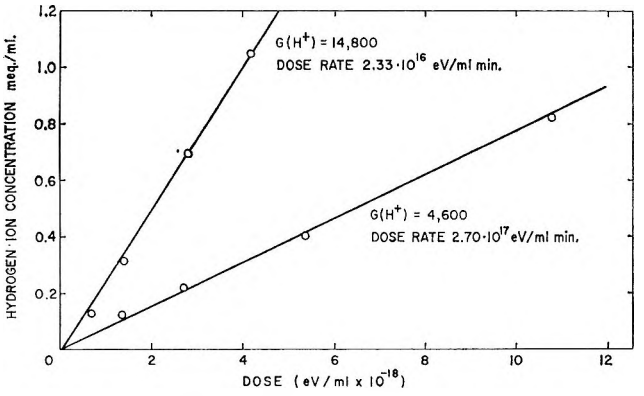

Figure 2. Total acid yield from trichloroethylene irradiated in the presence of oxygen.

Effect of Dose Rate. The $G(H^+)$ value was 4600 at a dose rate of 2.70×10^{17} eV/(ml min) and 14,800 at a dose rate of 2.33×10^{16} eV/(ml min) (see Figure 2). Theoretical examination of the kinetics of a simple radiation-initiated chain reaction shows that the yield is inversely proportional to the square root of the dose rate. The dose rate dependence of the above values is to the -0.48 power. This very good agreement with theory shows that the radiation-induced oxidation is a normal chain reaction.

Effect of Temperature. The overall yields were sensitive to changes in temperature indicating that one of the reactions in the mechanism has a strong thermal dependence. Irradiations were made at -196 (frozen state) and at $-70°$ (liquid state). In both cases the total acid yields became almost negligible, about 1/100 of that at 30°. On the other hand, irradiations above room temperature showed increased yields as indicated in Table I.

Table I: Effect of Temperature on Yields

Temp, °C	$G(H^+)$
30	4600
47	5300
71	6900
87	8300

An Arrhenius plot of the above data generates an activation energy value of 2.2 kcal/mol. It is not known which reactions in the mechanism would have such an activation energy, although reactions 6, 7, or 8 are the most likely possibilities.

Effect of Inhibitor. Diisopropylamine is used as a stabilizer in trichloroethylene. Solutions of 0.05% of this compound in TCE were irradiated for various times. The acid yields were negligible at the relatively short exposure but continued to increase with increasing exposure. The diisopropylamine was found to function as a radical scavenger. Its concentration was very inadequate to neutralize the acid products. Its original effectiveness in prohibiting the chain reaction declines as it is decomposed by radiation.

Diphenylpicrylhydrazyl (DPPH) is used as a radical scavenger in radiation studies. A 5×10^{-3} *M* solution of DPPH in TCE was irradiated. There was no acid produced, adding confirmation to the presence of free radicals in the mechanism.

Postirradiation Effect and Mechanism. The radiation-induced oxidation of TCE exhibited a striking postirradiation effect. After the exposure periods, which varied from 10 min to 1 hr, the product yields continued to increase two- to fourfold over a period of days. Behavior of this type could only be attributed to the slow decomposition of a metastable intermediate. All of the analytical techniques described in the previous section were used in an attempt to identify the intermediate. Although these attempts were unsuccessful, information has been gathered about the system.

The intermediate is fairly stable in TCE at room temperature. The rate of product buildup, after irradiation, takes place over a period of days. At 85° the reaction is accelerated so that it is essentially complete in about 2 hr. The presence of oxygen is essential to this process. If the oxygen or air is evacuated from an irradiated sample, there is no further increase in products.

Experiments have shown that the concentrations of all three products continue to increase after the irradiation is stopped. None of the individual yields are en-

hanced at the expense of others. The mechanism will have to be consistent with this fact.

The mechanism believed most likely to be in accord with the experimental facts is the following.

$$C_2HCl_3 \longrightarrow Cl\cdot + C_2HCl_2\cdot \quad (4)$$

$$C_2HCl_3 + Cl\cdot \longrightarrow CHCl_2CCl_2\cdot \quad (5)$$

$$CHCl_2CCl_2\cdot + O_2 \longrightarrow CHCl_2CCl_2OO\cdot \quad (6)$$

$$2CHCl_2CCl_2OO\cdot \longrightarrow CHCl_2CCl_2OOCCl_2CHCl_2 + O_2 \quad (7)$$

$$CHCl_2CCl_2OO\cdot + CHCl_2CCl_2\cdot \longrightarrow CHCl_2CCl_2OOCCl_2CHCl_2 \quad (8)$$

$$CHCl_2CCl_2OOCCl_2CHCl_2 \rightleftharpoons 2CHCl_2CCl_2O\cdot \quad (9)$$

$$CHCl_2CCl_2O\cdot \longrightarrow CHCl_2COCl + Cl\cdot \quad (10)$$

$$CHCl_2CCl_2O\cdot \longrightarrow ClHC\overset{O}{\diagup\diagdown}CCl_2 + Cl\cdot \quad (11)$$

$$CHCl_2CCl_2O \longrightarrow CHCl_2\cdot + COCl_2 \quad (12)$$

$$CHCl_2\cdot + 0.5O_2 \longrightarrow CO + HCl + Cl \quad (13)$$

Reactions 4 through 6 appear to be most reasonable and fairly well established by previous work in this general area.[2,4,6] References 4 and 6 report on the chlorine-photosensitized oxidation of trichloroethylene, whereas ref 2a and b are on the radiation-induced oxidation of tetrachloroethylene. The mechanism beyond reaction 6 is still questionable. Only one of the radiation reports[2b] even mentions a postirradiation effect, and no accounting is made for this effect in their mechanisms. Huybrechts,[6] on the other hand, using a gas phase chlorine-photosensitized reaction noted that some oxidation occurred after the light was switched off. This small fraction of the overall reaction was explained by reaction 9 occurring in the gas phase or on the walls. It was postulated that the bulk of the reaction took place by the combination of peroxy radicals to form alkoxy radicals. Also in this gas phase work, DCAC was the main product while TCE oxide and phosgene were only side products.

Although complete quantitative data on the kinetics of the postirradiation effect were not obtained, it was found that a larger fraction of the products were produced after short irradiation times than after long irradiation times. This implies that the concentration of the intermediate builds up to a steady state. The intermediate, which has been postulated to be the peroxide compound in reaction 9, would then decompose to yield additional products over a period of days at room temperature and much faster at elevated temperatures. These facts are in agreement with the postulated mechanism.

Identification of the peroxide would substantiate the mechanism. Although the intermediate is fairly stable, peroxides are difficult to analyze and attempts thus far have been unsuccessful.

Since this paper was submitted for publication, an abstract of a Russian report on the subject has appeared.[7] The authors studied the radiation chemical oxidation of TCE and analyzed the three products by gas chromatography. The TCE oxide was separated and identified. Its ir spectrum is shown, and the prominent peaks at 1350 and 970 cm^{-1} correspond to those used in this work. A postirradiation effect was not mentioned and may have been missed because of their long irradiations and large conversions. This may account for a mechanism different from ours, but we cannot comment on this as we have been unable to obtain the original full publication.

Acknowledgments. The authors would like to thank W. C. Gottschall for helpful discussions.

(6) G. Huybrechts and L. Meyers, *Trans. Faraday Soc.*, 62, 2191 (1966).

(7) V. A. Poluektov, Yu. Ya. Mekhryushev, and S. A. Lyapina, *High Energy Chem.*, 3 (6), 475 (1969).

Reactions Involving Electron Transfer at Semiconductor Surfaces. II. Photoassisted Dissociation of Nitrous Oxide over Illuminated Ferric Oxide and Zinc Oxides[1]

by Joseph Cunningham,* J. J. Kelly, and A. L. Penny

Department of Chemistry, University College, Belfield, Dublin 4, Ireland *(Received July 22, 1970)*

Publication costs assisted by the Air Force Office of Scientific Research, through the European Office of Aerospace Research

Gaseous nitrous oxide dissociated when contacted at 20° with illuminated surfaces of powdered zinc oxides or ferric oxide. The quantum efficiency of photoassisted dissociation over pure zinc oxide was small for all conditions used in this work, being only $\sim 10^{-5}$ when high pressures of N_2O ($\sim$500 Torr) were present during illumination and when photons had energies greater than the zinc oxide bandgap of 3.2 eV. Lower quantum efficiency ($\phi \sim 10^{-6}$) was observed for photons of energies <3.2 eV, but no detectable photoassisted dissociation was observed with photons of energy <2 eV incident on zinc oxide. For pure and doped zinc oxides and for ferric oxide correlations are established between photoassisted dissociation and photocurrents measured in films of the same oxide. Observed results can be accounted for in terms of photoproduced changes in the boundary layer potential resulting from depletive chemisorption of nitrous oxide onto the oxide surface.

Introduction

Previous work by the authors[2] demonstrated that gaseous nitrous oxide was dissociated to a small extent when contacted in the dark at 20° with freshly activated surfaces of n-type semiconductors. The present paper reports results of additional N_2O dissociation produced by illuminating these surfaces and considers whether or not this photoassisted dissociation proceeds *via* the same mechanism as that proposed for the dark dissociation.

According to the interpretation previously proposed, only steps Ia, Ib, and Ic of the following widely used mechanism for heterogeneously catalyzed dissociation of nitrous oxide[3,4] are needed to explain the observed kinetics and extent of dissociation over n-type metal oxides, MO, in the dark at 20°

Weak chemisorption

$$MO(s) + N_2O(g) \longrightarrow \{N_2O(ads)\ldots MO(s)\} \quad (Ia)$$

Localization of an electron from the conduction band of the oxide

$$\{N_2O(ads)\ldots MO(s)\} \longrightarrow \{N_2O^-(ads)\ldots (MO)^+(s)\} \quad (Ib)$$

Dissociation of $N_2O^-(ads)$

$$\{N_2O^-(ads)\ldots (MO)^+(s)\} \longrightarrow N_2(g) + \{O^-(ads)\ldots (MO)^+(s)\} \quad (Ic)$$

Neutralization of surface charge by hole transfer

$$\{O^-(ads)\ldots (MO)^+(s)\} \longrightarrow \{O(ads)\ldots MO(s)\} \quad (Id)$$

Desorption of oxygen

$$2\{O(ads)\ldots MO(s)\} \longrightarrow \{O_2(ads)\ldots MO(s)\}^* \quad (Ie)$$

$$\{O_2(ads)\ldots MO(s)\}^* \longrightarrow O_2(g) + MO(s)$$

A central feature of this mechanism for the dark N_2O dissociation was that, since (Ib) was the rate-determining step, both the kinetics and the extent of dissociation were controlled by buildup of an electrically charged double layer, having effectively the form $\{O^-(ads)\ldots (MO)^+(s)\}$ rather than $\{N_2O^-(ads)\ldots MO^+(s)\}$ because (Ic) is fast. The dark dissociation decreased to a very slow rate at 20° when the boundary layer potential reached a limiting value E_0.

At surfaces already bearing an electrical double layer of form $\{O^-(ads)\ldots (MO)^+(s)\}$ and potential E_0, photons of appropriate wavelengths may excite electrons to the conduction band either from discrete levels[5] associated with $O^-(ads)$

$$\{O^-(ads)\ldots (MO)^+(s)\} \xrightarrow{h\nu} \{O(ads) + e(MO)^+(s)\} \quad (IIa)$$

or from valence band levels existing in the solid[6]

(1) This work is supported in part by the Air Force Office of Scientific Research through the European Office of Aerospace Research, OAR, United States Air Force under Contract AF 61-052-67C-0044.

(2) J. Cunningham, J. J. Kelly, and A. L. Penny, *J. Phys. Chem.*, **74**, 1992 (1970).

(3) (a) K. Hauffe, R. Glang, and H. J. Engell, *Z. Phys. Chem. (Leipzig)*, **201**, 223 (1952); (b) Y. Saito, Y. Yoneda, and S. Makishima, *Actes Congr. Int. Catal., 2nd, 1960*, **2**, 1937 (1961).

(4) W. D. Schulz and J. Scheve, *Z. Anorg. Allg. Chem.*, **366**, 231 (1969).

(5) D. B. Medved, *J. Phys. Chem. Solids*, **20**, 255 (1961).

(6) S. R. Morrison, *Advan. Cat.*, **7**, 259 (1955).

$$\{O^-(ads)\ldots(MO^+)(s)\} \xrightarrow{h\nu} \{O^-(ads) + (e + h)(MO)^+(s)\} \quad (IIb)$$

The symbols $e(MO^+)$ and $(e + h)(MO^+)$ refer, respectively, to an electron and electron plus hole produced by light in an oxide lattice with a depletion layer. In terms of mechanism Ia–Ie, the reactive intermediates produced by transitions IIa and IIb might produce additional N_2O dissociation *via* any of three processes: (i) by electrons freed at the surface in (IIa) interacting with adsorbed N_2O as in (Ib) and (Ic); (ii) by holes, h, produced in (IIb) migrating to the surface to reduce the boundary layer potential as in (Id) and so to make possible further dissociation *via* (Ib) and (Ic); (iii) by reaction of O(ads) with N_2O(ads). Processes i, ii, and iii correspond to illumination enhanced processes, possible even at the dark surface, and an objective of the work here described was to evaluate, if possible, their individual contributions to photoassisted dissociation of N_2O over ferric oxide and zinc oxides. A further objective was to evaluate contributions by dissociative paths which would be negligible at unirradiated surfaces. Important among mechanisms of this latter type could be (IIb) followed by

$$(e + h) + N_2O(ads) \longrightarrow N_2O^*(ads) \longrightarrow N_2 + O(ads) \quad (III)$$

This involves transfer to an adsorbed molecule of the energy released by recombination of radiation produced electron and hole and merits consideration because other workers have presented evidence for similar processes in reactions over irradiated catalysts.[7]

The importance of nonradiative pathways for dissipating the energy of recombination of radiation-induced electrons and holes has been clearly demonstrated in recent work on F-center formation in irradiated alkali halides.[8,9]

The system N_2O–ZnO offered many advantages for the study of these questions: *first*, the optical absorption edge for ZnO occurs at 385 nm at room temperature so that electrons, holes, and excitons[10,11] are conveniently produced by exposure to medium-pressure Hg lamps; *second*, there is extensive background information in the literature on photocatalytic,[12–16] photoluminescent,[17,18] and photoconductive[19–24] processes in zinc oxides; *third*, the ability of nitrous oxide to interact dissociatively with electrons is firmly established[25–29] and participation of excited states in N_2O dissociation has been suggested in some systems,[30,31] although disputed by other workers.[32,33]

Experimental Section

Materials. Details of the origin, surface area, electron concentration, and dark reactivity of the zinc oxides and ferric oxide used in the present work have been given previously,[2] together with full details of the heat-treatment and vacuum conditions needed to ensure reproducible activity of samples towards nitrous oxide later admitted at 20°. High purity gases and standard gas-handling techniques employed have also been described.[2]

Illumination. The same light source, a Hanovia 125-W medium-pressure mercury arc lamp, was used for the majority of studies reported on photoconductivity and photoassisted reaction. The lamp was enclosed in a Pyrex water-cooled jacket to filter out unwanted infrared radiation and restrict light reaching the sample to wavelengths greater than 290 nm. After an initial warming up period of 5 min the output of the lamp, as monitored by a uv meter (Ultraviolet Products Inc., San Gabrielle, Calif.) or by observations of the current in the lamp circuit, was stable and reproducible to ±5%. The range of wavelengths transmitted could be further controlled by circulating filter solutions[34,35a]

(7) G. M. Shabrova, V. I. Vladmirova, B. M. Kadenatsi, V. B. Kazanskii, and G. B. Pariiskii, *J. Catal.*, **6**, 411 (1966).
(8) D. Pooley, *Proc. Phys. Soc. London*, **89**, 723 (1966).
(9) D. Pooley, *Proc. Phys. Soc. London (Solid State Physics)*, **1**, 323 (1968).
(10) G. Heiland, E. Mollwo, and F. Stockman, *Solid State Phys.*, **8**, 191 (1959).
(11) J. J. Hopfield, *J. Phys. Chem. Solids*, **10**, 110 (1959).
(12) W. M. Ritchey and J. G. Calvert, *J. Phys. Chem.*, **60**, 1465 (1956).
(13) W. Doerffler and K. Hauffe, *J. Catal.*, **3**, 171 (1964).
(14) F. Steinbach, *Z. Phys. Chem. (Frankfurt am Main)*, **61**, 235 (1968).
(15) I. S. McLintock and M. Ritchie, *Trans. Faraday Soc.*, **61**, 1007 (1965).
(16) G. A. Korsumovskii, *Zh. Fiz. Khim.*, **34**, 510 (1960).
(17) R. L. Weiher and C. W. Tait, *Phys. Rev.*, **185**, 1114 (1969).
(18) R. Nink, *Z. Naturforsch.*, **24**, 1329 (1969).
(19) J. McK. Nobbs, *J. Phys. Chem. Solids*, **29**, 439 (1968).
(20) R. J. Collins and D. G. Thomas, *Phys. Rev.*, **112**, 388 (1958).
(21) W. Doerffler and K. Hauffe, *J. Catal.*, **3**, 156 (1964).
(22) D. A. Melnick, *J. Chem. Phys.*, **26**, 1136 (1957).
(23) E. Molinari, F. Cramarossa, and F. Paniccia, *J. Catal.*, **4**, 415 (1965).
(24) E. Segal and M. Teodorescu, *Rev. Roumaine Chim.*, **12**, 75 (1967).
(25) R. D. Iyengar and A. C. Zettlemoyer, *J. Colloid Sci.*, **20**, 857 (1965).
(26) G. Scholes and M. Simic, *Nature (London)*, **202**, 895 (1964).
(27) N. H. Sargent, R. W. Robinson, and A. C. Blair, *Can. J. Chem.*, **46**, 3511 (1968).
(28) J. H. Warman, K. D. Asmus, and R. E. Schuler, *Advan. Chem. Ser.*, **82**, 25 (1968).
(29) V. Pravdic, A. E. Wilcox, and A. C. Zettlemoyer, *Surface Sci.*, **13**, 280 (1968).
(30) R. A. Holyroyd, *J. Chem. Phys.*, **48**, 1331 (1968).
(31) R. A. Holyroyd, *J. Phys. Chem.*, **72**, 759 (1968).
(32) J. T. Richards and J. K. Thomas, *Trans. Faraday Soc.*, **66**, 621 (1970).
(33) R. R. Hentz and R. J. Knight, *J. Phys. Chem.*, **72**, 4684 (1968).
(34) W. W. Wladimiroff, *Photochem. Photobiol.*, **5**, 243 (1966).
(35) (a) W. C. Fernelius and J. J. Burbage, *Inorg. Syn.*, **2**, 227 (1946). (b) This is the wavelength of the shortest wavelength line of the Hg lamp emission spectrum transmitted by the indicated filter solution.

through the cooling jacket. A copper sulfate–ferric alum solution was used to filter out wavelengths shorter than 364 nm,[35b] and solutions of $Ni(CN)_4^{2-}$ were used to transmit only wavelengths greater than or equal to 546 nm.[35b] Table I lists intensity transmitted through each filter solution at wavelengths of prominent lines in the mercury emission spectrum as measured with a Zeiss PMQ II monochromator and M4Q III detector. The total photon flux at the sample position was monitored with the uv meter for each filter solution and converted into absolute values by calibrating the uv meter against a uranyl oxalate actinometer. Quantum efficiencies were calculated on this basis (Table I).

Table I

(a) Spectral Distribution of Light Incident on Oxide Surfaces through Various Filter Solutions, Path Length 1 cm

Wavelength, nm	Relative intensity[a] transmitted through Pyrex walls and (a) water	(b) 0.8 *M* $CuSO_4$/ 0.01 *M* ferric alum soln	(c) 0.02 *M* $K_2Ni(CN)_4$/7 *M* KCN
296.7	0.11	0.0	0.0
302.2	0.45	0.0	0.0
312.5	2.3	0.0	0.0
313.2	2.0	0.0	0.0
334.1	1.3	0.0	0.0
364.0	55.7	2.3	0.0
365.0	19.5	0.68	0.0
366.0	11.6	0.45	0.0
404.2	25.8	23.2	0.0
407.8	1.8	1.6	0.0
435.8	88.5	86.0	0.0
546.0	100.0	97.0	77.5
576.0	25.0	23.8	18.4
578.0	25.0	23.8	18.4
Σ(photons/sec)[b]	3.2×10^{19}	2.3×10^{19}	1.1×10^{19}

(b) Quantum Efficiencies for Photoassisted Dissociation of N_2O over ZnO

Wavelength, nm	$296 < \lambda < 385$	$385 < \lambda < 546$	$546 \leqslant \lambda$
Quantum efficiency	1.1×10^{-5}	2×10^{-6}	4×10^{-7}

[a] Measured with Zeiss PMQ II monochromator and M4Q III detector, and corrected for wavelength variation of detector response. [b] Measured total flux of photons incident at the sample position, as calibrated with an actinometer.

Reaction System for Studying Photoassisted Dissociation. In order to expose as large a fraction as possible of the sample to light the oxide powder was arranged in a layer approximately 1–2 mm thick in an annular vessel and total lamp output was incident on 230 cm^2 of this layer (Figure 1a). In blank runs, a chromel–alumel thermocouple inserted into this layer just beneath the illuminated surface indicated that temperature rise associated with irradiation did not exceed *ca.* 2°. It was known from previous studies that this temperature rise would have a negligible effect upon the rate of the dark reaction of N_2O over the activated surface or upon the conductivity of an oxide film. After activating the oxide by heating to 400° for 16 hr, system pressure was 10^{-6} Torr and leak rate was 10^{-5} Torr/hr as measured with a Mullard 10G-15 ionization gauge. In order to avoid N_2O dissociation upon incandescent filaments this gauge was not used after N_2O was admitted to the system. Total system pressures (0.1–600 Torr) were then measured either by extended range Pirani gauges or metal Bourdon-type gauges (Edwards type and Leybold type). The pressure of noncondensable product gas present in the system after contact time, t_c, with N_2O was measured with Pirani gauge heads (Edwards type G5C-1 and G5C-2), undissociated N_2O being frozen into the trap indicated in Figure 1a. In order to avoid the possibility of mercury-photosensitized reactions, mercury was rigorously excluded from the vacuum systems used. Blank experiments with N_2O in the reaction vessel but no oxide powder established that illumination did not then produce any detectable gas product.

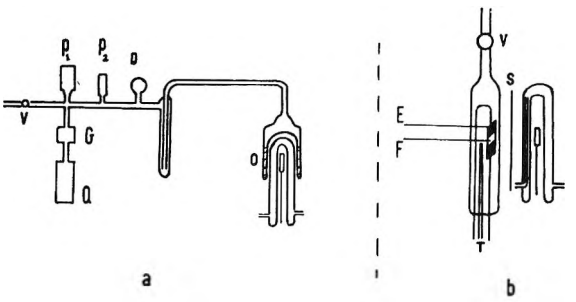

Figure 1. (a) Schematic diagram of apparatus for studying photoassisted dissociation: O, irradiation vessel with oxide powder (shaded) surrounding water-cooled lamp; V, metal valve; P_1, P_2, and D, Pirani and Bourdon gauges; G, variable leak; Q, quadrupole mass spectrometer. (b) Schematic diagram of apparatus for studying photoconductivity in oxide film F, deposited on gold electrodes E, with thermocouple T and shutter S.

Photoconductivity. Oxide films *ca.* 0.1 mm thick were deposited from aqueous suspension onto glass substrates having previously deposited gold electrodes. The films were activated *in vacuo* at 400° and their dark conductivity was measured by d.c. and a.c. methods as previously described.[2] Light from the water-cooled Pyrex-jacketed Hanovia mercury arc lamp was incident on the films through an additional Pyrex wall of the vacuum envelope of the conductivity cell (Figure 1b). For steady-state values of the dark or photoconductivity, good correspondence was found between measurements made by d.c. and a.c. techniques. Plots of conductivity *vs.* illumination time (illumination being started only after the lamp had reached its steady-state output) were obtained by feeding the d.c. from a Keith-

Table II

	Li–ZnO	ZnO	In–ZnO	Fe_2O_3
Surface area, m^2/g[a]	1.1	4.0	0.1	3.2
n_D, donor concn[a]	3×10^{16}	9×10^{16}	4×10^{18}	
n_e, concn of mobile carriers[a]	2.7×10^{14}	3×10^{16}	1.8×10^{18}	
Photoassisted dissoc rate (ml N_2/hr) 10 Torr N_2O	5.4×10^{-3}	7.8×10^{-3}	7.0×10^{-3}	1.0×10^{-3}
Dark reaction rate, ml N_2/hr	2.8×10^{-5}	2.5×10^{-6}	2.4×10^{-4}	2.5×10^{-4}
ΔE, V	0.16	0.2	0.03	0.06
E_0, V[a]		1.0	1.5	

[a] Values from ref 2.

ley 602 Electrometer to a potentiometric Y-t recorder (Advance Electronics type).

Analysis. By connecting a quadrupole mass spectrometer to the reaction system, analysis was carried out on reactant and products. The product gas of the decomposition was entirely nitrogen. At no stage of the reaction was photodesorption of oxygen observed.

Results

A. Dissociation of N_2O over Illuminated Oxides. i. Illumination at Wavelengths > 290 nm. Since the initial rate of N_2O dissociation over activated oxides in the dark was much greater than the greatest observed photoassisted rate, it was found convenient first to allow the dark reaction to proceed to virtual completion. When a slow reproducible dark reaction was thus achieved, illumination was commenced. The quantity of N_2 product present in the system after illumination could then be corrected for the residual dark reaction.

The additional dissociation of N_2O (pressure = 10 Torr) produced over powdered ZnO by illumination with light of wavelength > 290 nm is illustrated in Figure 2. The rapid initial formation of N_2 over the activated oxide in the dark is indicated by curve a where V_N, the volume of N_2 (ml at STP) produced per square meter of ZnO, is plotted against contact time. Approach to a slow residual dark reaction rate after approximately 1 hr is evident in this plot. Upon illumination an additional linear growth of N_2 product with time was observed which greatly exceeded the residual dark reaction. On ceasing illumination the rate of N_2 production returned to the dark rate observed prior to illumination. Curve b of Figure 2 illustrates the results observed when activated ZnO was illuminated prior to and during admission and reaction of N_2O. During continuous illumination the rate of N_2 production did not decrease to the low value observed after 1 hr as shown in curve a.

Photoassisted dissociation of N_2O was also observed over Li–ZnO (ZnO doped with 463 ppm of lithium), over In–ZnO (ZnO doped with 110 ppm of indium) and

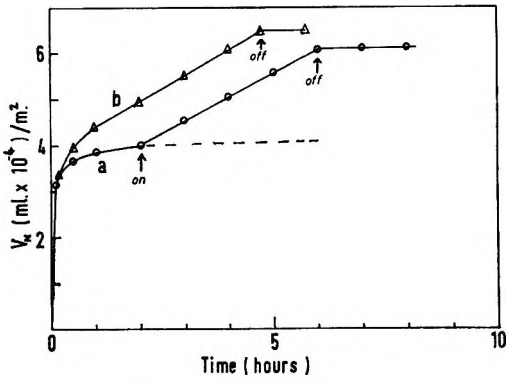

Figure 2. Growth of nitrogen product V_N, with contact time between N_2O (10 Torr) and activated ZnO surface at 20°: (a) N_2O contacted in dark, commencement and termination of illumination indicated by arrows; (b) N_2O contacted with ZnO under illumination.

over Fe_2O_3. Rates of product formation during illumination did not differ greatly for the three zinc oxides despite considerable differences in surface area and in carrier concentration as shown in Table II. For the N_2O–Fe_2O_3 system a slow residual dark reaction was reached only after a time interval of 3–4 days. The photoassisted reaction was then studied, and at constant N_2O pressure the rate of N_2 formation was constant over periods of 3–4 hr, as for ZnO.

ii. Dependence of Rate of Photoassisted Dissociation on N_2O Pressure. The rate of N_2 formation *via* photoassisted dissociation over the four oxides (*i.e.*, the difference between the total rate and the residual dark reaction rate) was observed to be constant for intervals of up to 4 hr at fixed N_2O pressure. The dependence of this rate on N_2O pressure is illustrated in Figure 3. Curve a refers to ZnO activated at 400° *in vacuo*, equilibrated with N_2O at 20° until more than 95% of the dark reaction was complete, and then illuminated with light of wavelengths > 290 nm. Curve c refers to Fe_2O_3 which had been treated in the same manner.

iii. Wavelength Dependence of Photoassisted Dissociation over ZnO. Data for curve b of Figure 3 were

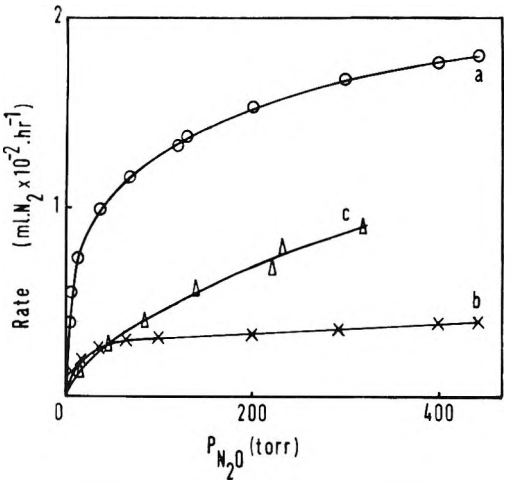

Figure 3. Variation in rate of photoassisted dissociation of N_2O with pressure of N_2O over (a) ZnO, $\lambda > 290$; (b) ZnO, $\lambda > 364$; (c) Fe_2O_3, $\lambda > 290$.

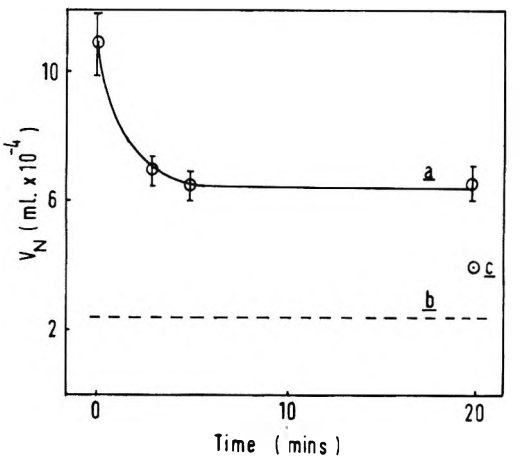

Figure 4. ZnO "memory effect": (a) N_N, the volume of N_2 produced by contacting 50 Torr N_2O with ZnO for 30 min following illumination of the equilibrated ZnO under vacuum for 1.5 hr. The time interval between termination of illumination and introduction of N_2O is given on abscissa. (b) Volume of N_2 produced by contacting 50 Torr N_2O with the equilibrated ZnO not preirradiated for 30 min in the dark. (c) V_N, as in (a) but equilibrium pressure $O_2 = 1.0 \times 10^{-3}$ Torr introduced during interval between termination of illumination and introduction of N_2O.

obtained for a ZnO sample which had received the same treatment as that used for curve a except that light reaching the sample was restricted to wavelengths > 364 nm using filter b. The overall light intensity incident on the oxide was reduced by 27% by the filter solution. The extent of photoassisted dissociation was reduced by 75%. Thus, as expected, light inside the band edge of ZnO ($\lambda < 385$ nm) was more efficient in producing dissociation. Further evidence that photons of energy less than the band gap of ZnO were contributing to N_2O dissociation was obtained when various solutions of $Ni(CN)_4^{2-}$ were used to restrict light incident on the ZnO to progressively longer wavelengths. Dissociation was observed for wavelengths up to 546 nm. Quantum efficiencies for chemical decomposition of N_2O (*i.e.*, number of N_2 molecules produced per photon) for three spectral regions are listed in Table I. The difference in quantum efficiency observed using filters a ($\lambda > 290$ nm) and b ($\lambda > 364$ nm) gave the value for quantum efficiency in the region of the band gap ($290 < \lambda < 364$ nm). Similarly the difference in quantum efficiency observed for decomposition using filters b and c gave a value for the wavelength region $364 < \lambda < 546$ nm. The value for $\lambda > 546$ nm was obtained by using filter c.

iv. "Memory Effect." A "memory effect" corresponds to a greater dark dissociation rate over an oxide surface which had been preilluminated than over the unilluminated surface. Such an effect is illustrated for ZnO in Figure 4. The lower dotted line (b) shows the measured value (2.4×10^{-4} ml) of product N_2 detected after a 0.5-hr reaction in the dark over a surface previously equilibrated with 50 Torr N_2O. Data on the upper curve (a) were obtained by condensing the gaseous N_2O in contact with the oxide into a liquid nitrogen trap and illuminating the surface for 1.5 hr at pressures of the order of $1-5 \times 10^{-4}$ Torr, corresponding to N_2 product from prior dark reaction. When illumination was ended, N_2O was evaporated to contact the oxide surface *either* immediately *or* after the interval indicated on the abscissa of Figure 4. The difference between the upper and lower plots exceeds the indicated experimental error, thus confirming a "memory effect" which persisted for more than 20 min after illumination. A similar "memory effect" was observed for Fe_2O_3.

Oxygen decreased the magnitude of the "memory effect" in ZnO. For a sample preirradiated for 1.5 hr as described above and then exposed to 1.0×10^{-3} Torr O_2 immediately after irradiation was ended, the volume of N_2 produced by a subsequent 0.5-hr dark reaction was considerably lower than that observed for the untreated preirradiated oxide, as shown by point c of Figure 4.

B. Photoconductivity of Oxides; $\lambda > 290$ nm. Irradiation of zinc oxides with light corresponding to fundamental absorption produces photoconductivity.[19-24] Section a of Figure 5 illustrates the increase in current observed when an activated Li–ZnO film was illuminated at 20° with light of $\lambda > 290$ nm. This photocurrent did not attain a constant value within the 3 min shown. Section b shows the decrease in current observed when N_2O (0.6 Torr) was introduced to the film during illumination. Section c illustrates the initial sharp decrease in current of the oxide film in the presence of N_2O which occurred when illumination was ended. This was followed by a slower decay towards the value in curve d, obtained when N_2O (0.6 Torr) was contacted with an activated Li–ZnO film in the dark. The rates of decrease in photocurrent shown in sections b and c of Figure 5 increased as N_2O pressure was increased.

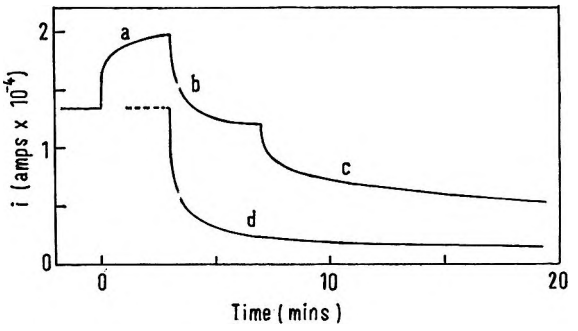

Figure 5. Variation of current flow through a Li–ZnO film with illumination and exposure to N_2O at 20°. (a) The increase in current i through an activated film under illumination followed by (b) the decrease due to exposure of film to 0.6 Torr N_2O, (c) further decrease in current on termination of illumination, (d) dark current decrease on exposing an activated film to 0.6 Torr N_2O.

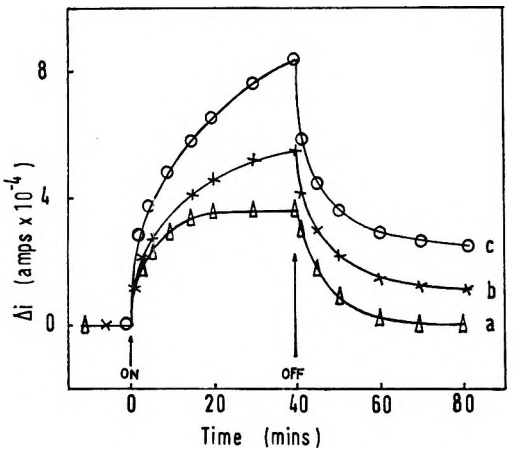

Figure 6. Variation of photoconductivity of ZnO with N_2O pressure. Δi, the increase in current through ZnO film, previously equilibrated with 0.6 Torr N_2O and illuminated under (a) 0.6 Torr N_2O, (b) 0.05 Torr N_2O, (c) continuous vacuum, current decreased on termination of illumination.

Figure 6 presents results of a sequence of measurements which established how the change in photocurrent, Δi, of ZnO depended on N_2O pressure. The dark current was first reduced to a constant value by contacting the ZnO film with 0.6 Torr N_2O for 40 min. Subsequent illumination ($\lambda > 290$ nm) of the equilibrated film in the presence of 0.6 Torr N_2O produced an increase in current, Δi, as shown in curve a. An equilibrium photocurrent (*i.e.*, Δi constant) was established within 20 min of the start of illumination. This establishment of an equilibrium photocurrent was observed for N_2O pressures greater than 0.5 Torr. Illumination was ended after 40 min and the current decayed rapidly to the value observed prior to illumination (*i.e.*, Δi decreased to zero). The half-life for decay of the photocurrent (time taken for photocurrent to decrease to half the Δi value reached after 40-min irradiation) was 4 min. When N_2O pressure was reduced to 5×10^{-2} Torr, no change occurred in the background dark current. Illumination at this pressure produced a faster increase in current as shown in curve b, an equilibrium photocurrent was not established within 40 min and the increase observed after 40-min irradiation was greater than for curve a. When illumination was ended, the current decayed more slowly than for curve a the half-life decay was 5.5 min. Illumination of the ZnO film at a residual pressure of 1×10^{-5} Torr (curve c) produced the greatest increase in current and, as for curve b, an equilibrium photocurrent was not established within 40 min. Decay of the photocurrent at this pressure was slower than for curve b and half-life for decay was 7 min. Thus the current remained $\geq 10\%$ above the dark current value for some hours after the end of illumination.

Similar results were found for Li–ZnO and Fe_2O_3 films which had been equilibrated with N_2O. Increasing N_2O pressure decreased the rate of increase and the magnitude of the photocurrent and increased the rate of decay of the photocurrent (*i.e.*, decreased the half-life). For N_2O pressures greater than 0.5 Torr an equilibrium photocurrent was established within 20 min of the start of irradiation, as for the ZnO case. The greatest relative increase in photocurrent of the zinc oxides (*i.e.*, the largest ratio of photocurrent to dark current) was observed for the oxide of lowest conductivity Li–ZnO, in agreement with the results of other workers.[20,21] No photocurrent could be detected for In–ZnO films in the presence of N_2O.

Discussion

It was shown in a previous paper that growth of surface potential to a limiting value, E_0, associated with accumulation of negatively charged surface species *via* (Ib) and (Ic), could explain observed kinetics of N_2O dissociation over oxide surfaces in the dark.[2] The limited extent of N_2O dissociation attainable in the dark and accompanying decreases in conductivity were explained within this framework. Figure 7a illustrates (schematically) electronic-energy states within a semiconductor and close to its initially clean surface. Figure 7c represents electronic energy states after equilibration of the surface with N_2O in the dark produces the limiting surface potential, E_0. In understanding the dark reaction results, the important consequence of E_0 was repulsion of electrons into the bulk, thereby suppressing (Ib), the rate-determining step of the dark dissociation at the oxide surface.

As discussed recently by Kwan, *et al.*,[36] and by Fukazawa, *et al.*,[37] photoexcitation can produce important modifications of chemisorption processes at surfaces bearing negatively charged oxygen species. The following processes contribute to such modifications: (II-

(36) T. Kwan, K. M. Sancier, Y. Fujita, M. Setaka, S. Fukazawa, and J. Kirino, *J. Res. Inst. Catal., Hokkaido Univ.*, 16, 53 (1968).

(37) S. Fukazawa, K. M. Sancier, and T. Kwan, *J. Catal.*, 11, 364 (1968).

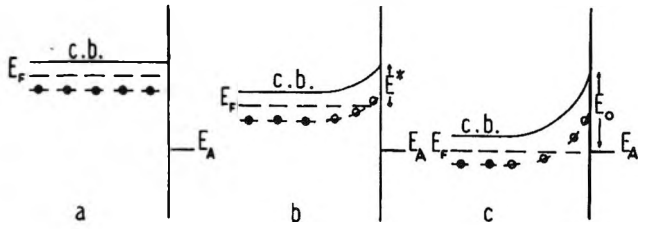

Figure 7. Energy diagram of n-type semiconductor (a) before, (b) after partial, and (c) after equilibrium chemisorption of acceptor species: c.b., conduction band; E_F = Fermi level, E^* surface barrier potential; E_0, limiting surface barrier potential; E_A, energy level of adsorbed species.

a′), electrons, promoted by photons from negatively charged surface species, migrate into bulk conduction-band states, if they escape electron-hole recombination; and (IIb′), holes, produced by photoabsorption within the depletion layer of the semiconductor particles, migrate towards the negatively charged surface. For an *n*-type semiconductor surface dark-equilibrated with the electron-attaching gas before illumination (see Figure 7c), photoeffects IIa′ and b′ have the same net effect, reduction of the amount of excess negative charge stored adjacent to the surface. Consequently, the *illuminated* surface may be represented as bearing a surface potential E^*, lower than for the dark-equilibrated surface (*cf.* Figure 7b). A quantitative calculation of the reduction in surface potential effected by illumination would require detailed treatment of the various absorption and charge equilibria at the surface. This would involve the species, O, O^-, O_2^-, N_2O, O_2, etc., and, since surface concentrations of these species have not yet been measured in the conditions of our experiments, quantitative evaluation of the change in surface produced by illumination will not be attempted at this time. The preceding discussion shows, however, that it is reasonable to represent the qualitative effect of illumination as a fractional reduction in surface potential (*cf.* Figure 7). It will be shown in the following paragraphs that photoinduced phenomena involving N_2O at illuminated oxide surfaces can be qualitatively understood on this basis.

The magnitude of increases in conductivity caused by illumination, Δi^*, decreased as increasing pressures of N_2O were maintained over the illuminated surface (*cf.* Figure 6). Conversely, the rate of photoassisted dissociation of N_2O over the illuminated surface increased with P_{N_2O} in the manner illustrated by Figure 3. Processes Ia, Ib, and Ic, which were established as the mechanism of N_2O dissociation over the same surfaces in the dark, can also account for these photoeffects, since they have the net effect of converting a mobile carrier into a relatively immobile surface O^- fragment and a gaseous N_2 fragment. Process Ib, which is rate-determining for N_2O dissociation in the dark, leads to kinetic expressions 1, 2, and 3.

$$\text{Rate} = \frac{-\mathrm{d}[N_2O(g)]}{\mathrm{d}t} = \frac{\mathrm{d}[N_2(g)]}{\mathrm{d}t} = \frac{\mathrm{d}[O^-(\text{ads})]}{\mathrm{d}t} = k_b[N_2O(\text{ads})]n_s \quad (1)$$

$$n_s = n_b \exp[-(eE_0/kT)] \quad (2)$$

$$R_d = k_b\{N_2O(\text{ads})\}n_b \exp[-(eE_0/kT)] \quad (3)$$

Expression 2 assumes a Boltzmann distribution between the number of carriers in the bulk, n_b, and their effective concentration, n_s, at a surface which bears the limiting surface potential E_0, after dark-equilibration. A corresponding set of expressions, 4, 5, and 6, can be written for the illuminated surface, on the assumptions that (Ib) is still the rate-determining step for N_2O dissociation and that illumination reduces the surface potential to a new value E^*.

$$\text{Rate}^* = \frac{-\mathrm{d}[N_2O(g)]}{\mathrm{d}t} = \frac{\mathrm{d}[N_2(g)]}{\mathrm{d}t} = \frac{\mathrm{d}[O^-(\text{ads})]}{\mathrm{d}t} = k_b\{N_2O(\text{ads})\}n_s^* \quad (4)$$

$$n_s^* = n_b^* \exp[-(eE^*/kT)] \quad (5)$$

$$R^* = k_b[N_2O(\text{ads})]n_b^* \exp[-(eE^*/kT)] \quad (6)$$

The effective concentration of carriers at the illuminated surface, n_s^*, is higher than at the dark-equilibrated surface, (*cf.* the conductivity results). The same rate constant, k_b, is taken for (Ib) at thei lluminated and at the dark surface.

The rates evaluated from experimental results were R_d and $(R^* - R_d)$ and experimentally R_d was less than 5% of R^* except for Fe_2O_3. Expression 7 should then be a valid approximate relationship for zinc oxides and shows that

$$R_d/R^* - R_d \simeq n_b/n_b^* \exp[-e(E_0 - E^*)/kT] \quad (7)$$

rate of N_2O dissociation *via* (Ib) and (Ic) are enhanced at the illuminated surface to an extent depending exponentially on reduction, ΔE, in surface potential. If n_b/n_b^* is approximated to 1 and the measured rates of R_d and $(R^* - R_d)$ are employed in (7), values of ΔE = 0.03–0.2 eV can be derived. Undue significance should not be attached to values of ΔE derived in this manner. Comparison of ΔE values with E_0 value calculated for boundary-layer expressions shows, however, that the derived values are fully consistent with the fractional reduction in surface potential assumed in the present treatment. (See Table II.)

Pressure of undissociated gas phase N_2O remained effectively constant while kinetic data were taken on photoassisted dissociations because <0.1% of admitted N_2O was dissociated. For such conditions, (6) requires a constant rate of photoassisted dissociation whenever stationary values of E^* are established. Con-

ductivity measurements (*cf.* Figure 6) indicated that a photostationary state was achieved in *ca.* 20 min for P_{N_2O} values >0.5 Torr. The constant rate of photoassisted dissociation experimentally observed at higher P_{N_2O} values and at longer times (illuminations up to 10 hr were studied) are thus fully consistent with expression 6.

Expression 6 also indicates that the photorate should vary with P_{N_2O} in the same manner as $[N_2O(ads)]$. Unfortunately, it was not possible experimentally to determine the form of the absorption isotherm for N_2O on the oxides studied, because absorption was very slight at 20° and was complicated by the dark reaction. Crawford and Tompkins,[38] however, have shown that physical adsorption of N_2O on other solids, CaF_2 and BaF_2, obey a Freudlich isotherm, $N_2O(ads) \propto P_{N_2O}{}^n$ with n taking values of 0.2–0.5. If a Freudlich isotherm also applies for N_2O on the oxides studied here (*i.e.*, for process Ia), then plots of log (rate*) against log P_{N_2O} should be linear with slope n. Experimental data on pressure dependence of rate* obeyed such a relationship with n values of 0.25 for ZnO and 0.8 for Fe_2O_3.

When illumination ceased, the additional current decayed in the manner illustrated by Figure 6 and decay was more rapid the higher the pressure of N_2O above the surface. Analysis of the kinetics of these decays showed them to follow an Elovich-type expression 8, in which

$$\Delta i = a \log (t + t_0) + b \qquad (8)$$

Δi is the decrease in current at time t (from the maximum value noted during illumination) and a, b, and t_0 are constants. According to other workers,[5,21-24] such kinetic behavior may be attributed to electron localization by adsorbed species. In terms of step Ib and of Figures 7b and 7c, this corresponds to regrowth of surface potential from E^* towards its limiting value, E_0, *via* electron localization at $N_2O(ads)$. Inspection of Figure 6 shows that the "half-life" of photoconductivity after the end of illumination, *i.e.*, the times required for photoconductivity to decay by 50% was *ca.* 7 min under continuous evacuation and *ca.* 4 min at P_{N_2O} = 0.6 Torr. Elovich-type plots indicated that 25% of the enhanced conductivity would persist *in vacuo* to times > 15 min after the end of illumination. This accounts for the observed "memory effects," in which surfaces preilluminated *in vacuo* retained significant additional activity for N_2O dissociation for periods > 15 min after illumination. The presence of another gas known to localize electrons at the surface was expected to decrease the half-life of conductivity and of memory effects after illumination. Oxygen admitted to a preilluminated ZnO surface produced these effects (*ca.* point c in Figure 4).

Our observations on zinc oxides showing: (a) that quantum efficiency of photoassisted N_2O dissociation was $\sim 10^{-5}$ even with photons of energies greater than the ZnO band gap; (b) that similar quantum efficiencies were obtained for pure, indium-doped, and lithium-doped samples; and (c) that photons with energies lower than the band gap did promote N_2O dissociation, can be qualitatively accounted for, as follows, with (Ib) as the rate-limiting step. (a) Quantum efficiency for photoassisted dissociation cannot exceed that for electron promotion to the surface according to the suggested mechanism. Photon flux at the oxide surfaces was *ca.* 10^{17} cm^{-2} in our work and, with this flux of photons of λ = 365 nm incident on ZnO single crystals, Collins and Thomas[20] have measured a quantum efficiency of *ca.* 5×10^{-5}. (b) For various zinc oxide samples with dark conductivities differing by four orders of magnitude, Collins and Thomas report similar quantum efficiencies for promotion of electrons to the surfaces of their single crystal samples, provided that photon flux was *ca.* 10^{17} cm^{-2}. Similar quantum efficiencies for photoassisted dissociation of N_2O over the various zinc oxides are consistent with these observations. (c) Photoconductivity and photodesorption of oxygen has been observed on zinc oxide surfaces for wavelengths (500–600 nm) far outside the band edge of ZnO single crystals (385 nm). Both observations imply reduction of the surface potential which, in turn, would lead to photoassisted dissociation, as observed.

A comprehensive qualitative explanation of the observed photoeffects at the (N_2O/n-type oxide) interface is thus seen to be possible with a mechanism based on reduction of surface potential by illumination and consequent dissociation *via* (Ib) and (Ic). It is pertinent to enquire briefly if other mechanisms may also account for the observed results. The observed "memory" effects, persisting for minutes after illumination, would not be consistent with mechanisms requiring $N_2O(ads)$ to interact with photoproduced excitons, since the latter would disappear within *ca.* 10^{-8} sec of their formation. It is possible to envisage excitonlike states forming by slow electron-hole recombination after illumination, but their concentrations at the surface would necessarily be very low. The vanishingly small probability for *random* encounter between low concentrations of excitonlike states produced by recombination and the immeasurably small surface coverage by $N_2O(ads)$, leave process IIb followed by steps outlined below as the exciton-based mechanism possibly consistent with the "memory" effects and other results involving N_2O at the illuminated surface:

Migration of holes towards surface, (s), and electrons into bulk, b

$$(e + h)[MO^+ - O^-(ads)] \longrightarrow h_s + e_b \qquad (IIIa)$$

Localization of holes adjacent to adsorbed species, thus reducing surface potential

(38) V. A. Crawford and F. C. Tompkins, *Trans. Faraday Soc.*, **46**, 504 (1950).

$$h_s + N_2O(ads) \longrightarrow [h - N_2O(ads)]_s \quad (IIIb)$$

and

$$h_s + O^-(ads) \longrightarrow [h - O^-(ads)]_s \quad (IIIb')$$

Process Ib, migration of electrons to surface against reduced surface potential
Electron-hole recombination adjacent to adsorbed species, giving excitonlike states

$$e_s + [h - N_2O(ads)] \longrightarrow (e + h)^* - N_2O(ads) \quad (IIIc)$$

$$e_s + [h - O^-(ads)]_s \longrightarrow (e + h)^* - O^-(ads) \quad (IIIc')$$

Utilization of energy of excitonlike state of the solid, to dissociate $N_2O(ads)$

$$(e + h)^* - N_2O(ads) \longrightarrow N_2 + O(ads) \quad (IIId)$$

Although the observed kinetics and the memory effects in photoassisted N_2O dissociation might be explicable by such an exciton-based mechanism with (Ib) the rate-determining step, a convincing case for operation of the mechanism cannot presently be made because direct evidence for (IIIb) is lacking. Localization of photoproduced holes adjacent to $N_2O(ads)$ has not been established. Several workers have proposed that the competing process, IIIb', occurs on semiconductor surfaces bearing chemisorbed oxygen,[6] and on this basis it was expected that the presence of low oxygen pressures together with N_2O during illumination of the oxide surface would sharply reduce the overall rate of photoassisted dissociation if the exciton-based mechanism were important. Tests revealed, however, that oxygen pressures of 10^{-3} Torr did not significantly reduce the rate of photoassisted dissociation of N_2O.

Acknowledgments. The authors are grateful to D. O. Carpenter, New Jersey Zinc Company, for supplying the zinc oxide materials, to Dr. Moruzzi and Mr. Austin of Liverpool University for assistance with setting up the quadrupole mass spectrometer, and to Mr. Brady of this department for extensive assistance with the vacuum systems. Support of this work by funds from AFOSR is gratefully acknowledged.

An Electron Spin Resonance Study of the Photoionization of Thymine. The Thymine Cation and Anion Radicals[1]

by Michael D. Sevilla

Department of Chemistry, Oakland University, Rochester, Michigan 48063 *(Received October 1, 1970)*

Publication costs assisted by Oakland University

Ultraviolet irradiation of thymine at 77°K in both alkaline and acid glasses is shown to produce thymine cation radicals. The mechanism is considered to be biphotonic, *i.e.*, photoionization from the metastable triplet state. In the alkaline glass the esr spectra show the presence of the electron, produced by photoionization, as well as the π-cation radical. The thymine π anion is produced in the alkaline glass by photobleaching the trapped electron which then reacts with the parent compound. In the acid glass products of electron attachment are found as well as the cation radical. The esr spectra for the cation radicals in the acid and alkaline glasses have been reduced to hyperfine couplings which are found to be nearly identical. For the cation in the acid glass, the results are $A_{CH_3}^{H} = 20.4$ G, $A_{\parallel}^{N_1} = 11.8$ G, $A_{\perp}^{N_1} \leq 2$ G, $g_{\perp} = 2.0026$, and $g_{\parallel} = 2.0046$. The π anion shows only a 16-G splitting due to interaction with the C_6 proton. The results for the cations suggest little effect due to protonation of the nitrogens on the observed hyperfine splittings. McLachlan SCF–MO calculations of the spin density are found to be in good agreement with the experimental results for the cation radical. The cation and anion radicals are discussed in terms of the radiolysis of thymine single crystals and are suggested to be precursors to the observed radical species.

Introduction

The cation radicals of several purines have been reported to be produced through photolysis in frozen aqueous solutions at low temperatures.[2] The mechanism has been suggested to be photolysis of the metastable triplet state of these species. However, for the pyrimidine compounds, *e.g.*, thymine and cytosine, cation radicals are not produced at pH 7.[2] In agreement with these results Shulman and coworkers have found through both optical and esr methods that the neutral thymine and cytosine molecules do not show phosphorescence or appreciable population of the triplet state.[3,4] By increasing the pH to 12 where thymine has lost its N_3 proton, phosphorescence and esr signals due to the triplet were observed by these workers with a decay time of 0.60 sec.[5] Evidence was also presented which suggested an esr triplet resonance for thymine (pH 12) with both N_1 and N_3 protons removed (see Figure 1). From this previous work it is reasonable to expect that under conditions of high pH and low temperature thymine should photoionize from its excited triplet state.

This work reports an esr study in which the thymine π-cation radical is shown to be a product of the photoionization of thymine in an alkaline ice glass. Perhaps unexpected from previous work the cation is produced by photolysis of thymine in an acid glass as well. The anion radical of thymine is also produced by electron attachment in the alkaline glass.

Ion radicals have been shown to be products of the radiolysis of a crystalline pyrimidine, cytosine.[6] The results found here for thymine are used to propose a mechanism for product formation in the radiolysis of thymine single crystals involving the cation and anion as intermediates.

Experimental Section

Both acid and alkaline glasses were employed in this work. The glasses are produced by cooling solutions of 8 *N* NaOH or 6 *M* H_3PO_4 and the solute (thymine) in a 4 mm o.d. quartz tube to 77°K. To improve resolution of the esr signal deuterated glasses were usually employed.[7] The photolysis was performed at 77°K outside the esr cavity. A helical, low pressure mercury lamp was employed for the photolysis.

The esr spectrometer used in this study is a Varian V-4500-10A equipped with a Fieldial, low noise klystron, frequency meter, and dual cavity. Measurements of the hyperfine splittings and g values were made *vs.* peroxylamine disulfonate ($A_N = 13.0$ G and $g = 2.0056$).

Thymine was obtained from Calbiochem (Grade A).

Results

1. Thymine in an Alkaline Glass. Photolysis of

(1) This work was supported by the Division of Biology and Medicine of the U. S. Atomic Energy Commission.

(2) C. Helene, R. Santus, and P. Douzou, *Photochem. Photobiol.*, **5**, 127 (1966).

(3) R. G. Shulman and R. O. Rahn, *J. Chem. Phys.*, **45**, 2940 (1966).

(4) J. W. Longworth, R. O. Rahn, and R. G. Shulman, *ibid.*, **45**, 2930 (1966).

(5) Phosphorescence due to singly ionized thymine is reported at lower pH's in much lower intensity (ref 2 and 3).

(6) J. N. Herak and V. Galogaza, *J. Chem. Phys.*, **50**, 3101 (1969).

(7) (a) M. D. Sevilla, *J. Phys. Chem.*, **74**, 669 (1970); (b) M. D. Sevilla, *ibid.*, **74**, 2096 (1970).

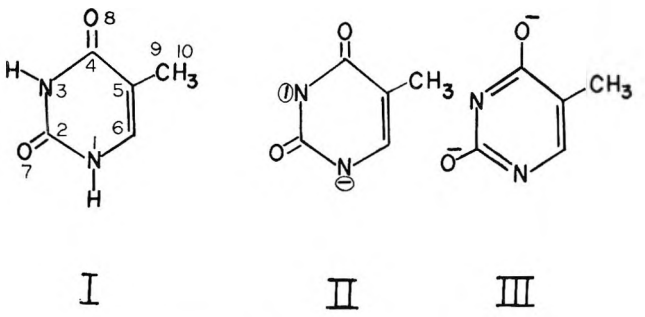

I II III

Figure 1. Structures of thymine in acid (I) and alkaline (II, III) glasses.

thymine (77°K) in an 8 *N* NaOD (92% D) glass at concentrations of 0.25 mg/ml[8] for as little as 15 sec produces a dark blue color in the glass. The sample is found to phosphoresce in the visible region during photolysis and for a few seconds after the photolysis is terminated. The later results suggest a significant population of the triplet state during photolysis.[4] The esr spectrum observed immediately after photolysis is shown in Figure 2A. The large singlet at $g = 2.0007$[9] and the blue color in the glass are characteristic of trapped electrons.[10] The remaining hyperfine structure is attributed to the species produced by photoionization. Since at pH >14 thymine is most likely unprotonated at the 1 and 3 positions, the species produced by loss of an electron (see Figure 1) is a monoanion. However, for ease of discussion the species will be considered a π-cation radical. The π-electron system, as will be shown, has lost one electron.

Photobleaching the sample containing the electron and π cation with light from an ir-visible lamp causes the electron to become mobile. The electron reacts with the π cation to form thymine and with thymine to form the π anion.[11] The result is a spectrum which is assumed to consist of approximately equal concentrations of the π cation and π anion (Figure 2B).[12] Warming the sample to $-130°$ results in the loss of the π-cation signal; however, the signal due to the π anion remains. Owing to the fact that the spectrum found for π anion is overlapped with a decay product of the π cation, the anion was prepared by a separate method. This method involves the photolysis of 10^{-2} *M* $K_4Fe(CN)_6$ to produce electrons in the deuterated alkaline glass which upon photobleaching react with thymine (5×10^{-4} *M*). This technique has been described in detail by other workers.[13] The spectrum due to the thymine π anion produced in this manner at 77°K is shown in Figure 2C. This spectrum consists of two hyperfine components separated by 16 G with $\Delta H_{m.s.} \cong 12$ G. Molecular orbital calculations (see below) suggest this splitting arises from the C_6 proton. This is verified by the production of the π anion of 6-methyluracil by the method described above. The 6-methyluracil anion shows a quartet spectrum with a 15.4-G

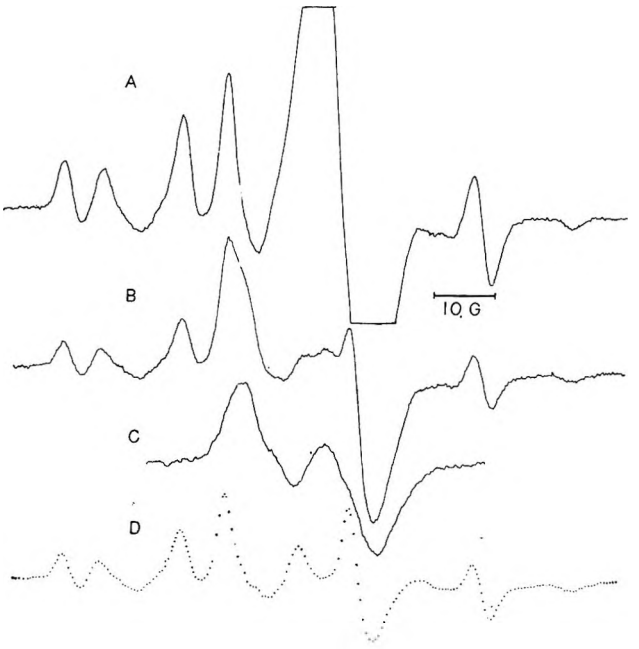

Figure 2. Esr spectra produced by the photoionization of thymine in an alkaline D_2O glass: A, the spectrum of the thymine π-cation radical taken immediately after photolysis at 77°K. The large central component is due to the electron; B, spectrum produced by photobleaching the electron in A and consisting of the superimposed spectra of the π-cation and anion radicals; C, π-anion radical (only) in an alkaline glass produced by electron attachment to thymine; D, spectrum of the π cation resulting from the subtraction of C from B.

hyperfine splitting. The intensity ratios are near 1:3:3:1 and leave no doubt that this is the methyl proton splitting.[14a] This shows the origin of the hyperfine interaction in the thymine (5-methyluracil) anion to be the C_6 proton.

A simple subtraction of the spectrum in Figure 2C from 2B gives the dotted curve (Figure 2D) which is solely due to the cation. The two components obscured in Figure 2A by the electron signal are now clearly resolved. However, the uncertainty in the subtraction technique is such that these components should be considered semiquantitative.

Upon warming of the sample containing the anion

(8) This low concentration should prevent appreciable aggregation.

(9) M. J. Blandemer, L. Shields, and M. C. R. Symons, *Nature (London)*, **199**, 902 (1963).

(10) P. B. Ayscough, R. G. Collins, and F. S. Dainton, *ibid.*, **205**, 965 (1965).

(11) This species is a trianion. For convenience it is called a π anion since the π system has gained one electron.

(12) Of course, electron reactions with impurities would result in more cation than anion.

(13) R. A. Holroyd and J. W. Glass, *Int. J. Radiat. Biol.*, **14**, 445 (1968).

(14) (a) M. D. Sevilla, results in preparation for publication. (b) The identification was facilitated by the production of IV by an alternant method, *i.e.*, the reaction of O^- with thymine [see L. S. Myers, J. F. Ward, W. T. Tsukamoto, D. E. Holmes, and J. R. Julca, *Science*, **148**, 1234 (1965); N. Nazhat and J. Weiss, *Trans. Faraday Soc.*, **66**, 1302 (1970)].

and cation decay product to −90° a further reaction occurs. The anion protonates (H_2O glass) to form the 5-methyl-5,6-dihydrouracil-5-yl or "thymyl" radical which shows a characteristic eight-line spectrum extending over 141 G. This reaction has been investigated previously by other workers.[13] The decay product of the π-cation radical has been identified as the radical produced by loss of a proton from the methyl group[14] (structure IV).

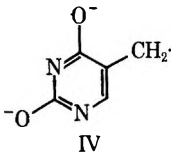

IV

2. Thymine in an Acid Glass. Photolysis of 0.5 mg/ml of thymine in 6 *M* H_3PO_4 at 77°K produces a spectrum attributed to the cation radical. In the absence of electron scavengers the cation spectrum is overlapped by a spectrum of the "thymyl" radical. Hydrogen atoms are also present in the spectrum most likely due to the reaction of electrons and H_3O^+.[10] Again the sample phosphoresces visibly during and immediately after photolysis, although the intensity is less than was found in the alkaline glass. To observe a spectrum of the positive ion relatively free from another signal, thymine solutions of D_3PO_4 (95% D) were saturated with N_2O at *ca.* −50°. Photolysis of this solution at 77°K produces a spectrum due to the positive ion (Figure 3). The electron reacts to form N_2O^- which further decays to ·OD.[10] In the acid glass the spectrum of ·OD is broad and unresolved and does not significantly interfere with that of the positive ion.[15] A comparison of Figures 2D and 3 shows that the spectra of the π-cation and cation radicals are remarkably similar.

Discussion

1. Spectral Analysis. Several properties of the spectrum of the thymine positive ion in the acid glass suggest a large splitting due to the methyl protons. First is the large total width of 85 G. For organic radicals such widths usually occur when there are large β-proton splittings. Second, the ratio of peak heights of 0.8:2.6:3.2:1.0 for the major components in Figure 3 suggest a freely rotating methyl group (theoretical 1:3:3:1). Third, the line widths of *ca.* 4 G are relatively narrow for a glassy spectrum. This property suggests some motional averaging such as a rotating methyl group. The spectrum also shows other hyperfine components which are anisotropic in nature (note ends of spectrum). Such line shapes would be expected for a single anisotropic nitrogen hyperfine coupling.[7,16] Similar arguments hold for the π-cation radical in the alkaline glass.

Molecular orbital calculations discussed below also suggest a large methyl splitting and a single nitrogen splitting (position 1). Other magnetic nuclei at positions 3(N) and 6(H) are predicted to have small splittings.

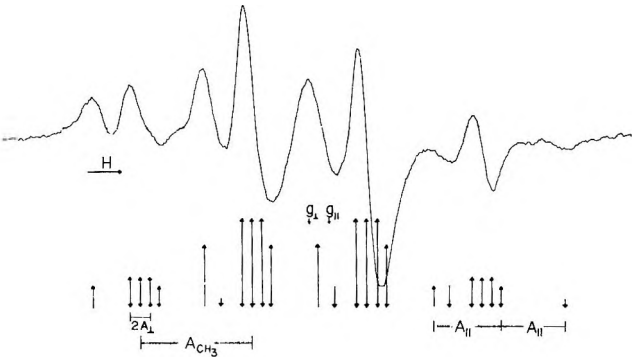

Figure 3. Esr spectrum of the thymine cation radical produced by photoionization of thymine at 77°K in a 6 *M* D_3PO_4 glass. The sample was saturated with N_2O prior to photolysis to scavenge electrons. The stick reconstruction is based on theoretical parameters described in the text.

If it is assumed that the nitrogen at position 1 has axial symmetry (generally a good approximation), the spectrum can be readily interpreted. The spin Hamiltonian for a molecule containing a single anisotropic hyperfine splitting under the assumption of axial symmetry has been solved. The transitions for such a system with the addition of an isotropic methyl group coupling are given by the relation[17,18]

$$h\nu = (^1/_3 g_\parallel + {}^2/_3 g_\perp)\beta H + A_{CH_3}{}^H M_{CH_3} + A_N M_N + [^1/_3(g_\parallel - g_\perp)\beta H + B_N M_N](3\cos^2\theta - 1) \quad (1)$$

where $A_{CH_3}{}^H$, A_N, and B_N are in units of megacycles per second and are the isotropic methyl, isotropic nitrogen, and anisotropic nitrogen hyperfine splittings, respectively.

In glassy or polycrystalline substances values of θ equal to zero and $\pi/2$ produce various maxima and minima in the spectrum.[19] Positions in magnetic field of these extrema are given by

$$H(\theta = 0) = \frac{h\nu}{g_\parallel \beta} - \frac{g_e}{g_\parallel} A_\parallel M_N - \frac{g_e}{g_\parallel} a_{CH_3} M_H \quad (2)$$

$$H(\theta = \pi/2) = \frac{h\nu}{g_\perp \beta} - \frac{g_e}{g_\perp} A_\perp M_N - \frac{g_e}{g_\perp} a_{CH_3} M_H \quad (3)$$

(15) There is an interfering signal which increases the amplitude of the component at $g_\perp$.

(16) N. Edelstein, A. Kwok, and A. H. Maki, *J. Chem. Phys.*, **41**, 179 (1964).

(17) F. J. Adrian, *ibid.*, **36**, 1692 (1962).

(18) This relation is exact only at $\theta = 0$ and $\pi/2$. An exact solution for all angles θ has been found [R. Nieman and D. Kivelson, *ibid.*, **35**, 156 (1961)]. This solution, of course, results in the same relations at $\theta = 0$ and $\pi/2$.

(19) P. W. Atkins and M. C. R. Symons, "The Structure of Inorganic Radicals," Elsevier, Amsterdam, 1967, pp 268–271.

where $A_{||} = a_N + 2b_N$, $A_\perp = a_N - b_N$, and a_{CH_3}, a_N, b_N correspond to A_{CH_3}, A_N, B_N converted into units of gauss.

Analysis of the spectrum of the positive ion (Figure 3) in terms of the parameters in eq 2 and 3 yields $a_{CH_3}^H = 20.4 \pm 0.1$ G, $A_{||}^N = 11.8 \pm 0.2$ G, $A_\perp^N \leq 2$ G,[20] $g_{||} = 2.0026 \pm 0.0002$, and $g_\perp = 2.0046 \pm 0.0006$. A similar analysis for the π-cation radical in the alkaline glass gives $a_{CH_3}^H = 20.5 \pm 0.2$ G, $A_{||}^N = 12.0 \pm 0.3$ G, $A_\perp^N \leq 2$ G, $g_{||} = 2.0023 \pm 0.0002$, and $g_\perp = 2.0042 \pm 0.0006$.

The large uncertainty in $g_\perp$ is due to the fact that the components used to measure $g_\perp$ are overlapped. Consequently only an approximate value could be determined from an analysis of the line shape of these components. The values of $g_{||}$ are less uncertain since the end components of the spectrum which determine $g_{||}$ are free from overlap. A stick reconstruction based on the parameters for the cation in the acid glass is shown in Figure 3. The agreement between theory and experiment is excellent and indicates that the analysis is correct. The diagram also compares favorably with the results found in the alkaline medium.

The hyperfine parameters found for the cation and the π cation are nearly identical. Only the g values and line shapes of the various components distinguish the two radicals. These results suggest a very small or negligible effect due to the differences in protonation. This is a somewhat surprising result.

For later comparison to theoretical calculations it is of interest to determine a_N and b_N. Solution of simultaneous equations employing the experimental values of $A_{||}^N$ and $A_\perp^N$ yields $4 < a_N < 5.3$ and $4 > b_N > 3.3$ for both radicals.

2. Spin Density Calculations. McLachlan SCF–MO calculations of the spin density have been performed for comparison to the experimental results. Such MO calculations have been shown to give good agreement with the hyperfine splittings found for the purine and pyrimidine anions[21] and should provide an adequate description of the spin density in these molecules.

Spin density calculations are performed for both the protonated (cation) and unprotonated (π-cation and π-anion) radicals. The calculation for the protonated case employs MO parameters suitable for structure I in Figure 1,[22] while the calculations for the unprotonated case employs parameters suitable for structures II and III.[22,23] These MO parameters are given in Table I and have been employed in similar molecules with good results.[21,22]

The table lists the hyperfine splittings calculated from the spin density distribution. Values of Q employed for the cations are $Q_N^N \approx +27$,[22b,23] $Q_{CH_3}^H \approx +40$,[22b] and $Q_{CH}^H \approx -30$.[22b] The values $Q_{CH}^H \approx -24$, $Q_N^N \approx +27$, and $Q_{CH_3}^H \approx +20$ are employed for the anion radical.[22b] For the cation radicals a comparison of the theoretical splittings with the experimental results for each calculation shows that the major features are generally correctly predicted, *i.e.*, a large methyl splitting of *ca.* 20 G, only one nitrogen with a significant splitting, and a small splitting for the proton at position 6. Only the result for the proton splitting at position 6 in case I is not in good agreement. A more detailed comparison for the unprotonated thymine π cation shows the calculation based on structure III is in better agreement with the nitrogen hyperfine splitting than that based on structure II. This suggests that structure III (minus one electron from its π system) is the predominant valence state for the π cation.

One aspect of the experimental results for the cation radicals is intriguing. It is the fact that the observed hyperfine splittings for the two cation radicals show no apparent effect of protonation. This is in reasonable accord with the theoretical calculations (I and III)

Table I: Theoretical Spin Densities and Hyperfine Splittings

	Cation			Anion
	I	II	III	III
McLachlan Spin Densities[a]				
Position 1	0.150	0.335	0.115	0.165
2	−0.008	−0.013	0.083	−0.037
3	−0.004	−0.006	−0.011	0.140
4	−0.019	−0.011	0.078	0.304
5	0.457	0.441	0.465	−0.050
6	0.194	0.024	0.064	0.457
7	0.035	0.064	0.056	−0.006
8	0.112	0.098	0.058	0.033
9	0.003	−0.002	0.006	0.000
10	0.081	0.071	0.087	−0.005
MO Parameters				
h_N	1.5	0.8	0.8	0.8
k_{C-N}	0.8	0.8	1.08	1.08
h_O	1.2	1.2	2.0	2.0
k_{C-O}	1.6	1.6	1.0	1.0

Theoretical Splittings, G

		(Exptl)			(Exptl)		(Exptl)
1(N)	4.1	4–5.3	9.1	3.1	4–5.3	4.5	*b*
3(N)	0.1	<2	0.2	0.3	<2	3.8	*b*
5(CH_3)	18.3	20.4	17.6	18.6	20.5	1.0	*b*
6(H)	5.8	<4	0.7	1.9	<4	11.0	16

[a] $\lambda = 1.0$. [b] No other splittings are found for the thymine anion; however, the line width of 12 G sets an upper limit for these values. The lack of resolution and the large splitting for the C_5 proton suggest values somewhat smaller than the theoretical values for these splittings.

(20) The magnitude of $A_\perp$ is assumed to be less than one-half the line width.

(21) M. D. Sevilla, *J. Phys. Chem.*, **74**, 805 (1970).

(22) (a) A. Streitwieser, "Molecular Orbital Theory for Organic Chemists," Wiley, New York, N. Y., 1962; (b) G. Vincow in "Radical Ions," E. T. Kaiser and L. Kevan, Ed., Interscience, New York, N. Y., 1968.

(23) C. L. Talcott and R. J. Myers, *Mol. Phys.*, **12**, 549 (1967).

which predict little effect on the methyl proton splitting and only a moderate effect on the $a_{N(1)}$ splitting.

It should be noted that calculations for one of the other tautomeric forms of the protonated molecule, *i.e.*, where the oxygens are protonated rather than the nitrogens, would employ similar MO parameters as used for calculation III.[24] Since this would result in little difference in the observed hyperfine splittings for the various tautomers, there is no way to distinguish between these tautomers by means of their methyl proton and nitrogen hyperfine splittings alone. Only a complete resolution of the esr spectra in single crystals or in solution would settle this question.

The theoretical results for the single thymine anion splitting suggest a smaller value than is found experimentally. The fact that the anion of 6-methyluracil gave a large methyl proton splitting (15.4 G) is good evidence that a high spin density is found at position 6. For anions the Q for a methyl is approximately 20 *vs.* 24 for an α proton.[22b] The spin density indicated by experiment is then approximately 0.67 (thymine anion) and 0.77 (6-methyluracil anion). Using an SCF method Baudet, Berthier, and Pullman have calculated the spin densities for the protonated uracil anion and cation.[25] For the anion the calculated spin density at position 6 is 0.64, and the spin density at position 5 of the cation is 0.56. The result found for the anion is, therefore, in good agreement with the spin density at position 6 found for the unprotonated thymine anion. However, the inclusion of the effect of the 5-methyl group and the lack of nitrogen protons in their calculations would be expected to alter the spin density distribution somewhat. Pullman has performed a simple HMO calculation for the protonated thymine cation.[26] This calculation predicts the same general features as those found in Table I.

Summary and Conclusions

The evidence for the production of the thymine cation radical in the acid glass and a thymine π cation in an alkaline glass is considered strong. Phosphorescence is observed in both alkaline and acid glasses. This suggests an appreciable population of the triplet state which is necessary for photoionization. The electron is found after photolysis of thymine in the alkaline glass and products of electron reactions (*e.g.*, H) are found in the acid glass. Finally the hyperfine couplings found from the analysis of the esr spectra for these radicals are in good agreement with the proposed radical's structure and with theoretical splittings.

The identification of the cation and anion radicals in this work is of significance to radiolysis studies of thymine single crystals. These species should be prime radical species formed upon radiolysis. Ionic species have been previously suggested as products of the radiolysis of pyrimidines and purines.[27] At present radiolysis studies of thymine[28-32] at 77°K do not give evidence of ionic species. However, these species may be stabilized at lower temperatures than have been thus far employed.

In the radiolysis of thymine monohydrate at 77°K two radical species have been identified.[31] These radicals are

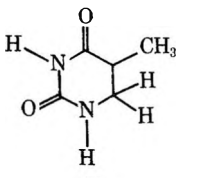

V

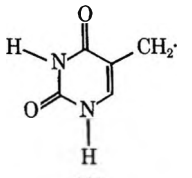

VI

The radicals are formed in approximately equal concentrations. The production of V has been attributed to hydrogen atom attack. In this mechanism the H atoms originate by loss of a hydrogen from the CH_3 group of thymine. This produces VI. Other workers have also stressed the importance of hydrogen atoms in the radiolysis of thymine[28,29,32] and other crystalline pyrimidines.[33]

In view of the results found in this work and by Holroyd and Glass[13] an alternate hypothesis must be considered for radical production in the radiolysis of thymine. In this mechanism the radiation ionizes thymine to form the cation and by electron attachment the anion. The anion then reacts with the water in the crystal (protonates) to form V, whereas the cation reacts by loss of a proton to form the second radical species, VI.

Several experimental observations add some weight to the latter hypothesis. (1) The two radical species found in the radiolysis of thymine are found to be products of the positive and negative ions of thymine. (2) Radiolysis of cytosine is found to produce the positive and negative ions at 77°K.[6] This shows ionic species

(24) (a) A number of calculations of the total energy of the tautomers of the neutral purine and pyrimidine molecules have been performed [see B. Pullman and A. Pullman, "Quantum Biochemistry," Interscience, New York, N. Y., 1963; B. Pullman, E. D. Bergmann, H. W. Feilchenfeld, and Z. Neiman, *Int. J. Quantum Chem.*, **3**, 103 (1969); B. Pullman, H. Berthod, and M. Dreyfus, *Theoret. Chim. Acta*, **15**, 265 (1969); N. Bodor, M. J. S. Dewar, and A. J. Harget, *J. Amer. Chem. Soc.*, **92**, 2929 (1970)]. However, the total energies of the tautomers of the radical ions have not been listed. (b) It is also possible that the thymine cation is protonated at an exocyclic oxygen in the phosphoric acid glass. However, the low pK for protonation at such a position (pK $\sim$ 0) and the increased acidity of the cation radical over the neutral molecule make this somewhat unlikely.

(25) J. Baudet, G. Berthier, and B. Pullman, *C. R. Acad. Sci.*, **254**, 762 (1962).

(26) A. Pullman, *J. Chim. Phys.*, **61**, 1666 (1964).

(27) See ref 26 for example.

(28) W. Gordy, B. Pruden, and W. Snipes, *Proc. Natl. Acad. Sci. U. S.*, **53**, 751 (1965).

(29) H. C. Heller and T. Cole. *ibid.*, **54**, 1486 (1965).

(30) M. G. Ormerod, *Int. J. Radiat. Biol.*, **9**, 291 (1965).

(31) J. Hütterman, *ibid.*, **17**, 249 (1970).

(32) T. Henriksen and W. Snipes, *Radiat. Res.*, **42**, 255 (1970).

(33) J. B. Cook, J. P. Elliot, and S. J. Wyard, *Mol. Phys.*, **13**, 49 (1967).

are produced in the radiolysis of crystalline pyrimidines. (3) Radiolysis of anhydrous crystals of thymine at room temperature does not produce V.[34] However, VI is produced. This suggests that water is necessary for production of V. This agrees with a protonation mechanism but not with an H-atom addition mechanism. (4) Recent work on the radiolysis of 5-methyl cytosine single crystals indicates the anion is an initial product which later converts into the protonated species.[34]

Finally, it is of interest to point out that the proposed mechanism may be applicable to the radiolysis of DNA where thymidine ion radicals would be expected to form.[13]

Acknowledgment. The author wishes to thank Dr. Jürgen Hütterman for communication of his results prior to publication.

(34) J. Hütterman, private communication.

Coordination Effects on the Spectrum of Uranium(IV) in Molten Fluorides[1]

by L. M. Toth

Reactor Chemistry Division, Oak Ridge National Laboratory, Oak Ridge, Tennessee 37830 *(Received May 28, 1970)*

Publication costs assisted by the Oak Ridge National Laboratory

The spectrum of U(IV) in molten fluoride solutions (primarily LiF–BeF_2 mixtures) exhibits a variation with melt composition which has been attributed to a change in the U(IV) coordination number. An equilibrium between two species $UF_8^{4-} \rightleftarrows UF_7^{3-} + F^-$ adequately explains the data. The identity of the species in fluoride-rich solvents has been established as UF_8^{4-} by comparison of the melt spectra with crystal spectra of known coordination. Although crystal spectra of 7-coordinated U(IV) are more complicated, such a comparison suggests that the species present in fluoride-deficient melts is predominantly UF_7^{3-}.

Introduction

The spectrum of U(IV) in molten fluoride solvents has been previously attributed to possibly an 8- or 9-coordinated species by comparison with spectra obtained in aqueous and other molten salt systems.[2] There has been no implication that more than the one species exists in molten fluoride solutions. Spectra of U(IV) in other molten salt media, principally chlorides, have been attributed to 8-coordinated species in the LiCl–KCl eutectic[3] and equilibria between 6- and lower coordinated species in the KCl–$AlCl_3$ solvent system.[4] The work in these chloride media has shown, first, that significantly different complex ions are present in these solvents and, second, that redox equilibria involving these U(IV) ions are (or may be) significantly affected by the nature of the particular complex ion present.[4]

In contrast to the details described for U(IV) in molten chlorides, coordination effects for U(IV) in molten fluorides have never been demonstrated because of the difficulty involving in containing the fluoride melt in an optical cell at temperatures of 500° and greater. The diamond-windowed spectrophotometric cell[5] has eliminated this problem and has permitted the initiation of detailed studies on various cations in molten fluoride solvents.

The importance of understanding the complex ion nature of U(IV) in molten fluoride solutions rests not only with an explanation of the coordination effects but also with a demonstration of the results of these effects on the uranium redox chemistry. A future extension of this work will then endeavor to demonstrate the roles which various complexes of U(IV) play on the stability of U(III)–U(IV) mixtures in molten fluorides. This is of practical interest in the Molten Salt Reactor Experiment at this laboratory which ultilizes a U(III)–U(IV) mixture in molten fluoride solution as the reactor fuel. The first step and subject of this paper is therefore a demonstration of the coordination chemistry active in molten fluoride solutions.

(1) Research sponsored by the U. S. Atomic Energy Commission under contract with the Union Carbide Corp.

(2) J. P. Young, *Inorg. Chem.*, **6**, 1486 (1967).

(3) D. M. Gruen and R. L. McBeth, *J. Inorg. Nucl. Chem.*, **9**, 290 (1959).

(4) J. R. Morrey, *Inorg. Chem.*, **2**, 163 (1963).

(5) L. M. Toth, J. P. Young, and G. P. Smith, *Anal. Chem.*, **41**, 683 (1969).

Experimental Section

Sample Preparation. All solutions, whether for melt or crystal spectra, were prepared in the same manner. Within a helium atmosphere drybox of <1 ppm H_2O content, individual components of the sample were weighed and loaded into a nickel pot fitted with a graphite liner. The mixtures were fused and bubbled with anhydrous HF (99.9% purity) for a period of 2–4 hr through a graphite dipleg immersed in the melt. A final flush with dry helium served to remove excess HF from the solutions. The samples destined for melt spectra were quenched and returned to the drybox for further handling. The samples for crystal spectra were held above the fusion temperature for approximately 1 hr and then cooled slowly at approximately 2°/hr for crystal growth.

Melt Spectra. Samples (~0.5-g solid chunks) for melt spectra were loaded into a diamond-windowed spectrophotometric cell, previously described[5] as the best known method of obtaining quantitative molten fluoride spectra. The cell was transferred within an air-tight helium-filled chamber from the drybox to a vacuum spectrophotometric furnace designed to hold molten samples of fluoride salts without contamination during the measurement of their absorption spectra. The furnace and procedure has been previously described.[6] Spectra were taken on a Cary 14H recording spectrometer equipped with standard Cary digital readout and tapepunch accessories. The spectra were corrected for base line absorbance and appropriate scale factors included through manipulation on an IBM computer. Resultant spectra were then plotted on a Calcomp plotter.

Crystal Spectra. KTh_2F_9 was prepared by growing from a melt of composition KF–ThF_4 (38:62 mol %) in which 2.5 mol % of the ThF_4 had been substituted for UF_4. The crystals were grown as the primary phase by cooling at 2°/hr from 950 to 850°. A Debye–Scherrer powder pattern of the crystals agreed with the previously reported pattern for KTh_2F_9.

Crystals of approximately 0.5 cm^2 area and 1 mm thick were isolated and polished flat in a drybox. They were mounted in a holder, loaded into the air-tight transfer chamber (previously mentioned), and placed in the high-temperature vacuum spectrophotometric furnace with no exposure to room air. Subsequent procedures for room temperature to 550° spectra were the same as described in the melt operation of the previous section.

7:6 KF–ThF_4 was grown as the primary phase from a melt of composition KF–ThF_4 (57:43 mol %) in which 4.6 mol % of the ThF_4 had been substituted for UF_4. A Debye–Scherrer powder pattern of the crystals agreed with the previously reported pattern for $K_7Th_6F_{31}$.

Cs_3ThF_7 was grown as the primary phase from a melt of composition CsF–ThF_4 (85:15 mol %) in which 10 mol % of the ThF_4 had been substituted for UF_4. A Debye–Scherrer powder pattern agreed with the previously reported pattern for Cs_3ThF_7.

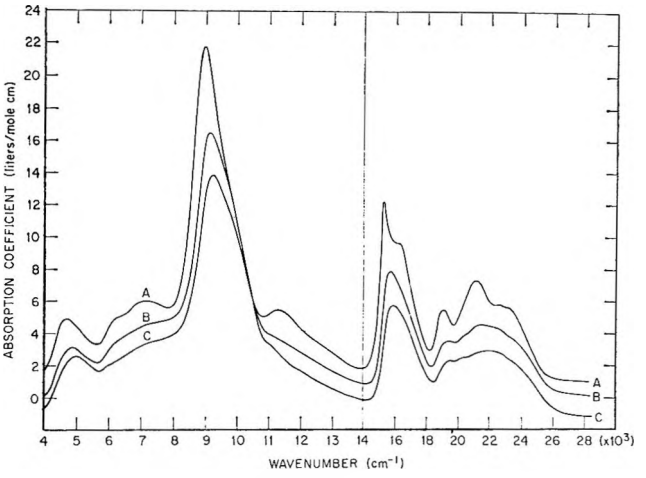

Figure 1. Solvent composition effect on the spectrum of approximately 1 mol % U(IV) in molten fluorides at 550°. The trend from curves A to C is from fluoride-rich to fluoride-deficient systems. Solvents: curve A, LiF–NaF–KF (46.5:11.5–42.0 mol %); curve B, LiF–BeF_2 (66:34 mol %); curve C, LiF–BeF_2 (48:52 mol %). The spectra are spaced one absorption coefficient unit apart to prevent overlap.

Results and Discussion

The spectrum of U(IV) at 550° as a function of solvent composition is shown in Figure 1. U(IV) exhibits different absorption spectra as the solvent changes from alkali fluoride rich to alkali fluoride deficient. This trend in solvent composition is regarded in the Lewis concept as moving from a basic to an acidic solvent. In the LiF–BeF_2 system, it depends on the equilibrium between bridged and nonbridged fluorides[7]

$$-Be-F-Be^{(-)} + F^- \rightleftharpoons -Be-F^{(-)} + {}^{(-)}F-Be- \quad (1)$$

The equilibrium shown in eq 1 presumes that Be^{2+} forms BeF_4^{2-} tetrahedra with either bridging or nonbridging fluorides. Solutions with fluoride ion concentrations in excess of that required for BeF_4^{2-} with no bridging are considered basic, whereas those with increasing degrees of fluoride bridging due to decreases in $[F^-]$ are considered acidic (see, for example, Figure 3 of ref 7).

The alkali fluoride solvent of composition LiF–NaF–KF (46.5:11.5:42.0 mol %) represents a system of no bridged fluorides. It is therefore the highest degree of basicity obtainable at 550°. Similar degrees of basicity could be approached by increasing the LiF–BeF_2 solutions over that of the 66:34 mol % composition, but the melting point of such a mixture becomes too high to emphasize some of the lower temperature features.[8]

(6) J. P. Young, *Inorg. Chem.*, 6, 1486 (1967).
(7) C. F. Baes, Jr., *J. Solid State Chem.*, 1, 159 (1970).

[Henceforth in this discussion, the solvent of composition 66:34 mol % $LiF-BeF_2$ will be referred to as "L_2B" and that of 48:52 mol % as the eutectic composition.[8]] It was for this reason that the LiF–NaF–KF solution was taken as the basic extreme in Figure 1. It should be emphasized, however, that the trend manifested in the LiF–NaF–KF solvent is present also in the $LiF-BeF_2$ system at 550° over to the solidus curve at 31 mol % BeF_2.

The changes in the absorption spectra of Figure 1 demonstrate the effect of the melt composition on the U(IV) spectrum. Crystal spectra of different coordination numbers (to be discussed later with respect to Figures 4–6) suggest that the melt spectra variations are due to altering the F^- coordination number around U(IV). It shall be shown then that competitive reactions involving equilibria of eq 1 and the two-species model of eq 2 adequately describe the spectral results

$$yF^- + UF_{x-y}^{4-(x-y)} \rightleftharpoons UF_x^{4-x} \qquad (2)$$

where the coordination number of UF_x^{4-x} is greater than that of $UF_{x-y}^{4-(x-y)}$. Changes in F^- due to changing solvent composition (such as in $LiF-BeF_2$ mixtures[7]) and/or changes in the temperature can then be expected to shift the equilibrium of eq 2 to one side or the other and thus alter the coordination number of U(IV) in the melt.

Although all U(IV) spectra in fluoride melts thus far investigated reveal general features of similarity in the regions 8000–10,000, 15,000–17,000, and 19,000–24,000 cm^{-1}, careful examination reveals that within these regions and elsewhere differences in both band position and *intensity* enable the identification of at least two distinct species in the melts (and three in fluoride crystals).

Figure 1 shows the effect of solvent composition on the spectrum of U(IV) at 550°. In going from a melt environment of high F^- activity (curve A) to one of low activity (curve C), a trend from one species designated as UF_x^{4-x} towards another, $UF_{x-y}^{4-(x-y)}$, is clearly demonstrated. Especially evident is the marked decrease in the intensity of the spectra with corresponding decreases in the F^- activity.

Figures 2 and 3 show the temperature effect on the U(IV) spectrum in the L_2B and $LiF-BeF_2$ eutectic solvents, respectively. The inclusion of temperature effects on the U(IV) spectrum is necessary to emphasize the differences in the spectra of the two species in solution because only in curve 3E does the $UF_{x-y}^{4-(x-y)}$ species appear essentially alone. From both figures it is seen that the species present in regions of high F^- activity is also the dominant form of U(IV) at lower temperatures. Therefore UF_x^{4-x} is designated as the low-temperature, higher coordinated form and $UF_{x-y}^{4-(x-y)}$ as the high-temperature, lower coordinated form.

From curves 1A, 2A, and 3A it is possible to list those

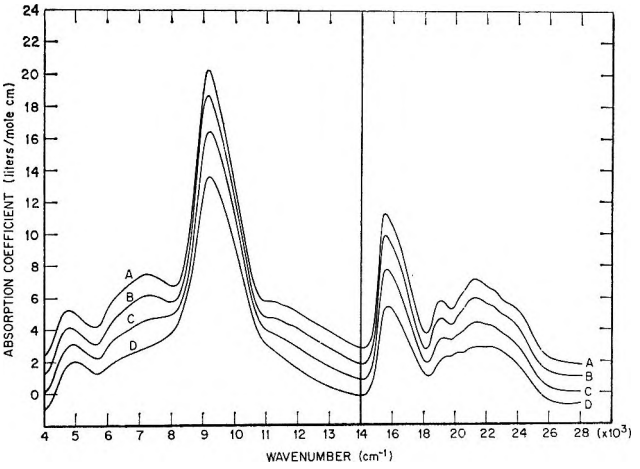

Figure 2. Temperature effect on the spectrum of approximately 1 mol % U(IV) in $LiF-BeF_2$ (66:34 mol %): curve A, 460°; B, 500°; C, 550°; D, 690°. The spectra are spaced one absorption coefficient unit apart to prevent overlap.

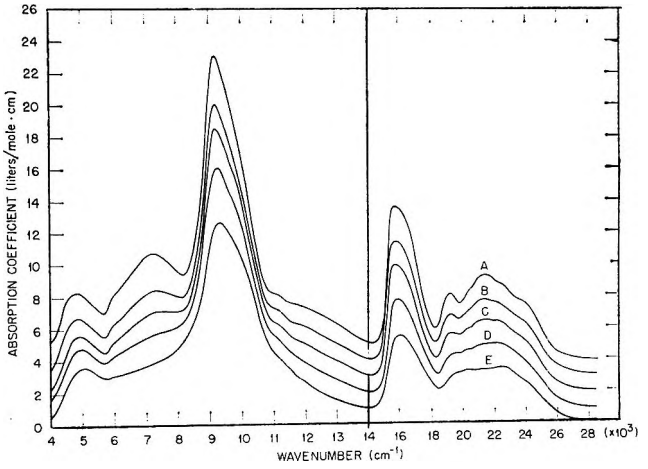

Figure 3. Temperature effect on the spectrum of approximately 1 mol % U(IV) in $LiF-BeF_2$ (48:52 mol %): curve A, 360°, B, 450°; 490°; D, 550°C; E, 690°. The spectra are spaced one absorption coefficient unit apart to prevent overlap.

transitions characteristic of UF_x^{4-x} and from 2D and 3E those of $UF_{x-y}^{4-(x-y)}$. Because curve 1A represents U(IV) in a solvent system of abundant F^-, it is assumed that this spectrum represents pure UF_x^{4-x} and that the absorption coefficient, ϵ, for this species can be read directly. However, values of ϵ at 550° for the $UF_{x-y}^{4-(x-y)}$ species cannot be read directly because the other curves at 550° represent mixtures of the two species (*cf.* curves 2C and 3D). It is nevertheless evident from curve 3D that $\epsilon_{9250\ cm^{-1}}$ for $UF_{x-y}^{4-(x-y)}$ is less than 14 l. mol^{-1} cm^{-1}. Table I lists the characteristic peaks of both species along with these noteworthy values of ϵ at 550°.

Most characteristic of UF_x^{4-x} are the transitions in the 6000–8000-cm^{-1} region, the intensity of the 9100-cm^{-1} peak (20.8 l. mol^{-1} cm^{-1}), and the prominent

(8) L. V. Jones, *et al.*, *J. Amer. Ceram. Soc.*, **45**, 80 (1962).

Table I: Characteristic Transitions (in $cm^{-1} \times 10^{-3}$) for UF_x^{4-x} and $UF_{x-y}^{4-(x-y)}$ Taken from Figures 1–3

UF_x^{4-x}	$UF_{x-y}^{4-(x-y)}$
4.7	4.95
6.2	
7.1	
9.1 (20.8)[a]	9.25 (≤14)[b]
15.25 (11.0)	15.85
16.30 (8.7)	16.7
19.0	19.4
21.1 (6.8)	20.25
22.5	22.5
23.2	

[a] Absorption coefficients at 550° in l. mol^{-1} cm^{-1} for some major peaks were read from Figure 1 and are given in parentheses. [b] Estimated.

peak at 21,100 cm^{-1}. The transition at 11,500 cm^{-1} in curve 1A is not listed as characteristic of this species because it is not seen in either curve 2A or 3A. The peak at 16,300 cm^{-1} is at most only a shoulder in curves 2A and 3A but has been seen under enough circumstances to be recognized as characteristic of this species.

The $UF_{x-y}^{4-(x-y)}$ species has a small peak at 5000 cm^{-1} but is virtually devoid of transitions in the 6000–8000-cm^{-1} regions (*cf.* curve 3E). The absence of any well-resolved peaks at 19,000 and 21,000 cm^{-1} is also typical of this species. Most characteristic of the $UF_{x-y}^{4-(x-y)}$ spectrum is the overall weakness in its intensity which clearly distinguishes it from the UF_x^{4-x} spectrum.

Identification of the U(IV) Species in Solution. Identification of the UF_x^{4-x} and $UF_{x-y}^{4-(x-y)}$ species was made by comparing their spectra with spectra obtained from U(IV)-doped fluoride host crystals of the general formula $A_xTh_yF_{4y+x}$ where A is an alkali metal. Dilute amounts of U^{4+} were substituted into Th sites where the coordination number of fluoride around the thorium

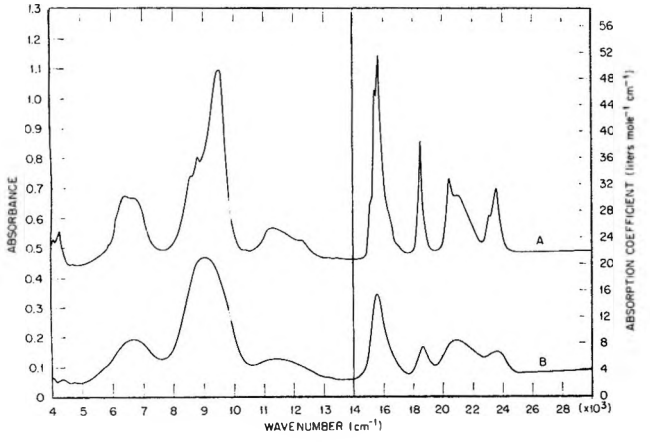

Figure 4. 9-Coordinated crystal spectrum of U(IV) at room temperature, curve A, and 550°, curve B. The crystal is KTh_2F_9 doped with 1.5 mol % UF_4.

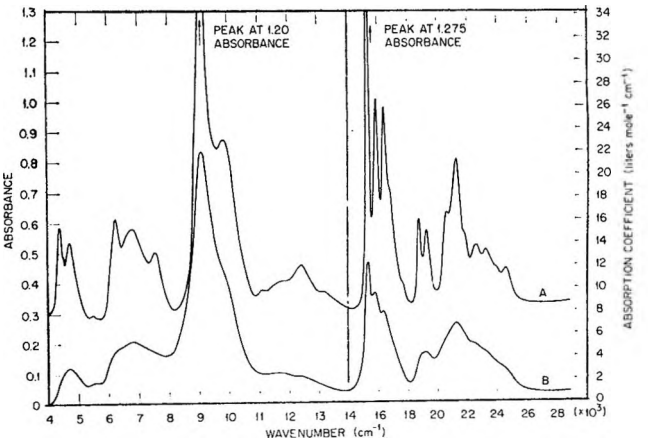

Figure 5. 8-Coordinated crystal spectrum of U(IV) at room temperature, curve A, and 550°, curve B. The crystal is $K_7Th_6F_{31}$ doped with 2.0 mol % UF_4.

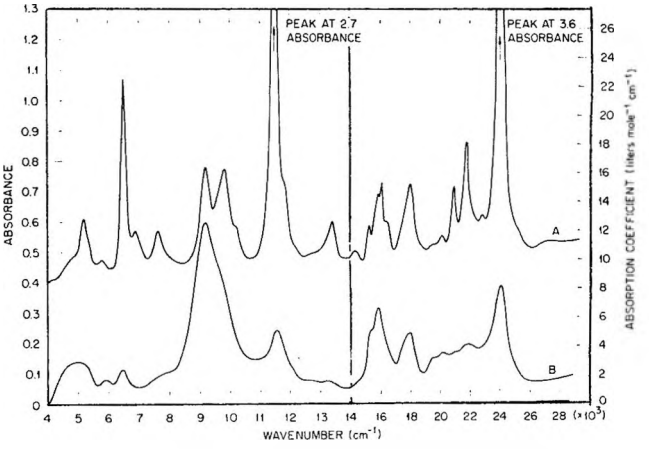

Figure 6. 7-Coordinated crystal spectrum of U(IV) at room temperature, curve A, and 550°, curve B. The crystal is Cs_3ThF_7 containing 1.65 mol % UF_4.

Table II: Characteristic Transitions (in $cm^{-1} \times 10^{-3}$) for 9-, 8-, and 7-Coordinated U(IV) in Fluoride Host Crystals KTh_2F_9, $K_7Th_6F_{31}$, and Cs_3ThF_7, Respectively, at 550° Taken from Figures 4–6

Coordination no.		
9	8	7
	4.7	5.0
	6.25	
6.65	6.80	
9.05 (19.0)[a]	9.1 (22.1)	9.20 (12.6)
11.5		
15.5 (15.5)	15.35 (9.8)	15.3 (4.1)
	15.85 (7.6)	15.8 (5.6)
	16.40	16.4
18.6	18.9	19.4
	19.25	20.1
20.8	21.3	
23.7	22.6	22.8
	24.5	

[a] Absorption coefficients in l. mol^{-1} cm^{-1} for some major peaks are given in parentheses.

site had been determined by X-ray crystallography. Coordination numbers of 9, 8, and 7 are obtainable in this fashion with 9 and 8 being the most common. Spectra representative of these coordination numbers are shown in Figures 4–6 with pertinent transitions and absorption coefficients listed in Table II.

The spectrum of 1.5 mol % U(IV) doped into the 9-coordinated thorium site of KTh_2F_9 (crystal structure analogous to 9-coordinated KU_2F_9[9]) at room temperature and 550° is shown in Figure 4. Characteristic of the 9-coordinated species is the very weak, if any, transition in the 4000–5000-cm^{-1} region, the broad, intense (ϵ 19 l. mol^{-1} cm^{-1} at 550°) peak which has a shoulder on the low-energy side of the band, and the general profile of the 18,000–25,000-cm^{-1} region.

The spectrum of 2.0 mol % UF_4 doped into the 8-coordinated thorium site of $K_7Th_6F_{31}$ is shown in Figure 5. [By analogy to $Na_7Zr_6F_{31}$ it is known[10] that each thorium site is coordinated to eight fluorine atoms arranged in an Archimedian antiprism.] Features characteristic of 8-coordination at 550° are transitions in the 4000–5000 and 6000–8000-cm^{-1} regions, a strong peak at 9100 cm^{-1} (ϵ 22.1 l. mol^{-1} cm^{-1}) with shoulder on the high-energy side, profile of the 15,000–17,000-cm^{-1} region with maximum on the low-energy side at 15,300, peak at 19,000 (which here is split), and prominent peak at 21,300 cm^{-1}. These features are practically identical with those listed in Table I for UF_x^{4-x} in peak position as well as intensity. The extra peak at 15,850 cm^{-1} for the 8-coordinated crystal could be the result of splitting the 16,300 peak of the UF_x^{4-x} solution species in the same manner which the 19,000-cm^{-1} peak of UF_x^{4-x} appears split in the 8-coordinated crystal. The close agreement of these two spectra, both in position and intensity, leads to the identification of the UF_x^{4-x} species as UF_8^{4-}.

The identity of the lower coordinated $UF_{x-y}^{4-(x-y)}$ species is not as simple to determine because no fluoride crystals with 6-coordination nor ordered crystals with 7-coordination around Th^{4+}, U^{4+}, or Zr^{4+} sites have been reported. However, the similarity of the 8-coordinated chloride spectrum of U(IV) in the LiCl–KCl eutectic[3] to that of the 8-coordinated fluoride spectrum of Figure 1A leads one to conclude that the spectrochemical series effect on actinide spectra is small (see also Jorgensen, ref 11) and therefore the spectrum of 6-coordinated U(IV) in Cs_2UCl_6 might be compared with that of the $UF_{x-y}^{4-(x-y)}$ species in Figure 1C. No evidence for the existence of UF_6^{2-} in molten fluoride solutions is obtained from such a comparison.

Considerations of 7-coordinated U(IV) in fluoride crystals are extremely complicated because there are no ordered fluoride crystals of 7-coordinated fluoride around the quadrivalent heavy metal atom site. Disordered (or defect) crystals of type M_3NF_7[12] exist (where M = Na^+, K^+, Cs^+, or NH_4^+ and N = U^{4+}, Th^{4+}, or Zr^{4+}) and have only a statistical occupancy of $7F^-$ around the N^{4-} site. Nevertheless, an examination of the U(IV) spectrum in such a disordered crystal was made to evaluate the effect of disordering on the absorption spectrum. The spectrum of 1.65 mol % U(IV) in Cs_3ThF_7 at room temperature is shown in Figure 6A. No resemblance to other U(IV) spectra reported here is evident. Upon heating, a gradual, reversible change in the spectrum occurs until at 550° the spectrum of Figure 6B is obtained. The values at 200 and 350° for the 6450-cm^{-1} peak are 0.8 and 0.32; for 11,400 cm^{-1}, 1.5 and 0.9; for 17,890 cm^{-1}, 0.50 and 0.45, and for 24,000 cm^{-1}, 1.75 and 1.15 absorbance units, respectively. Realizing then that the peaks in these positions are remnants of the room temperature species which are rapidly dropping and assuming that they become insignificant at slightly higher temperatures, there is a striking similarity between the resultant spectrum and the $UF_{x-y}^{4-(x-y)}$ spectrum in both position and intensity. [It was not possible to go higher in temperature because reactions of the crystal surface with furnace atmosphere contaminants caused excessive light scatter. Repolishing the crystal removed the surface damage, but the temperature was limited to 550°.] These resultant peaks at 550° from Figure 6B are listed in Table II as characteristic of 7-coordinated U(IV). The dramatic spectral changes with temperatures can be explained as thermal shifts in the atom positions causing a uniform distribution of $7F^-$ about U^{4+} much like that which might occur in the melt. The proof of this hypothesis would, of course, require a high-temperature crystal structure determination (a measurement which was not available). From the gradual change in the spectrum upon heating as well as the phase diagram of CsF–ThF_4,[13] no high-temperature polymorphs of Cs_3ThF_7 are suggested. Therefore it seems most likely that the atoms in the Cs_3ThF_7 crystal have merely undergone slight thermal displacements.

It is then plausible to conclude that $UF_{x-y}^{4-(x-y)}$ in the melt is UF_7^{3-}. Equation 2 would then become

$$F^- + UF_7^{3-} \rightleftharpoons UF_8^{4-} \qquad (3)$$

Future work on the spectra of U(IV) in fluoride crystals will endeavor to establish these points more firmly. However, for the moment, some consideration will be given to the estimation of UF_8^{4-} and UF_7^{3-} concentrations in the various melt compositions.

Because of the maximum fluoride ion concentration

(9) G. Brunton, *Acta Cryst.*, **B25**, 1919 (1969).

(10) J. H. Burns, R. D. Ellison, and H. A. Levy, *ibid.*, **B24**, 230 (1968).

(11) C. K. Jorgensen, "Absorption Spectra and Chemical Bonding in Complexes," Pergamon Press, Elmsford, N. Y., and Oxford, 1962, p 107.

(12) W. H. Zachariasen, *Acta Cryst.*, **1**, 265 (1948).

(13) R. E. Thoma and T. S. Carlton, *J. Inorg. Nucl. Chem.*, **17**, 88 (1961).

in the LiF–NaF–KF solutions, it is presumed that the equilibrium of eq 3 is shifted heavily over to the extent that the species seen in Figure 1A is almost entirely UF_8^{4-}. The $n\epsilon_{9000\ cm^{-1}}$ 20.8 l. /mol^{-1} cm^{-1} is the extinction coefficient of pure UF_8^{4-}. Inspection of Figures 3E and 6E suggests that the UF_7^{3-} species has essentially no shoulder in the 6000–8000-cm^{-1} region and thus the slight shoulder there in Figure 1C represents approximately 10–20% UF_8^{4-}. Using 15% UF_8^{4-} content in a simple Beer's law calculation for two species, $\epsilon_{9000\ cm^{-1}}$ is 14.0 for UF_7^{3-} from Figure 1C. Then with $\epsilon_{9000\ cm^{-1}}$ 20.8 and 14.0 for UF_8^{4-} and UF_7^{3-}, respectively, it is calculated that approximately 40% of the total uranium in L_2B (Figure 1B) is UF_8^{4-}. Although these are only estimates, the trend from pure UF_8^{4-} to predominantly UF_7^{3-} with decreasing fluoride ion concentration is supported by spectral as well as equilibrium considerations. For example, in going from L_2B to the eutectic composition, the activity of F^- decreases by approximately a factor of 4.[7] The equilibrium of eq 3 then predicts correctly that the UF_8^{4-}/UF_7^{3-} ratio should decrease accordingly by a factor of 4 (*cf.* values estimated above for UF_8^{4-} and UF_7^{3-}).

Finally, in the model of eq 3, no consideration of possible fluoride bridging from uranium to beryllium is mentioned and certainly must occur at some point when the concentration of BeF_2 becomes high enough. The comparison of U(IV) spectra reported here with U(IV) in NaF–ZrF_4 melts where bridging is expected to be less prevalent shows that the spectra are not measurably affected by bridging in LiF–BeF_2 solutions with $BeF_2 \leq 52$ mol %. Future work will endeavor to evaluate the extent of fluoride bridging in LiF–BeF_2 melts of these and higher BeF_2 concentrations through more detailed studies of the spectra.

Conclusions

Coordination effects on U(IV) have been demonstrated in molten fluoride solutions and explained as a function of the fluoride ion concentration. The U(IV) species predominant in fluoride-rich systems has been shown to be UF_8^{4-}. There is evidence to believe that on decreasing the fluoride ion concentration, a 7-coordinated species is produced.

$$UF_8^{4-} \rightleftharpoons UF_7^{3-} + F^-$$

In melts of intermediate composition, with neither an excess or a deficiency of fluoride ion, *e.g.*, LiF–BeF_2 (66:34 mol %), there is an approximately equivalent amount of UF_7^{3-} and UF_8^{4-}. By analogy, ThF_4 and ZrF_4 are expected to exhibit a similar coordination equilibrium

$$ThF_8^{4-} \rightleftharpoons ThF_7^{3-} + F^-$$

$$ZrF_8^{4-} \rightleftharpoons ZrF_7^{3-} + F^-$$

depending on the fluoride ion concentration.

The spectra and temperature effects for U(IV) shown in Figure 2 are almost identical with those reported by Morrey for U(IV) in molten $ZnCl_2$.[4] Based on this similarity, it is suggested that U(IV) in $ZnCl_2$ represents a similar equilibrium between 7- and 8-coordinated species.

Acknowledgments. The advice on fluoride crystal structures and usage of unpublished results from G. D. Brunton and helpful discussions with C. F. Baes and F. F. Blankenship are gratefully acknowledged. Thanks are also extended to G. P. Smith, Jorulf Brynestad, and associates, Metals and Ceramics Division at this laboratory, for their interest and support in this research.

Infrared and Proton Nuclear Magnetic Resonance Studies of Adducts of Tin(II) and -(IV) and Titanium(IV) Halides with Diisopropyl Methylphosphonate[1]

by C. Owens, N. M. Karayannis, L. L. Pytlewski, and M. M. Labes*

Department of Chemistry, Drexel University, Philadelphia, Pennsylvania 19104 *(Received May 6, 1970)*

Publication costs assisted by Drexel University

Diisopropyl methylphosphonate (DIMP) forms monomeric 2:1 adducts with Sn(II), Sn(IV), and Ti(IV) halides which are characterized by means of ir and proton nmr spectroscopy. The monomeric character of these compounds was established by molecular weight determination. The proton nmr spectra, which do not exhibit any additional splittings other than those observed for free DIMP, and infrared data (ν_{P-O}, ν_{M-O}, and ν_{M-X}) suggest that the two DIMP groups are probably trans to each other. The adoption of a cis configuration is obviously sterically hindered by the bulky DIMP groups. On the basis of the above evidence the $MX_4 \cdot 2DIMP$ (M = Ti, Sn) adducts were assigned a trans-octahedral and $SnX_2 \cdot 2DIMP$ a trans-planar configuration. X-Ray studies revealed that the crystalline complexes belong to the triclinic system, space group $P\bar{1}$. The $SnCl_2 \cdot 2DIMP$ and $SnBr_2 \cdot 2DIMP$ adducts are of about the same structure, as is also the case for the $SnCl_4 \cdot 2DIMP$ and $SnBr_4 \cdot 2DIMP$ adducts. $SnI_4 \cdot 2DIMP$ exhibits a different X-ray powder pattern than those of the latter two complexes.

Introduction

Neutral phosphonate and phosphate esters easily form 2:1 adducts with Sn(II), Sn(IV), Ti(IV), and Zr(IV) halides.[2-4] Although adducts of the type $MX_4 \cdot 2L$ (M = Ti, Sn, Zr, etc.) are normally cis-octahedral,[5-7] trans-octahedral isomers are stabilized when there is sufficient steric interaction to overcome symmetry effects and the tendency to maximize p_π–d_π bonding.[7] Adducts of Sn(II) halides have been studied but to a lesser extent.[8]

The ν_{M-O} and ν_{M-X} vibrations of metal tetrahalide adducts with phosphine, arsine, and amine oxides were identified in a number of recent studies.[9-12] Since neutral phosphonate esters are weaker donors than phosphine oxides,[13] it seemed appropriate to undertake a low-frequency ir study of metal complexes of these esters. Further, it seemed probable that the presence of isopropoxy groups in DIMP might lead to sufficiently severe steric effects, imposing a trans configuration to the $MX_4 \cdot 2DIMP$ adducts mentioned above. In fact, preliminary examinations of molecular models of cis- and trans-octahedral DIMP adducts of this type clearly demonstrated that stabilization of the cis configuration would be highly improbable due to steric effects. Accordingly, characterization studies of Sn(II), Sn(IV), and Ti(IV) halide–DIMP adducts[2] were undertaken. The present paper deals with the preparation and characterization of these compounds.

Experimental Section

Chemicals. Water-free DIMP was provided by Edgewood Arsenal, Md. The purest commercially available metal halides and solvents were utilized.

Preparation of the Adducts. As already reported,[2] the 2:1 adducts of DIMP with tin and titanium halides were prepared by mixing solutions of ligand and salt (in 2:1 molar ratio) in carbon tetrachloride or tetrahydrofuran and allowing the resulting mixtures to stand at room temperature for crystal formation. Alternatively, the mixture was refluxed for *ca.* 1 hr and the solvent was removed by distillation under reduced

(1) Partially abstracted from the Ph.D. Thesis of C. Owens, Department of Chemistry, Drexel Institute of Technology, Philadelphia, Pa., 1969.

(2) N. M. Karayannis, C. Owens, L. L. Pytlewski, and M. M. Labes, *J. Inorg. Nucl. Chem.*, **32**, 83 (1970).

(3) B. Kautzner and P. C. Wailes, *Aust. J. Chem.*, **22**, 2295 (1969).

(4) A. N. Pudovik, A. A. Muratova, E. G. Yarkova, and V. N. Marsheva, *Zh. Obshch. Khim.*, **38**, 2522 (1968).

(5) E. L. Muetterties, *J. Amer. Chem. Soc.*, **82**, 1082 (1960).

(6) C.-I. Brändén, *Acta Chem. Scand.*, **17**, 759 (1963).

(7) D. S. Dyer and R. O. Ragsdale, *Inorg. Chem.*, **8**, 1116 (1969), and references therein.

(8) J. S. Morrison and H. M. Haendler, *J. Inorg. Nucl. Chem.*, **29**, 393 (1967).

(9) J. P. Clark, V. M. Langford, and C. J. Wilkins, *J. Chem. Soc. A*, 792 (1967).

(10) Y. Kawasaki, M. Hori, and K. Uenaka, *Bull. Chem. Soc. Jap.*, **40**, 2463 (1967).

(11) S. H. Hunter, V. M. Langford, G. A. Rodley, and C. J. Wilkins, *J. Chem. Soc. A*, 305 (1968).

(12) F. E. Dickson, E. W. Gowling, and F. F. Bentley, *Inorg. Chem.*, **6**, 1099 (1967); F. E. Dickson, E. W. Baker, and F. F. Bentley, *J. Inorg. Nucl. Chem.*, **31**, 559 (1969); *Inorg. Nucl. Chem. Lett.*, **5**, 825 (1969).

(13) N. M. Karayannis, C. Owens, L. L. Pytlewski, and M. M. Labes, *J. Inorg. Nucl. Chem.*, **31**, 2767 (1969), and references therein.

Table I: Properties and Analytical Data of Diisopropyl Methylphosphonate–Metal Halide Adducts

Adduct	Color	Molecular wt, g/mol Theor	Molecular wt, g/mol Found	Mp, °C	Analytical data[c] Metal or halogen, % Calcd	Metal or halogen, % Found	C, % Calcd	C, % Found	H, % Calcd	H, % Found
$SnCl_2 \cdot 2DIMP$	Pale yellow	550	551.5	88–89	12.89	12.41[a]	30.58	29.55	6.23	5.88
$SnBr_2 \cdot 2DIMP$	Pale yellow	639	619.5	110–110.5	25.01	24.25[a]	26.32	25.31	5.36	4.68
$SnCl_4 \cdot 2DIMP$	White	621	620	89–89.5	19.12	18.60[b]	27.08	25.61	5.52	5.55
$SnBr_4 \cdot 2DIMP$	White	799	810	116–116.5	40.02	40.05[a]	21.05	21.13	4.29	4.25
$SnI_4 \cdot 2DIMP$	Dark reddish	987	865	101–101.5	12.03	11.60[b]	17.04	16.87	3.47	3.43
$TiCl_4 \cdot 2DIMP$	Orange-yellow			95	8.71	9.05[b]	30.57	30.33	6.22	5.85

[a] Halogen. [b] Metal. [c] P analyses generally agree with the theoretical values, *e.g.*, $SnBr_4 \cdot 2DIMP$: Calcd 7.76, Found 7.86; $SnI_4 \cdot 2DIMP$: Calcd 6.28, Found 5.85.

pressure. Crystalliue 2:1 adducts of DIMP with $SnCl_2$, $SnBr_2$, $SnCl_4$ $SnBr_4$, SnI_4, and $TiCl_4$ were obtained by these procedures. Purification and recrystallization of these compounds were accomplished from carbon disulfide, by use of the H-shaped recrystallization cell previously described.[14] Analyses (Schwarzkopf Microanalytical Laboratory, Woodside, N. Y.) and some properties of these compounds are given in Table I.

Attempts at the preparation of 1:1 or 2:1 adducts of DIMP with some additional metal halides ($FeCl_2$, $FeCl_3$, $MnCl_2$, $NiBr_2$, $ZnCl_2$, TiF_4) led to viscous liquid final products. $TiBr_4$ forms a dark brown unstable solid adduct of the type $TiBr_4 \cdot 2DIMP$ in 87% yield. In all of these cases complex formation was confirmed by the negative shifts of the ν_{P-O} vibration.[13-15]

Molecular Weights, Conductance, and X-Ray Studies. Molecular weights of the crystalline adducts were determined cryoscopically in benzene by use of a Beckmann freezing point apparatus and are given in Table I. These determinations clearly indicate that the adducts are monomeric in benzene. $SnI_4 \cdot 2DIMP$ shows a somewhat lower molecular weight than that calculated for the monomer. This may be due to partial dissociation of this adduct in solution. Molar conductances of the adducts in chloroform and in nitromethane, obtained as described elsewhere,[14] demonstrate that all these compounds behave as nonelectrolytes in these solvents. X-Ray powder diffraction patterns were obtained on a Norelco X-ray diffractometer using Cu Kα radiation and a scintillation counter as detector. Powder patterns of the two Sn(II) adducts are almost identical, and these compounds are of about the same structure. $SnCl_4 \cdot 2DIMP$ and $SnBr_4 \cdot 2DIMP$ also have very similar X-ray patterns, but that of $SnI_4 \cdot 2DIMP$ is different from those of the former adducts. $TiCl_4 \cdot 2DIMP$, although melting at 95° (Table I), is relatively unstable and collapses to a liquid when allowed to stand at room temperature. No X-ray data were obtained for this adduct. Additional X-ray studies on the tin halide adducts were made by obtaining Laue photographs of crystals (about 1 mm on edge) by using a Polaroid camera, equipped with a zinc sulfide fluorescent screen on a Picker X-ray generator having a copper target source for inhomogeneous X-rays. Laue photographs taken with the incident X-ray beam parallel to each of the crystallographic axes showed a complete lack of any elements of symmetry in each case, leading to the conclusion that these crystalline adducts belong to the triclinic crystal system, space group $P1$. Further crystallographic studies of these adducts are in progress.

Proton Nmr Spectra. The proton nmr spectra of the free ligand and its adducts were obtained on a Varian A60A nmr spectrometer in $CDCl_3$. Chemical shifts were determined with reference to tetramethylsilane (internal standard). Table II summarizes the nmr data.

Table II: Nuclear Magnetic Resonance Data (in $CDCl_3$)

Compound	Chemical shifts, ppm H–C–O	CH_3–C	CH_3–P[a]
DIMP	4.38	1.00	1.21
$SnCl_2 \cdot 2DIMP$	5.10	1.45	1.93
$SnBr_2 \cdot 2DIMP$	5.08	1.47	1.98
$SnCl_4 \cdot 2DIMP$	5.12	1.43	1.91
$SnBr_4 \cdot 2DIMP$	5.18	1.47	1.99
$SnI_4 \cdot 2DIMP$	4.70	1.34	1.49
$TiCl_4 \cdot 2DIMP$	5.20	1.45	1.99

[a] P–H coupling constant was 18.5 Hz.

Infrared Spectra. Ir spectra were obtained on Nujol mulls between IRTRAN 2 (zinc sulfide) (4000–700 cm^{-1}) and polyethylene (700–200 cm^{-1}) windows on a Perkin-Elmer 621 spectrophotometer, and the more significant data are presented in Table III.

Results and Discussion

Proton Nmr Spectra. The most significant feature of

(14) N. M. Karayannis, C. Owens, L. L. Pytlewski, and M. M. Labes, *J. Inorg. Nucl. Chem.*, **31**, 2059 (1969).

(15) F. A. Cotton, R. D. Barnes, and E. Bannister, *J. Chem. Soc.*, 2199 (1960).

Table III: ν_{P-O}, ν_{M-O}, ν_{M-X}, and Far-ir Ligand Bands of DIMP–Metal Halide Adducts (cm^{-1})[a]

Compound	ν_{P-O}	$\Delta\nu_{P-O}$	ν_{M-O}	ν_{M-X}	ν_{ligand}(450–200 cm^{-1})
DIMP	1241 vs				420 m, vb, 338 w, 305 w, 276 s, 272 sh, 263 m, 256 m, 242 s, 223 sh, 217 s, 211 m, 205 sh
$SnCl_2 \cdot 2DIMP$	1120 vs	−121	323 vs[b]	330 vs, b	420 w, b, 337 sh, 276 s, 272 sh, 264 m, 255 m, 242 s, 221 sh, 217 m, b, 208 m, b
$SnBr_2 \cdot 2DIMP$	1127 vs	−114	304 s[c]	234 vs	441 m, 419 m, b, 330 sh, 275 s, 272 sh, 263 m, 252 s, 227 sh, 222 sh, 212 sh, 205 sh
$SnCl_4 \cdot 2DIMP$	1130 vs	−111	315 s, sh[d]	327 vs	445 m, b, 418 m, b, 340 sh, 276 s, 267 sh, 250 m, sh, 243 s, 220 sh, 218 s, 215 sh, 206 sh
$SnBr_4 \cdot 2DIMP$	1127 vs	−114	290 m	228 vs, b	437 m, b, 365 sh, 340 b, 275 s, 268 sh, 262 m, 248 sh, 241 sh, 217 sh
$SnI_4 \cdot 2DIMP$	1115 vs	−126	277 m-s[e]	<200	430 m, b, 339 w, 277 m-s,[e] 270 sh, 268 sh, 262 m, 252 s, 243 s, 223 sh, 217 s, 211 m, 205 sh
$TiCl_4 \cdot 2DIMP$	1163 vs	−78	*f*	*f*	445 m, 425 m, b, 277 sh, 274 s, 268 sh, 261 m, 252 s, 242 s, 221 m, b, 211 m

[a] Abbreviations: s, strong; m, medium; w, weak; v, very; b, broad; sh, shoulder. [b] Shoulder at 318 cm^{-1}. [c] Shoulder at 316 cm^{-1}. [d] Shoulder at 335 cm^{-1}. [e] Overlap of ν_{M-O} and ligand absorptions. [f] The $TiCl_4$ adduct exhibits bands at 355 sh, 345 sh, 338 sh, 336 s, 330 s, 305 sh. ν_{Ti-O} and ν_{Ti-Cl} certainly occur in this region, but assignments are not possible.

the nmr spectra of the adducts is that they do not exhibit any additional splittings of the various proton signals, other than those observed in the free ligand in $CDCl_3$. The proton nmr spectra of the new adducts show great similarity to those reported for uranyl nitrate adducts of organophosphoryl compounds.[16,17] Thus, downfield chemical shifts, relative to the resonance positions for the protons in the free ligand, are of comparable magnitudes for the adducts reported (Table II) and for a number of $UO_2(NO_3)_2 \cdot 2L$ (L = monodentate organophosphoryl ligand) adducts.[17] Moreover, the spectra of the uranyl complexes also do not show further splittings of the proton bands of the free ligand.[17] The crystal structure determination of a representative adduct of this type, *i.e.*, $UO_2(NO_3)_2 \cdot 2(C_2H_5O)_3PO$, established that two bidentate nitrato and two phosphoryl ligands are in the plane perpendicular to the linear uranyl ion, and that the two triethylphosphato groups are trans to each other.[18] The nmr evidence available is not conclusive, since if a rapid exchange in ligand protons between cis and trans adducts occurred, only one set of signals would be observed. Nevertheless, the fact that no additional splittings of the proton signals occur, in combination with the ir evidence (*vide infra*), appears to be in favor of trans configurations for the adducts under discussion.

Downfield changes in chemical shifts are more pronounced for the protons closer to the phosphoryl group, *i.e.*, those of the methine group and the methyl attached to phosphorus (Table II), as would be expected.[17] The methyl protons of the isopropyl group are also deshielded upon complex formation.[17] The above changes and their magnitude are indicative of formation of strong bonds between the metal ion and the phosphoryl oxygen. This should be anticipated, since tin and titanium halides, as well as uranyl compounds, generally form strong complexes with phosphoryl ligands.[19] It is noteworthy, in this connection, that adducts of the above salts with DIMP are among the few complexes of this ligand that can be easily isolated.[2]

Infrared Spectra (4000–700 Cm^{-1}). The ir spectra of the adducts are characterized by large negative shifts of the phosphoryl-stretching vibration frequency (Table III), which clearly indicate coordination of the ligand to the metal ion through the P–O oxygen.[15] The other vibrational bands of DIMP at 1350–700 cm^{-1} are negligibly affected by complex formation. In fact, DIMP shows the following bands in this region:[2,14] 1309 m (PCH_3), 1241 s (ν_{P-O}), 1173 m, 1139 m, 1106 m (all three characteristic of the (P)–O–C stretch in isopropyl esters), 1008 vs, 980 vs ((C)–O–P stretch), 912 m, 895 m (PCH_3, occurring as a doublet), 787 m ((C)–O–P stretch, asymmetric). The corresponding bands in two representative complexes are: $SnCl_2 \cdot 2DIMP$: 1305 m, 1173 sh, 1120 vs (ν_{P-O}), 1092 m, 1010 vs (sh), 991 vs, 920 w, 896 w, 872 w, 791 m; $SnI_4 \cdot 2DIMP$: 1309 m, 1173 sh, 1115 vs (ν_{P-O}), 1088 m, 1018 vs, 991 vs, 920 sh, 895 w, 870 w, 792 m. The new adducts are characterized by the absence of ir water bands. The

(16) T. H. Sidall and C. A. Prohaska, *Inorg. Chem.*, **4**, 783 (1965).
(17) J. L. Burdett and L. L. Burger, *Can. J. Chem.*, **44**, 111 (1966).
(18) J. E. Fleming and H. Lynton, *Chem. Ind. (London)*, 1409 (1959); 1415 (1960).
(19) I. Lindqvist, "Inorganic Adduct Molecules of Oxo-Compounds," Springer-Verlag, Berlin, 1963.

ν_{P-O} absorptions of the adducts occur as single bands (Table III). In complexes of the type $MX_4 \cdot 2L$ (L = monodentate oxoligand, characterized by a Z–O group: Z = C, N, P, S, etc.), splittings of the ν_{Z-O} vibration have been interpreted in terms of interaction of two donor groups in the cis position.[20,21] In fact, many adducts of this type with nonsterically hindered pyridine *N*-oxides, which have a cis configuration,[22] exhibit splittings of the ν_{N-O} vibration.[10,21] Thus, the absence of splittings of ν_{P-O} in the adducts reported is also in favor of a trans configuration for these compounds.

Low-Frequency Infrared Spectra. Far-ir spectra of 2:1 complexes of monodentate ligands with metal halides generally provide stereochemical information.[25-26] In the case of cis-$MX_4 \cdot 2L$ adducts (C_{2v} or lower symmetry) four metal–halogen stretching vibrational bands are allowed, whereas for high symmetry trans isomers (D_{4h}) only one ν_{M-X} band is allowed.[23,24] The presence of lower symmetry components in the ligand field of *trans*-$MX_4 \cdot 2L$ adducts would, however, lead to the appearance of more than one ν_{M-X} band.[24] Cis-octahedral $MX_4 \cdot 2L$ compounds also exhibit splittings of the ν_{M-L} mode, while the trans isomers show a single ν_{M-L} band.[23] On the other hand, trans-planar $MX_2 \cdot 2L$ complexes (D_{2h} symmetry) show one ν_{M-X} and one ν_{M-L} ir-active band, while the cis-planar (C_{2v} symmetry) show two ir bands of each kind.[25,26]

The low-frequency ir spectra of the new adducts (Table III, Figures 1 and 2) allow tentative assignments of ν_{M-X} and ν_{M-O} bands in most cases. Arbitrary assignments are made for ν_{M-O} and ν_{M-Cl} due to the close proximity of these modes. These absorptions generally occur at frequencies below 350 cm^{-1}. The bands assigned as ν_{Sn-Br} in both $SnBr_4$ (Figure 1) and $SnBr_2$ (Figure 2) adducts occur at 0.7–0.75 of the frequency of the ν_{Sn-Cl} absorptions.[23] ν_{Sn-O} overlaps with ν_{Sn-Cl} in the chloride adducts, but is quite distinct in the adducts of the corresponding bromides. In $SnI_4 \cdot 2DIMP$, ν_{Sn-O} probably overlaps with the ligand band at *ca.* 275 cm^{-1} (Table III, Figure 1). The latter adduct has an almost identical spectrum with that of free DIMP in the 350–200-cm^{-1} region, since ν_{Sn-I} presumably occurs below 200 cm^{-1}, as would be expected.[23] The assignment of bands at 315–270 cm^{-1} as ν_{Sn-O} in Sn(IV) halide–DIMP complexes is justified if the strength of DIMP as a donor is taken into consideration. In fact, the ν_{Sn-O} modes in the corresponding adducts with phosphine oxides, which are considerably stronger donors than DIMP,[13] have been identified in the 428–310-cm^{-1} region.[9,11]

High resolution far-ir spectra of the Sn(II) halide adducts exhibit a shoulder at 318–316 cm^{-1} (Table III, Figure 2). Comparison of the spectra of the chloride and bromide adduct leads to the assignment of this band to a splitting of the ν_{Sn-O} mode. In view of the tendency of Sn(II) to form tricoordinated compounds,

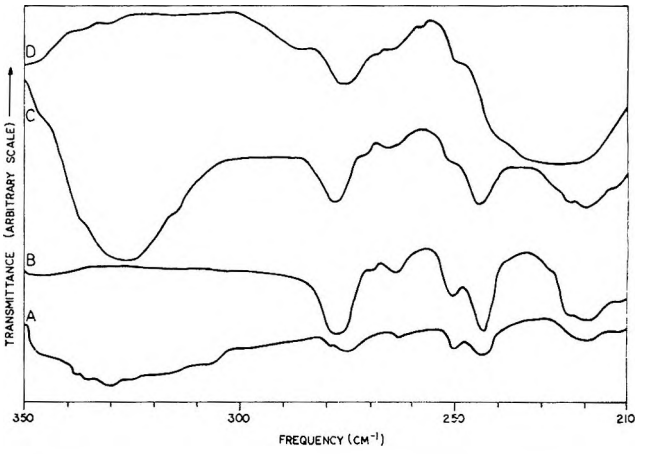

Figure 1. Far-ir spectra (350–210 cm^{-1}) of Nujol mulls of: A, $TiCl_4 \cdot 2DIMP$; B, $SnI_4 \cdot 2DIMP$; C, $SnCl_4 \cdot 2DIMP$; D, $SnBr_4 \cdot 2DIMP$.

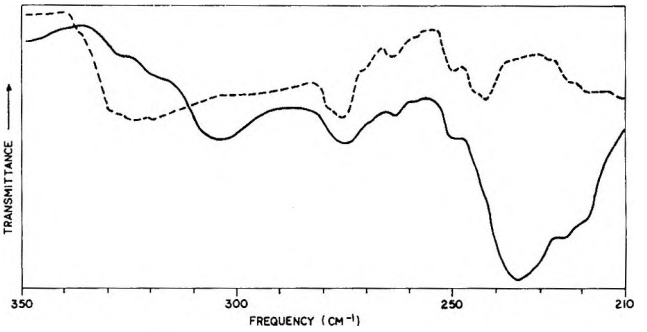

Figure 2. Far-ir spectra (350–210 cm^{-1}) of Nujol mulls of: (———), $SnBr_2 \cdot 2DIMP$, and (- - -), $SnCl_2 \cdot 2DIMP$ (transmittance, arbitrary scale).

Morrison and Haendler suggest that $SnX_2 \cdot 2L$ adducts with sulfoxides and pyridine *N*-oxides might contain one ligand group outside the coordination sphere of the metal ion, but do not rule out the possibility of a tetracoordinated square-planar structure.[8] The splitting of ν_{Sn-O}, in combination with the occurrence of ν_{P-O} as a single band, leads to the conclusion that both DIMP groups are in the first coordination sphere of Sn(II). No apparent splitting of the ν_{Sn-X} band is observed, as indicated by the ν_{Sn-Br} absorption, which is quite sharp (Figure 2). Thus, far-ir evidence is in favor of a trans-planar configuration for these adducts.[25,26] Some deviation from pure D_{2h} symmetry undoubtedly occurs (splitting of ν_{Sn-O}), but its extent is small, since the ν_{Sn-X} bands are not split. Introduction of lower sym-

(20) M. F. Lappert, *J. Chem. Soc.*, 542 (1962).
(21) C. J. Wilkins and H. M. Haendler, *ibid.*, 3174 (1965).
(22) D. S. Dyer and R. O. Ragsdale, *Chem. Commun.*, 601 (1966).
(23) R. J. H. Clark, *Spectrochim. Acta*, 21, 955 (1965), and references therein.
(24) I. R. Beattie, G. P. McQuillan, L. Rule, and M. Webster, *J. Chem. Soc.*, 1514 (1963); I. R. Beattie and L. Rule, *ibid.*, 3267 (1964).
(25) R. J. H. Clark and C. S. Williams, *Inorg. Chem.*, 4, 350 (1965).
(26) J. R. Allkins and P. J. Hendra, *J. Chem. Soc. A*, 1325 (1967).

metry components to the ligand field, arising through the presence of nonlinear M–O–P groupings,[6,27] and the arrangement of the bulky DIMP molecules in space, may be generally expected in metal complexes of this ligand.[13,28]

ν_{Sn-O} overlaps with ν_{Sn-Cl} in $SnCl_4 \cdot 2DIMP$ and occurs as a shoulder of a ligand band in $SnBr_4 \cdot 2DIMP$ (Table III, Figure 1). In the former adduct ν_{Sn-Cl} is probably split as indicated by a shoulder at 335 cm^{-1}. In the corresponding bromide adduct ν_{Sn-Br} overlaps with ligand absorptions, occurring as a broad band. In $SnI_4 \cdot 2DIMP$ ν_{Sn-O} is completely masked by the absorptions of the ligand, while ν_{Sn-I} lies beyond the range of the spectrophotometer available. The overlaps mentioned above make the observation of splittings in the ν_{Sn-O} and ν_{Sn-Br} modes impossible. It is, nevertheless, quite clear that no splittings of the extent observed in *cis*-$SnX_4 \cdot 2L$ adducts[24] occur. The far-ir evidence is, thus, also in favor of a distorted trans-octahedral configuration for the $SnX_4 \cdot 2DIMP$ adducts. The low-frequency spectrum of the only Ti(IV) complex studied (Table III, Figure 1) may be attributed to either a cis- or a severely distorted trans-octahedral configuration.

In conclusion, a number of monomeric 1:2 adducts of Sn(II), Sn(IV), and Ti(IV) halides with DIMP were studied by means of ir and proton nmr spectroscopy. The combined evidence provided by the far-ir and nmr spectra and the fact that ν_{P-O} generally occurs as a single band may be considered as strongly in favor of a distorted trans-planar configuration for the Sn(II) adducts and a distorted trans-octahedral structure for the Sn(IV) compounds. Nmr evidence and the single character of ν_{P-O} are also in favor of a trans-octahedral structure for $TiCl_4 \cdot 2DIMP$ but the low-frequency ir spectrum of this adduct is characterized by considerable splittings of the ν_{Ti-Cl} and ν_{Ti-O} modes. In view of the trans configuration of the Sn(IV) analogs and the steric effects introduced by the presence of the bulky ligand,[7,24] it is most probable that these splittings are due to a severely distorted trans rather than a cis configuration. The position of the ν_{M-O} bands (tentative assignments) in the low-frequency spectra of the new adducts suggests that DIMP is a significantly weaker donor than phosphine oxides.[9,11] This is due to the inductive effect of the alkoxy groups.[13,29] Raman studies would substantiate the ir assignments; we intend to undertake these studies as soon as the proper instrumentation becomes available.

The tin adducts reported here easily decompose at elevated temperatures, yielding phosphonato polymers with simultaneous elimination of isopropyl halide. Thus, $SnCl_4 \cdot 2DIMP$ forms bis(methylphosphonato)-Sn(IV) as a final product, which is a cross-linked polymer.[30] Differential scanning calorimetric studies established that the decomposition temperatures of the Sn(II) adducts lie between 171 and 176° and those of the Sn(IV) adducts between 190 and 210°.[1] The Ti(IV) analogs decompose at lower temperatures, and the fact that $TiCl_4 \cdot 2DIMP$ is unstable at room temperature may be due to initiation of the elimination of isopropyl chloride under these conditions.

Acknowledgment. The support of U. S. Army Edgewood Arsenal, Maryland, under Contract No. DAAA 15-67-C-0644 is gratefully acknowledged.

(27) F. A. Cotton and R. H. Soderberg, *J. Amer. Chem. Soc.*, **85**, 2402 (1963).

(28) C. V. Berney and J. H. Weber, *Inorg. Chem.*, **7**, 283 (1968); W. Byers, A. B. P. Lever, and R. V. Parish, *ibid.*, **7**, 1835 (1968).

(29) I. Lindqvist and B. Fjellström, *Acta Chem. Scand.*, **14**, 2055 (1960).

(30) C. Owens, L. L. Pytlewski, N. M. Karayannis, J. Wysoczanski, and M. M. Labes, *Polymer Lett.*, **8**, 81 (1970).

Cohesive Energies in Polar Organic Liquids. II. The *n*-Alkyl Nitriles and the 1-Chloroalkanes

by Edwin F. Meyer,* Terrence A. Renner, and Kenneth S. Stec

Chemistry Department, De Paul University, Chicago, Illinois 60614 *(Received June 22, 1970)*

Publication costs assisted by the Chemistry Department, DePaul University

Additional support is presented for the importance of induction energies in polar liquids. Quantitative estimates are made of all three types of cohesive energies for the normal nitriles and chlorides, and a relationship between induction energy and $\alpha\mu^2$ for a given liquid is suggested. The present approach to studying cohesive energies is shown to be inapplicable to the *n*-alcohols, presumably due to strong association of hydrogen bonds.

The qualitative effect of a permanent dipole on total cohesion in fluids is well known. When the permanent dipoles of adjacent molecules are properly aligned, electrostatic attraction results (orientation energy). The same is true when a permanent dipole confronts polarizable matter and induces a temporary dipole therein (induction energy). Both these effects serve to enhance the dispersion attraction which is present among nonpolar molecules. Earlier work[1] indicates that the induction energy is larger than the orientation energy, in spite of the fact that theoretical expressions for interactions between two molecules give larger values for orientation. (The apparent explanation for the discrepancy is that while the pairwise interaction is stronger for two permanent dipoles than for a permanent and an induced dipole, there are many more of the latter interactions occurring at a given instant than the former in a liquid of moderate polarity.) In order to get an idea of the generality of this observation, we have applied the same approach[1] to the *n*-alkyl nitriles and the 1-chloroalkanes, and have considered briefly the normal alcohols.

Theoretical Section

The details of the method have been explained.[1] Briefly, the members of homologous series of polar molecules are placed into a "corresponding state" with the normal paraffins. The total cohesive energy is taken to be equal to the energy of vaporization from this state, and the variation of this energy with the length of the "nonpolar" part of the molecule is studied. Separation of orientation, induction, and dispersion energies is permitted by the postulate that, as successive CH_2 groups are added to a polar molecule, each type of energy changes in a characteristic way: dispersion increases (linearly), orientation decreases, and induction is virtually constant.

The energy of vaporization is plotted *vs.* the effective number of CH bonds in each molecule—"effective" because for a polar molecule, the "dispersion equivalence" of the polar group is estimated using the Slater–Kirkwood equation.[2] For example, it is found that the carbonyl group has the same dispersion energy as 2.50 CH bonds. Similarly, the nitrile, chloride, and hydroxyl groups are equivalent to 3.14, 3.10, and 0.57 CH bonds, respectively. Thus, the effective number of CH groups in acetonitrile is 6.14; in ethyl chloride, 8.10, etc.

When plots for the polar series and the paraffins are made on the same coordinates, it is observed that the curve for the polar series approaches a straight line (at high CH values) whose slope equals that of the straight line paraffin plot, though it is displaced upward from it. Beyond the point at which the plots become parallel, the displacement of the polar curve from the nonpolar one represents the induction energy for the higher members of the polar series. The assumption is made that the induction energy for each member is directly proportional to its average polarizability, $\bar{\alpha}$, defined as the sum of the polarizabilities[3] of the constituent groups of the molecule divided by the number of groups. Values are as follows: CH_3, 18.80; CH_2, 12.51; CO, 12.71; CN, 18.48; Cl, 25; and OH, 7.28. The $\bar{\alpha}$ decreases slightly as the hydrocarbon part of the molecule gets longer, but becomes effectively constant above C_{10}. For the lower members of the series, the induction energy is obtained by multiplying the value for the higher members by the ratio of $\bar{\alpha}$'s for the lower and higher members.

The dispersion energy for a given member of the polar series is the energy corresponding to the intersection of the paraffin line and the CH value for that member; its orientation energy is the difference between the total cohesive energy and the sum of induction and dispersion. It is a simple matter to estimate the magni-

(1) E. F. Meyer and R. E. Wagner, *J. Phys. Chem.*, 70, 3162 (1966).

(2) H. Margenau, *Rev. Mod. Phys.*, 11, 1 (1939).

(3) Group polarizabilities were taken from E. A. Moelwyn-Hughes, "Physical Chemistry," Macmillan, New York, N. Y., 1964, p 385.

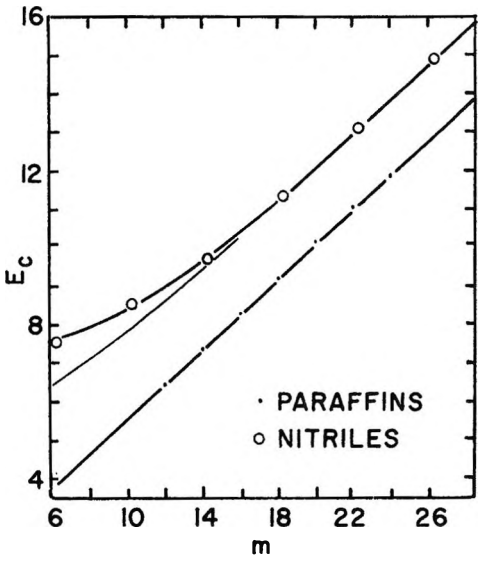

Figure 1. Cohesive energy (kcal/mol) *vs.* *m*, the effective number of CH bonds in the molecule. The reference state is hexane at 0°.

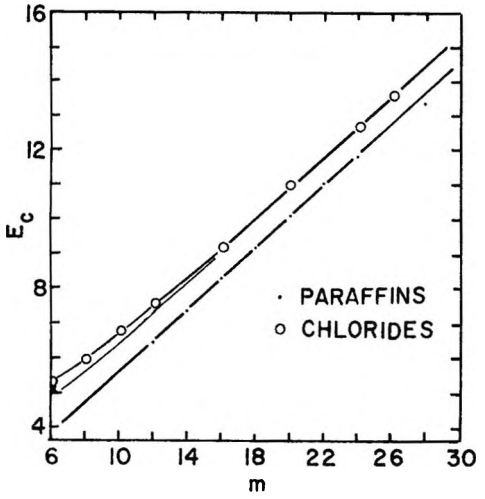

Figure 2. Cohesive energy (kcal/mol) *vs.* *m*, the effective number of CH bonds in the molecule. The reference state is hexane at 0°.

tudes of all three energies from the plots in Figures 1 and 2.

Experimental Section

Vapor pressures were measured for the even-numbered *n*-alkyl nitriles from C_2 to C_{12} inclusive. Thermal expansions were measured for the last four members of this series. Acetonitrile and butyronitrile were purchased from Chemical Samples Company and were better than 99.9% pure (by vpc) as received. The remaining nitriles were purchased from Lachat Chemicals. Capronitrile and lauronitrile were better than 99.9% pure as received; caprylonitrile (99.5%) and caprinitrile (99.4%) were distilled on a spinning-band column to 99.9% purity. All were dried over Linde Molecular Sieve prior to use.

Vapor pressures were measured ebulliometrically. The C_2 and C_8 measurements employed an apparatus designed after Swietoslawski;[4] the C_4, C_6, C_{10}, and C_{12} data were obtained with a boiler similar to that developed by Ambrose.[5] The latter is far superior. Pressures above 7 cm were measured with a mercury manometer; below this pressure, with a manometer containing Dow-Corning 704 silicone oil. The cathetometer used was precise to 0.05 mm. Temperatures were measured with a National Bureau of Standards certified mercury in glass thermometer for the C_2 nitrile. The remainder of the measurements were made with an NBS certified platinum resistance thermometer which had become available in the course of the work. The vapor pressures of the C_6 and C_{12} nitriles were obtained using a comparative technique similar to that described by Ambrose.[5] Helium was used to apply the external pressure to the liquid–vapor equilibrium.

The dilatometer used for the nitrile thermal expansion measurements has been described.[6] For the C_3, C_8, and C_{12} nitriles, mercury in glass thermometers were used (below 100°, NBS; above 100°, ASTM certified); for the C_{10}, the platinum resistance thermometer was used. Stem corrections were applied to all temperatures measured with the glass thermometers.

Thermal expansion data were also required for the C_8 and C_{10} *n*-alkyl chlorides. The compounds were purchased from Eastman and were about 96% pure. Repeated distillation produced purities of 99.7 and 99.5%, respectively. Data were obtained with a Westphal balance technique. Temperatures were measured with the platinum resistance thermometer. All weights were corrected to *in vacuo* values using Macurdy's table.[7]

Results

1. Nitriles and Chloroalkanes. The vapor pressure data were fitted by least squares to Antoine equations. The coefficients are presented in Table I, along with the standard deviations for log *p*.

The density data were fitted by least squares to cubic equations in temperature. The coefficients are presented in Table II, along with standard deviations and comparisons with literature values at one temperature. The experimental data on which these equations are based are presented in Table III.

These equations, combined with those in the standard references and the recently published Antoine equations for the 1-chloroalkanes,[8] allow estimation of the

(4) W. Swietoslawski, "Ebulliometric Measurements," Reinhold, New York, N. Y., 1945, p 6.

(5) D. Ambrose, *J. Sci. Instrum.*, 41 (1968).

(6) R. E. Wagner and E. F. Meyer, *J. Chem. Educ.*, 45, 349 (1968).

(7) L. B. Macurdy, "Treatise on Analytical Chemistry," I. M. Kolthoff, *et al.*, Ed., Interscience, New York, N. Y., 1967, Part I, Vol. 7, p 4264.

(8) H. R. Kemme and S. K. Kreps, *J. Chem. Eng. Data*, 14, 98 (1969).

Table I: Fit of Vapor Pressure Data to Antoine Equation, Log $p = A(B/c + t)$

Compd	Temp range, °C	A	B	C	Standard deviation × 10^3	Bp
Acetonitrile	41– 82	6.23655	1397.9228	239.275	0.14	81.66 ± 0.01
Butyronitrile	30–120	6.117724	1444.5851	223.359	0.27	117.593 ± 0.004
Capronitrile	76–168	6.0914423	1567.4925	208.825	0.42	163.445 ± 0.01
Caprylonitrile	101–147	6.1675139	1753.3277	203.572	1.50	
	147–206	5.9421261	1577.1114	183.311	0.65	205.01 ± 0.05
Caprinitrile	108–158	6.1823635	1843.1004	186.624	0.067	
	158–245	6.0157661	1723.4800	174.619	0.23	242.19 ± 0.05
Lauronitrile	120–189	6.5422995	1542.7539	139.860	1.80	
	167–282	6.0731708	1853.7022	166.103	0.10	276.059 ± 0.006
Methyl chloride[a]	−75 to −25	6.1087635	955.45438	250.126	1.02	−24.14
Ethyl chloride[a]	−56 to +13	6.0082587	1039.6943	239.643	0.41	+12.26

[a] Data from J. Timmermans, "Physico-Chemical Constants of Pure Organic Compounds," Elsevier, New York, N. Y., 1950.

Table II: Fit of Density Data to Cubic Equation, $\rho_t = a + bt + ct^2 + dt^3$

Compd	Temp range, °C	a	$b \times 10$	$c \times 10^4$	$d \times 10^9$	ρ	ρ_{lit}[a]	Standard deviation × 10^4
1-Chlorooctane	18–150	0.88972	−8.4935	3.6918	−4.3020	0.8686^{25}	0.8692^{25}	1.4
1-Chlorodecane	16–144	0.88736	−8.5645	11.1738	−6.2968	0.8665^{25}	0.8659^{25}	1.2
Capronitrile	32–101	0.82232	−8.7292	7.6397	−4.8979	0.79669^{30}	0.79713^{30}	0.28
Caprylonitrile	32–153	0.82886	−7.7277	1.2211	−1.5420	0.80575^{30}	0.80582^{30}	0.60
Caprinitrile	29–145	0.83399	−7.1003	1.6674	−0.31717	0.81283^{30}	0.81240^{30}	0.49
Lauronitrile	32–152	0.83822	−7.2216	2.8560	−1.7911	0.81633^{30}	0.81685^{30}	0.22

[a] Data for chloroalkanes from B. M. Coursey and E. L. Heric, *J. Chem. Eng. Data*, **14**, 426 (1969). Data for nitriles from Timmermans, see footnote *a* Table I.

three types of cohesive energies present in the nitrile and chloride series. The temperature which puts each liquid into the appropriate "corresponding state" is obtained from the thermal expansion data, and its energy of vaporization at this temperature is calculated from its Antoine equation constants through the Clausius–Clapeyron equation.

$$\Delta E = RT\left[\frac{2.303BT}{(C + t)^2} - 1\right]$$

Justification for assuming gaseous ideality lies in the low values of vapor pressure (about 10 cm) in the "corresponding states." The resulting plots are presented in Figures 1 and 2. The magnitude of each type of energy for each compound and the temperature at which the value applies are given in Table IV.

A refinement of our earlier work[1] indicates that the induction energies in the 2-ketones depends on the length of the hydrocarbon chain length. The adjusted values of the three types of cohesive energy are therefore included in Table IV.

In order to examine the effect of temperature on the magnitudes of these energies, similar plots were attempted for higher temperature "corresponding states." Qualitatively, the changes with temperature are small. Before anything quantitative can be said about them, however, compressibility data for the vapors in question must be obtained. Using the second virial coefficient data of McGlashan and Potter[9] for the *n*-alkanes, we find that significant amounts of attractive energy remain in the equilibrium vapor when the "corresponding state" is *n*-hexane at 40°. (The plots in this paper correspond to *n*-hexane at 0°.) This invalidates our equating the total cohesive energy to the energy of vaporization in the higher temperature state. We must therefore postpone evaluation of the effect of temperature until we obtain compressibility data for the vapors in question.

2. n-Alcohols. The method was applied to the *n*-alcohols in spite of the presence of strong hydrogen bonding. The characteristic behavior of the cohesive energy *vs. m* plots was not expected, since insertion of successive CH_2 groups into a strongly hydrogen-bonded liquid probably does not break up the association to any great degree. However, it was of interest to compare the effect of additional CH_2 groups in the *n*-alcohols with that of additional CH_2 groups in the *n*-alkanes on the cohesive energy in "corresponding states."

(9) M. L. McGlashan and D. J. B. Potter, *Proc. Roy. Soc., Ser. A*, **267**, 478 (1962).

Table III: Primary Data

Vapor Pressure

Acetonitrile		Butyronitrile		Capronitrile[b]		Caprylonitrile		Caprinitrile		Lauronitrile[a]		Lauronitrile[b]	
t, °C	p, mm	t, °C	p, mm	t, °C	p, mm	t, °C	p, mm	t, °C	p, mm	t, °C	p, mm	t, °C	p, mm
41.82	183.46	30.640	26.94	70.774	30.617	101.246	25.997	108.040	8.4617	120.705	4.163	167.718	33.141
46.09	217.71	39.030	40.93	76.141	39.001	106.100	32.004	111.917	10.202	126.333	5.570	178.958	50.23
46.11	217.76	49.913	67.81	82.810	51.925	112.769	42.133	117.152	13.034	131.603	7.266	190.187	74.18
50.36	257.18	59.226	101.46	92.202	76.579	117.529	51.027	128.464	21.515	134.660	8.404	195.922	89.68
55.37	310.47	67.536	141.67	98.080	96.391	121.908	60.545	135.359	28.725	147.597	14.996	201.883	108.56
60.64	376.19	77.313	205.88	101.861	111.21	124.915	67.918	143.074	39.091	157.997	23.065	215.378	163.66
65.91	452.96	86.710	287.39	110.708	153.50	131.215	84.53	151.621	54.121	166.643	32.238	225.868	220.87
70.74	533.63	93.675	363.97	121.888	224.79	137.106	104.73	158.767	70.160	175.168	43.841	233.818	274.20
76.31	641.39	100.638	456.12	129.523	287.57	142.383	126.03	169.479	101.69	182.950	57.898	240.599	327.60
81.87	764.99	100.701	457.00	138.882	383.33	147.001	146.67	179.642	141.50	189.557	72.658	248.909	404.22
81.89	765.14	107.041	556.65	143.493	439.05	151.204	168.78	189.546	191.87			256.233	482.91
		112.904	663.44	155.913	622.19	156.771	201.23	198.994	252.75			263.541	573.85
		117.254	752.64	162.462	740.54	159.935	222.42	209.649	339.27			271.512	687.37
		120.223	818.84	168.482	864.65	164.567	255.79	222.429	473.06			282.078	865.10
						171.678	315.47	232.093	600.15				
						178.920	387.45	243.753	788.32				
						179.168	390.19	245.364	815.92				
						188.340	500.65						
						196.265	614.13						
						204.136	744.97						
						206.070	779.90						

Density Data

Capronitrile		Caprylonitrile		Caprinitrile		Lauronitrile		1-Chlorooctane		1-Chlorodecane	
t, °C	ρ, g/ml	t, °C	ρ, g/ml	t, °C	ρ, g/ml	t, °C	ρ, g/ml	t, °C	ρ, g/ml	t, °C	ρ, g/ml
32.14	0.79489	32.62	0.80366	29.10	0.81315	32.91	0.81469	18.29	0.8744	16.82	0.8732
40.22	0.78814	43.44	0.79551	40.35	0.80511	39.38	0.81014	30.36	0.8641	24.25	0.8672
51.32	0.77885	51.39	0.78923	49.04	0.79875	53.51	0.80010	37.34	0.8580	42.71	0.8524
62.13	0.76975	60.85	0.78193	59.31	0.79118	59.25	0.79606	49.10	0.8482	53.83	0.8435
70.96	0.76245	72.59	0.77280	84.17	0.77293	69.58	0.78876	60.04	0.8393	60.82	0.8379
81.27	0.75383	82.02	0.76549	94.31	0.76521	79.79	0.78150	69.99	0.8307	73.53	0.8277
91.54	0.74504	91.58	0.75792	104.34	0.75770	90.85	0.77361	72.21	0.8288	83.07	0.8205
101.39	0.73657	101.76	0.74984	115.40	0.74939	101.23	0.76620	85.83	0.8169	94.33	0.8115
		101.75	0.74984	133.88	0.73522	101.27	0.76620	100.26	0.8039	105.50	0.8020
		111.96	0.74162	144.73	0.72675	111.53	0.75874	116.69	0.7887	111.87	0.7966
		121.85	0.73377			121.03	0.75178	136.66	0.7695	122.95	0.7872
		131.29	0.72604			131.66	0.74403	149.77	0.7564	134.85	0.7767
		141.86	0.71738			140.87	0.73714			143.93	0.7685
		152.69	0.70815			152.43	0.72844				

[a] Pressure measured with oil manometer. [b] Pressure measured *via* vapor pressure of water using comparative ebulliometry.

Table IV: Contributions to Total Cohesion (kcal/mol)

Compd	Temp, °C	E_c	E_{disp}	E_{ind}	E_{orient}	% dispersion	% induction	% orientation
Acetonitrile	26.0	7.54	3.9	2.6	1.0	52	34	41
Butyronitrile	53.7	8.55	5.7	2.2	0.6	67	26	7
Capronitrile	83.3	9.73	7.5	2.0	0.2	77	21	2
Caprylonitrile	103.2	11.33	9.2	2.0	0.1	81	18	1
Caprinitrile	119.3	13.10	11.1	1.9	0.1	85	15	
Lauronitrile	131.9	14.88	12.9	1.9	0.0	87	13	
Chloromethane	−90.0	5.35	3.9	1.1	0.4	73	21	6
Chloroethane	−35.4	5.98	4.8	0.9	0.3	80	15	5
1-Chloropropane	−2.9	6.81	5.7	0.8	0.3	84	12	4
1-Chlorobutane	19.4	7.62	6.6	0.8	0.2	87	10	3
1-Chlorohexane	55.7	9.22	8.4	0.8	0.0	91	9	
1-Chlorooctane	79.1	11.01	10.2	0.8	0.0	93	7	
1-Chlorodecane	99.3	12.71	12.0	0.7	0.0	94	6	
1-Chlorododecane	116.0	14.54	13.8	0.7	0.0	95	5	
Acetone	14	7.08	5.0	1.3	0.8	70	18	12
2-Butanone	40	7.62	5.9	1.3	0.4	78	17	5
2-Pentanone	51	8.29	6.8	1.2	0.3	82	14	4
2-Heptanone	78	9.99	8.5	1.2	0.3	85	12	3
2-Nonanone	96	11.48	10.3	1.1	0.1	89	10	1
2-Undecanone	111	13.09	12.0	1.1	0.0	92	8	
2-Tridecanone	123	14.89	13.8	1.1	0.0	92	8	

It should be pointed out that the possibility of significant cohesive energy remaining in the equilibrium vapor may invalidate our equating the total cohesive energy to the energy of vaporization in this series. Compressibility data for the lower alcohols (the ones most likely to have significant attractive energy in the equilibrium vapor) are not available in the temperature range of our study. A calculation for methanol using the virial equation of Bottomley and Spurling[10] indicates that 50 cal must be provided to take the equilibrium vapor to the ideal gas state at 55°. This is negligible for our purposes; however, we are interested in this quantity at 20° for methanol. There are no reliable data at this temperature.

Antoine equations are given for the *n*-alcohols from C_3 to C_{10} and beyond by Kemme and Kreps.[8] For methanol we used the Antoine equation of Nakanishi;[11] for ethanol, the data in Stull's compilation.[12] Francis equations for the thermal expansion of the alcohols were provided by R. C. Wilhoit of Thermodynamics Research Center.[13] The calculated cohesive energies and their corresponding temperatures are listed in Table V and are plotted in Figure 3.

Table V: Cohesive Energies for *n*-Alcohols

n-Alcohol	Temp, °C	Cohesive energy
C_1	19.8	8.66
C_2	38.7	9.63
C_3	67.2	10.09
C_4	83.7	10.63
C_5	98.0	11.30
C_6	107.9	11.89
C_7	112.4	12.69
C_8	122.5	13.31
C_9	128.9	13.90
C_{10}	131.4	15.11
C_{12}	143.6	16.17

Discussion

Figures 1 and 2 differ from similar plots for the 2-ketones[1] in the expected manner. The nitriles possess a larger dipole moment and can induce larger dipoles in their neighbors; consequently the induction energy contribution should be greater than in the 2-ketones, and the parallel straight lines are indeed farther apart. The orientation contribution should be larger as well, and the curve does lie farther above its "asymptote" for the smaller members of the series. Opposite changes are expected for the chlorides, which possess a smaller dipole moment, and these changes do occur in the appropriate direction.

The values for orientation and induction energies support the earlier conclusion[1] that induction is quite important in the interaction of neutral polar molecules in the liquid state, more important actually than orientation. Support for the magnitude of the induction

(10) G. A. Bottomley and T. H. Spurling, *Aust. J. Chem.*, **20**, 1789 (1967).

(11) K. Nakanishi, H. Shirai, and K. Naksato, *J. Chem. Eng. Data*, **13**, 188 (1968).

(12) W. R. Stull, *Ind. Eng. Chem.*, **39**, 517 (1947).

(13) R. C. Wilhoit, private communication.

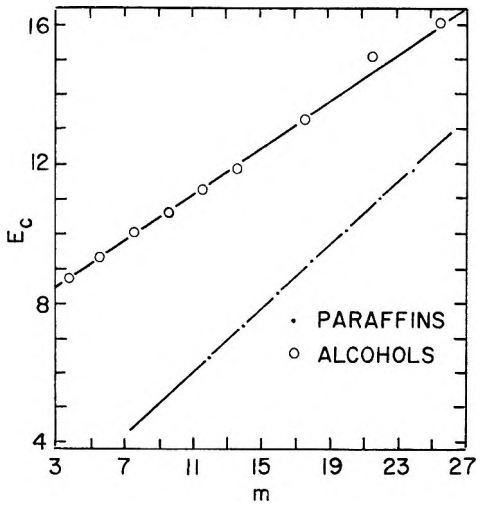

Figure 3. Cohesive energy (kcal/mol) *vs.* m, the effective number of CH bonds in the molecule. The reference state is hexane at 0°. There is indication that the high point for the C_{10} alcohol is due to an erroneous density value.

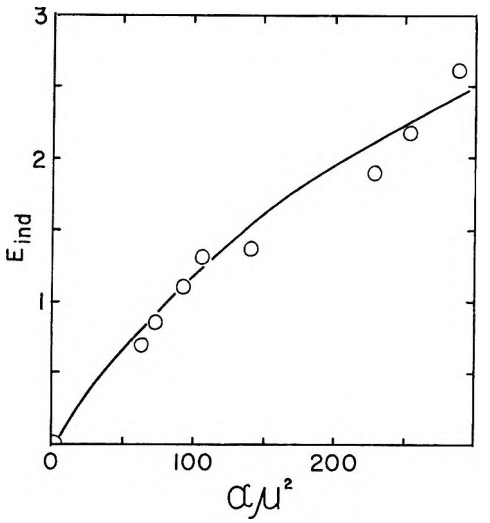

Figure 4. Induction energy *vs.* $\alpha\mu^2$ (see text). The circles represent, in order of increasing energy: alkane, $C_{10}Cl$, C_3Cl, C_{13} ketone, C_4 ketone, acetone, C_{12} nitrile, C_4 nitrile, and acetonitrile. E_{ind} is in kcal/mol and $\alpha\mu^2$ is in (esu^2 cm^5/molecule) $\times$ 10^{61}.

energies obtained with this method may be found in the work of Weimer and Prausnitz.[14] These authors developed an approach to solvent selection based on the energy density concept, using polar and nonpolar solubility parameters. Correlation of limiting activity coefficient data for nonpolar hydrocarbons in polar solvents with these solubility parameters allows prediction of activity coefficients to within 10% for 45 systems. An expression for induction energy is produced in their development, which provides approximate values for comparison with ours.

	E_{ind}, kcal/mol		
	Ketones	Nitriles	Chlorides
Weimer and Prausnitz	1.1	1.7	0.5
Present work	1.1	1.9	0.7

That two methods involving entirely different approaches to evaluating cohesive energies produce this kind of agreement is support for the validity of both.

A general relationship between induction energy and the properties of a polar liquid would be very useful. The theoretical expression usually cited for induction energy is[1]

$$E_{ind} = -\frac{2\alpha\mu^2}{r^6}$$

Using the gas-phase dipole moment[15] and the average polarizability defined above, and our calculated values of induction energy for the ketones, nitriles and chlorides, we are able to test this relationship. If the group molar volumes used to put these series into "corresponding states" are valid, r^6 is the same for all compounds, and a plot of E_{ind} *vs.* $\alpha\mu^2$ should yield a straight line passing through the origin. This turned out not to be the case; however, the points did define a rather smooth curve, and an explanation was sought in the derivation of the above expression for induction energy.

This frequently quoted expression assumes that the length of the dipole is negligible compared with the distance between the interacting centers. In a liquid this might very well be too gross a simplification. A better approximation is

$$E_{ind} = -\frac{A\alpha\mu^2}{r^6}\left[1 - B\frac{l^2}{r^2} + C\frac{l^4}{r^4}\right]$$

where l = length of the dipole, and A, B, and C are constants related to the average orientation of the dipole relative to the matter into which a dipole is being induced.[16] If we simplify this by ignoring the last term and letting l^2 be proportional to μ^2, we can write

$$E_{ind} = -A'\alpha\mu^2[1 - B'\mu^2]$$

where A' and B' are readily evaluated empirically by plotting $E_{ind}/\alpha\mu^2$ *vs.* μ^2. Experimental induction energies are reproduced with an average error of 0.06 kcal/mol when $A' = 0.0128$ and $B' = 0.0195$ (see Figure 4). Because induction energy is relatively insensitive to temperature, this plot allows estimation of the induction energy for any liquid whose dipole moment and average polarizability are known.

The cohesive energy plot for the alcohols is a straight line. This indicates, first of all, that the influence of each successive CH_2 group is the same. The slope of the alcohol plot is 0.34 kcal/CH compared with 0.46 kcal/CH for the paraffins, however. The H bond may cause the corresponding states idea to break down in the sense that there is not an average value of r char-

(14) R. F. Weimer and J. M. Prausnitz, *Hydrocarbon Process. Petrol. Refiner*, **44**, 237 (1965).

(15) "Selected Values of Electric Dipole Moments for Molecules in the Gas Phase," NSRDS-NBS 10, U. S. Government Printing Office, Washington, D. C., 1967.

(16) E. A. Moelwyn-Hughes, *ibid.*, pp 304–305.

acteristic of the molecule as a whole. Because of association, the average distance between OH groups is very likely less than the average distance between CH_2 groups. As a result, when an average r is assigned to the alcohols, the OH groups are in fact at a smaller value of r, while the CH_2 groups are at a larger one. This would lead to a smaller contribution per CH_2 to cohesion for the alcohols, since the average distance between CH_2 groups is greater than in the corresponding alkanes. It would also prevent an estimate of the magnitude of the dispersion contribution in the alcohols, for while each alcohol is in the same corresponding state, there is no guarantee that it is the same one that the alkanes are in.

The observation that the alcohol plot is linear from C_1 to C_{12} indicates that the degree of association changes very little, if at all, as successive CH_2 groups are added. The present approach to studying cohesive energies is thus not applicable to strongly hydrogen-bonded molecules.

There is evidence that in flexible, long chain molecules coiling occurs in the vapor phase to a greater extent than in the liquid phase.[17] This would have the effect of invalidating our equating cohesive energy to energy of vaporization. The latter quantity would be too small by the energy of coiling. In fact, the plot for the paraffins shows a slight dropping off beginning with the C_{11} compound. Calculations using second virial coefficient data indicate that the drop-off cannot be due to imperfections in the vapor phase; it may be due to the coiling phenomenon. The excellent linearity of the plot below C_{11} indicates that coiling is not significant in this range, and as long as we base our interpretation on these points any coiling of vapor phase molecules would have no effect on our assumption.

Equating cohesive energy with the energy of vaporization may be validly questioned even for molecules which are not long chains. We believe our doing so in the present study is justified for the following reasons. Any difference in internal energy of a given molecule in the vapor and liquid phases arises either from a change in the number of classical degrees of freedom or from a change in vibrational frequency of one or more of the nonclassical degrees of freedom.

In the first case, the strong vibrational frequencies will definitely be nonclassical in both phases, and the translational degrees of freedom will be classical in both phases. There may be some question regarding those rotational degrees of freedom which become torsional oscillations in the liquid phase. In the vapor they are classical, and as long as the frequency of oscillation in the liquid is low enough ($h\nu$ less than kT) no new nonclassical degrees of freedom will be introduced on condensation, and the classical ones will contribute the same number of $^1/_2kT$'s whether in the liquid or vapor phase. For the energies involved (*ca.* 1% of a bond energy) $h\nu$ is less than kT. This is less likely the case for strongly interacting molecules, and in such a situation our approach may be questioned. However, in defense of our conclusions, the fact that we are comparing molecules of very similar geometry and energy (paraffins and nitriles, etc.) would lead to a certain degree of cancellation of any errors introduced through our equating cohesive energy and vaporization energy. This matter is very complex; we are not aware of a better way of treating it at present.

In the second case, the relative magnitudes of chemical and physical bonds (about 100 to 1) indicate that changes in the frequency of nonclassical modes on condensation should not be more than a few per cent.

Acknowledgments. Thanks are due the Research Corporation for a grant toward the purchase of the platinum resistance thermometer and Mueller bridge used in most of this research and for a stipend for K. S. S. Dr. R. C. Wilhoit of the Thermodynamics Research Center was very helpful in providing thermal expansion data; Dr. D. Ambrose of the National Physical Laboratory very kindly supplied the Chebyshev constants relating the vapor pressure of water to its temperature for the comparative ebulliometric measurements.

(17) L. A. Wall, J. H. Flynn, and S. Straus, *J. Phys. Chem.*, **74**, 3237 (1970).

Effect of Surface Groups of Carbon on the Adsorption and Catalytic Base Hydrolysis of a Hexaamminecobalt(III) Ion

by Akira Tomita* and Yasukatsu Tamai

Chemical Research Institute of Non-Aqueous Solutions, Tohoku University, Katahira-cho, Sendai, Japan
(Received March 2, 1970)

Publication costs borne completely by The Journal of Physical Chemistry

Kinetic data are presented for the adsorption of a hexaamminecobalt(III) ion from an aqueous solution onto several kinds of carbon and for the base hydrolysis catalyzed by carbon. The content of surface acidic groups of carbons, including a carbon black and an active carbon, was modified by oxidation or methylation. The pH value of solution has a significant effect on the adsorption rate: an addition of NaOH increases the rate, and HCl retards the adsorption. The observed rate constant increases with the amount of surface acidic groups and the amount of carbon. These results are consistent with the proposed mechanism which involves adsorption of complex ion on such acidic groups of carbon. Apparent activation energy for adsorption on carbon was estimated at 21 $\sim$ 23 kcal/mol. The rate constant for base hydrolysis of the same complex ion was also found to have a close relation to the amount of surface acidic groups of carbon catalysts. It is suggested that the active sites for hydrolysis may be such acidic groups which are also the active sites for the adsorption.

Introduction

Carbon catalyzes a number of different kinds of chemical reactions.[1] In the field of coordination chemistry, carbon is often used as a catalyst in the preparation of Co(III) complexes[2] or in the racemization of optically active Co(III) complexes.[3] The mechanistic details of this heterogeneous reaction or the mechanism of the adsorption process which must be the most important step of the reaction are not understood at present. The study of the adsorption and the reaction of metal complexes on carbon would give not only a guiding principle for preparing new coordination compounds but also some information about the reaction mechanism on metal catalysts supported on carbon carriers.

Several factors may influence the rate and the mechanism of reaction on carbon. In the present paper, we shall confine our attention to the chemical nature of the carbon surface. The functional groups on carbon have been characterized by various organic and physical methods.[4] Boehm[5] reported the presence of four different kinds of acidic surface oxides. The nature of carbon surface varies with the kind, the amount, and the distribution of these functional groups. It has been shown that acidic groups on carbon play a very important role in adsorption of organic compounds[6,7] from aqueous solution.

In the present study, we prepared carbons having different amounts of acidic groups by various methods of modification and investigated the relationship between the surface acidity and the adsorption rate of a $[Co(NH_3)_6]^{3+}$ ion onto carbon. The second object of this paper is to determine the dependence of the catalytic activity of carbon on the surface acidity. The test reaction chosen for this purpose was the base hydrolysis of $[Co(NH_3)_6]^{3+}$ into $[Co(NH_3)_5(OH)]^{2+}$ in the presence of carbon.[8]

Experimental Section

Materials. Deionized distilled water and reagent grade chemicals were employed. $[Co(NH_3)_6]Cl_3$ was prepared as described in the literature[9] and characterized analytically and spectrophotometrically. Two kinds of carbon with different surface area were employed in this work: (1) a carbon black "Seast 305 (HAF)" supplied by Tokai Electrode Mfg. Co., and (2) a commercial active carbon (AC) obtained from Kanto Chemical Co., Inc.

Modification of Carbon. To prepare carbon samples of various known contents of surface oxides for adsorption study, the surface of the carbon was oxidized with HNO_3, $(NH_4)_2S_2O_8$, and O_2 by the method of Boehm.[5] Partial methylation of surface carboxyl or

(1) R. W. Coughlin, *Ind. Eng. Chem. Prod. Res. Develop.*, **8**, 12 (1969).

(2) F. Basolo and R. G. Pearson, "Mechanisms of Inorganic Reactions," Wiley, New York, N. Y., 1958, p 355.

(3) B. E. Douglas, *et al.*, *J. Amer. Chem. Soc.*, **76**, 1020 (1954); *J. Inorg. Nucl. Chem.*, **24**, 1355, 1365 (1962); **26**, 601, 609 (1964).

(4) J. B. Donnet, *Carbon*, **6**, 161 (1968).

(5) H. P. Boehm, *Angew. Chem.*, **76**, 742 (1964); **78**, 617 (1966); *Advan. Catal.*, **16**, 179 (1966).

(6) D. Graham, *J. Phys. Chem.*, **59**, 896 (1955).

(7) R. W. Coughlin, F. S. Ezra, and R. N. Tan, *J. Colloid Interface Sci.*, **28**, 386 (1968).

(8) J. Bjerrum, "Metal Ammine Formation in Aqueous Solution," Haase, Copenhagen, 1941, p 285.

(9) J. Bjerrum and J. P. McReynolds, *Inorg. Syn.*, **2**, 216 (1946).

Table I: Rate Constants for Adsorption and Hydrolysis and Properties of Carbon

Carbon	Modifier	Surface area, m^2/g	NaOH consumption, mequiv/100 g	$k_{ads} \times 10^3$, min^{-1} 30°	$k_{ads} \times 10^3$, min^{-1} 50°	$k_{hyd} \times 10^3$, min^{-1}, 30°
HAF		81	2.2	0.069	0.735	3.29
HAF-n3	3% HNO_3	82	5.7		0.682	
HAF-n2	6% HNO_3	78	7.9		0.790	4.41
HAF-n7	18% HNO_3		7.0		0.69	5.40
HAF-n1	30% HNO_3	78	10.1		1.04	7.48
HAF-n6	42% HNO_3		12.5		1.20	8.07
HAF-n4	60% HNO_3	71	14.7		1.74	9.34
HAF-a1	$(NH_4)_2S_2O_8$	94	19.4		1.64	14.0
HAF-o1	O_2	170	40.1		19.3	34.9
AC-d1	CH_2N_2	1120	14.9	0.685	6.27	
AC		1230	32.7	2.36	20.8	160
AC-o1	O_2	1120	38.7	4.61	42.3	
AC-n4	30% HNO_3		105	7.40	74.2	
AC-n3	60% HNO_3		111	9.96	98	
AC-o2	O_2	1100	118	8.97	83.0	

hydroxyl groups was carried out using the technique of Studebaker, *et al.*[10] The amount of surface acidic groups decreased as shown in Table I.

Surface Area and Acidity. Nitrogen adsorption measurements were made at liquid nitrogen temperature, and the surface area was calculated by the method of Joyner, *et al.*[11] The acidic groups were determined by shaking with excess standard base for an equilibration period of 24 hr and back-titrating with standard HCl.

Adsorption Rate. The weighed sample of the complex was dissolved in the required volume of solvent, and the solution was allowed to reach a constant temperature in a water bath before the weighed sample of carbon was added. A number of amber tubes (40 ml) were mounted on a shaker in a water bath incubator and were shaken at a rate of 150 times/min. After different intervals of time they were removed rapidly and cooled in order to inhibit the further progress of the adsorption. The carbon was removed by centrifugation or filtration, and the content of $[Co(NH_3)_6]^{3+}$ ion was analyzed by measuring the optical absorbance at 474 mμ. The rate was followed by the absorbance of small aliquots of the supernatant solution. Spectral measurement was made using 1-cm silica cells in a Hitachi EPU-2 or a Cary 14 spectrophotometer.

Hydrolysis Rate. As the hydrolysis occurred only in the presence of ammonia, aqueous ammonia (1.5 *N*) was used as a solvent unless otherwise stated. The spectrophotometric method was used to follow the rate of base hydrolysis. Measurements were made at 474 mμ where a relatively large absorption difference occurred between $[Co(NH_3)_6]^{3+}$ and $[Co(NH_3)_5(OH)]^{2+}$.

Results

The B.E.T. surface area and the quantities of NaOH consumed are summarized in Table I for various types of carbon. Pretreatment of these samples is designated by an appended "n," "a," and "o" for oxidation by HNO_3, $(NH_4)_2S_2O_8$, and O_2, or "d" for methylation by CH_2N_2. The quantities of $NaHCO_3$ and Na_2CO_3 consumed were also determined. They are not listed in this table because they were found to have a close relation to the total acidity (NaOH consumption) as reported by Boehm.[5]

Upon addition of carbon to the solution of $[Co(NH_3)_6]Cl_3$, the yellow color due to the $[Co(NH_3)_6]^{3+}$ ion disappeared gradually and the solution became colorless. The fact that no other bands were observed under these conditions suggests all cobaltic ions were completely adsorbed onto carbon. The kinetic data were plotted for a first-order process, log $C_0/(C_0 - C)$ *vs.* t where C_0 (m*M*) is the initial concentration of the complex ion and C (m*M*) is the amount of the complex ion per unit volume that has disappeared in time t. Except for the very initial region, a straight line was obtained. The concentration at the later region was represented by the equation

$$C = C_0(1 - \alpha e^{-k_{ads}t}) \quad (1)$$

Table II: Activation Parameters

Carbon	E_a, kcal/mol	Log A, min^{-1}
HAF	23	7.4
AC-d1	21	12.2
AC	21	12.4
AC-o1	22	13.2
AC-o2	22	13.6

(10) M. L. Studebaker, E. W. D. Huffman, A. C. Wolfe, and L. G. Nabors, *Ind. Eng. Chem.*, **48**, 162 (1956).

(11) L. G. Joyner, E. B. Weinberger, and C. W. Montgomery, *J. Amer. Chem. Soc.*, **67**, 2182 (1945).

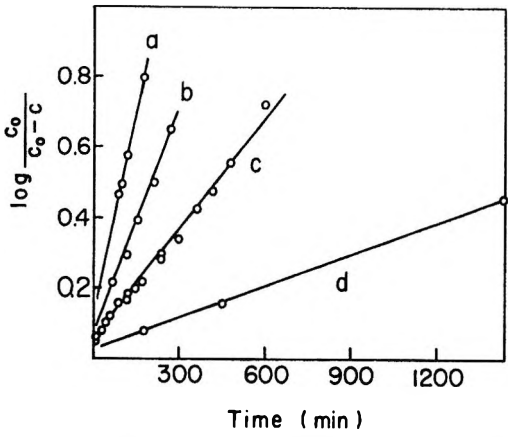

Figure 1. Adsorption of $[Co(NH_3)_6]^{3+}$ on carbons: initial concentration, 16 mM × 10 ml; temperature, 30.0°: carbons (0.01 g) are: a, AC-o2; b, AC-o1; c, AC; and d, AC-d1.

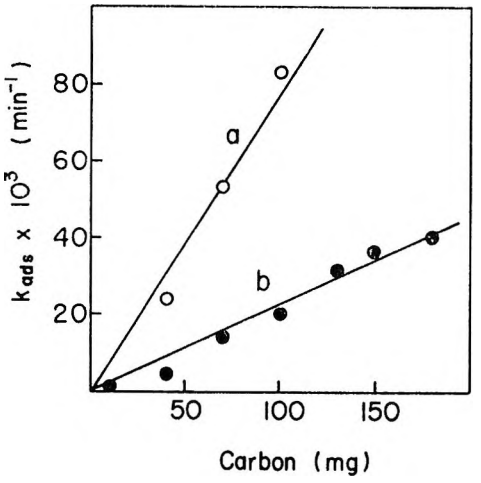

Figure 2. Effect of the amount of carbon on the rate of adsorption: solution, 16 mM × 10 ml; temperature, 50.0°; carbon: a, AC-o2; and b, AC.

where α is a constant. Typical plots for AC series are shown in Figure 1, and an apparent rate constant k_{ads} was determined from the slope of the linear part. Table II lists activation parameters obtained by the measurements at 30, 50, and 60°.

Figure 2 shows the relationship between the observed rate constant k_{ads} and the amount of carbon. Considering that the plots are linear and pass the original point, the rate constant can be expressed as a linear function of the amount of carbon.

The effect of pH on the rate is very significant. Excess acids inhibit the adsorption as judged from the results in Figure 3. However, upon addition of appropriate amounts of HCl (curve d in Figure 3), rate plots do not obey the above equation. The adsorption is almost inhibited at an early stage, and the rate increases gradually as the extent of the adsorption progresses. When the amount of NaOH added increases, both intercept (α in eq 1) and slope (k_{ads})

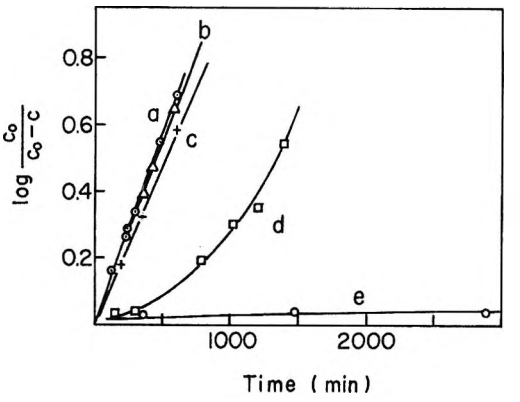

Figure 3. Effect of HCl on the rate of adsorption on AC. The ratios, HCl/Co, are: a, 0.00; b, 0.07; c, 0.14; d, 0.35; and e, 0.70.

of the rate plot become larger. The observed rate constant, k_{ads}, may be represented as

$$k_{ads} = k_1 + k_2[OH] \quad (2)$$

where $k_1 = 2.30 \times 10^{-3}$ min^{-1} and $k_2 = 0.172$ l mol^{-1} min^{-1} at 30.0°.

In order to study the mechanism of adsorption, the stoichiometry of adsorbed species was determined by analyzing NH_3 and Cl^- remaining in solution (see Table III). The fact that NH_3 is liberated during the adsorption was evidenced by sweeping NH_3 out of the solution with a stream of air and into a solution containing Nessler reagent. The pH of the solution rose considerably, but the linearity of the rate plots was held under usual conditions. Exceptional is the case shown in Figure 3. The amount of NH_3 shown in Table III was obtained by titrating with HCl. The amount of cobalt ion adsorbed was calculated from the disappearance of the band at 474 mμ. The ratio, NH_3/Co, is always higher than two and can be regarded as fairly constant. The above fact is in contrast with the case of the adsorption of $[Cu(NH_3)_n]^{2+}$ on silica

Table III: NH_3 and Cl^- in Solution[a]

AC, mg	Time, hr	Co_{ads}, μmol	NH_3 in soln, μmol	NH_3/Co_{ads}	$Cl^-/Co_{initial}$
100	0.5	26.2	60.7	2.3	
100	2.0	50.6	130.2	2.6	
100	4.0	78.2	207	2.6	
100	24.0	160.0	398	2.5	3.0
10	8.0	21.1	51.7	2.5	3.0
10	24.0	37.7	94.3	2.5	3.0
10	72.0	67.0	173	2.6	3.0
10	[b]	118.6[c]	318	2.7	3.0

[a] Initial concentration of $[Co(NH_3)_6]Cl_3$; 16 mM × 10 ml, temperature, 30.0°. [b] Temperature was raised to 60°. [c] Number of adsorbed layers is approximately two.

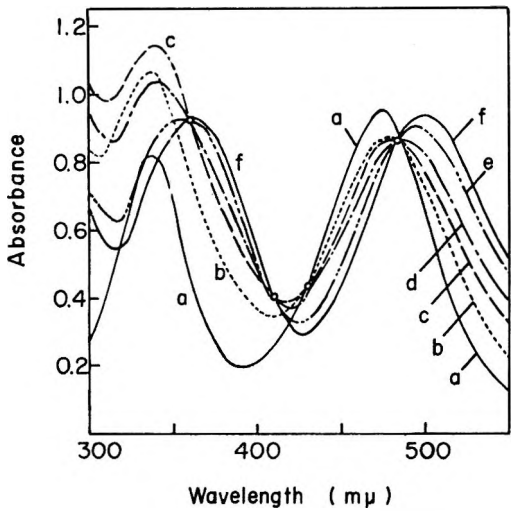

Figure 4. Spectral change during base hydrolysis catalyzed by AC (0.1 g); $[Co(NH_3)_6]^{3+}$; 16 mM in 1.5 N NH_3 aqueous solution, 10 ml; temperature, 30.0°; times from mixing with catalyst are: a, 0; b, 2; c, 4; d, 8; e, 14; f, 35, 168, and 1200 min.

gel reported by Smith, *et al.*,[12] who observed that the NH_3/Cu ratio in adsorbed species is higher than that of primary complex species initially in solution. Chloride ion was determined volumetrically by Mohr's method. It was noteworthy that no Cl^- ions in $[Co(NH_3)_6]Cl_3$ were adsorbed on carbon but remained in solution.

Figure 4 shows the spectral change during the catalytic base hydrolysis of the $[Co(NH_3)_6]^{3+}$ ion into the $[Co(NH_3)_5(OH)]^{2+}$ ion. The absorption maxima of these complexes are at 474 and 503 mμ, and it has been assumed that absorbance at these wavelengths changes linearly with concentration. The change of absorbance at 474 mμ was plotted in the pseudo-first-order expression against time, and the observed rate constant, k_{obs}, was obtained. Generally speaking, the decrease in the absorption at 474 mμ in this system is due to conversion to the hydroxo complex and/or irreversible adsorption onto the carbon. The method of judgement for these alternatives is very simple: the absorbance at 503 mμ decreases at the same rate as that at 474 mμ if only irreversible adsorption occurs, whereas if only hydrolysis occurs, the sum of concentrations calculated from these two bands must remain constant. The apparent rate constant must be the sum of constants for adsorption, k_{ads}, and for hydrolysis, k_{hyd}, because k_{obs} and k_{ads} are the first-order rate constants with respect to the concentration of $[Co(NH_3)_6]^{3+}$.

$$k_{obs} = k_{ads} + k_{hyd} \quad (3)$$

The amount of disappeared cobalt ions, which is necessary for the calculation of k_{ads}, was determined from the concentrations of $[Co(NH_3)_6]^{3+}$ and $[Co(NH_3)_5(OH)]^{2+}$ ions in solution. These concentrations could be estimated from the absorbance at 474 and 503 mμ by assuming the absence of any other species which have a significant contribution to the absorbance in this region. The ratio k_{hyd}/k_{obs} varies from zero to unity with experimental conditions, especially with the concentration of NH_3 and the amount of carbon. Figure 4 and Table IV show that k_{hyd}/k_{obs} is nearly unity in 1.5 N NH_3 solution. This ratio decreases with decreasing concentration of NH_3 and the amount of carbon. In order to avoid this complexity, the concentration of NH_3 was made 1.5 N for the comparison of the catalytic activity of carbons.

Table IV: Competition between Adsorption and Hydrolysis

AC, mg	Co^{3+},[a] mM	NH_3, N	$k_{obs} \times 10^3$, min^{-1}	k_{hyd}/k_{obs}[b]	τ_{488},[c] min
100	16	1.5	160	1.0	6
100	10	0.15	4.22	0.38	60
100	16	0.060	4.53	0.02	300
100	16	0.00	2.36	0.0	[d]
10	10	0.15	0.58	~0.0	~2000
10	16	0.00	0.10	0.0	[d]

[a] $[Co(NH_3)_6]^{3+}$, 10 ml. [b] $k_{hyd} = k_{obs} - k_{ads}$. [c] Time required for the peak shift to 488 mμ. [d] No shift was observed.

It is assumed that the value k_{hyd} can be used as an indication of the catalytic activity of carbon. These rate constants are summarized in Table I together with other properties of carbons.

Discussion

It is evident from Table I that the adsorption rate constants are closely related to surface acidities rather than surface areas. In view of the correlations with the total acidity on the carbon surface (Figures 5 and 6), it seems likely that the adsorption may be initiated, for example, in the following manner.

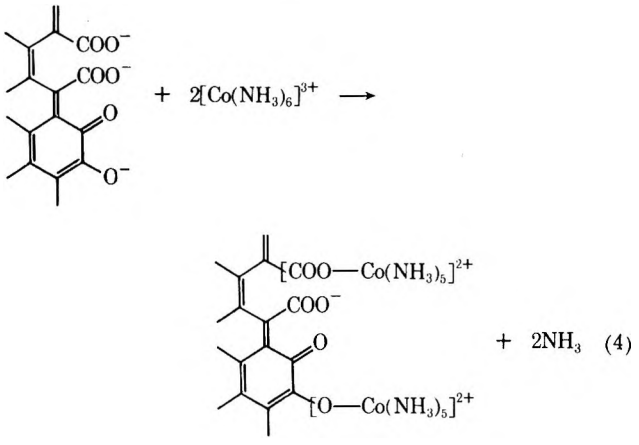

(12) G. W. Smith and H. W. Jacobson, *J. Phys. Chem.*, **60**, 1008 (1956).

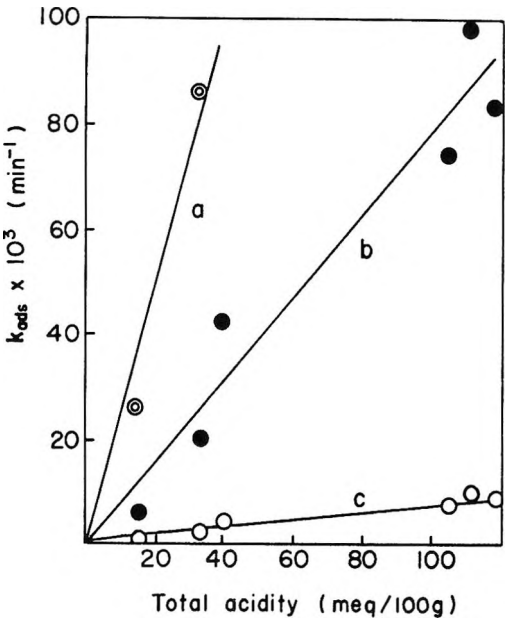

Figure 5. Dependence of observed rate constants for adsorption on total acidity of AC series: temperatures are: a, 64.9; b, 50.0; and c, 30.0°.

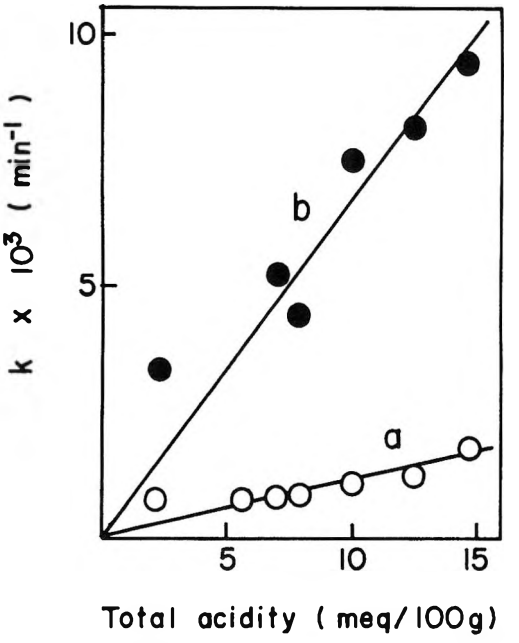

Figure 6. Dependence of observed rate constants on total acidity of HAF series: a, adsorption at 50.0°; b, hydrolysis at 30.0°.

If such groups on a carbon surface are the active sites for adsorption, it is supposed that the electrostatic nature of the surface and the solute would be one of the most important factors. Evidences in favor of this expectation were obtained from the following experiments.

(1) The rate of adsorption increased upon addition of NaOH. In the higher pH region, –COOH and –OH groups on the carbon surface dissociate into $-COO^-$ and $-O^-$ anionic groups. The complex *cation*, $[Co(NH_3)_6]^{3+}$, would interact with these negatively charged sites more readily than the undissociated neutral sites.

(2) Decrease of these negatively charged sites, on the contrary, retarded the adsorption. These groups may be blocked by methylation with CH_2N_2, and the absorption onto AC-d1 was much slower than that onto AC as was expected. Protonation of these groups also retards the adsorption as illustrated in plot e and an induction period as in plot d in Figure 3. The induction period was followed by an increase of rate due to the neutralization of HCl with the librated NH_3.

(3) Contrary to the present case, the reaction rate of complex *anions*, such as $[Co\ edta]^{2-}$ or $[Co(NO_2)_6]^{3-}$, varied inversely as the surface activity of carbon. A detailed account of these reactions will be described in subsequent communications.

The absorption of the complex ion onto carbon (eq 4) facilitates the subsequent reactions. More NH_3 molecules were substituted by water and/or hydroxide ion according to eq 5, unless NH_3 was added to the solution in excess. Table III indicates that the amount of NH_3 in solution is 2.5 times the amount of complex ion adsorbed. Considering that a part of NH_3 molecules does not dissolve in solution but adsorbs on carbon, at least three molecules of NH_3 seem to be replaced from one $[Co(NH_3)_6]^{3+}$ ion upon adsorption. Consequently, the value $(m + n)$ in eq 5 must be 2 or above.

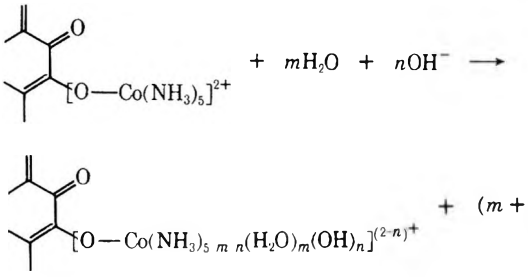

When the amount of a complex ion was sufficiently large compared with carbon, the multilayer formation was observed after a long time for adsorption. One example is shown at the bottom of Table III. A possible explanation for this phenomenon may include the formation of a polynuclear cobalt complex involving two hydroxide ion bridges. Many examples for this type of polynuclear complexes have been reported.[13] Table III demonstrates that NH_3 molecules dissociate from the complex ion in the second layer, too. This fact can be reasonably interpreted by the bridge formation. This model is, however, highly speculative, and further work would be required to explain fully this multilayer formation.

A close relationship between the rate of hydrolysis and the total acidity was also observed and is shown

(13) "Gmelins Handbuch der Anorganischen Chemie," Kobalt, **58**, B-2, Verlag Chemie, GmbH, Weinheim, 1964, pp 621–633.

in Figure 6 (plot b). It may be concluded that the active sites for hydrolysis are also the acidic functional groups on the carbon surface, and the initiation step for hydrolysis is the same as that described in eq 4. Further substitution of NH_3 like eq 5 might be depressed in the present case, because the concentrated aqueous ammonia was used as a solvent. The hydroxide ion attacked the Co–O bond rather than the Co–N bond, and the product, $[Co(NH_3)_5(OH)]^{2+}$, was obtained as shown in the following equation.

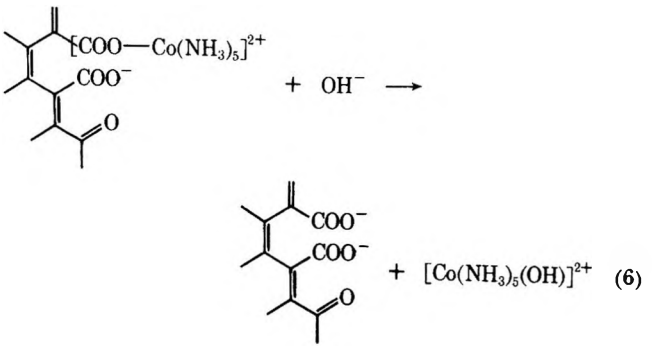

(6)

Noise Spectra Associated with Hydrochloric Acid Transport through Some Cation-Exchange Membranes[1]

by Masao Yafuso and Michael E. Green*

The City College of The City University of New York, New York, New York 10031
(Received August 7, 1970)

Publication costs assisted by The City College of the City University of New York

The noise spectra and some other electrical phenomena associated with transport of hydrogen ion across a cation-exchange membrane have been studied at currents great enough to cause the formation of a depletion layer. Under these conditions, one obtains noise spectra which show a frequency dependence of approximately ω^{-2} at low frequencies and ω^{-4} at high frequencies. Combined with data on voltage drops as a function of time and distance from a membrane, we find the principal noise source to be within 40 μm of the membrane surface. The frequency at which the change in slope occurs was measured as a function of current, temperature, and concentration. The total current can be split into a diffusion contribution and a contribution from H^+ and OH^- ions from dissociation of water. The corresponding electric field for dissociation is calculated from the Onsager equation. The frequency at which the change of slope occurs, taken at constant field, is a function of temperature, with an activation energy of 16.4 ± 0.9 kcal/mol, and the dissociation flux is proportional to this frequency. Possible sources for the noise are considered.

Introduction

In a previous paper[2] we reported some results on the noise spectra associated with the transport of various ions through several cation- and anion-exchange membranes. It was not possible at that time to give a mechanism for the generation of the noise, except to note that it was associated with the formation of the depletion layer (the layer formed in front of the membrane when the current exceeds the maximum current density which the ions in solution can maintain).[3]

The critical current density has been measured by many authors, and from this the thickness of the diffusion layer has been estimated and descriptions of the associated phenomena given in terms of diffusional fluxes.[4] However, a microscopic model for these processes does not appear to be available at the present time. Gregor and Miller[5] did attempt to estimate the field at which water dissociation occurs from a kinetic argument, but their model seems, at least, incomplete.

By studying noise spectra, one can get kinetic data not limited to the slowest step of the overall process, and this has been applied in various systems of semi-

(1) Based upon a dissertation submitted to The City University of New York by M. Y. in partial fulfillment of the requirements for the degree of Doctor of Philosophy.

(2) (a) M. E. Green and M. Yafuso, *J. Phys. Chem.*, **72**, 4072 (1968); (b) M. E. Green and M. Yafuso, *ibid.*, **73**, 1626 (1969).

(3) F. Helferich, "Ion Exchange," McGraw-Hill, New York, N. Y., 1962, p 399.

(4) (a) A. M. Peers, *Discuss. Faraday Soc.*, **21**, 124 (1956); (b) K. S. Spiegler, U. S. Office Saline Water Res. Develop. Prog. Rep. 1968.

(5) H. Gregor and I. F. Miller, *J. Amer. Chem. Soc.*, **86**, 5689 (1964).

conductors.[6] Applications to membrane studies have also been made by physiologists.[7]

In this work, we have chosen a single system which gives well defined results, HCl on either of two similar polystyrene sulfonate resin membranes. From the work reported earlier[2] we hoped to find a single relaxation time which could be tied to a single process. Some tentative models have been investigated, none of which seems to be able to account for all the data.

Experimental Section

The ion-exchange membranes were the same ones described earlier.[2] Most of the studies were carried out with MC 3235 cation exchange membrane.

Some modifications were made on the measuring system. The noise cell was changed to a Plexiglas box 4.0 × 10.9 cm with a middle divider which had a flared hole in the middle. The membrane was taped onto the hole with black friction tape. A hole on the tape determined the exposed surface area. A cover for this cell had five holes over each compartment. Four holes held the two current carrying electrodes and the two amplifier electrodes. Two more holes over each compartment were used to circulate heating oil through glass tubing that extended into the solution.

The instrumental setup was similar to that used previously[2] except for the use of the Tektronix 3L5 spectrum analyzer. The noise was picked up through the inner electrodes by a P85AH Philbrick operational amplifier wired as a follower with a gain of 100. A 0.5-μF capacitor in series with the input blocked dc voltage. The amplified noise was amplified further when necessary with a Hewlett-Packard 466A amplifier, then passed to the 3L5 through the Kronheit Model 3100A band pass filter. (The Kronheit filter was used to reduce the total signal entering the 3L5 by cutting off the low-frequency signals. This was necessary since the 3L5 had approximately a 30-db dynamic range in power.) The output from the 3L5 was then fed into a Keithley 610C electrometer on which all readings were made. The fluctuating voltage was time averaged by means of a 3000-μF capacitor attached across the electrometer input. The input electrodes were connected directly to another electrometer (Keithley 610B) to read simultaneously the voltage drop across the membrane. Measurements were made in the manual mode (point by point) as scanning the noise spectrum produced serious problems. The bandwidths were calibrated using a known noise source (General Radio Model 1340B). Data in Figure 5 are given as power spectra (power per unit bandwidth). The spectrum analyzer did not have a linear dispersion as specified. In addition, calibration was complicated by an instability of the zero frequency position. Calibrations of the dispersion were made with sine wave signals of known frequencies.

Voltage *vs.* distance from membrane and noise *vs.* distance measurements were made using a tapered tungsten microelectrode which was attached to an S. S. White Industrial Miniprobe Model 356-8245Y. This miniprobe had a 3.5-mm maximum movement corresponding to a 180° turn of an Allen wrench attachment. By attaching a stationary protractor on the movement and a pointer on the turn screw it was possible to divide the 3.5 mm total displacement into 180 parts or 1.9×10^{-3} cm/deg.

The microelectrode was prepared by passivating 10-mil tungsten wire in saturated potassium nitrate solutions.[8] The tapered wire was coated except for the very tip with nail polish (wax and dissolved Plexiglas were unsatisfactory) and slipped into a hypodermic needle which acted as a holder. The size of the exposed electrode tip was measured under the microscope with calibrations on the eyepiece and found to be about 2×10^{-3} cm (20 μm).

The microelectrode was connected to an electrometer (Keithley 610B) for voltage measurement and to a P85AH Philbrick preamplifier for total noise measurements. In this way total noise and membrane voltage were monitored simultaneously. The ground was attached to another tungsten wire at the opposite side of the membrane surface. The electrometer output was fed into a Tektronix Type 3A72 dual trace amplifier plug-in with a Type 564 storage oscilloscope. The voltage–time behavior was photographed with the C-27 oscilloscope camera. A family of voltage–time curves for various current densities was put on a single photograph by using a triggered sweep. The pulse caused by the switch that closed the circuit was used as the trigger. To minimize pickup the first stage, including the electrometer, was put on the first shelf of a metal cart and covered on three sides with aluminum foil. The point of contact of the electrode with the membrane was determined by the bending of the electrode.

Results

The family of voltage–time curves for MC 3235 cation-exchange membranes at three different HCl concentrations can be seen in Figure 1. Similar curves have been reported by others.[4b,9] The time lag in the voltage change corresponds to the finite time required for the depletion of electrolytes from the membrane surface and the formation of a steady-state concentration gradient. The same time lag is observed before the onset of noise. This suggests strongly that cation

(6) (a) K. M. van Vliet and J. Blok, *Physica*, 22, 231 (1956); (b) K. M. van Vliet, J. Blok, C. Riis, and J. Stekette, *ibid.*, 22, 525, 723 (1956).

(7) (a) H. E. Derksen and A. A. Verween, *Science*, 151, 1388 (1965); (b) A. A. Verween and K. L. Schick, *Nature*, 316, 688 (1967); (c) W. H. Calvin and C. F. Stevens, *Science*, 155, 842 (1967).

(8) D. J. Ives and G. J. Janz, "Reference Electrodes," Academic Press, New York, N. Y., 1961.

(9) N. Lakshminarayanaiah, "Transport Phenomena in Membranes," Academic Press, New York, N. Y., 1969, pp 230–231.

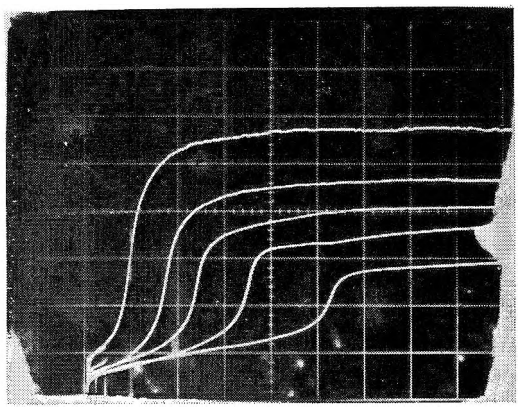

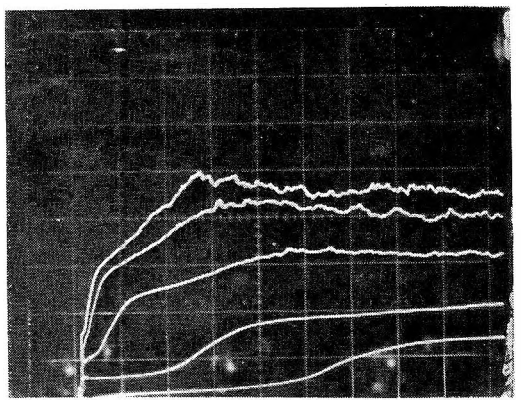

Figure 1. Voltage–time curves for HCl and MC3235, 5 sec/div, 0.225 V/div: (a) 0.050 M HCl. From top to bottom in mA/cm²: 67, 60, 42, 37, and 33; (b) 0.010 M HCl. From top to bottom in mA/cm²: 67, 50, 33, 17, and 12.

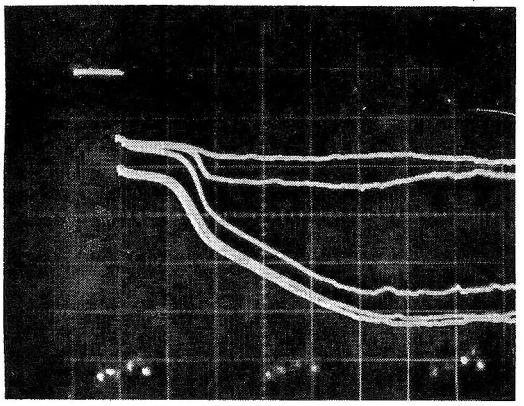

Figure 2. Voltage–time curves at distances, x, from membrane MC 3142, 0.025 M HCl, 44 mA/cm², 2 sec/div, 0.2 V/div. From top to bottom, x in 10^{-4} μm: 0, 40, 200, 800, and 1200.

exchange noise is intimately related to the formation of a depletion layer. The time lag for MC 3142 cation-exchange membrane with sodium chloride and the absence of a time lag with the MA 3148 anion-exchange membrane were reported previously.[2]

Some secondary voltage changes can be seen in the

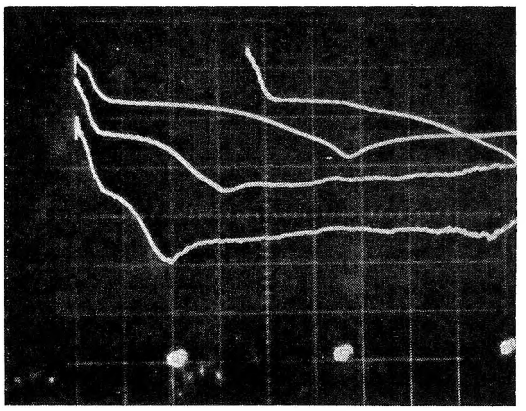

Figure 3. Voltage–time curve with microelectrode touching and possibly penetrating the membrane. MC 3142, 0.025 M HCl, 1 sec/div, 0.050 V/div. From top to bottom, J in mA/cm²: 33, 33, 44, and 55. Note: The first run at 33 mA/cm² triggered after the sweep was initiated.

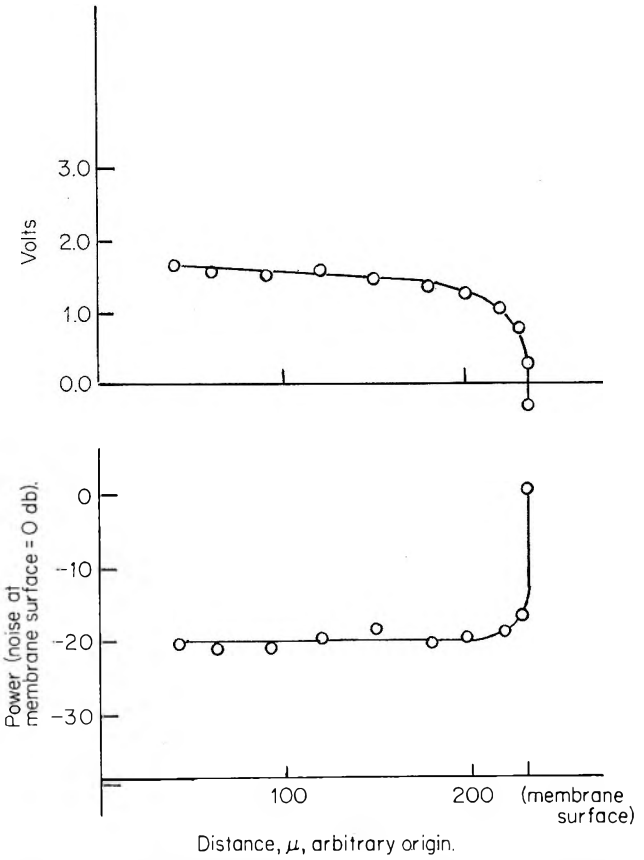

Figure 4. Membrane volts and noise *vs.* distance for MC 3235, 0.025 M HCl, 83 mA/cm².

cation-exchange membrane curves at low concentrations and high current densities (Figure 1b). These changes were eliminated when the electrode was brought to within 40 μm of the membrane surface on the depleted side. The voltage–time curves at various distances from the membrane can be seen in Figure 2. Some voltage changes with time were observed with the electrode touching and possibly slightly penetrating the membrane. This can be seen in Figure 3.

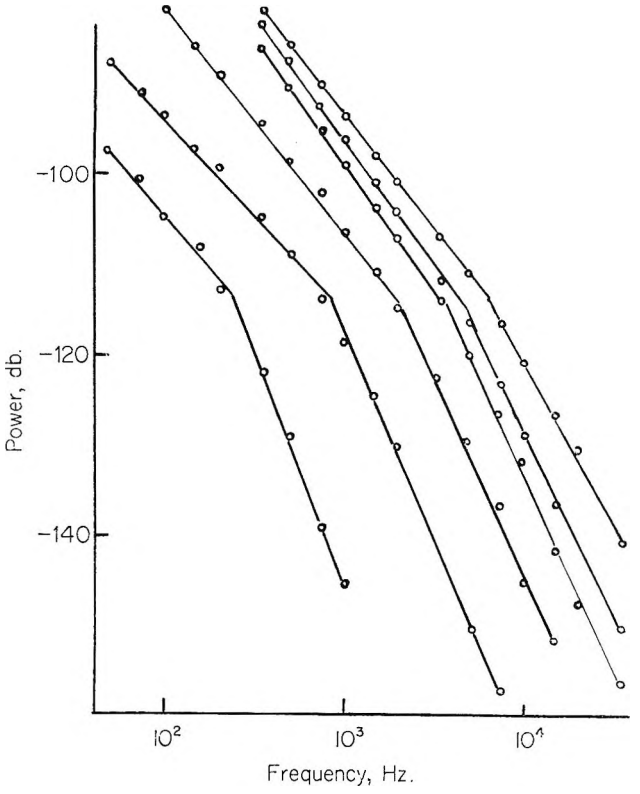

Figure 5. Power spectra of 0.050 *M* HCl with MC 3235 at 30° obtained with the 3L5 spectrum analyzer. From top to bottom in mA/cm²: 76, 59, 50, 45, 35, and 31.

The relation of steady-state ir drop across the electrodes with distance from the membrane and the total noise with distance were also plotted. The membrane and the total noise with distance were also plotted. The results (Figure 4) show a sharp drop in voltage when the electrode contact with the membrane was accompanied by a simultaneous increase in noise. (Note: The voltage inversion that was recorded may have been due to electrode asymmetry.) The sharpest changes in noise and voltage occurred within 40 μm of the membrane surface.

The power spectra obtained for 0.050 *M* HCl with MC3235 at 30° are shown in Figure 5. Similar curves were obtained at 19, 40, and 49° and for 0.025 *M* HCl at the same temperatures. The feature of interest that was common to all was the intersecting straight lines. The point of intersection shifts to higher frequencies with increasing current density.

Discussion

The electrical properties recorded in Figures 1–4 help to locate the noise source. The sharp change in voltage that occurs after a time lapse can be attributed to the drop in conductivity with electrolyte depletion at the membrane surface. This depletion is a consequence of the Donnan equilibrium between the membrane and solution phases. The stable electrostatic potential at the interface opposes penetration of the membrane by ions. As a result the counterion transport number in the membrane is larger than in the solution phase. This difference causes electrolyte depletion at the membrane surface, creating a concentration gradient of sufficient magnitude to maintain the flux. At the critical current density the diffusional flux has reached a maximum, and any further increase in the flux must come from water dissociation.[4] The voltage–time curves for currents exceeding the critical current density are characterized by a sharp voltage change; after a time lapse secondary voltage changes following depletion can be attributed to the formation of a steady-state concentration profile.

We reported earlier[2] that for cation-exchange membranes, noise was not measurable until the critical current density was exceeded.

In addition a time lag for the appearance of noise was observed. These observations suggested that the observed cation noise was dependent on the formation of a depletion layer. The time lag observed in the voltage–time curves makes the relation even more obvious. The voltage–time curves at different distances from the membrane (Figure 2) and the voltage and noise with distance curves (Figure 4) show that the region of interest lies within 40 μm of the membrane surface. The fact that some of the secondary voltage changes referred to previously are cut off at 40 μm suggests that the concentration gradient extends beyond this distance. The sharp drop in voltage from a distance of 40 μm to the membrane surface shows that most of the voltage drop measured is across the depleted region and not across the membrane itself.

The behavior of noise with distance is interesting (Figure 4). The noise level rises sharply when the electrode contacts the membrane. This may be the result of contact noise or the diminishing of an internal resistance that was causing power dissipation. The former should give a step function response at the point of contact, whereas the latter should give a continuous first derivative of the noise–distance curve. Our micromanipulator was not sensitive enough to make this distinction.

The HCl power spectra were of considerable interest. The two intersecting lines of approximately ω^{-2} and ω^{-4} dependence resembled a normal relaxation spectrum passing through a low pass filter. When the point of intersection (obtained by extrapolation) was plotted against current density a linear relationship was obtained (Figure 6).

$$J = \varkappa f + \beta \qquad (1)$$

where f is the frequency at the point of intersection, J is the current density, $\varkappa$ is the slope, and β is the intercept.

Experimentally $\varkappa f$ is not observable when the current falls below the critical current density. This suggests that $\varkappa f$ is the added flux due to water dissociation and

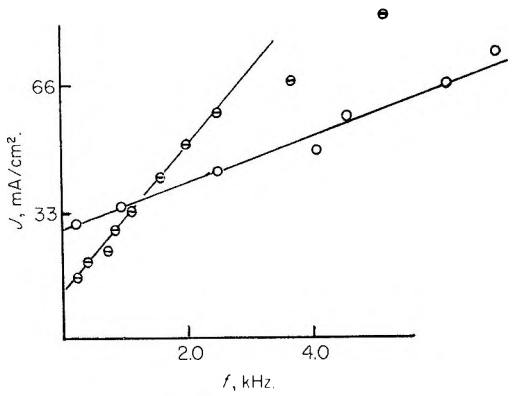

Figure 6. Plot of $J = \varkappa f + \beta$ (eq 1), where f is frequency where the power spectrum slope in Figure 6 changes: O, 0.050 M HCl, 30°; ⊖, 0.025 M HCl, 30°.

β is the flux due to the diffusion of HCl. Then β must be of the form[10]

$$\beta = -FD\frac{\partial C}{\partial X} \tag{2}$$

where D is the coefficient of diffusion given by $(\mu_{H^+} - \mu_{Cl^-})\frac{kT}{e}/(\mu_{H^+} + \mu_{Cl^-})$,[11] F is Faraday's constant, and C is the concentration. The values of the mobilities, μ, for the temperatures of interest are given in Table I.

Table I: Mobilities Calculated from Diffusion Activation Energies Cited in Ref 12 in m²/V Sec

$D = D_0 \exp(-E_a/RT)$

$D_0(H^+)$	$= 22.17 \times 10^{-7}$ m²/sec	$E_a(H^+)$	= 3.230 kcal
$D_0(OH^-)$	$= 23.89 \times 10^{-7}$ m²/sec	$E_a(OH^-)$	= 3.610 kcal
$D_0(Cl^-)$	$= 25.40 \times 10^{-7}$ m²/sec	$E_a(Cl^-)$	= 4.220 kcal

Temp, °K	μ_{H^+} (× 10⁸)	μ_{OH^-} × 10⁸	μ_{Cl^-} × 10⁸
292	33 58	18.47	6.978
303	39 56	22.33	9.728
313	45.53	26.19	10.61
322	51.84	30.40	12.68

The mobilities were calculated from the activation energies cited by Longsworth.[12]

Since μ_{H^+} is about 5 times as large as μ_{Cl^-} the term $(\mu_{H^+}\mu_{Cl^-})/(\mu_{H^+} + \mu_{Cl^-})$ can be approximated roughly by μ_{Cl^-}. The β can be written in the form

$$\beta = \beta_0 \exp(-E_a/RT) \tag{3}$$

where E_a is the activation energy of the mobility of the chloride ion. The plot ln β *vs.* $1/T$ is given in Figure 7. Values for E_a of 3.8 ± 0.8 kcal were obtained which can be compared to 4.22 kcal reported in the literature.[12]

$\varkappa$ has the dimensions of C/m² which is a surface charge density term. The plot of ln $\varkappa$ *vs.* $1/T$ can be seen in Figure 8 to be an approximate straight line

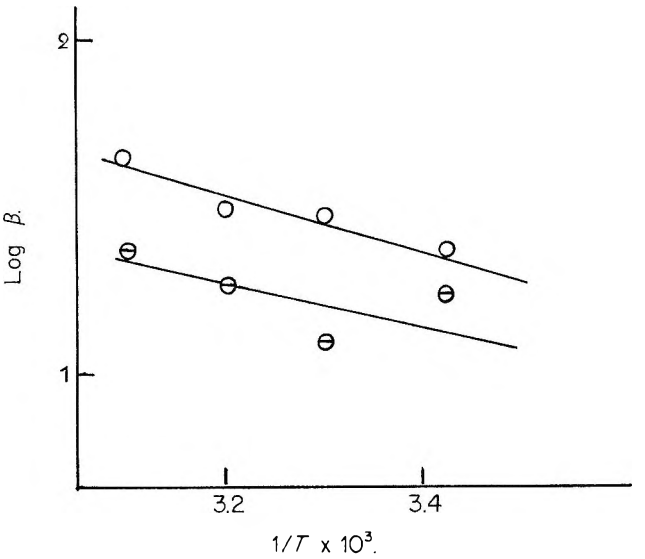

Figure 7. Plot of log β *vs.* $1/T$; here β is defined by eq 1: O, 0.050 M HCl, MC 3235; ⊖, 0.025 M HCl, MC 3235.

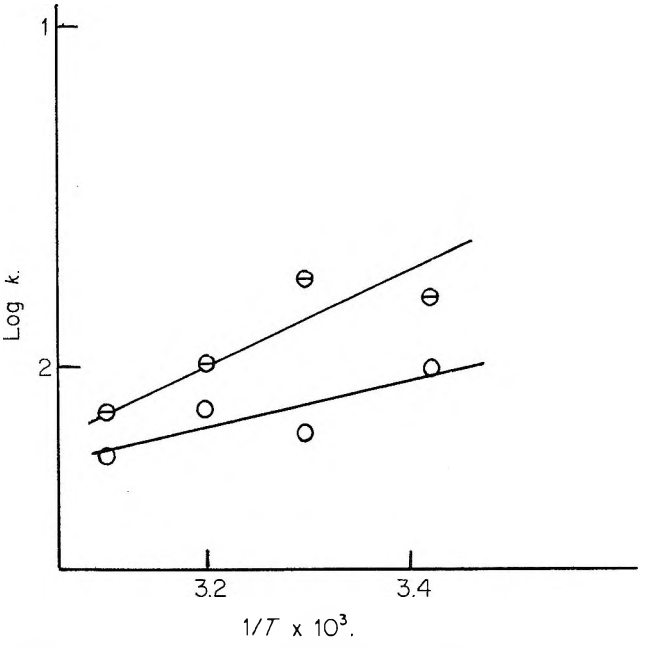

Figure 8. Plot of ln $\varkappa$ *vs.* $1/T$, where $\varkappa$ is defined by eq 1: O, 0.050 M HCl, MC 3235; ⊖, 0.025 M HCl, MC 3235.

with slopes of 1.9×10^3 and 3.3×10^3 for 0.050 and 0.025 M HCl, respectively.

Since flux is the product of conductivity and the electric field, $\varkappa f$ and β can be expressed in the following form

$$\varkappa f = C_{OH^-}(\mu_{H^+} + \mu_{OH^-})FE \tag{4}$$

$$\beta = C_{Cl^-}(\mu_{H^+} + \mu_{Cl^-})FE \tag{5}$$

(10) H. S. Harned and B. B. Owen, "The Physical Chemistry of Electrolyte Solutions," 3rd ed, Reinhold, New York, N. Y., 1958, p 118.

(11) See ref 10, p 120.

(12) L. G. Longsworth, "Electrochemistry in Biology and Medicine," T. Shedlovsky, Ed., Wiley, New York, N. Y., 1956, p 225.

where C's are the concentrations, μ's are the mobilities, F is Faraday's constant, and E is the electric field in V/m. Values of κ and β are given in Table II.

Table II: Values of κ and β at Various Temperatures and Concentrations

Concn, M	Temp, °K	κ, C/m²	β, A/m²
0.050	292	0.096	230
0.050	303	0.062	290
0.050	313	0.073	310
0.050	322	0.054	430
0.025	292	0.153	168
0.025	303	0.177	118
0.025	313	0.099	176
0.025	322	0.072	227

By applying Onsager's equation for the field dissociation of weak electrolytes to water, the three variables C_{OH^-}, C_{Cl^-}, and E can be determined.

Onsager's equation[13] is given by $K_w = K_0F(b)$ where K_0 is the dissociation constant in the absence of an external electric field. $F(b)$ and b have the form

$$F(b) = 1 + b + b^2/3 + b^3/18 + b^4/180 + \ldots \quad (6)$$

where

$$b = \frac{9.636 \times 10^{-12}E}{DT^2}$$

D is the dielectric constant, T is the absolute temperature, and E is the electric field in V/m.

The values of $F(b)$ and therefore K_w at various values of E were determined from eq 6. The flux due to water dissociation corresponding to E was determined from K_w and β

$$K_w = C_{H^+}C_{OH^-} = (C_{Cl^-} + C_{OH^-})C_{OH^-} \quad (7)$$

The OH^- concentration is given by

$$C_{OH^-} = \frac{-\beta}{2F(\mu_{H^+} + \mu_{Cl^-})E} + \sqrt{\left(\frac{\beta}{2F(\mu_{H^+} + \mu_{Cl^-})E}\right)^2 + K_w} \quad (8)$$

The values of E corresponding to the various values of f can be determined by dividing J_{diss} by κ where J_{diss}, the flux due to water dissociation, is given by

$$J_{diss} = \kappa f = C_{OH^-}FE(\mu_{H^+} + \mu_{OH^-}) \quad (9)$$

The effect of E on f at various temperatures can be seen in Table III.

It was assumed earlier that f is a function of the rate constants of the process. The rate constant k is given by

$$k = k_0 \exp\left(-\frac{E_a - E_{el}}{RT}\right) \quad (10)$$

Table III: The Values for f for Various Temperatures and Concentrations of HCl at a Field of 3.16×10^7 V/m[a]

Concn	Temp, °K	f, H_2
0.050	292	689
0.050	303	2453
0.050	313	4133
0.050	322	8994
0.025	292	524
0.025	303	1219
0.025	313	3619
0.025	322	8020

[a] Values were obtained *via* eq 4–9.

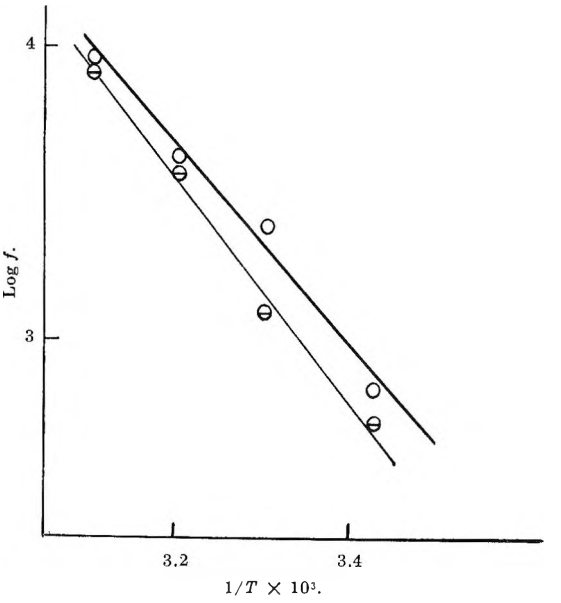

Figure 9. Log f *vs.* $1/T$ at a constant electric field strength of 3.16×10^7 V/m. Equation 1 defines f. ○, 0.050 M HCl; ⊖, 0.025 M HCl. See Table III.

where E_a is the activation energy and E_{el} is the energy due to the electric field.

Assuming that the activation energy is field independent its value can be obtained by finding $\partial \ln f/(\partial\, 1/T)$ at a constant value of E.

The linear plots for two different concentrations, 0.050 and 0.025 M HCl, can be seen in Figure 9 at a field of 3.16×10^7 V/m. Values of -15.5 and -17.3 kcal were obtained for 0.050 and 0.025 M, respectively.

Before any models can be proposed another factor must be considered. The power spectrum of a single relaxation process has the form[14]

$$G(\omega) = \frac{\tau}{1 + \omega^2\tau^2}$$

(13) L. Onsager, *J. Chem. Phys.*, **2**, 599 (1934).

(14) (a) K. M. van Vliet and J. R. Fasset, "Fluctuation Phenomena in Solids," R. E. Burgess, Ed., Academic Press, New York, N. Y., 1965, p 267 ff; (b) M. Lax, *Rev. Mod. Phys.*, **32**, 25 (1960).

Table IV: Slopes of the HCl Spectra in Terms of d(log power)/d(log f) (α and γ are the First and Second Slopes of Figure 5, Respectively, and Are Functionally Defined by Eq 11)

Concn, M	Temp, °K	J, mA/cm²	α	γ
0.050	292	22	2.7	5.1
0.050	292	28	2.3	4.7
0.050	292	41	2.4	4.3
0.050	292	50	2.2	4.5
0.050	292	67	2.3	3.6
0.050	292	74	2.2	3.4
0.050	303	31	2.5	5.0
0.050	303	35	2.0	5.0
0.050	303	44	2.4	4.2
0.050	303	50	2.6	4.5
0.050	303	57	2.6	4.5
0.050	303	67	2.5	3.8
0.050	303	75	2.4	3.7
0.050	313	33	2.0	4.7
0.050	313	42	2.2	4.5
0.050	313	50	2.6	4.0
0.050	313	60	2.5	4.0
0.050	313	75	2.3	3.6
0.050	322	34	2.4	4.7
0.050	322	50	2.0	3.9
0.050	322	62	2.5	4.2
0.050	322	75	2.5	4.2
0.025	292	20	2.7	4.6
0.025	292	23	2.9	4.6
0.025	292	28	2.9	4.1
0.025	292	33	2.8	4.7
0.025	292	42	2.9	4.6
0.025	292	50	2.8	4.7
0.025	292	59	2.4	5.0
0.025	292	67	2.2	4.8
0.025	292	84	2.5	4.4
0.025	303	16	2.2	4.7
0.025	303	18	1.9	5.0
0.025	303	23	2.5	5.0
0.025	303	28	2.2	5.0
0.025	303	33	2.2	4.7
0.025	303	42	2.1	4.5
0.025	303	50	2.1	4.3
0.025	303	59	2.2	4.5
0.025	303	67	2.4	5.0
0.025	303	84	2.4	4.7
0.025	313	18	1.9	4.0
0.025	313	25	1.9	4.5
0.025	313	30	1.9	4.7
0.025	313	35	2.1	4.7
0.025	313	47	2.3	4.6
0.025	313	59	2.4	3.8
0.025	313	75	2.4	3.8
0.025	322	31	2.2	4.0
0.025	322	31	2.2	4.0
0.025	322	29	1.9	4.3
0.025	322	33	2.8	4.5
0.025	322	40	2.6	4.5
0.025	322	52	2.6	4.5
0.025	322	62	2.5	4.1
0.025	322	75	2.4	3.8

where ω is the angular frequency $2\pi f$. The experimental power spectra have the form

$$G(\omega) = \frac{\text{constant}}{A\omega^{\alpha} + \beta\omega^{\gamma}} \tag{11}$$

where A and B are constants and α and γ have values of about 2.3 and 4.5, respectively. The experimental values for α and γ are given in Table IV. (The observed variation of α and γ with temperature, and of α with current density, is within experimental error.)

Theoretical Models. Several mechanisms based on the assumption that the sudden change in the slope of the power spectra signified a relaxation time were examined.

(*a*) *Space Charge Relaxation.* Space charge relaxation is given by[15]

$$\tau = \frac{\epsilon}{\sigma} \tag{12}$$

where τ is the relaxation time, ϵ is the permittivity of the medium, and σ is the conductivity given by

$$\sigma = F\sum C_i\mu_i \tag{13}$$

The symbols F, C_i, and μ_i represent Faraday's constant and the concentration and mobility of the ith ionic species, respectively. In this case three ions, H^+, OH^-, and Cl^-, are present.

The conductivity can be divided into two parts

$$\sigma = \sigma_{\text{diss}} + \sigma_{\text{HCl}} \tag{14}$$

where σ_{diss} is the conductivity due to water dissociation products and σ_{HCl} is the conductivity due to HCl. The former was obtained from eq 6 for various electric field strengths (Table III) and the latter from $\sigma_{\text{HCl}} = \beta/\epsilon$ where β is the intercept in eq 1. The bulk permittivity of water was used for ϵ. When these values were used it was found that the space charge relaxation time had a maximum that was shorter than the longest time observed experimentally.

(*b*) *Water Dissociation and Recombination.* The relaxation time of a small displacement from equilibrium of water dissociation is given by[16]

$$\tau = \frac{1}{k_d + k_R(C_{H^+} + C_{OH^-})} \tag{15}$$

However, this relaxation time cannot be assigned arbitrarily when the water dissociation is accompanied by other transport processes. The correct expression for the relaxation time must be derived from the solution of the transport equation under the proper boundary conditions.[14] Eigen and DeMaeyer[17] have found for a narrow layer of aqueous solution between two

(15) D. Corson and P. Lorraine, "Introduction to Electromagnetic Fields and Waves," W. H. Freeman, San Francisco, Calif., 1962, p 191.

(16) M. Eigen and L. DeMaeyer, "Techniques of Organic Chemistry," Vol. VIII, Part 2, A. Weissberger, Ed., Interscience, New York, N. Y., 1963, p 902.

(17) M. Eigen and L. DeMaeyer, *Z. Elektrochem.*, **60**, 1037 (1956).

electrodes (symmetric case: both ions have equal mobility) that the electrical flux is given by

$$J = Ak_d(0)F(b) \quad (16)$$

where A is a constant, k_d (0) is the dissociation rate constant at zero external field, and F(b) was defined earlier (eq 6). Then a power spectrum can be calculated from the correlation function derived from (16) using the Wiener–Khintchine theorem.[18] This should give a relaxation time that would be a function of the reciprocal of $k_d(0)F(b)$.

A direct comparison of eq 16 with the empirical relation $J_{diss} = \varkappa f$ (eq 1) shows that f is proportional to $k_d(0)F(b)$ and a plot of log f *vs.* $1/T$ should give the activation energy of $k_d(0)F(b)$. The observed value of 16.4 ± 0.9 kcal/mol is consistent with this.

The symmetric boundary condition used by Eigen and DeMaeyer (cation concentration zero at the cathode, anion concentration zero at the anode) may be approximately fulfilled by $C_{H^+} = 0$ at the membrane, $C_{OH^-} = 0$ at the solution side of the depletion layer. However, the symmetry requirement may not be satisfied, since there can be a surface charge at the membrane surface which is not matched at the solution side.

A complete solution to the problem would require, then, that the set of equations proposed by Eigen and DeMaeyer (Poisson equation, chemical equilibrium, continuity equation, and ion flux) be solved under appropriate boundary conditions. This would then have to produce the necessary form for the noise spectra. Given any linearized form for the transport equations, together with suitable boundary conditions, it is possible to compute noise spectra.[14] However, we are not aware of noise spectra as steep as those found experimentally here. (It is possible that the fluctuations, which range to 10 mV, cannot be treated in a linear manner in any case. If the decay of a fluctuation is slower than a simple exponential, the steep noise spectra could be expected. This appears possible in the context of water dissociation and the associated transport phenomena.) Under the circumstances we believe that a complete treatment of the transport equations expected near the membranes is warranted, and such work has been begun.

One more possibility must be considered. If there is a simple, single relaxation phenomenon, its noise, passed through a single stage low pass filter, would produce results similar to those observed. Various tests were done using white noise, externally supplied, as a test probe. We were unable to find evidence for the existence of such a filtering effect, but could not eliminate one final possibility. Figure 10 shows a possible equivalent circuit for such a filter and noise source, consistent with the tests made with the external white noise source. The noise source is represented by the symbol —⊜— with an internal resistance represented by R_1. The required capacitance is labeled C. These units are located in the narrow layer within 40 μm of the membrane surface where the HCl depletion is most severe and where the field-dependent water dissociation occurs. Outside this layer lies the larger region where the concentration gradient of HCl is found. The resistance of this region, represented by R_2, is much larger than R_1. This would explain why the filter could not be detected by a current source white noise fed through the probes. The overall impedance is dominated by R_2 which is frequency independent. This could also explain the voltage *vs.* distance and noise *vs.* distance curves of Figures 2 and 4. As electrode 2 moves toward the membrane, R_2 is gradually bypassed, thereby cutting off the secondary voltage changes associated with the formation of a steady-state concentration gradient (Figure 2). The overall voltage between the inner electrodes would fall sharply as the electrode bypassed R_2, and simultaneously the noise would increase since the dissipating resistance has been removed (Figure 4). This appears to be consistent with the results.

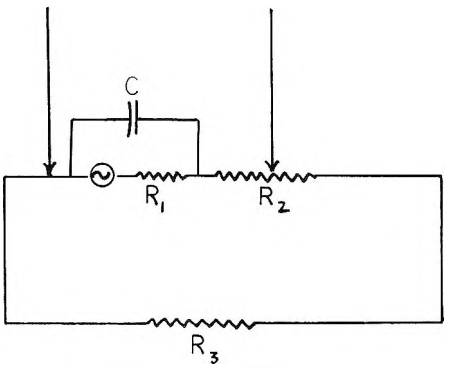

Figure 10. A possible equivalent circuit for the noise source. Arrows represent the probe microelectrodes: —⊜—, noise source; R_1, resistance of the depleted layer; C, capacitance in parallel with the noise source; R_2, resistance of the layer where the concentration gradient is found; R_3, the sum of all other resistances in the circuit.

The greatest difficulty is encountered when the requirements of the capacitance are evaluated. Estimates can be made using a parallel plate model given by

$$C = \frac{\epsilon A}{X} \quad (17)$$

where ϵ, A, and X are the permittivity, area, and plate separations, respectively. In addition

$$C = \frac{1}{2\pi Rf} \quad (18)$$

where R is the resistance R_1 of Figure 10 and f is less than 10 sec^{-1}, the turnover frequency required for the

(18) C. Kittel, "Elementary Statistical Physics," Wiley, New York, N. Y., 1958.

filter. The resistance, R_1, can be calculated from the equation

$$J = \sigma E \tag{19}$$

where σ is the specific conductivity. This gives the form

$$R = \frac{1}{\sigma}\frac{X}{A} \tag{20}$$

to give an equation for the permittivity

$$\epsilon = \frac{J}{2\pi f E} \tag{21}$$

Setting f at 10 sec^{-1}, E at 4×10^7 V/m, which sets J at 300 A/m^2, ϵ is found to be 1.2×10^{-7} F/m. This gives a dielectric constant of the order of 1.4×10^4 which is 170 times that of water.

It should be mentioned that high dielectric constants have been observed for polyelectrolyte solutions, *e.g.*, 1200 for DNA.[19] The very large polarizability required for values of this magnitude have been interpreted in terms of polarization of the ionic atmosphere of the rod-like polyelectrolyte.[20] The bulk of our ion-exchange membrane matrix cannot be made to fit this description. However, it is possible that loose ends of polysulfonates may exist at the membrane surface that could be polarized and stretched into the depleted layer where the very high field strength is found. Whether this condition could result in extremely high permittivity remains to be seen.

Summary

The electrical phenomena associated with transport of HCl through a cation-exchange membrane, including noise spectra, have been measured at high currents. The noise is generated very close to the membrane–solution boundary, and some possible explanations are considered.

(19) S. Takashima, *J. Mol. Biol.*, **1**, 455 (1963).

(20) J. P. McTague and J. H. Gibbs, *J. Chem. Phys.*, **44**, 4295 (1966).

Ion-Pair Formation and the Theory of Mutual Diffusion in a Binary Electrolyte

by M. J. Pikal

Department of Chemistry, University of Tennessee, Knoxville, Tennessee 37916 *(Received June 3, 1970)*

Publication costs borne completely by The Journal of Physical Chemistry

A theory of mutual diffusion in a binary electrolyte is developed using the conventional charged sphere-in-continuum model. However, instead of approximating the Boltzmann exponential by a truncated power series, the calculations are performed retaining the full Boltzmann exponential. As a result of this procedure, a term representing the effect of ion-pair formation appears in the theory as a natural consequence of the electrostatic interactions. The mobility of an ion pair is not an adjustable parameter but is determined by the theory. The theory is developed in terms of a power series in concentration and includes terms of order $c^{3/2}$, $c^{3/2} \log c$, and lower order terms. For the case of symmetrical electrolytes, the theory is in excellent agreement with experimental data. In the case of unsymmetrical electrolytes, theory and experiment are not in agreement. The latter result is taken as evidence that, *for unsymmetrical electrolytes* the "error" due to the incompatibility of the Boltzmann exponential with linear superposition of fields is more serious than the "error" which is introduced by using the truncated power series. Also, it is concluded that the diffusion theory is consistent with Bjerrum theory of ion-pair formation, but not consistent with the "contact" model. However, the diffusion theory does not seem consistent with the procedure of substituting the Bjerrum distance parameter for the contact parameter a.

I. Introduction

The first attempt to obtain a theory of the Fick's law mutual diffusion coefficient, D_v, based on the Debye–Hückel ion atmosphere model is contained in the classic 1932 paper of Onsager and Fuoss.[1] In this paper, we consider the extension of the Onsager–Fuoss theory to include, as a natural consequence of electrostatic interaction, the effect of electrostatic ion-pair formation.

We have three main objectives: (1) to demonstrate that the use of the complete Boltzmann exponential leads naturally to a term representing ion-pair formation, (2) to study the linear superposition–Boltzmann exponential problem, and (3) to provide an extended diffusion theory for use in future calculation of the Onsager coefficients, l_{ij}. We now proceed to a more detailed discussion of these objectives.

The Onsager–Fuoss theory leads to the correct limiting value of D_v, a result which is independent of any molecular model,[2] and also predicts that, in most dilute electrolytes, the ratio, $D_v/(1 + m\ \mathrm{d}\ \ln\ \gamma/\mathrm{d}m)$, should increase slightly with increasing concentration. Here, γ is the mean molal activity coefficient and m is the molality.

The experimental studies by Harned and coworkers[3] showed that data on dilute aqueous 1–1 electrolyte systems were consistent with the Onsager–Fuoss theory. However, in the case of aqueous 2–2[4a,b] electrolytes, significant deviations from the Onsager–Fuoss theory were observed. This deviation was attributed to the formation of ion pairs, and when the mobility of an ion pair was introduced as an adjustable parameter, reasonable agreement between theory and experiment resulted. However, if the ion pairs are formed by electrostatic interactions, a theory which calculates the effect of ion–ion interactions should include, as a direct result of this theory, a term which has its physical origin in ion-pair formation.[5] Thus, the mobility of the ion pair should be determined by the basic assumptions of the theory.

The failure of the Onsager–Fuoss theory to lead to an "ion-pair term" is likely due to the approximation made when the Boltzmann exponential was approximated by the first three terms of a series expansion, *i.e.*

$$n_{ji} = n_i \exp(-E_{ji}/kT) \approx n_i[1 - E_{ji}/kT + {}^1/_2(E_{ji}/kT)^2] \quad (1)$$

where n_{ji} is the local concentration of i ions near a reference j ion, n_i is the bulk concentration of i ions, E_{ji} is the energy of an i ion near the reference j ion, k is Boltzmann's constant, and T is the absolute temperature. The exponential expression is the Boltzmann distribution, while the approximation indicated is the truncated series approximation used by Onsager and

(1) L. Onsager and R. M. Fuoss, *J. Phys. Chem.*, **36**, 2689 (1932).

(2) D. G. Miller, *ibid.*, **71**, 616 (1967).

(3) See H. S. Harned and R. M. Hudson, *J. Amer. Chem. Soc.*, **73**, 652 (1951).

(4) (a) H. S. Harned and R. M. Hudson, *ibid.*, **73**, 3781 (1951); (b) H. S. Harned and R. M. Hudson, *ibid.*, **73**, 5880 (1951).

(5) R. M. Fuoss and L. Onsager, *J. Phys. Chem.*, **66**, 1722 (1962).

Fuoss. For configurations where the distance separating a cation and an anion is on the order of ionic diameters (*i.e.*, for "ion pairs"), $E_{ji}/kT > 1$ and the series approximation is not valid.

Physically, the truncation approximation ignores close range electrostatic interactions, and therefore one cannot expect ion-pair formation to be predicted by the Onsager–Fuoss theory. Thus, if the full Boltzmann exponential is retained in the development of a diffusion theory, one might expect ion-pair formation to be a natural result of the theory. We note that the theoretical result for equivalent conductance does not contain an ion association term if the Boltzmann exponential is truncated. However, use of the full exponential results in a term interpretable as an association term.[6,7] Our first objective will be to show that using the full Boltzmann exponential in a *diffusion* theory leads to an association term.

Concerning our second objective, we note that the full Boltzmann exponential is not consistent with the principle of linear superposition of ionic fields, which is an approximation also used in the theory. Thus, while the full Boltzmann exponential eliminates the "error" introduced by truncating the exponential series, the physical inconsistency thereby introduced must correspond to the introduction of another "error." Whether or not retaining the full exponential results in a net improvement is a question which can perhaps best be answered by a comparison between the resulting theory and experiment.

Theoretical studies of equivalent conductance,[6,7] and activity coefficients[8] in symmetrical electrolytes suggest that in symmetrical electrolyte systems where ion-pair formation would be expected, inclusion of the full exponential is a better approximation than truncating the series. However, the incompatibility of the Boltzmann exponential with the linear superposition of fields is expected to be more serious in the case of unsymmetrical electrolytes.[9] Thus the effect of retaining the full exponential remains an open question for unsymmetrical electrolytes. Since it is, mathematically, not necessary to restrict the diffusion theory to symmetrical electrolytes, the results of this research offer an opportunity to study the "linear superposition–Boltzmann exponential" problem in unsymmetrical electrolytes. Such a study is our second objective.

Our third objective concerns the need for an extended diffusion theory for use in a different theoretical problem. Recent interest in the Onsager transport coefficients,[2,10–12] l_{ij}, has made it desirable to obtain theoretical expressions for the l_{ij} based on the "ion atmosphere" model. The limiting law expressions for the l_{ij} can be obtained quite easily from equations given by Onsager and Fuoss.[1] This has been accomplished.[13] However, it is also of interest to evaluate the contribution of terms of higher order in concentration than $c^{1/2}$. In particular, the contribution of ion-pair formation to the l_{ij} is of interest since this information is important in establishing a detailed physical interpretation of the l_{ij}.

Miller[10] has shown that values of l_{ij} may be calculated from a knowledge of equivalent conductance, transference numbers, and thermodynamic diffusion coefficients (defined by eq 5). Therefore, theoretical expressions for l_{ij} may be derived by combining theories of equivalent conductance, transference numbers, and diffusion, if these theories are mutually consistent in their approximations.

Two theories of conductance in symmetrical electrolytes have been developed using the full Boltzmann exponential,[6,7] and a corresponding transference number theory may be obtained from the theoretical equations leading to the final conductance expression. Both conductance theories result in a term which may be interpreted as reflecting the phenomenon of ion-pair formation. However, the "ion-pair terms" differ in detail. Thus, the third purpose of this research is to provide an extended diffusion theory for use in calculating the l_{ij}, *and* to determine which conductance theory is most consistent with the extended diffusion theory. Also, since the extended diffusion theory turns out to be rather complex in form, a simplified approximate form will be developed which is more suitable for the calculation of the l_{ij}. The theory of the l_{ij}, as described above, is now complete and will be the subject of a later paper.

To best satisfy the above objectives, the diffusion theory developed here corresponds to retaining all terms of order c which are consistent with the mathematical model. In addition, the largest higher order terms are retained.

II. Theory of Mutual Diffusion

1. Preliminary Considerations. In an electrolyte containing only two kinds of ions, the condition of zero current flow requires that both ions move with the same velocity. Thus, the ion atmosphere of a given ion is displaced as a whole and develops no asymmetry. Thus, the relaxation effect, which plays an important role in the theory of conductance, is absent in the theoretical discussion of diffusion in binary electrolytes.[1] However, the electrophoretic effect is present in binary diffusion.

(6) R. M. Fuoss, L. Onsager, and J. F. Skinner, *J. Phys. Chem.*, **69**, 2581 (1965).

(7) D. Kremp, W. D. Kraeft, and W. Ebeling, *Ann. Phys. (Leipzig)*, **18**, 246 (1966).

(8) E. A. Guggenheim, *Trans. Faraday Soc.*, **56**, 1152 (1960).

(9) R. H. Stokes, *J. Amer. Chem. Soc.*, **75**, 4563 (1953).

(10) D. G. Miller, *J. Phys. Chem.*, **70**, 2639 (1966).

(11) R. Haase and J. Richter, *Z. Naturforsch. A*, **22**, 1761 (1967).

(12) H. S. Dunsmore, S. K. Jalota, and R. Paterson, *J. Chem. Soc. A*, 1061 (1969).

(13) (a) M. J. Pikal, unpublished research; (b) H. Schönert, *Z. Phys. Chem.*, **51**, 196 (1966); (c) J. Rastas, *Acta Polytech., Scand. Chem. Incl. Met. Ser.*, **50** (1966).

The electrophoretic effect is a hydrodynamic effect which is due to a local volume force in the liquid surrounding an ion. Thus, a given ion does not move with respect to a medium at rest, but due to the presence of the ion atmosphere, migrates in a medium which is itself in motion. For convenience we shall consider the one-dimensional case. The final result for the diffusion coefficient is equally applicable in three dimensions. The absolute velocity of a j ion may be written as a sum of two terms, where for K_j in one dimension

$$v_j = K_j\omega_j + \Delta v_j \tag{2}$$

where Δv_j is the velocity of the liquid surrounding the j ion, which is due to the presence of its ion atmosphere. K_j is the thermodynamic force on the ion and is given by the negative gradient of the electrochemical potential

$$K_j = -\frac{\mathrm{d}\mu_j^c}{\mathrm{d}x} + e_j\frac{\mathrm{d}\phi}{\mathrm{d}x} \tag{3}$$

where μ_j^c is the chemical potential and ϕ is the electrical potential. In diffusion, ϕ is the diffusion potential or potential due to the space charge, which is caused by unequal ionic mobilities, ω_j. In the model used here, the ionic mobilities, ω_j, are independent of composition and may be written in terms of the limiting ionic conductances, λ_i^0

$$\omega_i = \frac{\lambda_i^0 C \times 10^{-8}}{Fe|z_i|} \tag{4}$$

where C is the speed of light in cm/sec, F is Faraday's constant in coulombs, and $e|z_i|$ is the absolute value of the charge in the ion in esu.

Thus, the evaluation of the electrophoretic correction, Δv_j, is the central problem in a theory of diffusion in binary electrolytes. Once Δv_j is determined, one may easily calculate the thermodynamic diffusion coefficient, L, defined by[10]

$$J_L = -L\frac{\mathrm{d}\mu_{12}}{\mathrm{d}x} = LK \tag{5}$$

where J_L is the flux of solute relative to the solvent, μ_{12} is the chemical potential of the solute as a whole, and $K = \mathrm{d}\mu_{12}/\mathrm{d}x$.

The relationship between L and the commonly reported volume fixed diffusion coefficient, D_v, is given by[10]

$$\frac{L}{c} = \frac{D_v}{10^3RT\nu(1 + m\,\mathrm{d}\ln\gamma/\mathrm{d}m)} \tag{6}$$

where the units of L are mol^2 joules^{-1} cm^{-1} sec^{-1} and the units of D_v are cm^2 sec^{-1}. The symbol ν is the number of ions formed upon complete ionization of one solute "molecule," and R is the gas constant in joules. The concentration in mol/l. is given the symbol, c, and m is the molality. These units correspond to a flux in moles cm^{-2} sec^{-1} and a force in joules mol^{-1} cm^{-1}. For the theoretical development, it is more convenient to choose the flux units as solute "molecules"/cm^2 sec and the units of μ_{12} as ergs per solute "molecule."

Since $J_L = nv$, where n is the number of solute "molecules"/cm^3 and v is the common ionic velocity, we may write

$$\tilde{L} = n(K/v)^{-1} \tag{7}$$

where $\tilde{L}$ in (number of solute molecules)^2 erg^{-1} cm^{-1} sec^{-1} refers to the thermodynamic diffusion coefficient consistent with the above units. Thus, the problem is to determine the ratio, K/v.

From eq 2, we may express the ionic thermodynamic force in terms of the common ionic velocity and the electrophoretic correction

$$K_j = \rho_j v(1 - \Delta v_j/v) \tag{8}$$

where $\rho_j = 1/\omega_j$. The chemical potential of the solute, μ_{12}, is defined in terms of the chemical potential of the ions, $\mu_{12} \equiv \nu_1\mu_1^c + \nu_2\mu_2^c$, where ν_i are the stoichiometric coefficients for ionization. Using this definition and eq 2, we have

$$-\frac{\mathrm{d}\mu_{12}}{\mathrm{d}x} = K = \nu_1K_1 + \nu_2K_2 \tag{9}$$

From eq 8 and 9 it follows that

$$\frac{K}{v} = \nu_1\rho_1 + \nu_2\rho_2 - [\nu_1\rho_1(\Delta v_1/v) + \nu_2\rho_2(\Delta v_2/v)] \tag{10}$$

2. Electrophoretic Correction. We will now consider the theoretical calculation of the electrophoretic correction. If the forces on the ions are K_i, the total force per unit volume is $\sum_i n_iK_i$. This force is transmitted to the solvent molecules, and if we write n_0K_0 for the total force on the solvent molecules, the condition of mechanical equilibrium requires[14]

$$n_0K_0 + \sum_{\sigma=i,j} n_\sigma K_\sigma = 0 \tag{11}$$

Equation 11 is essentially the Gibbs–Duhem equation, and it states that there is no average net macroscopic force per unit volume.

Now, consider an element of volume $\mathrm{d}V_j$ at distance r from a j ion. Here the local concentration of i ions, n_{ji}, is not the same as the macroscopic average, n_i, since the presence of the j ion alters the local concentrations. The force on the solvent in $\mathrm{d}V_j$ remains $n_0K_0\mathrm{d}V_j$, however. Thus, the net force on the element of volume $\mathrm{d}V_j$ is given by

$$\left(\sum_\sigma n_{j\sigma}K_\sigma + n_0K_0\right)\mathrm{d}V_j = \sum_\sigma (n_{j\sigma} - n_\sigma)K_\sigma\,\mathrm{d}V_j \tag{12}$$

With $\mathrm{d}V_j$ in spherical coordinates, the force acting on

(14) D. D. Fitts, "Non-Equilibrium Thermodynamics," McGraw-Book Co., Inc., New York, N. Y., 1962.

a spherical shell of thickness dr around the reference ion, j, is given by

$$dF_j = \sum_\sigma K_\sigma(n_{j\sigma} - n_\sigma)(4\pi r^2\, dr) \quad (13)$$

This force is uniformly distributed over the shell, and hydrodynamically the situation is the same as if the force were acting on a solid sphere of radius r moving through a medium of vicosity η.[1,15] Since the ion atmosphere is symmetric, we may apply Stokes' equation to determine the velocity imparted to the shell by this force and find[16]

$$dv_j = dF_j/6\pi\eta r = (^2/_3\eta)\sum_\sigma K_\sigma(n_{j\sigma} - n_\sigma)r\, dr \quad (14)$$

To evaluate the velocity increment imparted to the reference ion by all the ions present in the atmosphere, we simply integrate eq 14 from the ionic separation at contact, a, to infinity and obtain

$$\Delta v_j = (^2/_3\eta)\sum_\sigma K_\sigma n_\sigma \int_a^\infty (n_{j\sigma}/n_\sigma - 1)r\, dr \quad (15)$$

To perform the indicated integration in eq 15, we must obtain the equilibrium ionic distribution, $n_{j\sigma}$, as a function of r. As previous workers have done,[1,6,17] we shall use the Boltzmann distribution and the approximation that the average energy of a σ ion in the presence of a j ion, $E_{j\sigma}$, is given by[18] $E_{j\sigma} = e_\sigma\psi_j^0$, thus giving

$$n_{j\sigma} = n_\sigma \exp(-e_\sigma\psi_j^0/kT) \quad (16)$$

where e_σ is the charge and ψ_j^0 is the average electrical potential at distance r from the reference j ion. For the potential, we shall use the usual Debye–Hückel approximation, as did Onsager and Fuoss[1]

$$\psi_j^0 = \frac{e_j}{D}\frac{e^{\kappa a}}{1+\kappa a}\frac{e^{-\kappa r}}{r} \equiv (e_j/D\mu)(e^{-\kappa r}/r) \quad (17)$$

where D is the dielectric constant of the medium and κ is defined by

$$\kappa^2 = (4\pi/DkT)e^2(n_1z_1^2 + n_2z_2^2) \quad (18)$$

It may appear inconsistent to use the Debye–Hückel potential, when we are attempting a solution of Δv_j correct to order c, instead of the more accurate (and more complex) potential found by Fuoss and Onsager for symmetrical electrolytes.[19] However, preliminary calculations have shown that the final results are identical up to and including terms of order c using either potential.

Combining eq 15, 16, and 17, we may write

$$\Delta v_j = (^2/_3\eta)\sum_\sigma K_\sigma n_\sigma \int_a^\infty [\exp(\beta_{\sigma j}e^{-\kappa r}/r) - 1]r\, dr \quad (19)$$

where

$$\beta_{\sigma j} \equiv -e_\sigma e_j/DkT\mu \quad (20)$$

If the exponential in eq 19 is expanded into a power series, eq 19 may be written in the form

$$\Delta v_j = (^2/_3\eta)\sum_\sigma K_\sigma n_\sigma\beta_{\sigma j}\int_a^\infty e^{-\kappa r}\, dr + (^1/_3\eta)\sum_\sigma K_\sigma n_\sigma\beta_{\sigma j}^2\int_a^\infty (e^{-2\kappa r}/r)\, dr + (^2/_3\eta)\sum_\sigma K_\sigma n_\sigma\int_a^\infty \sum_{n=3}(\beta_{\sigma j}{}^n e^{-n\kappa r}/n!r^{n-1})\, dr \quad (21)$$

3. The Onsager–Fuoss Result. The Onsager–Fuoss treatment of the diffusion problem[1] retained only the first three terms in the expansion of the exponential. Thus, the third term on the right-hand side of eq 21 was neglected. Neglecting this term and performing the integrations in eq 21, we obtain the Onsager–Fuoss approximation for the electrophoretic correction, representing the effect of "long-range" coulombic interaction, which may be written as

$$\Delta v_j^L = -(^2/_3\eta)(e_j/DkT)(1/\kappa(1+\kappa a)) \times [K_1n_1e_1 + K_2n_2e_2] + (^1/_3\eta)(K_1n_1e_1^2 + K_2n_2e_2^2)(e_j^2/DkT)^2[e^{2\kappa a}/(1+\kappa a)]^2Ei(2\kappa a) \quad (22)$$

where $Ei(2\kappa a)$ is the negative exponential integral function

(15) R. M. Fuoss and F. Accascina, "Electrolytic Conductance," Interscience, New York, N. Y., 1959, Chapter XIII.

(16) (a) For values of r near the contact distance a, the physical justification for using eq 14 differs somewhat from the model of hydrodynamic force transfer *via* the solvent, which is valid for large values of r[16b] (*i.e.*, values of r on the order of the radius of the ion atmosphere). We note that for small r, $n_{ji} \gg n_i \gg n_{jj}$. The probability of an i ion being within distance $a + \delta a$ from the j ion, which is essentially the fraction of j ions existing as ion pairs in a solution, is denoted by the symbol α and is given by

$$\alpha = \int_a^{a+\delta a} n_{ji}4\pi r^2\, dr$$

The force transfer, according to eq 13 is then

$$\Delta F_j = K_i\int_a^{a+\delta a} n_{ji}4\pi r^2\, dr = K_i\alpha$$

The corresponding velocity increment, resulting from configurations where $r \approx a$, is

$$(\Delta v_i)_{r\approx a} = \omega_{12}\Delta F_j$$

where ω_{12} denotes the mobility of the ion pair. Comparing this equation with eq 14, we see the approximation made in using eq 14 for configurations where $r \approx a$ is essentially that of using Stokes' law to represent the mobility of an ion pair, *i.e.*

$$\omega_{12} = {}^1/_6\pi\eta a$$

Thus, we expect that the more rigorous and systematic derivation of the electrophoretic effect given in the text of this paper will lead to the same result for the mobility of the ion pair. Although the use of Stokes' law in describing the mobility of an ion pair is an oversimplification, it is consistent with our hydrodynamic model. Moreover, we will see later that the resulting diffusion theory is in excellent agreement with experiment, indicating that the Stokes law approximation gives a reasonable description of the ion-pair mobility. (b) P. Résibois and N. Hassolle-Schermans in "Advances in Chemical Physics," Vol. XI, 1st ed, Prigogine, Interscience, New York, N. Y., 1966.

(17) R. M. Fuoss in F. Accascina, "Electrolytic Conductance," Interscience, New York, N. Y., 1959, Chapter IV.

(18) R. Fowler and E. A. Guggenheim, "Statistical Thermodynamics," Cambridge University Press, London, 1939, Chapter IX.

(19) R. M. Fuoss and L. Onsager, *Proc. Nat. Acad. Sci. U. S.*, **47**, 818 (1961).

$$Ei(x) = \int_x^\infty (e^{-u}/u)\,du \cong -0.5772 - \ln x + x,\ x < 0.2 \quad (23)$$

The next step is to express the forces, K_i, in terms of mobilities and velocity. From eq 8, the "zeroth approximation" is $K_i = \rho_i v$, which is the approximation made by Onsager and Fuoss. Since the electrophoretic correction is of order $c^{1/2}$ and higher, one can see, from the form of eq 22, that this approximation neglects terms in the final value for the electrophoretic effect which are of order c and higher. Making the substitution $K_i = \rho_i v$, we arrive at the final result of Onsager and Fuoss[1] for the electrophoretic correction

$$\Delta v^{OF}/v = (^2/_{3\eta})(e_j/DkT)(1/\kappa(1 - \kappa a)) \times [\rho_1 n_1 e_1 + \rho_2 n_2 e_2] + (^1/_{3\eta})[\rho_1 n_1 e_1^2 + \rho_2 n_2 e_2^2](e_j/DkT)^2(e^{2\kappa a}/(1 + \kappa a)^2)Ei(2\kappa a) \quad (24)$$

4. Extended Calculation of Electrophoretic Effect. The Onsager–Fuoss result, eq 24, contains approximations which result in several terms of order c being omitted. Firstly, the "zeroth approximation," $K_i = \rho_i v$, results in one term of order c being lost, which is however, of minor importance. More important, the neglect of all terms but the first three in the expansion of the Boltzmann equation results in the omission of another term of order c. This term, as we shall see, involves the association constant for ion-pair formation and, for solvents of low dielectric constant or with ions of high charge type, may become large, even at low concentrations.

We now write the electrophoretic correction as the sum of two terms

$$\Delta v_j = \Delta v_j^L + \Delta v_j^s \quad (25)$$

with Δv_j^L expressing the effect of long-range electrostatic interactions and being given by eq 22, and

$$\Delta v_j^s \equiv (^2/_{3\eta}) \sum_{\sigma=1,2} K_\sigma n_\sigma \int_a^\infty \sum_{n=3}^\infty \frac{\beta_{\sigma j}^n e^{-n\kappa r}}{n! r^{n-1}}\,dr \quad (26)$$

where Δv_j^s represents the effect of short-range interactions. Bringing the integral in eq 26 inside the summation sign and integrating by parts, we find

$$\Delta v_j^s = (^2/_{3\eta})\sum_\sigma K_\sigma n_\sigma S(x_{\sigma j}) + \Delta v_j^{sH} \quad (27)$$

$$\Delta v_j^{sH} \equiv -(^2/_{3\eta})\sum_\sigma \left(K_\sigma n_\sigma \sum_{n=3}^\infty \frac{\beta_{\sigma j}^n}{n!} \frac{(n\kappa)^{n-2}}{n-2} \int_{n\kappa a}^\infty \frac{e^{-u}}{u^{n-2}}\,du \right) \quad (28)$$

where

$$S(x_{\sigma j}) \equiv \sum_{n=3}^\infty \frac{\beta_{\sigma j}^n}{n!} \frac{e^{-n\kappa a}}{(n-2)a^{n-2}} = a^2 \sum_{n=3}^\infty \frac{x_{\sigma j}^n}{n!(n-2)} \quad (29)$$

$$x_{\sigma j} \equiv \frac{\beta_{\sigma j}}{a} e^{-\kappa a} = \frac{-e_\sigma e_j}{DkTa} \cdot \frac{1}{1 + \kappa a} \quad (30)$$

It should be noted that the first term in eq 27 is of order c in concentration, *i.e.*, directly proportional to n_σ. As will be shown later, the second term in eq 27, Δv_j^{sH}, contributes terms of order $c^{3/2}$ log c, $c^{3/2}$, and higher order terms. First, we shall consider the evaluation of the first term in eq 27 in terms of more familiar functions and then proceed to the evaluation of the $c^{3/2}$ log c and $c^{3/2}$ terms contained in the second term.

By the substitution, $1/(n-2) = \int_0^\infty e^{-(n-2)z}\,dz$, $S(x_{\sigma j})$ may be expressed in integral form. Making the substitution $y = x_{\sigma j}e^{-z}$, we find

$$S(x_{\sigma j}) = a^2 x_{\sigma j}^2 I(x_{\sigma j}) \quad (31)$$

where we define $I(x_{\sigma j})$ by

$$I(x_{\sigma j}) \equiv \int_0^{x_{\sigma j}} \frac{(e^y - 1 - y - y^2/2)}{y^3}\,dy \quad (32)$$

The integral in eq 32 was also encountered by Fuoss and Onsager in their study of the conductance problem.[20]

The function I(x) may be expressed in the following form

$$\mathrm{I}(x) = \frac{3}{2}\mathrm{K}(x) + \frac{1}{2x^2}\mathrm{F}(x) \quad (33)$$

where

$$\mathrm{K}(x) \equiv \frac{1}{3}\left[\mathrm{Ep}(x) - \frac{e^x}{x}\left(1 + \frac{1}{x}\right)\right] \quad (34)$$

$$\mathrm{F}(x) \equiv [1 + 2x + (^3/_2 - 0.5772)x^2 - x^2 \ln|x|] \quad (35)$$

The quantity, Ep(x), is the positive exponential integral function whose definition and asymptotic expansion for large x are given by

$$\mathrm{Ep}(x) \equiv \int_{-\infty}^x \frac{e^u}{u}\,du \approx \frac{e^x}{x}\left(1 + \frac{1!}{x} + \frac{2!}{x^2} + \cdots\right) \quad (36)$$

It is interesting to note that when $x_{\sigma j}$ is positive (*i.e.*, $\sigma = 1$; $j = 2$) and numerically large ($x_{12} \gg 1$), $S(x_{12})$ assumes a form which suggests that the term in $S(x_{12})$ has its physical origin in ion-pair formation. To illustrate this point we combine eq 31 and 33–36, and to first order in κ, for large x_{12}, we find

$$S(x_{12}) = a^2 \exp\frac{e_1 e_2 \kappa}{DkT} \cdot \frac{e^b}{b} = a^2 f^2 \cdot \frac{e^b}{b} \quad (37)$$

where the last expression results from the identification of the limiting law expression for the mean activity coefficient, f, as: $f = \exp[e_1 e_2 \kappa/2DkT]$. The Bjerrum parameter, b, where $b = |e_1 e_2|/DkTa$, is the ratio of the electrostatic energy between ions of opposite charge

(20) R. M. Fuoss and L. Onsager, *J. Phys. Chem.*, **67**, 621 (1963).

to the thermal energy, kT, when the ions are in contact.[21]

The product f^2e^b/b also appears in the theoretical expression for the degree of ion-pair formation[22] in a system where b is large. This product is directly proportional to α/c, where α is the fraction of ions which are paired, and c is the molar concentration. Thus, we see that the retention of the full exponential in the Boltzmann equation (eq 16) in the electrophoretic calculation leads to a term which physically represents the effect of ion-pair formation. We will see that this term does not cancel out in the final equation for the thermodynamic diffusion coefficient.

We now return to the second term in eq 27, denoted by Δv_j^{3H}. The evaluation of this term proceeds *via* integration by parts of eq 28. The basic procedure[23] is similar to the procedure used to derive eq 27 and 31. The results may be expressed in the form

$$\Delta v_j^{3H} = -\frac{1}{3\eta}\sum_\sigma K_\sigma n_\sigma \beta_{\sigma j}{}^3 \kappa Ei(3\kappa a) - \frac{2a^2}{3\eta}\kappa a \sum_\sigma K_\sigma n_\sigma x_{\sigma j}{}^2 \mathrm{I}^{\mathrm{H}}(x_{\sigma j}) \quad (38)$$

The function $\mathrm{I}^{\mathrm{H}}(x_{\sigma j})$ may be expressed as

$$\mathrm{I}^{\mathrm{E}}(x) = \mathrm{H}(x) + \mathrm{G}(x) \quad (39)$$

with

$$\mathrm{H}(x) = \frac{1}{2}\left[x\mathrm{Ep}(x) - 2\mathrm{Ep}(x) - e^x\left(1 - \frac{1}{x}\right)\right] \quad (40)$$

$$G(x) = [1.5 + \mathrm{Ep}(1) - 2.718 - \alpha_2] - \frac{1}{2x} + \left[\alpha_1 - 1 + 2.718 - \frac{\mathrm{Ep}(1)}{2}\right]x - \left(\frac{x}{2} - 1\right)\ln|x| \quad (41)$$

Here, α_1 and α_2 represent numerical evaluations of the infinite series; $\alpha_1 \equiv \sum_{n=3}^{\infty} 1/n!(n-2) = 0.19067$; $\alpha_2 \equiv \sum_{n=3}^{\infty} 1/n!(n-1) = 0.09961$. The positive exponential integral, $\mathrm{Ep}(x)$ is defined by eq 36.

It is interesting to note that the asymptotic expansion of $\mathrm{I}^{\mathrm{H}}(x)$ for large positive x is given by

$$\mathrm{I}^{\mathrm{H}}(x) \approx \frac{e^x}{x^3}\left(1 + \frac{6}{x} + \frac{36}{x^2} + \cdots\right) \quad x \gg 1 \quad (42)$$

while the corresponding approximation for $\mathrm{I}(x)$ is given by[24]

$$\mathrm{I}(x) \approx \frac{e^x}{x^3}(1 + 3/x + 12/x^2 + \cdots) \quad x \gg 1 \quad (43)$$

Thus, both $\mathrm{I}^{\mathrm{H}}(x)$ and $\mathrm{I}(x)$ approach a common limit as x increases, with $\mathrm{I}^{\mathrm{H}}(x)$ being the larger for positive finite x. Values of the functions $\mathrm{I}(x)$ and $\mathrm{I}^{\mathrm{H}}(-x)$ are tabulated in Table I for both positive and negative x.

Table I: Values of the Functions $\mathrm{I}(x)$ and $\mathrm{I}^{\mathrm{H}}(x)$

x	$\mathrm{I}(x)$	$\mathrm{I}(-x)$	$\mathrm{I}^{\mathrm{H}}(x)$	$\mathrm{I}^{\mathrm{H}}(-x)$
1.0	0.191	−0.148	0.091	0.077
1.4	0.283	−0.199	0.185	0.146
2.0	0.446	−0.268	0.403	0.287
3.0	0.804	−0.367	1.017	0.606
4.0	1.334	−0.451	2.068	1.105
5.0	2.160	−0.523	3.783	1.503
6.0	3.519	−0.587	6.563	2.059
7.0	5.873	−0.644	11.15	2.675
8.0	10.14	−0.696	18.94	3.346
9.0	18.23	−0.742	32.69	4.065
10.0	34.07	−0.785	57.94	4.829
12.0	132.5	−0.861	201.4	6.476
14.0	577.4	−0.927	801.2	8.266

It will be observed that both functions become very large for large positive x, indicating a large contribution from the higher order terms in the Boltzmann exponential when the Bjerrum parameter is large.

We now assemble the pieces of Δv_j^S by combining eq 27, 31, and 38, which after carrying out the summation over $\sigma(\sigma = i,j)$, yields

$$\Delta v_j^S = \frac{2}{3\eta}a^2[K_i n_i x_{12}{}^2 \mathrm{I}(x_{12}) + K_j n_j x_{jj}{}^2 \mathrm{I}(x_{jj}) - \frac{1}{3\eta}[K_i n_i \beta_{12}{}^3 + K_j n_j \beta_{jj}{}^3]\kappa Ei(3\kappa a) - \frac{2}{3\eta}\kappa a^3[K_i n_i x_{12}{}^2 \mathrm{I}^{\mathrm{H}}(x_{12}) + K_j n_j x_{jj}{}^2 \mathrm{I}^{\mathrm{H}}(x_{jj})] \quad (44)$$

The total electrophoretic contribution, up to order $c^{3/2}$, is then given by the sum of Δv_j^L and Δv_j^S, where these quantities are given by eq 22 and 44, respectively. However, for the calculation of the thermodynamic diffusion coefficient, L, by eq 7 and 10, the ratio $\Delta v_j/v$ is needed. Thus, we must eliminate K_j in favor of v in the theoretical expressions for Δv_j^L and Δv_j^S.

As stated previously, our objective is to retain all terms of order c and lower that are consistent with the use of the full Boltzmann exponential, and further, to retain the largest $c^{3/2}$ log c and $c^{3/2}$ terms. To this end, the following approximations will be made in eliminating K_j.

(1) In the first term in eq 22, we make the substitution

$$K_j = \rho_j v(1 + \Delta v_j^{LL}/v) \quad (45)$$

(21) The distance between the ionic centers at contact is a. This distance parameter must be as large as the sum of the ionic radii, but it may be larger due to solvation effects.

(22) See ref 15, Chapter XVI.

(23) The author will provide a more detailed version of the derivations in Section II4 for those who are interested.

(24) These results follow from the expressions for $\mathrm{I}(x)$ and $\mathrm{I}^{\mathrm{H}}(x)$ given by eq 33 and 34, and by eq 39–41, if one uses the asymptotic expansion of $\mathrm{Ep}(x)$ given in eq 36.

where Δv_j^{LL} is the limiting law approximation for the electrophoretic effect as given by the first term in eq 24.

(2) In all other terms in Δv_j, the zero-order approximation, $K_j \approx \rho_j v$, will be used. This procedure neglects a number of terms of order $c^{3/2}$ log c and $c^{3/2}$ which would result from higher order approximations for K_j. However, these neglected terms are small compared to the $c^{3/2}$ log c and $c^{3/2}$ terms contained in eq 44.[25] Following the procedure for the elimination of K_j outlined above and combining eq 7, 10, 18, 22, and 44, the theoretical result for the thermodynamics diffusion coefficient may be written in the form

$$\frac{n}{\bar{L}} = \frac{K}{v} = (\nu_1\rho_1 + \nu_2\rho_2)\Big\{1 + \frac{\nu_1\nu_2}{\nu}\cdot\frac{(\rho_1 - \rho_2)^2}{\nu_1\rho_1 + \nu_2\rho_2} \times \frac{1}{6\pi\eta}\cdot\frac{\kappa}{(1 + \kappa a)} - \frac{1}{\nu}\cdot\frac{(\nu_2\rho_1 + \nu_1\rho_2)^2}{(\nu_1\rho_1 + \nu_2\rho_2)}\cdot\frac{1}{12\pi\eta}\cdot\beta\kappa^2 Ei(2\kappa a) + \frac{\nu_1\nu_2}{\nu^2}\cdot\frac{(\rho_1 - \rho_2)^2(\nu_2\rho_1 + \nu_1\rho_2)}{(\nu_1\rho_1 + \nu_2\rho_2)}\cdot\left(\frac{1}{6\pi\eta}\right)^2\cdot\left(\frac{\kappa}{1 + \kappa a}\right)^2 - \frac{4a^2}{3\eta}\cdot\frac{\nu_1\nu_2\rho_1\rho_2}{\nu_1\rho_1 + \nu_2\rho_2}\cdot x_{12}^2 \mathrm{I}(x_{12})\cdot n - \frac{2a^2}{3\eta}\cdot\frac{[\nu_1^2\rho_1^2 x_{11}^2 \mathrm{I}(x_{11}) + \nu_2^2\rho_2^2 x_{22}^2 \mathrm{I}(x_{22})]}{\nu_1\rho_1 + \nu_2\rho_2}\cdot n - \frac{1}{\nu_1\nu_2\nu}\cdot\frac{1}{12\pi\eta}\cdot\frac{[\nu_2^2\rho_1 - \nu_1^2\rho_2]^2}{\nu_1\rho_1 + \nu_2\rho_2}\cdot\beta^2\kappa^3 Ei(3\kappa a) + \frac{4a^2}{3\eta}\cdot\frac{\nu_1\nu_2\rho_1\rho_2}{\nu_1\rho_1 + \nu_2\rho_2}\cdot x_{12}^2 \mathrm{I}^{\mathrm{H}}(x_{12})\kappa a\cdot n + \frac{2a^2}{3\eta}\cdot\frac{[\nu_1^2\rho_1^2 x_{11}^2 \mathrm{I}^{\mathrm{H}}(x_{11}) + \nu_2^2\rho_2^2 x_{22}^2 \mathrm{I}^{\mathrm{H}}(x_{22})]}{\nu_1\rho_1 + \nu_2\rho_2}\kappa a\cdot n\Big\} \quad (46)$$

Here, β denotes the concentration invariant portion of β_{12}; that is, β is given by eq 20 with $\sigma = 1, j = 2$, and $\mu = 1$.

5. Conversion to Practical Units. We wish to obtain L, the thermodynamic diffusion coefficient in macroscopic units, and also convert the molecular concentration, n, to concentration in mol $l.^{-1}$, c. The conversion factor is $10^{12}L/c = (10^{16}/N_0)(\bar{L}/n)$, where N_0 is Avogadro's number. We will also express the friction coefficient ρ_i in terms of the limiting ionic conductances, by using eq 4 and $\rho_i = 1/\omega_i$. For convenience, we denote the "thermodynamic mobility" of the solute, $10^{12}\ L/c$, by the symbol, M. Denoting the value of M at infinite dilution by M^0, we define the quantity ΔM by the equation

$$1/M = (1/M^0)\cdot(1 - \Delta M/M^0) \quad (47a)$$

We find that ΔM may be written in the form

$$\Delta M = \Delta M^{\mathrm{OF}} + \Delta M_1 + \Delta M_2 + \Delta M_{\mathrm{A}} + \Delta M_{\mathrm{H1}} + \Delta M_{\mathrm{H2}} + \Delta M_{\mathrm{H3}} \quad (47b)$$

The limiting "thermodynamic mobility" of the solute, M^0, may be written

$$M^0 = (10^{16}/N_0)\frac{C\cdot 10^{-3}}{Fe}\cdot\frac{\lambda_1^0\lambda_2^0}{\nu_1|z_1|\Lambda^0} \quad (47c)$$

The first term on the right in eq 47b, ΔM^{OF}, represents the Onsager–Fuoss terms for the effect of concentration on M, which may be written in the form

$$\Delta M^{\mathrm{OF}} = -(10^{16}/N_0)\cdot\frac{1}{\nu\nu_1\nu_2}\cdot\frac{p^2}{6\pi\eta}\cdot\frac{\kappa}{1 + \kappa a} + (10^{16}/N_0)\cdot\frac{1}{\nu(\nu_1\nu_2)^2}\cdot\frac{q^2}{12\pi\eta}\beta\kappa^2\cdot Ei(2\kappa a) \quad (47d)$$

Here, p and q denote the functions: $p = (\nu_2\lambda_2^0 - \nu_1\lambda_1^0)/\Lambda^0$; $q = (\nu_2^2\lambda_2^0 + \nu_1^2\lambda_1^0)/\Lambda^0$. The second term in eq 47b, ΔM_1, is the result of using the more accurate first-order approximation for K_j when eliminating K_j in the electrophoretic velocity. This term may be written in the form

$$\Delta M_1 = -(10^{16}/N_0)\cdot\left(\frac{Fe}{C\cdot 10^{-3}}\right)\cdot\frac{\nu_1|z_1|}{(\nu\nu_1\nu_2)^2} \times \frac{p^2 q}{(6\pi\eta)^2}\cdot\frac{\Lambda^0}{\lambda_1^0\lambda_2^0}\cdot\left(\frac{\kappa}{(1 + \kappa a)}\right)^2 \quad (47e)$$

The other five terms on the right-hand side of eq 47b are the result of using the full exponential in the Boltzmann distribution instead of the truncated series. These terms may be written as

$$\Delta M_2 = 10^{13}\cdot\frac{4\beta^2}{3\eta}\cdot\frac{\lambda_1^0\lambda_2^0}{\Lambda^{02}}\left[(\lambda_2^0/\lambda_1^0)\left(\frac{\nu_2}{\nu_1}\right)^2 \mathrm{I}(x_{11}) + (\lambda_1^0/\lambda_2^0)\left(\frac{\nu_1}{\nu_2}\right)^2 \mathrm{I}(x_{22})\right]\cdot\frac{c}{(1 + \kappa a)} \quad (47f)$$

$$\Delta M_{\mathrm{A}} = 10^{-3}\cdot\frac{4\beta^2}{3\eta}\cdot\frac{\lambda_1^0\lambda_2^0}{\Lambda^{02}}\cdot\mathrm{I}(x_{12})\cdot\frac{c}{(1 + \kappa a)^2} \quad (47g)$$

$$\Delta M_{\mathrm{H1}} = (10^{16}/N_0)\cdot\frac{1}{\nu(\nu_1\nu_2)^3}\cdot\frac{W^2\beta^2}{12\pi\eta}\cdot\kappa^3 Ei(3\kappa a) \quad (47h)$$

$$\Delta M_{\mathrm{H2}} = -10^{13}\cdot\frac{4\beta^2}{3\eta}\cdot\frac{\lambda_1^0\lambda_2^0}{\Lambda^{02}}\cdot\mathrm{I}^{\mathrm{H}}(x_{12})\cdot\frac{\kappa a}{(1 + \kappa a)^2}\cdot c \quad (47i)$$

$$\Delta M_{\mathrm{H3}} = -10^{13}\cdot\frac{2\beta^2}{3\eta}\cdot\frac{\lambda_1^0\lambda_2^0}{\Lambda^{02}}\cdot\left[\frac{\lambda_2^0}{\lambda_1^0}\left(\frac{\nu_2}{\nu_1}\right)^2 \mathrm{I}(x_{11}) + \frac{\lambda_1^0}{\lambda_2^0}\cdot\left(\frac{\nu_1}{\nu_2}\right)^2 \mathrm{I}^{\mathrm{H}}(x_{22})\right]\cdot\frac{\kappa a}{(1 + \kappa a)^2}\cdot c \quad (47j)$$

$$W^2 = \left[\frac{\nu_2^3\lambda_2^0 - \nu_1^3\lambda_1^0}{\Lambda^0}\right]^2 \quad (47k)$$

(25) These neglected terms were evaluated during preliminary calculations in which the elimination of K_j was carried out in such a way as to include all terms of order $c^{3/2}$ and $c^{3/2}$ log c. However, numerical calculations showed that in systems where the total contribution of $c^{3/2}$ log c and $c^{3/2}$ terms to L/c was significant, the $c^{3/2}$ log c and $c^{3/2}$ terms resulting from better approximations for K_j were nearly an order of magnitude smaller than the corresponding terms in eq 44.

III. Approximate Form of Diffusion Equation for Symmetrical Electrolytes

The complete extended diffusion theory given by eq 47 is quite complex, particularly since a number of concentration-dependent integral functions are present. However, as the following considerations will show, for symmetrical electrolytes, the terms of higher order than c may be expressed in rather simple form. First, we note that ΔM_{H1} is negligibly small for symmetrical electrolytes. Further, using the asymptotic expansions for $I^H(x_{12})$ and $I(x_{12})$, where $x_{12} = b/(1 + \kappa a)$, and using the approximation

$$\exp(x_{12}) \approx e^b f^2 \tag{48}$$

Where f is the Debye–Hückel limiting law value for the mean ionic activity coefficient, we find

$$\Delta M_A \approx 10^{13}\frac{4a^2}{3\eta}\cdot\frac{\lambda_1^0\lambda_2^0}{(\Lambda^0)^2}\cdot\frac{e^b}{b}(1 + 3/x_{12} + \cdots)f^2c + 10^{13}\frac{4a^2}{3\eta}\frac{\lambda_1^0\lambda_2^0}{(\Lambda^0)^2}\cdot\frac{e^b}{b}(1 + 3/x_{12} + \cdots)f^2\kappa a\cdot c \tag{49}$$

$$\Delta M_{H2} \approx -10^{13}\frac{4a^2}{3\eta}\cdot\frac{\lambda_1^0\lambda_2^0}{(\Lambda^0)^2}\cdot\frac{e^b}{b}\times(1 + 6/x_{12} + \cdots)f^2\kappa a\cdot c \tag{50}$$

It should be noted that, for large x_{12}, the second term in eq 49 is, numerically, nearly equal to ΔM_{H2}, but is of opposite sign. Thus, the sum $\Delta M_A + \Delta M_{H2}$ may be approximated by the first term in eq 49, at least for large b and small κa. Since, for large b, the largest terms of order $c^{3/2}$ are contained in $\Delta M_A + \Delta M_{H2}$, the above result suggests that a useful approximation for the complete diffusion equation for symmetrical electrolytes may be given by the equation

$$\Delta M \approx \Delta M^{OF} + \Delta M_1 + 10^{13}\frac{2\beta^2}{3\eta}\cdot\frac{(\lambda_2^{0\,2} + \lambda_1^{0\,2})}{\Lambda^{0\,2}}\times I(-b)c + 10^{13}\frac{4\beta^2}{3\eta}\frac{\lambda_1^0\lambda_2^0}{\Lambda^{0\,2}}I(b)f^2c \tag{51}$$

The preceding arguments have shown that eq 51 is an accurate representation of the complete extended diffusion theory for very large b and small κa. However, eq 51 turns out to be a rather good approximation for the "complete" theory even at moderate b and κa. To illustrate this fact, we note that a comparison of eq 51 and 47, with the approximation $\sqrt{\lambda_1\lambda_2} = \Lambda^0/2$, shows that the mathematical approximation made in eq 51 is equivalent to the statement

$$f_A(b,\kappa a) \equiv I(-b) + f^2I(b) \approx (1 + \kappa a)^{-2}\{I(x_{11}) + I(x_{12}) - \kappa a[I^H(x_{11}) + I^H(x_{12})]\} \equiv f_c(b,\kappa a) \tag{52}$$

In Figure 1, the ratio $f_c(b,\kappa a)/f_A(b,\kappa a)$ is plotted as a function of κa for various values of b. It will be observed that for values of b between 5 and 11 this ratio deviates from unity by about 20% at $\kappa a = 0.2$. As κa decreases, the ratio approaches unity, the approach to unity being very rapid for large b. Thus, eq 51 will be a usable approximation for the complete diffusion theory in real electrolytes.

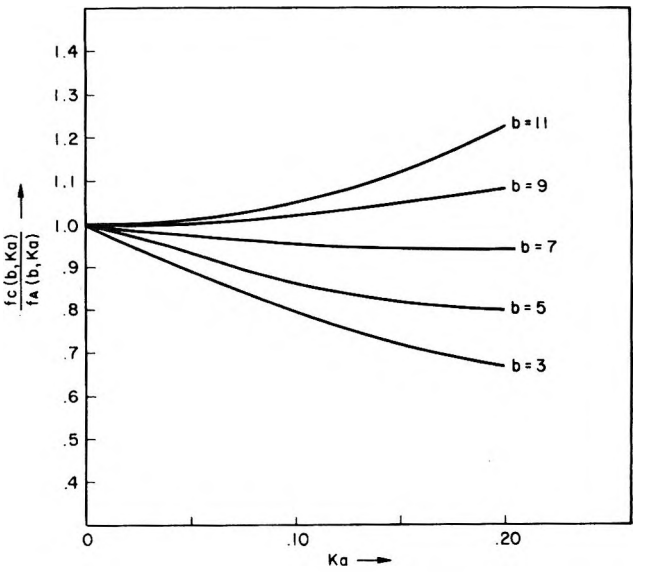

Figure 1. A test of the approximations made in deriving the simplified diffusion equation.

For example, an aqueous 2–2 electrolyte at 25° (with $a = 4$ Å) corresponds to $b = 7$. From Figure 1, it is evident that in this case the approximate diffusion equation is a very good approximation to the complete theory, even at $\kappa a = 0.2$. For aqueous 1–1 electrolytes at 25° ($a = 4$ Å), $b = 2$, and the $c^{3/2}$ terms are not well represented by the f^2 term in eq 51. In fact, there is no theoretical justification for the appearance of f^2 where b is small. However, since the dominant term in ΔM when b is small is ΔM^{OF}, eq 51 is a good approximation to the complete diffusion theory even for small b.

Since $\Delta M/M^0$ is small compared to unity in systems where eq 51 is valid, we may simplify eq 47a by writing

$$M = M^0 + \Delta M \tag{53}$$

Equation 53 with ΔM by eq 51 constitutes the final result for the approximate extended diffusion theory.

IV. Comparison with Experiment

The only data in the literature suitable[26] for testing the diffusion theory are the data of Harned and coworkers[3-5,27-29] for aqueous systems at 25°.

(26) To provide a meaningful test of the theory, the comparison of experiment with theory must be made with electrolyte systems at low strength, *i.e.*, where κa is about 0.2 or less. For larger κa the theory is expected to fail because mathematical approximations will fail, and more fundamentally, because the "ion atmosphere" model is not realistic.

(27) H. S. Harned and C. L. Hildreth, Jr., *J. Amer. Chem. Soc.*, **73**, 650 (1951).

(28) H. S. Harned and F. M. Polestra, *ibid.*, **75**, 4168 (1953).

1. Symmetrical Electrolytes. First we consider the comparison of theory and experiment for symmetrical electrolytes. Earlier studies[3] indicate aqueous 1–1 electrolytes are consistent with the Onsager–Fuoss theory.[1] Thus, if the extended theory is valid, ΔM^{OF} must be the major term in eq 47b. Numerical calculations show this is true. For example, in the case of 0.04 *m* NaCl, with $a = 4.0$ Å, $\Delta M^{OF} = 0.029$, while $\Delta M = 0.028$.[30-32] All terms other than ΔM^{OF} are much smaller than ΔM^{OF} and partially cancel. Since the experimental error in ΔM is on the order of ± 0.01, the extended theory reduces to the Onsager–Fuoss theory[1] in the case of aqueous 1–1 electrolytes. Physically, this means there is no significant effect due to ion-pair formation in dilute aqueous 1–1 electrolytes.

Since aqueous 2–2 electrolytes are characterized by large Bjerrum parameters (*i.e.*, $b \approx 7$), theoretical considerations[33,34] indicate significant ion-pair formation should be present, even in dilute solution. This conclusion is supported by various experimental observations.[35,36] Therefore, the observation that the mutual diffusion coefficients of aqueous $ZnSO_4$[4a] and aqueous $MgSO_4$[4b] are in poor agreement with the Onsager–Fuoss[1] diffusion theory is not unexpected. However, since the extended diffusion theory allows for short-range coulombic interactions (*i.e.*, ion pairing), we expect the extended theory to be a much better approximation than the Onsager–Fuoss theory. As shown in Figure 2, this expectation is more than satisfied.

In Figure 2, experimental values of M in aqueous $MgSO_4$ and $ZnSO_4$ are compared with the theoretical values. The experimental mutual diffusion coefficients were taken from the work of Harned and Hudson.[4a,b] Experimental values of $d \ln \gamma / dm$ were calculated from available activity coefficient data. The details of this calculation appear in the Appendix. In Figure 2 the estimated uncertainties in the experimental values of M ($\sim \pm 1\%$) are indicated by vertical lines. Theoretical values of M were computed[30] using, $a = 3.9$ Å. The choice of this particular value of a was prompted by Guggenheim's[37] theoretical analysis of activity coefficient data, in which the full Boltzmann exponential was retained. Guggenheim found good agreement between theory and experiment for aqueous 2–2 electrolytes when, $3.5 < a < 4.0$. For $ZnSO_4$ and $MgSO_4$, a value slightly less than 4.0 Å was indicated. Theoretical values of M calculated from the complete extended theory, eq 47, are indicated in Figure 2 by the solid curve. The dashed line refers to values of M calculated from the approximate extended theory, eq 51 and 53.

From Figure 2, we make the following observations: (a) within the resolution of Figure 2, the theoretical curves for $ZnSO_4$ and $MgSO_4$ are identical; (b) the complete extended theory is in very good agreement with the data, essentially within experimental error

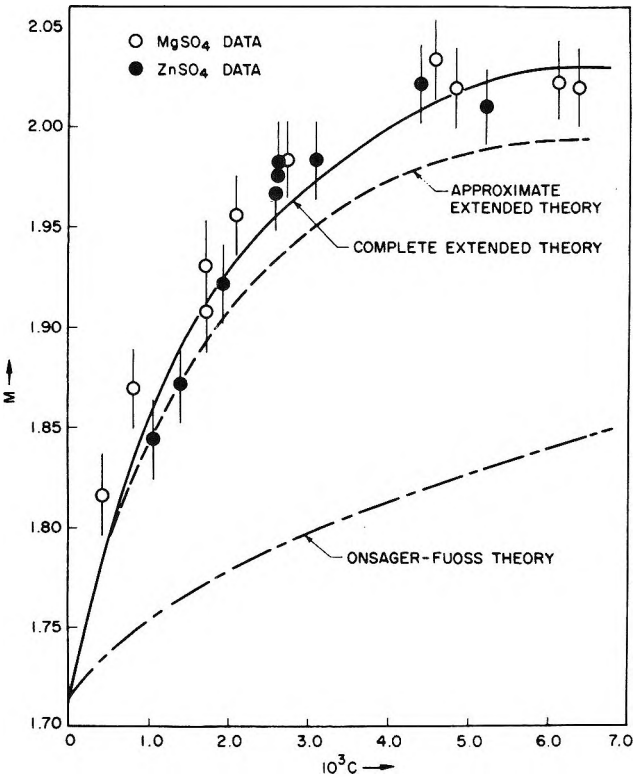

Figure 2. M for aqueous $MgSO_4$ and $ZnSO_4$ at 25°. Comparison of theory with experiment.

over the entire concentration range; (c) as expected, the approximate extended theory is a good approximation to the complete extended theory; (d) either extended theory is a great improvement over the Onsager–Fuoss theory. We note that both the complete and the approximate extended theories are quite sensitive to the choice of a. For example, if a is taken to be 4.5 Å, the theoretical values of M at 0.0026 M are about 4% lower than the corresponding value with $a = 3.9$ Å.

2. Unsymmetrical Electrolytes. We now consider the application of the extended diffusion theory to unsymmetrical electrolytes. First, we note that one cannot expect the same degree of success with unsymmetrical electrolytes as was enjoyed with symmetrical electrolytes. Still, one might expect the extended theory to be a better approximation than the Onsager–

(29) H. S. Harned and C. A. Blake, Jr., *J. Amer. Chem. Soc.*, **73**, 4255 (1951).

(30) The values of the fundamental constants were taken from the tabulation given in ref 4. Limiting ionic conductance data were taken from existing tabulations.[31,32]

(31) R. A. Robinson and R. H. Stokes, "Electrolyte Solutions," 2nd ed, Academic Press, New York, N. Y., 1959.

(32) H. S. Harned and B. B. Owen, "The Physical Chemistry of Electrolytic Solutions," 2nd ed, Reinhold, New York, N. Y., 1950.

(33) N. Bjerrum, *Kgl. Dan. Vidensk. Selsk.*, **7**, No. 9 (1926).

(34) R. M. Fuoss, *J. Amer. Chem. Soc.*, **80**, 5059 (1958).

(35) G. Atkinson and S. Petrucci, *J. Phys. Chem.*, **70**, 3122 (1966).

(36) C. W. Davies, "Ion Association," Butterworths, London, 1952.

(37) E. A. Guggenheim, *Trans. Faraday Soc.*, **56**, 1152 (1960).

Table II: Comparison of the Magnitudes of the Terms in Equation 47b at $\kappa a = 0.2$

Salt	$\dot{a}$	ΔM^{OF}	ΔM_1	ΔM_2	ΔM_A	ΔM_{H1}	ΔM_{H2}	ΔM_{H3}	$\Delta M(c)^a$	$\Delta M(c^{3/2})^b$
$ZnSO_4$	3.9	0.119	−0.002	−0.079	0.457	0.005	−0.171	−0.057	0.495	−0.223
$SrCl_2$	4.89	0.024	−0.002	−0.038	0.016	0.021	−0.003	−0.020	0.000	−0.002
$LaCl_3$	5.75	0.039	−0.002	−0.082	0.019	0.074	−0.005	−0.093	−0.027	−0.024

[a] $\Delta M(c) \equiv \Delta M^{OF} + \Delta M_1 + \Delta M_2 + \Delta M_A$. [b] $\Delta M(c^{3/2}) \equiv \Delta M_{H1} + \Delta M_{H2} + \Delta M_{H3}$.

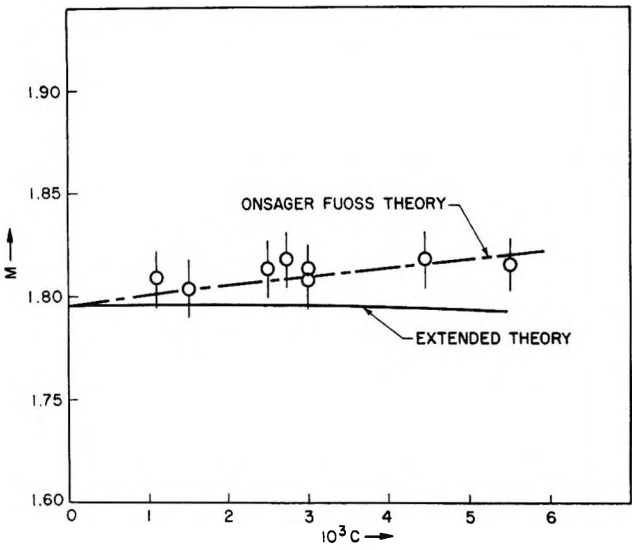

Figure 3. M for aqueous $SrCl_2$ at 25°. Comparison of theory with experiment.

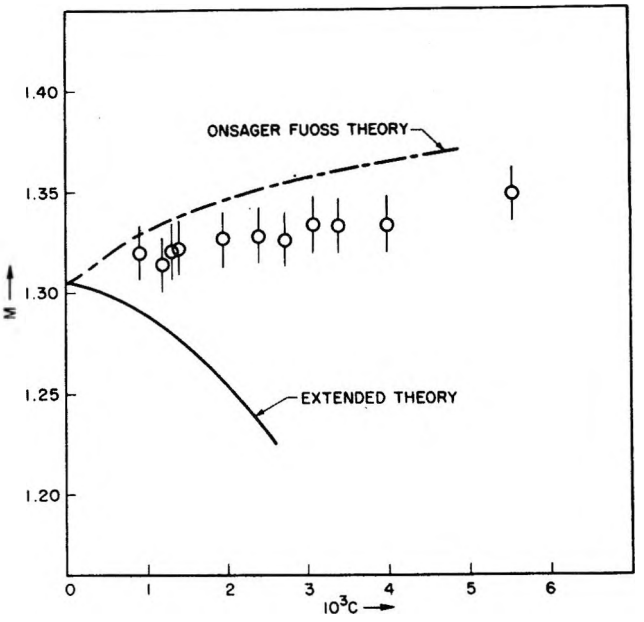

Figure 4. M for aqueous $LaCl_3$ at 25°. Comparison of theory with experiment.

Fuoss theory. However, as illustrated in Figures 3 and 4, this is not the case. In Figures 3 and 4, experimental data for aqueous $SrCl_2$ and aqueous $LaCl_3$ are compared with theory. Experimental mutual diffusion coefficients and activity coefficient derivatives were taken from the literature.[28,29] The theoretical calculations were performed[30] using $a = 4.89$ Å for $SrCl_2$[28] and $a = 5.75$ Å for $LaCl_3$.[38]

From Figure 3, one observes that, for $SrCl_2$, the Onsager–Fuoss theory appears to be a better approximation than the extended theory, although the extended theory is only slightly outside the range of experimental error. As shown in Figure 4, the discrepancy between the extended theory and experiment is more striking in the case of $LaCl_3$. Here, even in very dilute solutions, the extended theory is in serious disagreement with experiment. Although slightly better agreement with experiment at very low concentrations is obtained by choosing a smaller value of the "a" parameter, no physically reasonable value of a will fit the data.

Some insight into the reasons for the failure of the extended theory for $LaCl_3$ can be gained by comparing the contributions of the various terms in eq 47b. Such a comparison is presented in Table II for $ZnSO_4$, $SrCl_2$, and $LaCl_3$ at a concentration corresponding to $\kappa a = 0.2$. We first note that, as a first approximation, the terms, ΔM^{OF}, ΔM_1, ΔM_2, and ΔM_A may be classified as being of order c and lower. Similarly, the terms, ΔM_{H1}, ΔM_{H2}, and ΔM_{H3} may be classified as being of order $c^{3/2}$. The terms ΔM_A and ΔM_{H2}, which depend on the integral functions $I(x_{12})$ and $I^H(x_{12})$, may be interpreted as representing the effect of close range 1–2 coulombic interactions. Likewise, it seems reasonable to interpret the terms ΔM_2 and ΔM_{H3}, which depend on the integral functions $I(x_{ii})$ and $I^H(x_{ii})$, as representing the effect of close range i–i coulombic interactions.

In the context of the above considerations, an examination of Table II yields the following two observations. (1) Comparing $ZnSO_4$ and $LaCl_3$ we see that for $ZnSO_4$ the contribution of all terms of order $c^{3/2}$, denoted by $\Delta M(c^{3/2})$, is significantly smaller than the contribution of lower order terms, denoted by $\Delta M(c)$. Thus, the electrophoretic calculation is converging for $ZnSO_4$. However, in the case of $LaCl_3$, $\Delta M(c^{3/2}) \approx \Delta M(c)$, and the electrophoretic calculation is not converging. (2) For $ZnSO_4$, $|\Delta M_A + \Delta M_{H2}| \gg |\Delta M_2 + \Delta M_{H3}|$. Thus, the effect (on the mobility) of close range 1–2 coulombic interations is greater than the corresponding

(38) F. H. Spedding, P. E. Porter, and J. M. Wright, *J. Amer. Chem. Soc.*, 74, 2781 (1952).

effect of close range i–i coulombic interaction, which is physically reasonable. However, for $SrCl_2$ and $LaCl_3$, similar arguments lead to the conclusion that short range i–i coulombic interactions have a greater effect on the mobility than the corresponding 1–2 interactions, which seems absurd.

It seems likely that both the convergence problem and the physical absurdity discussed above have their origin in the incompatibility of the Boltzmann exponential with linear superposition of fields. For unsymmetrical electrolytes in high dielectric solvents like water, the physical inconsistency introduced by using the full Boltzmann exponential seems to result in a larger "error" than the "mathematical error" which would be introduced by truncating the exponential. Thus, it would appear that a successful theory of the effect of ion-pair formation on the properties of unsymmetrical electrolytes (in a high dielectric solvent) must avoid the simultaneous use of the full Boltzmann exponential and the linear superposition of fields approximation.

It would be interesting to compare the extended diffusion theory with data on unsymmetrical electrolytes in solvents of low dielectric constant. In this case, the theoretical results seem physically reasonable since the terms ΔM_A and ΔM_{H2} would be dominant. Thus, better agreement between theory and experiment may result for the unsymmetrical case. Unfortunately, to the author's knowledge, suitable data are not available.

V. Discussion of the Association Term

If it is arbitrarily assumed that a fraction α of the ions present in a symmetrical electrolyte exist as distinct ion pairs, having a mobility ω_m, the concentration dependence thereby introduced into M, denoted by ΔM_{IP}, may be written in the form[4]

$$\Delta M_{IP} = M^0\left[\frac{\omega_m(\omega_1 + \omega_2)}{\omega_1\omega_2} - 1\right]K_A f^2 c \qquad (54)$$

Here, ω_1 and ω_2 are limiting ionic mobilities, which are given in terms of limiting ionic conductances by eq 4. Here, α has been expressed in terms of the thermodynamic association constant, K_A, the mean molal activity coefficient of free ions, f, and the molar concentration, c, according to the mass action equation

$$\alpha \cong K_A f^2 c \qquad (55)$$

which is valid for $\alpha \ll 1$.

Comparing eq 54 with the approximate extended diffusion theory, eq 51, one observes a strong formal resemblance between the last term in eq 51 and 54. Both terms depend upon concentration through the factor f^2c.[39] In addition, using the asymptotic expansion of $I(b)$, we find $\beta^2 I(b) \approx a^2 e^b/b$. Theoretical treatments[22] of ion-pair formation in systems where b is large yield association constants which have the same exponential dependence on b as the product $\beta^2 I(b)$. Therefore, the last term in eq 51 represents the effect of ion-pair formation on the diffusion mobility, which we have given the symbol, ΔM_{IP}.

To find the theoretical value of the mobility of the ion pair, we equate the last term in eq 51 with the right-hand side of eq 54 and use the approximation $\omega_1 + \omega_2 = 2\sqrt{\omega_1\omega_2}$, giving

$$M^0[2\omega_m/\sqrt{\omega_1\omega_2} - 1]K_A = 10^{13}\frac{\beta^2}{3\eta}I(b) \qquad (56)$$

where M^0 is defined by eq 47c. Using the first two terms of the asymptotic expansion of $I(b)$ and expressing M^0 in terms of ω_i, we write

$$\left(\omega_m - \frac{\sqrt{\omega_1\omega_2}}{2}\right)K_A = \frac{1}{6\pi\eta a}\cdot\frac{2\pi N_0 a^3}{1000}\frac{e^b}{b}(1 + 3/b) \qquad (57)$$

To proceed with the calculation of the mobility of an ion pair, an electrostatic model for association must be chosen to fix the precise functional dependence of K_A on b. First, we consider the Bjerrum model which yields an association constant of the form[22,32,33]

$$K_A = \frac{4\pi N_0 \beta^3}{1000}Q(b) \qquad (58)$$

where $Q(b)$ is a complex function of b whose asymptotic expansion for large b is given by

$$Q(b) = \frac{e^b}{b^4}(1 + 4/b + \cdots) \qquad (59)$$

Combining eq 57–59 the mobility of the ion pair, for large b, becomes

$$\omega_m = \frac{1}{2}\sqrt{\omega_1\omega_2} + \frac{1}{2}\cdot\frac{1}{6\pi\eta a}\cdot(1 - 1/b) \qquad (60)$$

Thus, according to the electrostatic–hydrodynamic theory developed here, the mobility of the ion pair is greater than one-half the average single ion mobility, which means ion-pair formation increases the thermodynamic mobility.

It is of interest to examine the theoretical "effective hydrodynamic radius" of the ion pair, denoted by R, which is defined by Stokes' law

$$\omega_m = {}^1/_6\pi\eta R \qquad (61)$$

First, we express the limiting ionic mobility, ω_i, in terms of the "effective hydrodynamic radius" of the isolated ion, r_i, by equations identical in form with eq 61. Fuoss and Accascina[15] have shown that $r_1 = r_2 = a$. As these authors point out, this result is physically reasonable since the extent of "solvation" of a pair of oppositely charged ions is greater when isolated than when paired. Thus, r_i, which measures the

(39) The f^2 term in eq 51 is really the Debye–Hückel limiting law expression for the square of the mean ionic activity coefficient. However, to order $c^{3/2}$ in ΔM, f^2 in eq 54 is identical with f^2 in eq 51.

"solvated radius" of a free ion, should be greater than $a/2$, since $a/2$ measures the "solvated radius" of an ion when in a "contact" ion pair. In the context of this discussion, an ion pair is a contact ion pair if the separation between the two ions is the contact parameter a. Combining eq 60 and 61, and using the relation $\omega_i = {}^1/_6\pi\eta a$, we have, for large b

$$R = a(1 + 1/2b) \tag{62}$$

We note that, as expected,[16] in the limit of infinite b, the effective radius of the ion pair is a. However, for finite b, the effective radius of the ion pair is slightly greater than a. These conclusions are consistent with the Bjerrum association model, since for finite b, the Bjerrum model counts pairs of ions not in actual contact as ion pairs. However, for large b, most of the "Bjerrum ion pairs" are very nearly in contact.[40] Thus, we conclude that the extended diffusion theory is consistent with the Bjerrum association model.

For the contact model,[41] the association constant is given by

$$K_A = \frac{4\pi N_0 a^3}{3000} e^b \tag{63}$$

Here, the same development that led to eq 62 yields

$$R = 2a(1 - 1.5/b) \tag{64}$$

The result given in eq 64 does not seem consistent with the contact model. In the contact model, only those ions at electrostatic contact (*i.e.*, pairs of ions whose center to center distance is a) are counted as ion pairs. Yet, eq 64 suggests an ion pair is formed when two ions approach to hydrodynamic contact (*i.e.*, where the center to center distance is $2a$). Also the implication of eq 64 that R will decrease as b decreases (at constant a) is difficult to reconcile with the contact model. Therefore, we tentatively conclude that the extended diffusion theory is not consistent with the contact model.

Since the Fuoss–Onsager–Skinner (FOS) conductance theory[6] results in an ion pair term consistent with the contact model, while the Kremp–Kraeft–Ebeling (KKE) conductance theory[7] results in Bjerrum association, we conclude that the extended diffusion theory is most consistent with the KKE theory.

Since the same basic model[42] is used in both the extended diffusion theory and in the Bjerrum theory, it is not surprising that we find the extended diffusion theory to be consistent with Bjerrum association. In its development, the extended diffusion theory more closely resembles the FOS theory than the KKE theory. Therefore, it is surprising that the diffusion theory is consistent with the KKE theory and not fully consistent with the FOS theory.

Finally, we will comment on the controversy[43,44] over replacing the contact distance parameter a by the Bjerrum distance parameter $\beta/2$. According to Justice,[43,45] in a system where Bjerrum ion pairs form, the "distance of closest approach for unpaired ions" should be taken as $\beta/2$ rather than the contact distance a. If this point of view were valid, one would expect that a theory which leads naturally to Bjerrum association would also lead naturally to the appearance of $\beta/2$ in place of a in the "long-range" terms. Specifically, one would expect the appearance of a term which would combine with the terms denoted by ΔM^{OF} and thereby yield an expression differing from ΔM^{OF} only in that the a parameter in ΔM^{OF} has been replaced by $\beta/2$. However, none of the terms in the extended diffusion theory satisfies this requirement.

Since the appearance of $\beta/2$ in place of a does not occur naturally, it might be argued that one should *arbitrarily* replace a in ΔM^{OF} by $\beta/2$. However, with the substitution, the extended diffusion theory is no longer in agreement with the $MgSO_4$ and $ZnSO_4$ data.

Therefore, we tentatively conclude that although the extended diffusion theory predicts "Bjerrum association," the diffusion theory is not consistent with the substitution of $\beta/2$ for a in "long-range" terms.

Appendix

There exist two sets[46,47] of electromotive force data which allow activity coefficients for $ZnSO_4$ to be calculated. However, there is a distinct lack of agreement between the two sets of data below 0.005 *m*. For our purposes, we choose the data of Cowperthwaite and La Mer[47] since, as these authors note, their data are more consistent with freezing point data on aqueous $ZnSO_4$ and with data on other 2–2 electrolytes. Using the

(40) This statement follows from a calculation, according to the Bjerrum model, of the average separation between two ions constituting an ion pair, denoted by $\langle r\rangle_{ip}$. This calculation proceeds as follows: first, choose the Bjerrum probability function,[22,33] $P(r)$, to represent the probability that an anion is in a spherical shell of thickness dr at a distance r from a reference cation, where $P(r) \propto e^{\beta/r}4\pi r^2 dr$. Next consider a system of ion pairs where two ions are paired when their separation, r_{ip}, is within the limit, $a < r_{ip} < \beta/2$. The average separation of an ion pair, $\langle r_{ip}\rangle$ is then given by

$$\langle r\rangle_{ip} = \frac{\int_a^{\beta/2} e^{\beta/r} r^3 dr}{\int_a^{\beta/2} e^{\beta/r} r^2 dr}$$

Making the change of variables, $u \equiv \beta/r$, and repeated integration by parts, yields for large b, the result

$$\langle r\rangle_{ip} \approx a(1 + 1/b) \approx a$$

(41) R. M. Fuoss, *J. Amer. Chem. Soc.*, **80**, 5059 (1959).

(42) Using the Boltzmann distribution function, a continuous *integration* from the lower limit $r = a$ is used to calculate both the force transfer in the diffusion problem (eq 15) and the fraction of paired ions in the Bjerrum calculation. Physically, this means that, in both theories, "close-range interactions" include pairs of ions not in actual contact.

(43) J. C. Justice, *J. Chim. Phys.*, **66**, 1193 (1969).

(44) R. M. Fuoss, *ibid.*, **66**, 1191 (1969).

(45) J. C. Justice, *ibid.*, **65**, 353 (1968).

(46) U. B. Bray, *J. Amer. Chem. Soc.*, **49**, 2372 (1927).

(47) I. A. Cowperthwaite and V. K. La Mer, *ibid.*, **53**, 4333 (1931).

symbol E for the electromotive force of the cells studied by Cowperthwaite and La Mer, we define the deviation function, $Y(m)$, by the equation

$$Y(m) \equiv E + \frac{RT}{F} \ln (m) - 0.2392m^{1/2} \quad \text{(A-1)}$$

Numerical values of $Y(m)$ were calculated from the data and were found to be well represented by the empirical expression

$$Y = 0.41112 + 3.1965m \times \exp(-18.75m^{1/2}) - 0.4709m \quad \text{(A-2)}$$

where the numerical coefficients were determined by the method of least squares. The corresponding standard deviation was $\sigma = \pm 0.03$ mV. The empirical equation for $Y(m)$ that corresponds to the activity coefficient equation given by Harned and Hudson[4a] yields a standard deviation of $\sigma = \pm 0.2$ mV. Thus, eq A-2 is a great deal more consistent with the data than the expression for γ used by Harned and Hudson. Making the definition

$$E_0' \equiv E + \frac{RT}{F} \ln (m) \quad \text{(A-3)}$$

we may write the derivative of the activity coefficient in the form

$$\frac{d \ln \gamma}{dm} = \frac{-F}{RT} \frac{dE_0'}{dm} \quad \text{(A-4)}$$

Combination of eq A-1 through A-4 leads to the desired relation

$$1 + m\frac{d \ln \gamma}{dm} = 1 - 4.6552m^{1/2} + 18.3290m - 124.419(1 - 9.3749m^{1/2})m \times \exp(-18.75m^{1/2}) \quad \text{(A-5)}$$

Equation A-5 is valid up to 0.01 m.

Accurate activity coefficient data for dilute aqueous $MgSO_4$ at 25° are not available. However, as noted by Harned and Hudson,[4a] at moderate concentrations, experimental activity coefficients of $MgSO_4$ and $ZnSO_4$ are indistinguishable. Thus, following Harned and Hudson, we will assume the activity coefficients of $MgSO_4$ and $ZnSO_4$ are essentially equal in dilute solution.

Polynuclear Complex Formation in Solutions of Calcium Ion and Ethane-1-hydroxy-1,1-diphosphonic Acid. I. Complexometric and pH Titrations

by R. J. Grabenstetter and W. A. Cilley*

Miami Valley Laboratories, The Procter & Gamble Company, Cincinnati, Ohio 45224 *(Received December 10, 1969)*

Publication costs assisted by The Procter & Gamble Company

Complexometric and pH titrations have been used to study the complexation reactions between calcium ion and ethane-1-hydroxy-1,1-diphosphonic acid at 25° and pH 11.0 in 0.1 *M* tetramethylammonium chloride. Evidence is presented which indicates that polynuclear complexes are formed resulting ultimately in the formation of a micelle- or solidlike phase at concentrations of calcium ion above about 2×10^{-6} *M*. Log formation constants (overall) which best fit the experimental results are $\beta_{1,1} = 5.52 \pm 0.08$, $\beta_{3,2} = 18.78 \pm 1.4$, $\beta_{4,3} = 29.0 \pm 0.12$, $\beta_{7,4} = 48.23 \pm 0.44$, and K_0 (aggregation constant) $= 4.6 \pm 0.9$.

Introduction

It has recently been discovered that ethane-1-hydroxy-1,1-diphosphonic acid [CH_3–C(OH)(PO_3H_2)$_2$, EHDP™] and some of its salts have unique properties in biological systems which contain calcium.[1-3] Since this novel behavior is probably related to the formation of complexes between the diphosphonate and calcium, it was of interest to investigate the formation of such complexes.

The majority of measurements of the stability constants of complexes of metal ions with proton-binding anions has been carried out by measuring the change (lowering) in pH accompanying complex formation. The method[4] is convenient, rapid, and precise and can usually be used where methods demanding specific properties, *e.g.*, spectroscopic, cannot. The complexometric method of Irani and Callis[5] by contrast is applicable only when a well-defined precipitate (detected by nephelometry) can be formed in the presence of a complexing agent. The complexing and precipitating agents can then compete for the metal ion to establish a stable equilibrium at a controlled, constant pH. The complexometric method with certain modifications was found to be well suited to a study of complex formation by calcium with EHDP. An advantage of the method is the possibility of equilibrating the system at a constant free calcium ion concentration, the choice of which may be varied over a rather wide range (*e.g.*, 10^{-3} to 10^{-7} *M*).

There have been two prior studies of Ca–EHDP complexes, carried out by the potentiometric (glass electrode) method. Kabachnik, *et al.*,[6] have interpreted their data for titration of the acid in the absence of calcium in terms of the dissociation of four phosphonic acid protons and one hydroxyl proton. They postulate calcium complexes formed both with and without dissociation of the hydroxyl proton. Carroll and Irani[7] have reported an additional calcium complex in which one of the phosphonic acid protons remains undissociated. Other workers[8,9] have found it unnecessary to invoke the dissociation of the hydroxyl proton to fit the observed acid titration curves. The dissociation constants of the 1:1 Ca–EHDP complexes which were determined in these two studies[6,7] are shown in Table I. The difference in the log *K* of the 1:1 complex is reasonable in view of the difference in the supporting electrolyte and the ionic strength.

In both of the above potentiometric studies the authors made no mention of changes in the apparent stability constants of the mononuclear complexes with changes in the total concentration of EHDP. In both potentiometric and complexometric experiments during the present investigation an increase in concentration of EHDP caused a pronounced increase in the apparent stability constants for an assumed mononuclear calcium complex formed at pH 11. Since this behavior is indic-

(1) M. D. Francis, *Calc. Tiss. Res.*, **3**, 151 (1969).

(2) H. Fleisch, R. G. G. Russell, and M. D. Francis, *Science*, **165**, 1262 (1969).

(3) M. D. Francis, R. G. G. Russell, and H. Fleisch, *ibid.*, **165**, 1264 (1969).

(4) A. E. Martell and G. Schwarzenbach, *Helv. Chim. Acta*, **39**, 653 (1956).

(5) R. R. Irani and C. F. Callis, *J. Phys. Chem.*, **64**, 1398 (1960).

(6) M. I. Kabachnik, R. P. Lastovskii, T. Ya. Medved, V. V. Medyntsev, I. D. Kolpakova, and N. M. Dyatiova, *Dokl. Akad. Nauk SSSR*, **177**, 582 (1967) [*Dokl. Chem.*, **177**, 1060 (1967)].

(7) R. L. Carroll and R. R. Irani, *J. Inorg. Nucl. Chem.*, **30**, No. 11, 2971 (1968).

(8) R. J. Grabenstetter, O. T. Quimby, and T. J. Flautt, *J. Phys. Chem.*, **71**, 4194 (1967).

(9) R. L. Carroll and R. R. Irani, *Inorg. Chem.*, **6**, 1994 (1967).

Table I: Literature Values of the Dissociation Constants of 1:1 Calcium Complexes of EHDP at 25°

Medium	Log $K_{[CaHL]}$[a]	Log $K_{[CaL]}$	Reference
0.1 *M* KCl	...	−6.04	6
0.5 *M* $(CH_3)_4NCl$	−3.58	−5.74	7

[a] L = $CH_3C(OH)(PO_3^{2-})_2$.

ative of polynuclear complex formation, further experiments designed for analysis by the methods of Sillèn[10] were carried out.

Experimental Section

Materials. Calcium chloride dihydrate ("Baker Analyzed" reagent) and calcium nitrate (Matheson Coleman and Bell) were used without purification. Tetramethylammonium chloride (Matheson Coleman and Bell) was twice recrystallized from water. Tetramethylammonium hydroxide was synthesized for use in the pH titrations from the recrystallized chloride by anion exchange using the hydroxide form of Dowex 21-K or was obtained as the crystalline pentahydrate (Southwestern Analytical Chemicals) for the complexometric titrations. Decanoic acid (Eastman Organic Chemicals), after conversion into the methyl ester, was fractionally distilled, and the C_{10} cut was reconverted into the acid. The preparation of ethane-1-hydroxy-1,1-diphosphonic acid (H_4EHDP) was carried out by the action of acetic anhydride on phosphorous acid.[11] The H_4EHDP was recrystallized as the monohydrate from aqueous solution.

Anal. Calcd for $H_4EHDP \cdot H_2O$: C, 10.71; H, 4.46; P, 27.68; H_2O, 8.04. Found: C, 11.2; H, 4.6; P, 27.8; H_2O, 8.2.

pH Titrations. Potentiometric (pH) titrations were carried out with a Precision-Dow Recordomatic titrator (Precision Scientific Co.) using Beckman glass electrodes and a calomel glass sleeve reference electrode. The glass electrode was standardized at pH 7.0 using Beckman buffer solution. Titrations were carried out at room temperature in a magnetically stirred, covered cell under a blanket of nitrogen. The titrant solution was sufficiently concentrated relative to the titrand that the volume change during a tiration was less than 10% of the original volume. Both titrant and titrand were 0.1 *M* in tetramethylammonium chloride to minimize changes in ionic strength during titration. Titrations were carried out by adding standardized tetramethylammonium hydroxide to 25 ml of H_4EHDP solution.

Complexometric Titrations. These experiments were performed by recording the light transmittance of a solution containing EHDP and a calcium precipitating anion while calcium titrant was added in increments. The method was essentially that of Irani and Callis[5] except that tetramethylammonium decanoate was used as the precipitating agent instead of an oxalate salt. The determination of the solubility product of calcium decanoate is described in the Appendix. During the titrations temperature was maintained at 25.0 ± 0.1° by use of a jacketed beaker and water bath. The pH was maintained at 11.0 by the addition of tetramethylammonium hydroxide, as required, after each addition of calcium titrant. All solutions were made initially 0.1 *M* in tetramethylammonium chloride. Reduction of the data obtained from the complexometric titrations was accomplished by means of a Fortran version of the computer program Letagropvrid[12] with the inclusion of some changes taken from Letagropstyrd.[13]

Results and Discussion

Composition of Complexes. In Figure 1 are shown pH titration curves for two different concentrations of H_4EHDP in the presence of 2 mol of calcium chloride/mol of H_4EHDP. A titration curve of the acid in the absence of calcium is included for reference. It is evident that in the presence of calcium the pH between the second and fourth equivalence points is markedly lower than in

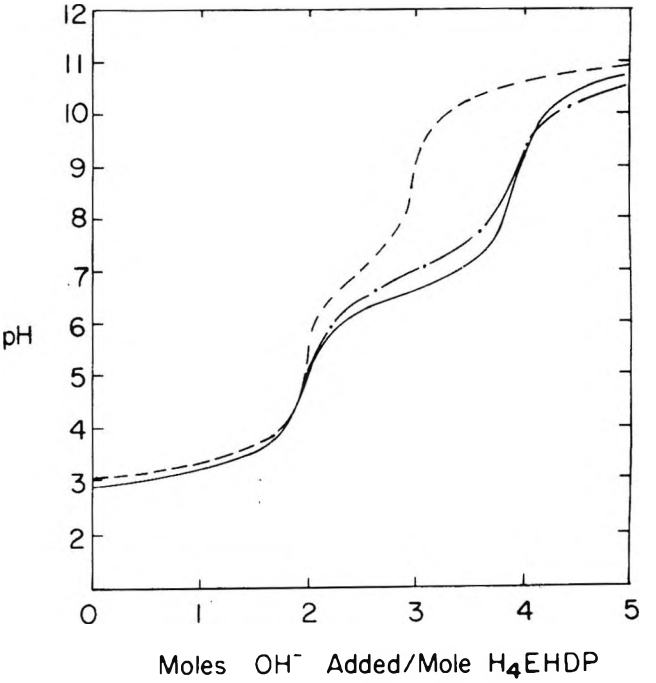

Figure 1. Titrations of H_4EHDP with tetramethylammonium hydroxide, 25°, μ = 0.1 *M* (TMACl): 5.0×10^{-4} *M* H_4EHDP with 0.0 *M* Ca^{2+}, — — —; 5.0×10^{-4} *M* EHDP with 1.0×10^{-3} *M* Ca^{2+}, —·—; 1.0×10^{-3} *M* H_4EHDP with 2.0×10^{-3} *M* Ca^{2+}, ———.

(10) L. G. Sillén, *Acta Chem. Scand.*, **15**, 1981 (1961).

(11) B. T. Brooks, *J. Amer. Chem. Soc.*, **34**, 496 (1912); O. T. Quimby, U. S. Patent 3,387,024 (June 4, 1968).

(12) M. Ingri and L. G. Sillén, *Ark. Kemi*, **23**, 97 (1964).

(13) L. G. Sillén, private communication.

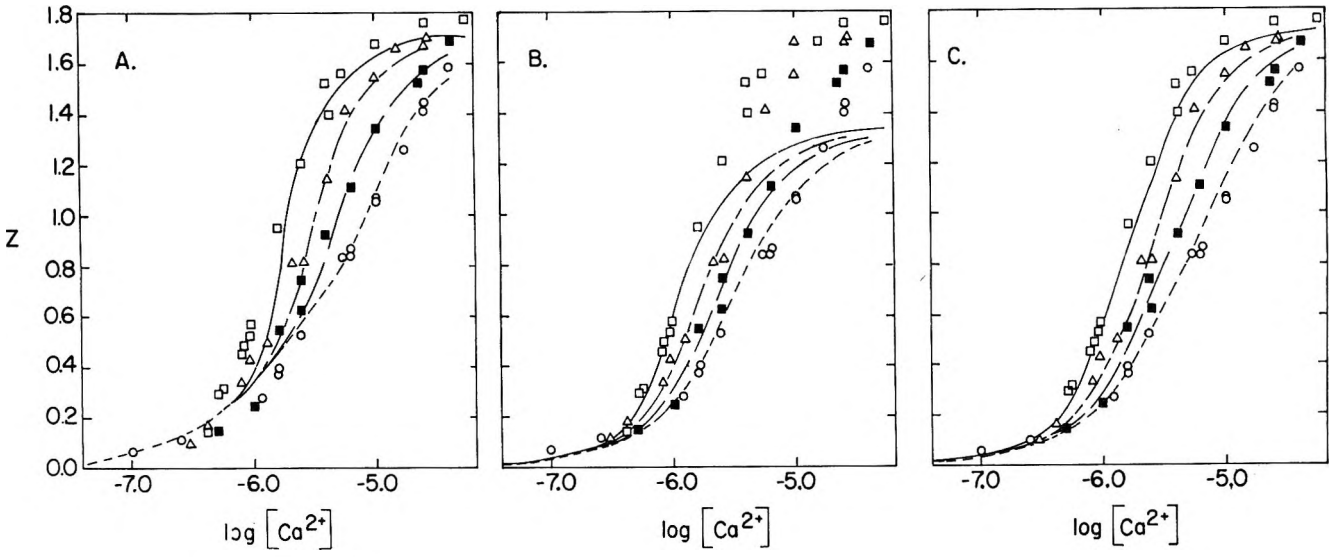

Figure 2. Z *vs.* log $[Ca^{2+}]$, 25°, μ = 0.1 M (TMACl): EHDP = 2.49 × 10^{-4} M, ○ and ——; EHDP = 5.02 × 10^{-4} M, ■ and — —; EHDP = 1.01 × 10^{-3} M, △ and —·—; 2.24 × 10^{-3} M, □ and ——. Lines are computed with assumed log formation constants: A, $\beta_{1,1}$ = 5.74, $\beta_{7,4}$ = 48.2, K_0 (see text) = 4.4; B, $\beta_{1,1}$ = 5.48, $\beta_{4,2}$ = 19.3, $\beta_{4,3}$ = 29.2; C, $\beta_{1,1}$ = 5.52, $\beta_{3,2}$ = 18.8, $\beta_{4,3}$ = 29.1, $\beta_{7,4}$ = 48.2, K_0 = 4.6.

the absence of calcium. Moreover, the degree to which the pH is lowered in this region is dependent on the total H_4EHDP concentration, an indication that polynuclear complexes are formed with calcium ion. Addition of calcium had little, if any, effect on the pH below the second equivalence point showing that complexes did not form in this low pH region. Titrations of H_4EHDP at 0.001 and 0.0001 M were also carried out in the presence of varying amounts of calcium ion. Through these experiments it was found that the pH lowering at constant EHDP concentration was dependent on the concentration of calcium. At the pH of the third equivalence point of the free acid it was found that the ratio of total calcium present in the system, C_{Ca}, to the amount of acid released ($[H^+]_r$) in the system during the complexing reaction, *i.e.*, $C_{Ca}/[H^+]_r$, approached a limiting value of 2.0 as the total calcium in the system approached zero. Since at this pH there is one proton associated with each uncomplexed ligand, and since essentially all calcium becomes bound as the total calcium approaches zero, this indicates that the ratio of bound calcium to proton released must also be 2:1. This is consistent with either a combining ratio of 2:1 (calcium/EHDP) or the existence of mixed calcium–protonic complexes of combining ratios other than 2:1. In the latter case a potentiometric (pH) study, in which bound calcium is indirectly measured by proton release, would give spurious results.

Complexometric Titrations. The formation number, $Z = (C_{Ca} - [Ca^{2+}])/C_{EHDP}$, was evaluated by complexometric titration at several levels of free calcium ion. Given in Table II are the experimental results at four total EHDP concentrations. Curves of Z *vs.* log $[Ca^{2+}]$ (Figure 2) clearly show the dependence of Z on EHDP

Table II: Experimental Z Values at Various Free Ca^{2+} Concentrations at 25°

C_{EHDP} × 10^3 = 2.24		1.01		0.502		0.249	
−log $[Ca^{2+}]$	Z	−log $[Ca^{2+}]$	Z	−log $[Ca^{2+}]$	Z	−log $[Ca^{2+}]$	Z
4.28	1.78	4.56	1.70	4.39	1.68	4.40	1.58
4.60	1.76	4.59	1.68	4.60	1.57	4.40	1.56
5.00	1.68	4.83	1.66	4.64	1.52	4.60	1.44
5.27	1.56	5.00	1.55	5.00	1.34	4.60	1.41
5.39	1.40	5.24	1.41	5.20	1.11	4.76	1.26
5.40	1.52	5.39	1.14	5.40	0.92	4.99	1.06
5.60	1.21	5.59	0.82	5.61	0.62	4.99	1.07
5.80	0.96	5.68	0.81	5.61	0.74	5.19	0.84
6.02	0.57	5.90	0.50	5.80	0.54	5.19	0.86
6.04	0.53	6.03	0.43	6.00	0.24	5.27	0.84
6.08	0.49	6.09	0.33	6.30	0.14	5.62	0.53
6.10	0.45	6.38	0.17	7.60	0.01	5.80	0.37
6.25	0.31	6.53	0.10			5.80	0.39
6.29	0.29	7.60	0.01			5.92	0.27
6.39	0.14					6.60	0.11
7.58	0.01					7.00	0.06
						7.58	0.00

concentration, indicating that the complexes are neither mononuclear nor homonuclear. Computations of the average composition of the complexes were made according to the method of Sillèn,[10] except that EHDP was arbitrarily treated as the nucleus or central group of the complex. To determine $\bar{p}$, the average number of Ca^{2+} bound per complex, and $\bar{q}$, the average number of EHDP bound per complex, it is necessary to evaluate the expression

$$\ln \alpha_0 = \text{constant} + R - \int_{\text{const } B} Z \, d \ln a \qquad (1)$$

where α_0 is the fraction of C_{EHDP}, not complexed by Ca^{2+}, and

$$R = \text{constant} - \int_{\text{const } B} \left(\frac{\partial Z}{\partial \ln B}\right)_a d \ln a = \frac{b + S}{B} \quad (2)$$

In these expressions Z is as defined previously, B and b denote total and free EHDP, respectively, while A and a denote total and free calcium, and S = the sum of the concentration of all complexes, *i.e.*, ΣC_{pq}. After finding R and α_0 it is possible to compute $\bar{p}$ and $\bar{q}$ by

$$\bar{p} = \frac{Z}{R - \alpha_0}; \quad \bar{q} = \frac{1 - \alpha_0}{R - \alpha_0} \quad (3)$$

The evaluation of R begins with plots of Z as a function of log a at each B, similar to those of Figure 2. In this step, a sigmoid curve was fitted to the experimental data by minimizing residuals, without regard to a chemical model. From the derived equation for each of these "best fit" curves, values of Z were interpolated for each B at several levels of constant log a. Equations for Z *vs.* ln B curves at constant a were derived and their slopes, *i.e.*, $(\partial Z/\partial \ln B)_a$, were computed at intervals of 0.1 log a for each experimental B concentration. These slopes, when plotted as a function of ln a produced bell-shaped curves for which areas were calculated. The area under each curve corresponds to $\int_{\text{const } B} (\partial Z/\partial \ln B)_a d \ln a$ and is the major computation required in finding R (integral of eq 2). The integration constant (eq 2) was set at 1.0 by assuming that at the lowest free calcium concentrations (10^{-7} M) $R = 1$. This value is based on the rationalization that at 10^{-7} M free calcium the concentration of all complex species is so low that the sum $(b + S)$ does not differ significantly from B (hence $R = 1$ (eq 2)). The derived R values are shown in Table III. Values of α_0 were obtained by numerically integrating the curves of Z *vs.* ln a using Simpson's rule. The constant of integration (eq 1) was set equal to -1 since α_0 must approach 1.0 as the total calcium approaches zero. Thus

$$\ln \alpha_0 = R - 1 - \int_{\text{const } B} Z \, d \ln a \quad (4)$$

The computed values of α_0 are also shown in Table III along with values of $\bar{p}$ and $\bar{q}$. In calculating $\bar{p}$ and $\bar{q}$ values, experimental points for which $0.1R \geq \alpha_0 \geq 0.9R$ were omitted to avoid undue influence on the values computed using eq 3 caused by taking the difference of two like numbers. A plot of $\bar{p}$ *vs.* $\bar{q}$ is given in Figure 3. From this plot, it is clear that very large complexes are formed in this system. Furthermore, there is no grouping of data which would indicate a natural preference for a particular complex. The data plotted in Figure 3 come rather close to a core-links approximation[14] (Figure 3, line A) the core being $CaEHDP^{2-}$ and each link being Ca_2EHDP. The deviation, however, is quite regular and sizable at high reagent concentrations and always in a direction indicating somewhat less calcium per complex than required by that approximation. One simple mechanism that comes much closer to fitting the observation at high reagent levels is the clustering of small "core–links" complexes. For example, a combination of individual 7:4 complexes produces line B of the $\bar{p}$, $\bar{q}$ diagram (Figure 3).

Table III: Derived Quantities from Turbidimetric Data

$-\log [Ca^{2+}]$	R	α_0	$\bar{p}$	$\bar{q}$
	$C_{EHDP} = 2.24 \times 10^{-3}$ M			
6.00	0.832	0.570	2.27	1.64
5.80	0.679	0.346	2.71	1.96
5.60	0.476	0.174	3.98	2.73
5.40	0.300	0.079	6.55	4.16
5.20	0.185	0.035	10.6	6.38
5.00	0.116	0.015	16.8	9.76
4.80	0.072	0.006	26.4	15.1
	$C_{EHDP} = 1.01 \times 10^{-3}$ M			
6.00	0.896	0.688	1.97	1.49
5.80	0.801	0.491	2.07	1.64
5.60	0.661	0.298	2.51	1.93
5.40	0.478	0.153	3.61	2.61
5.20	0.300	0.071	6.08	4.04
5.00	0.182	0.032	10.4	6.45
4.80	0.111	0.014	17.0	10.1
	$C_{EHDP} = 5.02 \times 10^{-4}$ M			
6.00	0.944	0.770	1.75	1.32
5.80	0.894	0.612	1.69	1.38
5.60	0.822	0.437	1.77	1.46
5.40	0.731	0.227	1.99	1.59
5.20	0.620	0.155	2.41	1.82
5.00	0.492	0.078	3.18	2.22
4.80	0.352	0.036	4.64	3.04
	$C_{EHDP} = 2.49 \times 10^{-4}$ M			
6.00	0.936	0.803	1.71	1.48
5.80	0.879	0.664	1.66	1.56
5.60	0.800	0.502	1.74	1.67
5.40	0.705	0.344	1.95	1.82
5.20	0.602	0.214	2.32	2.02
5.00	0.510	0.124	2.83	2.27
4.80	0.439	0.067	3.42	2.50

In a treatment separate from the above the data (Z, log $[Ca^{2+}]$) were analyzed by making use of Letagropvrid[12] assuming several combinations of small complexes, including those with calcium to ligand ratios of 1:1, 2:1, 1:2, 3:2, 4:3, 5:3, 7:4. For the least-squares refinement, a weighting factor, W_i, of 1.0 was assigned to all data points. The general approach to finding the most satisfying set of formation constants was to start with the simplest, a 1:1 complex, and progressively add assumed complexes (or delete previously

(14) L. G. Sillén, *Acta Chem. Scand.*, 8, 318 (1954).

used ratios) as long as the fit was significantly improved over previous sets. In making the judgment of whether a particular set was significantly better than a predecessor, use was made of the error square sum, U, which in this problem is $\Sigma W_i(Z_{i,calcd} - Z_{i,obsd})^2$ and σ_i, the "standard deviation" for Z_i, that is $(\Sigma W_i(Z_{i,calcd} - Z_{i,obsd})^2$ where n is the number of data points used and N is the number of constants. For a particular trial set of constants and set of data points the value of U is minimized by variation in the constants to reach the "best" values. When the number of constants and/or the number of data points employed is varied, a minimum in σ_i is sought. The judgment must then be made as to whether the σ_i for one set of constants is significantly better than that for another set. In Table IV we give the final values for several sets of assumed constants and the corresponding values of U and σ_i. It seems clear, both from the qualitative observation that the pH titration curves are dependent on concentration and from the behavior of σ_i, that some polynuclear complexes of calcium and EHDP are present in solution.

Table IV: Final Constants for Several Assumed Sets of Complexes

Set	Complex ratio (Ca/EHDP)	Log constant	U	$\sigma_i \times 10^2$
1	1:1	5.83	2.34	20.4
	2:1	10.74		
2	1:1	5.39	1.18	14.7
	2:1	9.87		
	3:2	20.13		
3	1:1	5.78	0.36	7.9
	2:1	9.25		
	3:2	19.28		
	7:4	48.91		
4	1:1	5.82	0.36	8.1
	7:4	48.99		
5[a]	1:1	5.48	0.06	4.4
	3:2	19.32		
	4:3	29.18		
6	1:1	5.56	0.36	8.0
	4:3	28.97		
	7:4	48.60		
7	1:1	5.72	0.32	7.6
	3:2	19.93		
	15:8	106.4		
8	1:1	5.87	0.51	9.6
	15:8	106.5		
9	1:1	5.74	0.36	8.1
	7:4	48.23		
	14:8	100.9		
	21:12	153.4		
10	1:1	5.52	0.23	6.4
	3:2	18.78		
	4:3	29.08		
	7:4	48.23		
	14:8	100.9		
	21:12	153.4		

[a] Data limited only to very low free calcium ion concentrations

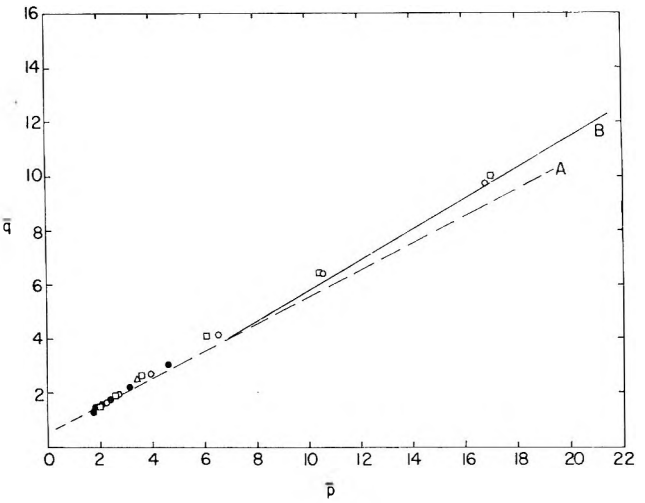

Figure 3. Derived values of $\bar{p}$ and $\bar{q}$, 25°, μ = 0.1 M (TMACl): EHDP = 2.49 × 10^{-4} M, Δ; EHDP = 5.02 × 10^{-4} M, ●; EHDP = 1.01 × 10^{-3} M, □; EHDP = 2.24 × 10^{-3} M, ○. Some points at low p,q are omitted for clarity. A, core–links hypothesis, — — —; B, clusters of 7:4 ratio, —.

It was found that two different sets of three constants were sufficient to describe the extremes of the formation curves. For example, a good fit was obtained at high Z values with the assumption of only 1:1 and 7:4 (Ca/EHDP) complexes (set 4, Table IV). This set of trial constants was then modified, and the fit at high Z values improved further at the expense of fit at low Z values, by the inclusion of an aggregation constant, K_0, representing the hypothetical reaction $Ca_7EHDP_4 + (Ca_7EHDP_4)_n \rightleftarrows (Ca_7EHDP_4)_{n+1}$. The final trial overall constants $\log \beta_{1,1} = 5.74$, $\log \beta_{7,4} = 48.23$, and $\log K_0 = 4.41$ (for $n = 1$ and 2) were used in calculating the lines plotted in Figure 2A.

Using only the lower free calcium ion concentrations a good fit was obtained in the region of lower Z values when a combination of 1:1, 3:2, and 4:3 (Ca/EHDP) complexes was tested (set 5, Table IV). The final trial constants $\log \beta_{1,1} = 5.48 \pm 0.08$, $\log \beta_{3,2} = 19.32 \pm 0.38$, and $\log \beta_{4,3} = 29.18 \pm 0.07$ were used in calculating the lines plotted in Figure 2B. By combination of these results a single set of complexes was found that would fit both ends of the data equally well, at the same time increasing the number of variable parameters from three to five. It is felt that, on the basis of the value of σ_i, the combined set of parameters of set 10 is a significant improvement over either set 4 or set 9. The best compromise constants (set 10, Table IV), fitted over the whole range of experimental calcium concentrations and employed in plotting the complete curves of Figure 2C, were $\log \beta_{1,1} = 5.52 \pm 0.08$, $\log \beta_{3,2} = 18.78 \pm 1.4$, $\log \beta_{4,3} = 29.08 \pm 0.12$, $\log \beta_{7,4} = 48.23 \pm 0.44$, and $\log K_0 = 4.6 \pm 0.9$. (The errors represent twice the standard deviation.)

The choice of the upper limiting ratio of 7:4 (Ca/EHDP), or its multiples, was based on the qualitative observation that the upper limit of Z was apparently close to 1.75. Certainly it is less than 2.0, which would stem from multiples of 2:1, and probably greater than 1.67, that is multiples of 5:3. However, the ultimate size of the aggregates cannot be judged from these measurements.

The system behaves as if a solid phase were present in certain regions of high Z values. Other physical measurements[15] have confirmed the presence of large aggregates, which for long periods of time are stable to precipitation. It does not seem unreasonable to think of the largest of these complexes or aggregates in terms of micelles or crystal nuclei. As such they would be expected to have some of the properties of a new phase. Indeed Sillèn[10] has referred to a solid as a set of "infinite complexes" and has pointed out that when a solid, the components of which are the same as those of the soluble complexes, is present in the system a plot of total metal concentration *vs.* total ligand concentration at constant free ligand concentration should be linear with a slope equal to the ratio of components present in the solid. When the data were plotted in this way (at constant free calcium ion concentration, since calcium was considered the ligand), the slope and thus the ratio of components in the aggregates present in the system was found to be approximately 1.75 for all calcium ion concentrations above about 2×10^{-6} M, even though no solid was visible. As stated above, the simplest complex having this ratio would be Ca_7EHDP_4. From the slope of the above plot and the observed values of $\bar{p}$, $\bar{q}$, we infer the existence of a continuous series of complexes consisting of aggregates of the Ca_7EHDP_4 complex. This inference led to the inclusion of the previously described aggregation constant, K_0, in parameter refinement.

The authors feel that the success of the present treatment verifies Sillèn's supposition that micellar systems may be described both as a solid solution (two-phase system) and as a system of very large complexes. Sillèn has also pointed out,[10] however, that when a "solid" phase is present the calculated value of the constant R (eq 2) will be lower than the true value representative of the solution phase alone. This low value of R would lead to overestimates of both $\bar{p}$ and $\bar{q}$ for the true soluble complexes, although it cannot be known by what amount unless the solid is physically separable from the solution. For this reason the data for calcium concentrations below 2×10^{-6} M are considered to give a more reliable estimate of the formation constants for the soluble complexes.

The authors are not aware of any other example of relatively large polynuclear complexes involving the calcium ion. Metal ions which form covalent bonds with oxygen, and consequently undergo olation during hydrolysis, have been most frequently encountered in such complexes.[16] Since calcium forms predominantly electrovalent bonds, the extension of the normal phosphonate complexes to a series of polynuclear species is surprising.

Appendix

Measurement of the Solubility Product of Calcium Decanoate Monohydrate and the Stability Constant of the Ca–Decanoate Complex. The solid which forms upon mixing solutions of a calcium and a decanoate salt is calcium decanoate monohydrate ($Ca(OOC(CH_2)_8CH_3)_2 \cdot H_2O$). The same phase always forms whether in the absence or presence of a sequestrant. The solubility of this solid was measured under the conditions used for the measurement of the complex formation between calcium and EHDP, *i.e.*, an ionic strength of 0.1 (tetramethylammonium chloride), 25°, pH 11.0, and the same rate of agitation and time of equilibration.

Procedure. The pH of a solution containing the required amounts of tetramethylammonium decanoate and tetramethylammonium chloride was adjusted to 11.0 with tetramethylammonium hydroxide, and the volume was adjusted to 250.0 ml. The system was kept under N_2 to avoid contamination by atmospheric CO_2. A solution of calcium nitrate was added dropwise until a permanent precipitate of calcium decanoate monohydrate formed under agitation. The suspension was agitated for a period of time equal to that used in attaining equilibrium in the complexometric experiments. A sample was then removed and filtered, and the clear filtrate was analyzed for total calcium and total decanoate. The experiment was repeated at several different concentrations of decanoate.

Results. The analytical results and the derived "apparent" ion product are given in Table AI. A plot of the "apparent" ion product *vs.* the total concentration of decanoate in solution is a straight line of slope 130.3×10^{-9} and intercept 2.48×10^{-9}. This line

Table AI: Analytical Concentrations of Ca and $C_9H_{19}COO^-$ in Solutions Equibrated with Solid $Ca(C_9H_{19}COO)_2 \cdot H_2O$

$C_{decanoate}$, $M \times 10^3$	C_{Ca}, $M \times 10^4$	Ion product $\times 10^9$ [a]
1.30	15.86	2.68
5.00	1.227	3.07
10.2	0.367	3.82
21.5	0.115	5.32
54.1	0.0325	9.52

[a] Ion product = $C_{Ca} \times (C_{decanoate})^2$.

(15) B. H. Wiers, *J. Phys. Chem.*, **75**, 682 (1971).

(16) L. G. Sillén, *Proc. Robert A. Welch Found. Conf. Chem. Res.*, **6**, 187 (1962) (published 1963).

may be expressed as IP = $K_{so}(1 + \beta[\text{decanoate}])$, where IP = $C_{Ca} \times (C_{decanoate})^2$, K_{so} = solubility product under the conditions of the experiment, and β = formation constant of the complex (Ca decanoate)$^+$. The intercept is the true solubility product, and the slope (βK_{so}) is a measure of the formation constant of the (Ca decanoate)$^+$ complex, since in the limit as C_{Ca} approaches 0.0, $C_{decanoate}$ approaches [decanoate]. The derived values are $K_{so} = 2.48 \pm 0.04 \times 10^{-9}$, where the error represents the 95% confidence limits, and $\beta = 52.5 \pm 0.9$ for which the error represents the standard deviation.

This formation constant is small and indicates a rather weak complex. The amount of calcium bound in the form of the decanoate complex was calculated for every derived Z value, and when significant, a correction was applied.

Acknowledgments. The authors gratefully acknowledge the assistance of L. G. Sillén in the use of the computer program Letagropvrid as well as helpful discussions with O. T. Quimby and B. H. Wiers, and the experimental assistance of P. Vanden Eynden and Adolf Bierman.

Polynuclear Complex Formation in Solutions of Calcium Ion and Ethane-1-hydroxy-1,1-diphosphonic Acid. II. Light Scattering, Sedimentation, Mobility, and Dialysis Measurements

by Brandon H. Wiers

Miami Valley Laboratories, The Procter & Gamble Company, Cincinnati, Ohio 45224 *(Received September 16, 1970)*

Publication costs assisted by The Procter & Gamble Company

Light scattering, sedimentation, electrophoretic mobility, and dialysis measurements were performed on solutions containing calcium chloride, ethane-1-hydroxy-1,1-diphosphonic acid (EHDP), and tetramethylammonium hydroxide. The data are interpreted as arising from polynuclear Ca_pEHDP_q aggregates having, in 1.5:1 Ca^{2+}/EHDP solutions, molecular weights of the order of 10^4 g/mol, radii of *ca.* 26 Å, and charges of *ca.* −20 esu.

Introduction

Complexometric and pH titration data of Grabenstetter and Cilley indicate that calcium ions and ethane-1-hydroxy-1,1-diphosphonic acid (EHDP™) interact to form polynuclear aggregates with very high molecular weights.[1] This is in contrast to the behavior of such ligands as mercaptoacetic acid,[2] malic acid,[3] and ethyleneglycolbis(β-aminoethyl ether)tetraacetic acid,[4] which have been reported to form complexes, M_pL_q, with such ions as Zn^{2+} and Cu^{2+} in which p and q are of the order of 4 to 6. It is significant that EHDP appears to produce polynuclear complexes with Ca^{2+} in which p and q attain values of the order of hundreds. Because of the unprecedented nature of these findings, it appeared appropriate to seek independent experimental evidence for the existence of the aggregates by means of the macromolecular techniques of light scattering, sedimentation, electrophoresis, and dialysis. This paper reports the results of such measurements.

Experimental Section

Chemicals. Untagged calcium chloride was "Baker Analyzed" $CaCl_2 \cdot 2H_2O$. $^{45}CaCl_2$ was obtained as an aqueous solution from Oak Ridge. Tetramethylammonium chloride (TMACl) obtained from Eastman was freed from its gross impurities by filtration of all stock solutions through 0.45-μ Millipore filters. Tetramethylammonium hydroxide (TMAOH) was obtained from Matheson Coleman and Bell in the form of a 25% aqueous solution and passed through a Dowex 21K exchange column in the hydroxyl form prior to use. Baker and Adamson silicotungstic acid (STA) was used without further treatment. Likewise, "Fisher Certified" ethylenediaminetetraacetic acid (EDTA) was

(1) R. J. Grabenstetter and W. A. Cilley, *J. Phys. Chem.*, 75, 676 (1971).

(2) D. D. Perrin and I. G. Sayce, *J. Chem. Soc.*, 82 (1967).

(3) C. F. Timberlake, *ibid.*, 5078 (1964).

(4) K. H. Schroder, *Acta Chem. Scand.*, 19, 1347 (1965).

used without further treatment. Untagged EHDP and ^{14}C-tagged EHDP were prepared by the addition of acetic anhydride to phosphorous acid.[5]

Apparatus. Light scattering measurements were made with a Brice-Phoenix light scattering photometer (Series 2000) in the early stages of the work and with a Sofica light scattering photometer (Model 7200) in the latter stages. The Brice-Phoenix instrument was modified[6] to permit a check of sample fluorescence and calibrated with Debye polystyrene.[7] The Sofica was calibrated with benzene. Unpolarized 4358-Å light was used as the incident radiation in both cases.

Refractive index increments were determined using a Brice-Phoenix differential refractometer calibrated with sucrose solutions.

Sedimentation data were obtained using a Spinco Model E analytical ultracentrifuge equipped with schlieren optics. For sedimentation velocity experiments standard Kel-F 12-mm cells were used. In the approach-to-equilibrium experiments, a capillary-type, single-sector Epon synthetic boundary cell was used. Sedimentation coefficients were determined by least-squares analysis of log x_H *vs.* time plots (where x_H is calculated from the maximal ordinate of the peak position). Peak areas in the approach-to-equilibrium runs were determined by planimetry from tracings of enlarged schlieren patterns.

Densities were determined by means of 25-ml pycnometers and a Sartorius direct reading analytical balance.

Viscosities were measured in a 10-ml Cannon-Fenske viscometer with a flow time for water of *ca.* 70 sec at room temperature.

Electrophoretic mobilities were obtained using a Spinco Model H Tiselius moving boundary electrophoresis instrument.

Radioactivity assays were performed with a Geiger-Mueller end window tube.

A Corning Model 12 pH meter was used for all pH measurements.

Procedures. All samples used in this study were prepared from prefiltered (0.30- or 0.45-μ Millipore filters) stock solutions and then refiltered prior to measurement under nitrogen pressure in a nitrogen atmosphere. Stock solutions of EHDP and EDTA were added to calculated amounts of stock TMACl, and pH was adjusted to greater than the desired value with TMAOH. Stock $CaCl_2$ was then added, and the pH was readjusted to the desired value while diluting to final volume. Scattering intensities were obtained at a series of angles between 25 and 135°. Depolarization ratios, dissymmetries, and fluorescence characteristics were determined and found to require no corrections.

Union Carbide dialysis tubing (No. 20) was prepared for use by repeated boiling and rinsing in singly distilled water followed by soaking in doubly distilled water to which a small amount of benzoic acid was added. Sections (10 in.) were cut and filled with 25 ml of solution, knotted, and placed in stoppered 50-ml graduate cylinders containing 25 ml of solvent. The cylinders were shaken on a Burrell shaker in a thermostat at 30 ± 1° until measurement.

Results and Discussion

If a "core + links" mechanism is obeyed by a metal–ligand system, as is approximately the case here,[1] and if sample solutions are prepared with identical Ca^{2+} to EHDP mole ratios and free Ca^{2+} ion concentrations, $[Ca^{2+}]$, negligible compared to total Ca^{2+} ion concentrations, $C_{Ca^{2+}}$, then the compositions of the systems are identical.[8] Symbolically, if $Z = (C_{Ca^{2+}} - [Ca^{2+}])/C_{EHDP}$ (where C_{EHDP} is the total EHDP concentration) is constant, then species distribution remains constant. Based on the previous studies,[1] this was ensured by restricting the samples used in this study to either 1.5 mol of Ca^{2+}/mol of EHDP or 1.75 mol of Ca^{2+}/mol of EHDP with $C_{EHDP} \gtrsim 1.25 \times 10^{-3} M$.

The properties measured in this study showed no dependence on the order of mixing of reagents. However, precipitates of Ca_2EHDP were discovered in the samples after long standing (weeks to months), suggesting a metastable equilibrium state for the complexes. The introduction of seed crystals into clear solutions did not hasten precipitation, however, so it was concluded that the test samples were at equilibrium at the time of study. The precipitation phenomenon was not investigated further in this work.

Light Scattering. Rayleigh ratios were obtained for two series of 1.5:1 Ca^{2+}/EHDP solutions in one of which all samples were prepared directly from appropriate stock solutions of $CaCl_2$ and EHDP, in the other of which samples were prepared by dilution with 1.0 M TMACl from a single sample containing 0.10 M EHDP and 0.15 M $CaCl_2$. In the first series quantities were chosen so as to maintain $[Cl^-]$ = constant = $C_{TMACl} + 2C_{CaCl_2} = 1.0\ M$; in the other the Cl^- contribution from $CaCl_2$ was neglected with the result that $[Cl^-] \gtrsim 1.0\ M$. Such variations as occurred in the ionic strength in the latter series did not introduce any significant error, however. Hence the two series of solutions are treated as one. In all samples adjustment was made to pH 11.0 using TMAOH.

As a check on the light scattering technique a series of silicotungstic acid (STA) solutions in a supporting electrolyte of 1.0 M NaCl was also measured. STA was chosen because of its excellent characterization in

(5) B. T. Brooks, *J. Amer. Chem. Soc.*, **34**, 496 (1912); O. T. Quimby, U. S. Patent 3,387,024 (1966).

(6) B. A. Brice, G. C. Nutting, and M. Halwer, *J. Amer. Chem. Soc.*, **75**, 824 (1953).

(7) The polystyrene sample was "Styron 1960" with $\tau = 3.16 \times 10^{-3}$ cm^{-1} obtained from P. Debye, Cornell University.

(8) R. S. Tobias and S. Y. Tyree, Jr., *J. Amer. Chem. Soc.*, **81**, 6385 (1959).

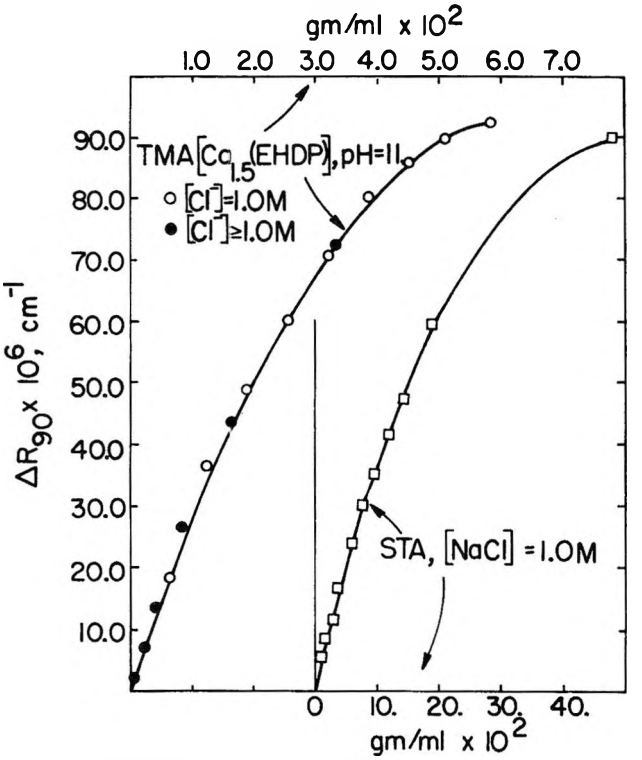

Figure 1. Rayleigh ratios of STA and TMA[$Ca_{1.5}$(EHDP)] solutions.

several previous studies.[9,10] The pH of the STA samples was not adjusted.

Excess Rayleigh ratios, $\Delta R_{90} = R_{90}(\text{soln}) - R_{90}(\text{solv})$, for the Ca–EHDP and STA solutions are displayed as a function of concentration in Figure 1. The range of Rayleigh ratio values is similar in the two cases; however, it is to be noted that the STA concentration range is much greater.

Refractive index measurements performed on the STA solutions yielded a value for the refractive index increment, dn/dc, of 0.1060 ± 0.0025 ml/g. This is to be compared with the value of 0.1065 ± 0.0014 ml/g reported by Johnson, Kraus, and Scatchard[11] and the value of 0.107 ml/g reported by Kronman and Timasheff.[9] The value of the refractive index increment obtained for TMA[$Ca_{1.5}$(EHDP)] in 1.0 M TMACl at pH 11.0 is dn/dc = 0.158 ± 0.004 ml/g.

The light scattering data were analyzed by the method of Tobias and Tyree,[8,12] *i.e.*, in terms of the equation

$$\frac{1}{N_{z'}} = \frac{\phi H'' \Psi'^2 m'}{\tau^*} - \frac{z'^2 m'}{2m_3} \qquad (1)$$

where $N_{z'}$ gives the degree of aggregation, ϕ is the solvent volume fraction, and m_3 is the molarity of the supporting electrolyte. The quantities Ψ', m', and z' are, respectively, the refractive index increment, molarity, and the magnitude of the negative charge of the quasi "monomeric component" defined, following Scatchard,[13] as follows.

$$\left[(\text{TMA})_{\bar{\nu}}\text{Ca}_{1.5}(\text{EHDP})^{-(1-\bar{\nu})} + (1-\bar{\nu})\text{TMA}^+ - \left(\frac{1-\bar{\nu}}{2}\right)\text{TMACl}\right]$$

With this definition it is found that $z' = 1 - \bar{\nu}$, $\Psi' = dn/dm' - (z'/2)(dn/dm_3)$, and $m_3 = 1.00 + (z'/2)m'$. Finally, we have that $\tau^* = (16\pi/3)\Delta R_{90}$ and $H'' = 8000\pi^3(n + n_0)^2/3N\lambda^4$, where n and n_0 are the refractive indexes of solution and solvent, respectively, N is Avogadro's number, and λ is the wavelength of the incident radiation.

The results of the analysis are shown in Figure 2. Here $1/N_{z'}$ is plotted *vs.* m' for each of several guesses at z'. The best value is that which renders the value of $1/N_{z'}$ independent of m'. This value is $z' \cong 0.7$. The corresponding degree of aggregation is found to be $N_{z'} = 33 \pm 3$ so that the total charge of the aggregates is $z = -20$. By definition the formula weight of the monomeric component is $M' = M_{\text{TMA[Ca}_{1.5}\text{(EDHP)]}} - (z'/2)M_{\text{TMACl}} = (336) - (0.35)(109.6) = 298$. Thus the aggregate molecular weight is $M = (9.8 \pm 1.0) \times 10^3$.

Sedimentation. Sedimentation coefficients were obtained at a rotor speed of 59,780 rpm for all of the TMA[$Ca_{1.5}$(EHDP)] samples examined in the light scattering experiments save one, *viz.*, the most dilute (1.25×10^{-3} M). Thus it appears necessary to use solutions containing *ca.* 5×10^{-3} M (*ca.* 0.2%) or greater to obtain useful schlieren data. All patterns obtained were unimodal and symmetrical.

Observed sedimentation coefficients, s, for TMA[$Ca_{1.5}$(EHDP)] samples were converted into standard conditions (20°) by means of the relation[14]

$$s_{20,w} = s\left(\frac{\eta_T}{\eta_{20}}\right)\left(\frac{\eta}{\eta_0}\right)\left(\frac{1-\bar{\nu}\rho_{20,w}}{1-\bar{\nu}\rho_T}\right) \qquad (2)$$

in which (η_T/η_{20}) is the viscosity of water at the ultracentrifuge operating temperature, T, relative to the viscosity of water at 20°, (η/η_0) is the viscosity of the solvent (1.0 M TMACl at pH 11.0) relative to water at temperature T, $\rho_{20,w}$ and ρ_T are the densities of water and solvent at 20° and at operating temperature, respectively, and $\bar{\nu}$ is the partial specific volume of TMA[$Ca_{1.5}$(EHDP)]. Values for (η_T/η_{20}) were obtained from the tables of Svedberg and Pedersen[15] and values

(9) M. J. Kronman and S. N. Timasheff, *J. Phys. Chem.*, **63**, 629 (1959).

(10) W. H. Nelson and R. S. Tobias, *Inorg. Chem.*, **2**, 985 (1963).

(11) J. S. Johnson, K. A. Kraus, and G. Scatchard, *J. Phys. Chem.*, **64**, 1867 (1960).

(12) R. S. Tobias and S. Y. Tyree, Jr., *J. Amer. Chem. Soc.*, **82**, 3244 (1960).

(13) G. Scatchard, *ibid.*, **68**, 2315 (1946).

(14) H. K. Schachman, *Methods Enzymology*, **4**, 32 (1957).

(15) T. Svedberg and K. D. Pedersen, "The Ultracentrifuge," Oxford University Press, London, 1940.

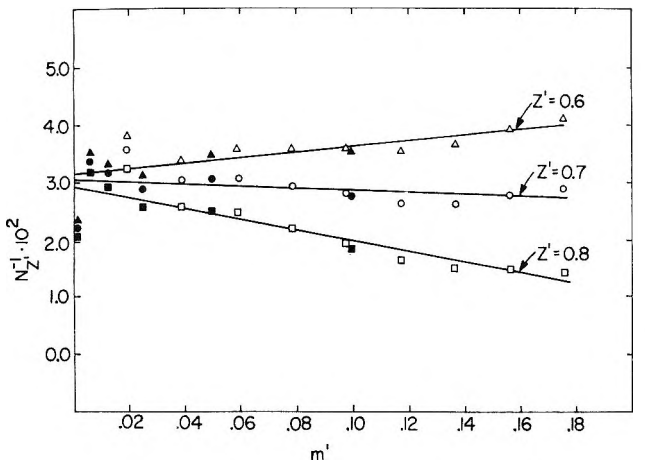

Figure 2. $N_{Z'}^{-1}$ *vs.* the molar concentration of TMA[$Ca_{1.5}$(EHDP)] with z' as a parameter.

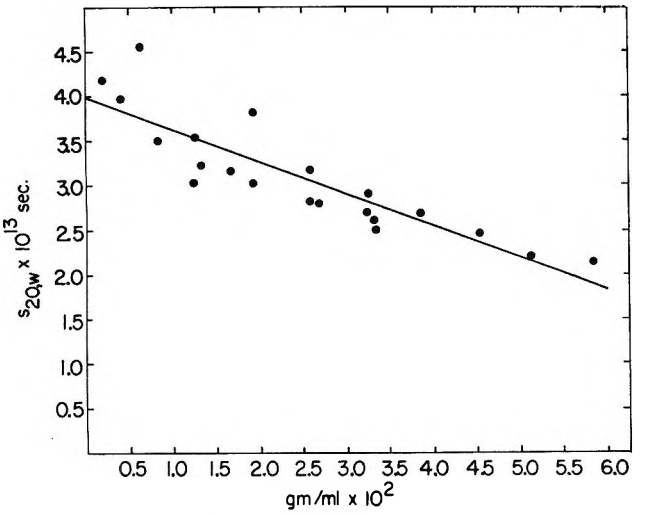

Figure 3. Sedimentation coefficients of TMA[$Ca_{1.5}$(EHDP)] solutions.

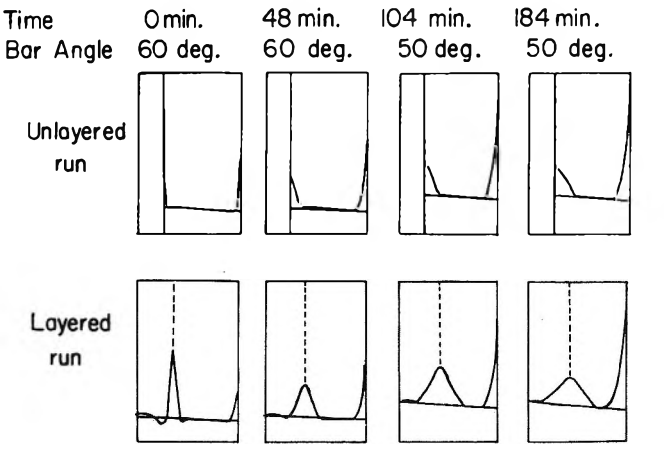

Figure 4. Ultracentrifuge patterns in "approach-to-equilibrium" experiments using a synthetic boundary cell containing 0.04 *M* TMA[$Ca_{1.5}$(EHDP)] in 1.0 *M* TMACl at pH 11.0 (TMAOH); operating speed 12,590 rpm.

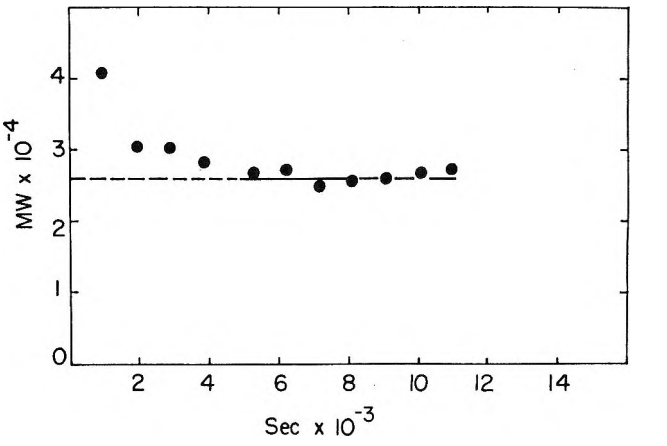

Figure 5. Time dependence of molecular weight estimated from 0.04 *M* TMA[$Ca_{1.5}$(EHDP)] in 1.0 *M* TMACl at pH 11.0.

for (η/η_0) were determined experimentally by measurements at 10.0, 21.1, 26.7, and 37.8°. The result was that within experimental error (η/η_0) was independent of temperature over the indicated range and equal to the value 1.169 ± 0.013. Over the range of rotor temperatures encountered in practice, ρ_T was found to be insignificantly different from unity. The room temperature densities of nine TMA[$Ca_{1.5}$(EHDP)] solutions in the concentration range 0.0196–0.176 *M* were found to vary linearly with concentration. Thus $\bar{v}$ was found to be independent of concentration with a value of 0.462 ± 0.009 ml/g.

To eliminate interparticle effects, $s_{20,w}$ values are plotted *vs.* concentration in Figure 3 and extrapolated to zero concentration. The line of least squares has the intercept $s^\circ_{20,w} = (3.99 \pm 0.27) \times 10^{-3}$ sec and a correlation coefficient of $R^2 = 0.779$.

A molecular weight estimate and a diffusion constant estimate were obtained from an "approach-to-equilibrium" ultracentrifuge experiment performed on a 0.04 *M* TMA[$Ca_{1.5}$(EHDP)] solution following the procedure of Ehrenberg[16] using a rotor speed of 12,590 rpm. In this method two experiments are performed using a synthetic boundary cell, one with and the other without solvent layering. From enlarged tracings of patterns such as shown in Figure 4 data are obtained which permit evaluation of the expression

$$\frac{s}{D} = \frac{k y_m}{\omega^2 r_m (A_l - A)} \tag{3}$$

where y_m is the distance from the base line to the intersection of the refractive index gradient curve and the meniscus in the unlayered run, A is the area under this curve, A_l is the area under the gradient curve obtained in the layered run, ω is the rotor speed, r_m is the distance of the meniscus from the center of the rotor, and k is the enlargement in the x direction. Equation 3 is based on

(16) A. Ehrenberg, *Acta Chem. Scand.*, 11, 1257 (1957).

the requirement of zero transport through the meniscus at all times during the experiment. The s/D values obtained in this way were converted into molecular weights by means of the equation

$$M = \frac{s}{D}\frac{RT}{1 - \bar{v}\rho} \quad (4)$$

where D is the diffusion constant, R the gas constant (8.314×10^7 ergs/(mol deg)), T is the absolute temperature, $\bar{v}$ the partial specific volume, and ρ the density of the solvent. As a function of time the calculated molecular weights vary as shown in Figure 5. Extrapolation to zero time of the least-squares line through all but the first four points yields the estimate $\bar{M}_w = (2.62 \pm 0.33) \times 10^4$. The first four points are thought to be especially uncertain for two reasons: because of the difficulty in determining the point of intersection of the refractive index gradient curve and the meniscus pattern of the unlayered run at short times, and because of the irregular shape of the curve in the layered run at short times. The diffusion coefficient determined for this sample, based on 17 exposures, is $D = (7.09 \pm 0.20) \times 10^{-7}$ cm^2/sec.

An estimate of $D^\circ_{20,w}$, the diffusion coefficient at standard conditions and zero concentration, is obtained by combining the value for $s^\circ_{20,w}$ obtained from the velocity runs with the molecular weight obtained from the approach-to-equilibrium runs. Using the values $s^\circ_{20,w} = 3.99 \times 10^{-13}$ sec and $\bar{M}_w = 2.62 \times 10^4$ g/mol, it is found that $D^\circ_{20,w} = 6.98 \times 10^{-7}$ cm^2/sec. This value is very close to the experimental diffusion coefficient, and the implied concentration dependence of D is quite similar to that of bovine serum albumin.[17] With this $D^\circ_{20,w}$ it is found that the frictional coefficient, f, appropriate to TMA[$Ca_{1.5}$(EHDP)] aggregates is equal to 5.80×10^{-8}, and with $\eta_{TMACl} = 1.171 \times 10^{-2}$ P it is found that the equivalent spherical radius of the aggregates is $R_e = 26.2$ Å. Using $\bar{M}_w = 2.62 \times 10^4$g/mol and the experimental partial specific volume, it is found[18] that the lower limit to the frictional coefficient is $f_{min} = 3.73 \times 10^{-8}$. This gives a ratio, f/f_{min}, equal to 1.55, a value similar to the values for globular proteins, indicating that the combined effects of asymmetry and hydration are small.

Electrophoresis and Dialysis Measurements. The electrophoretic pattern produced by the 0.04 M TMA-[$Ca_{1.5}$(EHDP)] solution used in the "approach-to-equilibrium" run is shown in Figure 6. The current used in the experiment was 6.0 mA, and the electric field strength, based on a specific conductivity for 1.0 M TMACl at pH 11.0 of $\kappa = 0.0281$ ohm^{-1} cm^{-1}, was 1.71 V/cm. The leading peak in the descending arm gave a mobility of $U = -9.03 \times 10^{-5}$ cm^2/(V sec). The trailing peak is assumed to be "anomalous," as are similar peaks obtained from experiments with purely separated proteins.[19] Using the mobility of the leading peak in combination with the estimated particle radius

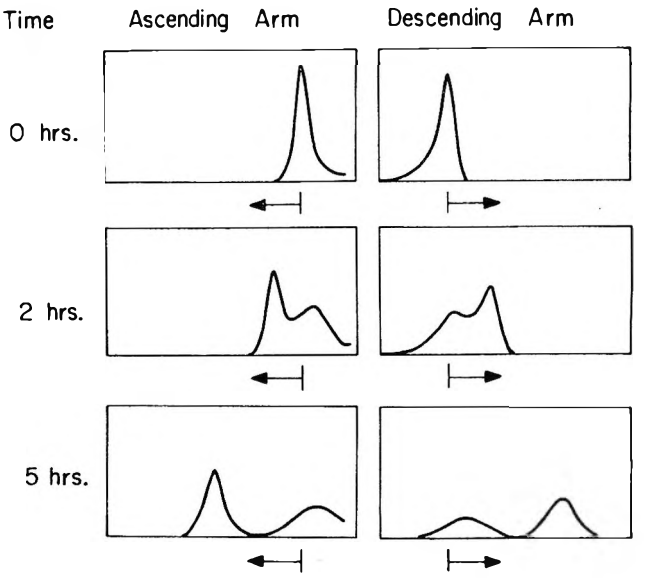

Figure 6. Electrophoresis patterns obtained from 0.04 M TMA[$Ca_{1.5}$(EHDP)] in 1.0 M TMACl at pH 11.0.

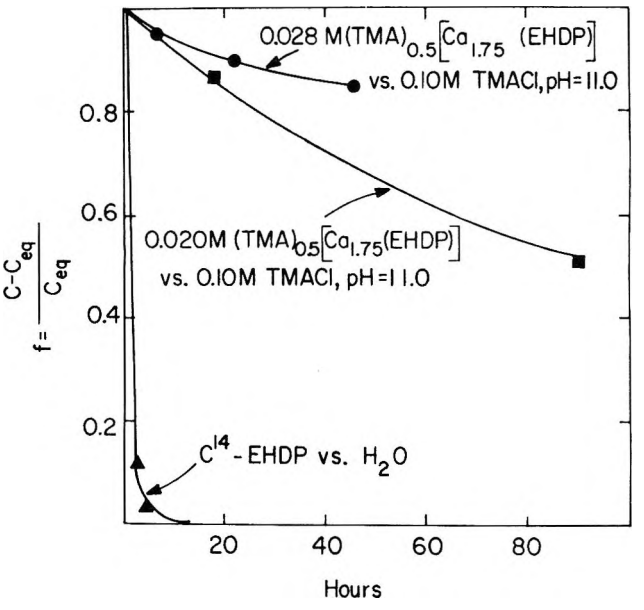

Figure 7. Fraction of undialyzed ^{14}C-EHDP as a function of time.

(26.2 Å), it is calculated from Henry's equation[20] that $z = -26$.

Dialysis experiments yielded the results shown in Figure 7. The calculations of the fraction of undialyzed ^{14}C-EHDP are based on measurements of radioactivity inside the dialysis tubing. As a check for adsorption and/or entrainment, measurements of radioactivity

(17) M. L. Wagner and H. A. Scheraga, *J. Phys. Chem.*, 60, 1066 (1956).

(18) C. Tanford, "Physical Chemistry of Macromolecules," Wiley, New York, N. Y., 1961, p 356 ff.

(19) R. A. Alberty, *J. Chem. Educ.*, 25, 426, 619 (1948).

(20) Reference 18, p 414 ff.

were also made on samples from the solutions outside the tubing. From lack of mass balance it was inferred that significant adsorption and/or entrainment did occur (2.5% at the termination of the 0.028 *M* experiment and 13.8% at the termination of the 0.020 *M* experiment) and that this increased with time. In addition to this, in both experiments precipitation occurred (probably Ca_2EHDP) prior to the desired time of completion of the experiments. Measurements were also made of $^{45}CaCl_2$ and $(TMA)_{0.5}[Ca_{1.75}(EDTA)]$ dialysis rates. In the first case an equilibrium distribution was reached in less than 2 hr with no apparent adsorption, and in the second case in less than 18 hr also with no significant absorption. These experiments clearly establish that the Ca_pEHDP_q aggregates depolymerize slowly and confirm that they have radii comparable to or greater than 24 Å, the mean radius of the pores of the dialysis tubing.

Summary and Conclusions

These results qualitatively corroborate the finding of Grabenstetter and Cilley[1] that high-molecular-weight polynuclear aggregates are formed from the reaction of Ca^{2+} with EHDP. This is significant both because of the size of the aggregates and because polynucleation with Ca^{2+} is heretofore unprecedented.

The numerical estimates of molecular weight obtained in this work disagree with one another and with that of the largest aggregates postulated by Grabenstetter and Cilley. The disagreement with their work undoubtedly stems from the use of generally higher concentrations in this work. It would be a rare circumstance if their constants were in fact transferable to the higher range both because of the inherent limitations of their calculational scheme and because of the strong possibility that these systems might be continuously aggregating systems.

The evidence from this work is consistent with the hypothesis that Ca_pEHDP_q systems undergo continuous aggregation up to a concentration point at the low end of the present range. That they are not continuously aggregating systems thereafter seems to be indicated by the overall linearity of the plot of light scattering data (Figure 2) and the regular decline of sedimentation coefficients (Figure 3). Both curves would be expected to show curvature otherwise.

The disagreement between light scattering and sedimentation molecular weight estimates is rather larger than expected based on this model. The evidence at this point is insufficient to conclude that the difference is significant, however, because the Ehrenberg sedimentation analysis does not account for high concentrations of supporting electrolyte. The effect of this neglect is to overestimate molecular weight, as deduced from equations derived by Gustafson and Martell.[21] However, should the electrolyte effect fail to account for the full extent of the discrepancy, it is quite possible that the systems are polydisperse. This remains an open question in spite of symmetrical unimodal schlieren patterns.[22] If the short-time results shown in Figure 5 were in fact significant, it would be concluded that the sample was polydisperse.[16] To resolve this question it is recommended that additional approach-to-equilibrium runs be done at different rotor speeds and different concentrations.

Acknowledgments. The author gratefully acknowledges fruitful theoretical discussions with K. W. Herrmann, L. Benjamin, and W. L. Courchene, the experimental assistance of W. L. Gagen, N. E. Gilman, H. H, Schumacher, H. W. Lampe, and J. Knappenberger, and the preparation of tagged EHDP by S. B. Affleck.

(21) R. L. Gustafson and A. E. Martell, *J. Amer. Chem. Soc.*, 82, 5610 (1960).

(22) J. R. Cann, "Interacting Macromolecules," Academic Press, New York, N. Y., 1970, Chapter 4.

Proton Exchange between Guanidinium Ion and Water in Water–*N*,*N*-Dimethylacetamide Mixtures[1]

by K. C. Tewari, F. K. Schweighardt, and N. C. Li*

Department of Chemistry, Duquesne University, Pittsburgh, Pennsylvania 15219 *(Received July 13, 1970)*

Publication costs assisted by the National Institutes of Health

The proton exchange between guanidinium ion (GuH^+) and water in water–*N*,*N*-dimethylacetamide (D) mixtures has been studied by means of proton nmr. At a temperature of 34 ± 1°, in the pH range 5.0–6.8 and over a concentration range of 30–50% (by volume) of water, the mean lifetime of proton at guanidinium sites is given by $1/\tau_{GuH^+} = [K_1(H_2O)^2][k_1K_w + k_2(H^+)]/[(D)(H^+)]$, where the constants K_1, k_1, k_2, and K_w refer to eq 1–3 and 10, respectively. The values of $K_1k_1K_w$ and K_1k_2 were determined to be 1.86×10^{-7} and 5.3×10^{-2}, respectively. These are compared with the values obtained when D = dimethyl sulfoxide (ref 3): $K_1k_1K_w = 6.8 \times 10^{-8}$, $K_1k_2 = 14.2 \times 10^{-2}$.

Introduction

It is well known that water molecules play an important role in proton transfer between protonated and unprotonated amines.[2] Recently Tewari, *et al.*,[3] studied the proton exchange between guanidinium ion (GuH^+) and water in water–dimethyl sulfoxide (DMSO) mixtures by means of proton nuclear magnetic resonance. The following mechanism was found to be consistent with their results

$$D_nGu(H)^+\cdots D + HOH = D_nGu(H)^+\cdots OH_2 + D \quad K_1 \quad (1)$$

$$D_nGu(H)^+\cdots OH_2 + OH^- \xrightarrow{k_1} D_nGu(H)^+\cdots OH^- + HOH \quad (2)$$

$$D_nGu(H)^+\cdots OH_2 + HOH \xrightarrow{k_2} D_nGu(H)^+\cdots OH^- + H_3O^+ \quad (3)$$

$$D_nGu(H)^+\ldots OH^- = D_nGu\ldots(H)OH \quad K_2 \quad (4)$$

$$D_nGu\ldots(H)OH = D_nGu + (H)OH \quad K_3 \quad (5)$$

where D represents an organic solvent molecule. The second and third steps are rate determining; the last two steps effect the proton transfer but are not rate determining. The values of $K_1k_1K_w$ and K_1k_2 were determined to be 6.8×10^{-8} and 14.2×10^{-2}, respectively, at a temperature of 34° in the pH range 5.7–8.5 and over a concentration range of 10–50% (by volume) of water.

In order to determine more explicitly the role organic solvents play in such exchange processes, we have further investigated the exchange of protons between guanidinium ion and water molecules in water–*N*,*N*-dimethylacetamide (DMAC) mixtures. DMAC was chosen because it is an analog of proline and hydroxyproline which contain no NH groups when present in peptide linkages. Guanidinium ion is of great interest because it is a well known denaturing agent for proteins.[4–6]

Experimental Section

Materials. Guanidinium chloride was obtained from Nutritional Biochemical Corp., and was used without further purification.

Anal. Calcd for CH_6N_3Cl: C, 12.57; H, 6.34; N, 43.98; Cl, 37.11. Found: C, 12.75; H, 6.35; N, 43.83; Cl, 36.94. Fisher Certified reagent grade *N*,*N*-dimethylacetamide was purified by successive vacuum distillations after drying over molecular sieves. Water used was deionized and doubly distilled. Aqueous sodium hydroxide was used to vary the pH of the solutions in the range 5.0–6.8. The largest value of the final concentration of the alkali was 2.0×10^{-3} mol/l. Under these conditions no sodium ion error was found. pH measurements were made with a Corning Model 10 pH meter equipped with Sargent Combination electrodes.

Nmr Measurements. Nmr spectra were obtained with a Perkin-Elmer R-20 nmr spectrometer, operated at 60 MHz and at an ambient temperature of 34 ± 1°. Care was taken to keep the radiofrequency power level well below saturation and the field homogeneity such that a resolution of 0.3 Hz or better was attained.

Line positions and widths were measured by means of

(1) This investigation was supported by the National Institutes of Health through Grant No. GM 10539-08.

(2) E. Grunwald and A. Y. Yu, *J. Amer. Chem. Soc.*, **90**, 29 (1968).

(3) K. C. Tewari, N. C. Li, and R. J. Kurland, *J. Phys. Chem.*, **73**, 2853 (1969).

(4) H. Edelhock, *Biochemistry*, **6**, 1948 (1967).

(5) C. Tanford, K. Kawahara, and S. Lapanje, *J. Amer. Chem. Soc.*, **89**, 729 (1967).

(6) Y. Nozaki and C. Tanford, *ibid.*, **89**, 736 (1967).

an externally monitored frequency sweep; these measurements are accurate to 0.1 Hz.

Rate Measurements. The reciprocal of the mean lifetime, $1/\tau_{GuH^+}$, of a proton at the amino group of guanidinium chloride in water–DMAC mixtures was calculated from the broadening of the amino line according to the equation for slow exchange.[7] The line frequency difference between the guanidinium ion and water signals is large enough here so that the GuH^+ line widths reflect lifetime broadening, *i.e.*, eq 6 applies. Moreover, contributions to $1/T_2$ from mechanisms such as scalar spin coupling with nitrogen-14 nuclei (which are rapidly relaxing *via* a quadrupolar mechanism) should remain sensibly constant over the range of experimental conditions employed.[3]

$$1/\tau_{GuH^+} = 1/T_2' - 1/T_2 \qquad (6)$$

In eq 6, T_2' is the measured transverse relaxation time of the exchange broadening and T_2 is the relaxation time due to all other processes except exchange. For a Lorentzian line, the full width at half-height in hertz is related to the transverse relaxation time by the equation

$$\Delta = 1/\pi T_2 \qquad (7)$$

The value of $1/T_2$ was obtained by plotting $1/T_2'$ *vs.* water concentration and extrapolating to zero water concentration; it was nearly identical with the value obtained in pure DMAC.

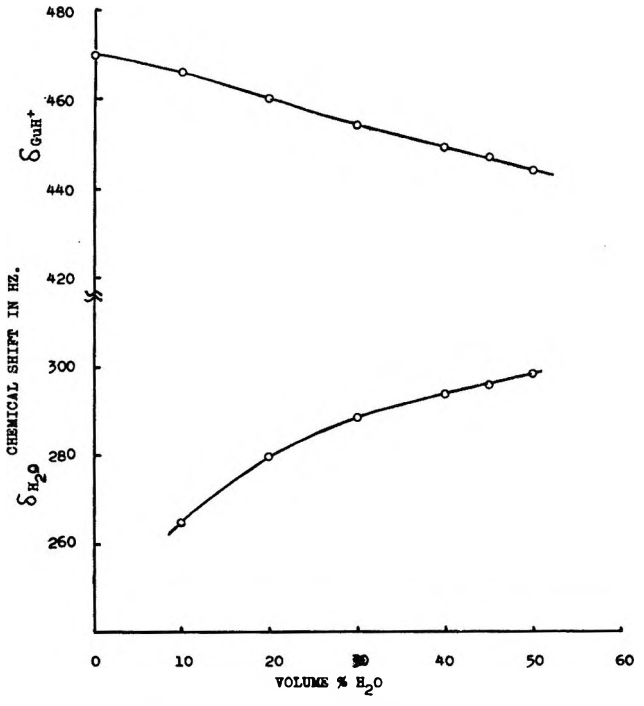

Figure 1. Variation of chemical shift (relative to external TMS and downfield from it) as a function of volume per cent H_2O in H_2O–DMAC solutions containing 0.900 *M* GuH^+.

Results

The amino groups of guanidinium chloride are equivalent and the chemical shift of 0.900 *M* GuHCl in pure DMAC is 470.0 Hz (relative to external TMS, uncorrected for magnetic susceptibility), with a line width of 4.7 Hz. For solutions of 0.900 *M* GuHCl in water–DMAC mixtures, the chemical shifts vary in the manner shown by Figure 1. Table I lists the values of

Table I: Specific Rates of Exchange for GuH^+ as a Function of $1/(H^+)$ and Volume Per Cent H_2O in H_2O–DMAC Mixtures[a]

$1/(H^+) \times 10^6$	Δ, Hz GuH^+	$1/\tau_{GuH^+}$
	30% H_2O	
1.4	5.5	2.51
2.4	5.6	2.82
4.0	5.9	3.80[b]
4.6	6.0	4.20
5.8	6.3	5.10
6.1	6.4	5.20[b]
6.8	6.5	5.60
	40% H_2O	
0.97	6.5	5.75
2.00	7.1	7.40
2.75	7.4	8.58
3.35	7.7	9.40
4.80	8.4	11.5
8.30	9.9	16.5
	45% H_2O	
1.58	7.9	10.30
2.24	8.4	11.6
2.88	9.0	13.6
4.57	10.2	17.2
7.94	12.8	25.44
	50% H_2O	
0.30	7.4	8.5
1.00	7.9	10.1
1.75	8.5	12.0
4.10	10.5	18.2

[a] (GuHCl) = 0.900 *M*, except where otherwise noted. [b] (GuHCl) = 0.700 *M*.

$1/\tau_{GuH^+}$ as a function of $-\log (H^+)$ in various water–DMAC mixtures where (H^+) is represented by the equation

$$(H^+) = 10^{-(pH'-f)} \qquad (8)$$

In eq 8, pH′ is the pH meter reading for a guanidinium chloride solution and f is a correction factor, obtained in separate experiments as the pH meter reading for 0.01 *M* HCl in a given water–DMAC mixed solvent, minus the pH meter reading for 0.01 *M* HCl in water as sol-

(7) J. A. Pople, W. G. Schneider, and H. J. Bernstein, "High Resolution Nuclear Magnetic Resonance," McGraw-Hill, New York, N. Y., 1959, p 221.

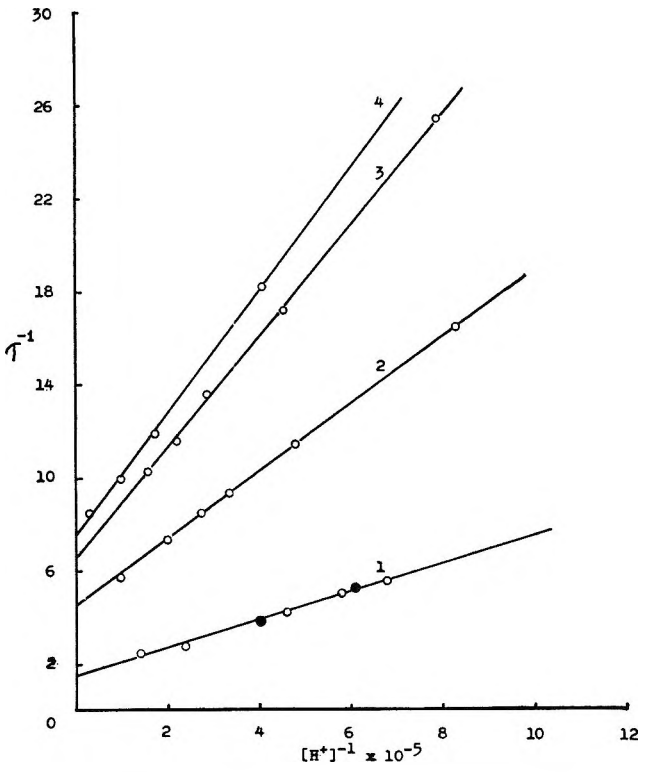

Figure 2. Plots of $1/\tau_{GuH^+}$ *vs.* $1/(H^+)$ for 0.900 *M* (○), and for 0.700 *M* (●) GuHCl in various H_2O–DMAC mixtures. The values of $(H_2O)^2/(DMAC)$: 1, 38.15; 2, 79.92; 3, 107.02; 4, 140.11.

vent. To ensure that the dissociation was complete in each medium, solutions of 0.001 *M* HCl were prepared and the resulting pH compared to that of 0.01 *M* HCl in the same medium. All solutions above 30% water v/v showed a unit pH change. A similar procedure was used by Kolthoff and Reddy[8] when they showed that HCl is completely dissociated in DMSO. The values of f in 30, 40, 45, and 50% water (per cent by volume in H_2O–DMAC mixed solvents) are 1.25, 1.08, 1.00, and 0.93 respectively.

Figure 2 summarizes the results obtained for the dependence of $1/\tau_{GuH^+}$ on $1/(H^+)$ at various values of $(H_2O)^2/(DMAC)$. The parentheses indicate molar concentrations and not activities. The equilibrium constants reported therefore are really quotients and not thermodynamic constants based on activities.

Discussion

It is of interest to compare the solvent role played by the two protophylic aprotic solvents DMAC and DMSO by way of a kinetic method, because of the growing use of mixed solvents as reaction media. In recent years many comparisons of solute behavior have been made for protophylic aprotic solvents.[9-12]

The upfield shift of the guanidnium ion signal as water concentration increases not only is due to proton exchange with water molecules but also reflects a solvent-dependent chemical shift. Since DMAC is more basic than water,[13,14] one would expect the signal of a guanidinium ion hydrogen-bonded to water to be at a higher field than that of a guanidinium ion hydrogen bonded to DMAC, as has been observed. The fact that only one guanidinium ion line is observed indicates that exchange (without a proton-transfer reaction occurring) between the various species GuH^+-$D_n(H_2O)_m$ is much more rapid than the corresponding line frequency differences. Moreover, since the chemical shift of the GuH^+ proton signal in pure DMAC is approximately independent of guanidinium chloride concentration, we infer that guanidinium chloride is very strongly hydrogen-bonded to DMAC, and we therefore write the guanidinium ion in pure DMAC as $D_nGuH^+ \ldots D$, where D is DMAC.

Changes in the line width of the water proton signal reflect not only the exchange between the guanidinium ion and water, but also the exchange between self-associated water and water bonded to DMAC molecules. For this reason, in calculating the specific rates of exchange for GuH^+, we have used only line width data for the guanidinium protons.

In considering a mechanism consistent with the observed rate law (see below), one feature of the results must be taken into account. Evidently exchange of water molecules (without proton transfer) among the various hydrogen-bonded species is fast. Moreover, in the pH range considered, almost all guanidinium is present as the guanidinium ion. We therefore postulate a mechanism given by eq 1–5, the same as that shown for the exchange in water–DMSO mixtures.[3] The rate-determining steps (which do not in themselves effect a proton transfer) are reactions 2 and 3, which involve the abstraction of a hydrogen ion from the partially aquated guanidinium complex by OH^- or H_2O, respectively. The actual proton transfer occurs through reactions 4 and 5, which may be either fast or slow, but are not rate determining; they involve an intramolecular proton transfer (referring to the complex $D_nGu(H)^+ \ldots OH^-$ as a molecule) and dissociation of water from the complex after the intramolecular proton transfer. The mechanism yields for $1/\tau_{GuH^+}$ the equation

$$\frac{1}{\tau_{GuH^+}} = \frac{K_1(H_2O)^2}{(D)(H^+)}[k_1K_w + k_2(H^+)] \qquad (9)$$

(8) I. M. Kolthoff and T. B. Reddy, *Inorg. Chem.*, **1**, 189 (1962).

(9) R. Alexander and A. J. Parker, *J. Amer. Chem. Soc.*, **89**, 5549 (1967).

(10) R. Alexander, E. C. F. Ko, Y. C. Mac, and A. J. Parker, *ibid.*, **89**, 3703 (1967).

(11) B. W. Clare, D. Cook, E. C. F. Ko, Y. C. Mac, and A. J. Parker, *ibid.*, **88**, 1911 (1966).

(12) A. J. Parker, *Chem. Rev.*, **69**, 1 (1969).

(13) I. M. Kolthoff, M. K. Chantooni, Jr., and S. Bhowmik, *J. Amer. Chem. Soc.*, **90**, 23 (1968).

(14) C. T. Ritchie and R. E. Uschold, *ibid.*, **89**, 2752 (1967).

where K_w is the equilibrium constant for the dissociation of water

$$H_2O = H^+ + OH^- \quad (10)$$

According to eq 9, from the slopes and intercepts of the linear plots of $1/\tau_{GuH^+}$ *vs.* $1/(H^+)$ at various values of $(H_2O)^2/(D)$, the same values of $K_1k_1K_w$ and K_1k_2, respectively, should be obtained. Table II lists the results derived from Figure 2. These values, obtained in H_2O–DMAC mixtures can be compared with the values in H_2O–DMSO mixtures:[3] $K_1k_1K_w = 6.8 \times 10^{-8}$; $K_1k_2 = 14.2 \times 10^{-2}$.

Table II: Values of $K_1k_1K_w$ and K_1k_2 from Data of Figure 2

Line	Vol % H_2O	$(H_2O)^2/$ (DMAC)	Slope $\times 10^5$	Inter-cept	$K_1k_1K_w$ $\times 10^7$	K_1k_2 $\times 10^2$
1	30	38.15	0.60	1.5	1.58	4.0
2	40	79.92	1.40	4.5	1.75	5.6
3	45	107.02	2.38	6.6	2.22	6.2
4	50	140.11	2.65	7.4	1.89	5.3
				Av	1.86	5.3

A plausible explanation for the difference in $K_1k_1K_w$ for H_2O–DMSO and H_2O–DMAC mixtures is as follows. The value of K_1 could be estimated if we had data on equilibrium constants of hydrogen bonding between GuH^+ and water, K_{G-W}, and between GuH^+ and D, K_{G-D}

$$K_1 = K_{G-W}/K_{G-D} \quad (11)$$

Although these data are lacking, the ratio of the K_1 values in the two mixtures may be considered to be given by the equation

$$\frac{K_1 \text{ (in } H_2O\text{–DMSO mixtures)}}{K_1 \text{ (in } H_2O\text{–DMAC mixtures)}} = \frac{K_{G-DMAC}}{K_{G-DMSO}} \quad (12)$$

Since DMSO is a slightly better electron donor than DMAC,[15,16] one might expect that K_1 in H_2O–DMSO mixtures would be slightly smaller than K_1 in H_2O–DMAC mixtures. Moreover, since reaction 2 is one between ions of opposite charges, the rate constant k_1 would be larger in a medium of smaller dielectric constant. The dielectric constants of DMSO and DMAC are 46.6 and 37.8,[12] respectively, so that k_1 would be smaller in H_2O–DMSO than in H_2O–DMAC mixtures. If K_w in the two mixed solvents is essentially the same, then the relative magnitudes of K_1 and k_1 in the two mixed solvents would lead to the expectation that the product K_1k_1 in H_2O–DMSO mixtures be smaller than in H_2O–DMAC mixtures, and this has been experimentally observed for the mixed solvents over a concentration range of 30–50% (by volume) of water.

The combination of eq 3, 4, and 5 gives essentially the equation for the acid dissociation of guanidinium chloride in the mixed solvents. A survey of the literature for a number of acids[10,11] shows that the pK_a values in *N*,*N*-dimethylformamide and in DMAC are in general about 1 unit larger than in DMSO. If one may correlate equilibrium constant with rate constant, then k_2 would be larger in DMSO than in DMAC by an order of magnitude. Thus, even though K_1 is slightly smaller in DMSO, the value of K_1k_2 in DMSO would still be greater than in DMAC. Our experimental results over a concentration range of 30–50% (by volume) of water show that K_1k_2 is 2.7 times as great in H_2O–DMSO mixtures as in H_2O–DMAC mixtures.

Acknowledgment. We wish to thank Professor A. A. Bothner-By for permission to use the R-20 Spectrometer at Carnegie-Mellon University.

(15) S. F. Ting, S. M. Wang, and N. C. Li, *Can. J. Chem.*, **45**, 425 (1967).

(16) Y. H. Shaw and N. C. Li, *ibid.*, **48**, 2090 (1970).

The Optical Activity of Trigonally Distorted Cubic Systems

by F. S. Richardson

Department of Chemistry, University of Virginia, Charlottesville, Virginia 22901 and Department of Chemistry, Princeton University, Princeton, New Jersey 08540 *(Received July 31, 1970)*

Publication costs borne completely by The Journal of Physical Chemistry

The optical rotatory properties associated with the ligand-field transitions of trigonal dihedral transition metal complexes are examined on a one-electron model. The chromophoric electrons localized on the octahedral ML_6 cluster are perturbed by a static trigonal field which originates with the nonligating parts of the ligand environment and with distortions of the ML_6 cluster from a regular octahedral geometry. The perturbation expansion of the wave functions is carried out to second order in the trigonal field (P). The net rotatory strength associated with the complete manifold of ligand-field transitions vanishes to first order on the one-electron model but is nonvanishing if second-order contributions are considered. The second-order contributions to the rotatory strength arise from the simultaneous actions of a trigonal perturbation (P_g) with gerade octahedral parentage and a trigonal perturbation (P_u) with ungerade octahedral parentage. The contributions due to d–p and d–f orbital mixing under the influence of P_u, and d–d mixing under the influence of P_g, are considered in detail. The influence exerted on the optical rotatory properties by chelate ring conformation, ring size, ring substituents, and distortions of the octahedral ML_6 cluster, are examined and predictions are made. Vibronic effects are discussed, but they are not explicitly treated in our model. The results obtained to first order in perturbation theory are similar to those previously obtained by Moffitt, Piper, and Karipedes, and Poulet on a static, one-electron model. In carrying the static, one-electron model to second order in perturbation theory, we obtain results which are in close agreement with the experimental CD data and which are easily interpreted in terms of specific structural features of trigonal dihedral metal complexes. Reduction of the general model to a crystal-field representation of the electronic states of the complex ion further aids in elucidating the essential symmetry-determined aspects of the optical rotatory properties. Although the static, one-electron model is not appropriate for making accurate quantitative calculations of the rotatory strength, it provides a simple and correct representation of the nodal structure in the electronic states of the ML_6 chromophore and in the interaction potential between the ML_6 chromophore and the ligand environment. The simplicity of this representation and the facility with which it can be used in making correlations between CD data and molecular structure make it particularly attractive.

I. Introduction

Considerable research effort has been focused on the optical rotatory and circular dichroic properties of transition metal complexes which possess trigonal dihedral (D_3) symmetry. The simplest examples of this class of metal complexes are $M(en)_3$ and $M(ox)_3$ in which three identical bidentate ligands (en = ethylenediamine and ox = oxalate anion) are coordinated to the metal ion. The ML_6 clusters (where L = ligating atoms) in these compounds deviate only slightly from octahedral (O_h) symmetry. The d → d type transitions are of particular interest for developing viable theoretical models of optical activity because: (a) their absorption bands lie in the experimentally accessible near-infrared, visible, and near-ultraviolet regions of the spectrum; (b) they are localized in a group with high inherent symmetry; and, (c) their optical absorption properties indicate that they are only weakly influenced by the ligand environment beyond the ML_6 cluster. For example, the visible absorption spectra of $[Co(en)_3]^{3+}$ and $[Co(ox)_3]^{3-}$ are nearly identical with those of $[Co(NH_3)_6]^{3+}$ and $[Co(H_2O)_3]^{3+}$, respectively, which suggests that the nonligating chelate ring atoms assert only a weak influence on the chromophoric electrons responsible for the ligand-field transitions. Furthermore, the observed intensities ($\epsilon \sim 40$–60) indicate that the electric-dipole selection rules are still principally determined by a molecular field of O_h symmetry. These results suggest that a perturbation model should be appropriate for treating any optical property which depends upon interactions between the d electrons localized in the ML_6 cluster and the nonligating parts of the ligand environment.

We restrict our attention in this paper to transition metal ions whose orbital ground states are nondegenerate and whose orbital excited states are triply degenerate in an octahedral ligand field. Most of the experimental circular dichroism studies with trigonal dihedral systems have been done on the tris complexes of Ni(II), Cr(III), Rh(III), and Ir(III), all of which have orbitally nondegenerate ground states and triply degenerate orbital excited states. Furthermore, we shall neglect spin–orbit interactions.

According to the quantum-mechanical theory of optical activity both the magnitude and the sign of the Cotton effect associated with an electronic transition $i \rightarrow j$ are determined by the rotatory strength, R_{ij}, of the transition. This quantity is defined by

$$R_{ij} = \text{Im}\ \langle\psi_i|\vec{\mu}|\psi_j\rangle\cdot\langle\psi_j|\vec{m}|\psi_i\rangle = \text{Im}\ (\vec{P}_{ij}\cdot\vec{M}_{ji}) \quad (1)$$

where Im indicates that the imaginary part of the scalar product between the electric-dipole transition moment $\vec{P}_{ij}$ and the magnetic-dipole transition moment $\vec{M}_{ji}$ is taken. According to the classical electron theory of optics, electrons in an optically active system are constrained to move along helical paths in their response to an incident light beam. This helical motion of the electrons (circulation + linear displacement of charge) generates the parallel electric and magnetic transition dipoles which appear in eq 1. In optically active molecules this constraint placed on the motion of the electrons arises from a net dissymmetry in the internal electric fields of the molecule. That is, the electrons move in an electrostatic potential field which lacks an inversion center, a mirror plane, and/or an alternating rotation–reflection axis. In eq 1, ψ_i and ψ_j are the total electronic wave functions for molecular states i and j. Since these many-electron functions cannot, in general, be obtained with sufficient accuracy for calculating spectroscopic properties, the usual procedure is to partition the molecule into several simpler parts. To zeroth order the molecule is represented as a composite of independent, noninteracting subsystems and interactions between the subsystems are then treated by perturbation methods. In most cases of general interest the individual chromophoric groups or subsystems are not dissymmetric so that the molecular optical activity is obtained only from the intergroup interactions. The general methods and approximations conventionally employed in the independent systems, perturbation approach to optical activity have been presented elsewhere and need not be rediscovered here.[1,2] The final expression for the rotatory strength obtained from the independent systems model includes four types of terms: (a) "two-electron" terms due to the pairwise couplings between electric transition dipoles located on two different groups; (b) "two-electron" terms due to the coupling between an electric transition dipole on one group and a magnetic transition dipole on another group; (c) "one-electron" terms which arise when the electric- and magnetic-dipole transition moments of a one-electron transition localized in a single, inherently symmetric group have parallel components due to the static perturbing influence of dissymmetrically disposed surrounding groups; and (d) contributions made by inherently dissymmetric groups considered in isolation. The "one-electron" terms are so designated because they involve the dynamical behavior of only one electron; the rest of the electrons in the molecule are assumed to provide an average or static field in which the "one-electron" must move when it responds to the incident light. The "two-electron" terms involve the coupled motions of two electrons, each localized in a different group, when they respond to the incident light.

In considering only the ligand-field transitions of trigonal dihedral metal complexes we can neglect terms of type (a) and terms of type (d) if we take as our chromophoric group an octahedral ML_6 cluster. This is possible since all pure d → d electronic transitions in this centrosymmetric system are electric-dipole forbidden. Certain of these transitions are, however, magnetic dipole allowed so that both (b) and (c) types of terms can contribute to the total rotatory strength. The relative importance of the "one-electron" and the "two-electron," electric–magnetic coupled oscillator terms is determined principally by the chromophoric properties of the ligand groups. In order for the electric–magnetic coupled oscillator mechanism to be effective three conditions must be satisfied: (a) the transition energy of the electric-dipole transition in the perturber group (ligand) must not be greatly different from the transition energy of the magnetic dipole ligand field transition to which it is coupled; (b) the coupled electric and magnetic oscillators must have large parallel components; and, (c) the distance between the coupled chromophores must not be large since the interaction, in general, has a steep inverse dependence on R, the group separation distance. The one-electron terms also have strong dependence on the geometrical dispositions and radial distances of the perturber groups with respect to the chromophoric group of interest. Although they are not directly dependent upon the energies of perturber states, they are strongly influenced by the sign and magnitude of the average, net charge density on each perturber group or atom. In the limit of completely nonoverlapping charge distributions between groups, the one-electron terms receive contributions only from those perturbers that carry a "net" charge. Furthermore, the magnitude of the one-electron terms depends upon the differences in transition energies between the electric-dipole allowed transitions and magnetic-dipole allowed transitions, centered in the ML_6 cluster, which mix in the presence of the dissymmetric ligand field.

It is fairly easy to speculate about the relative importance of various types of bidentate ligands in promoting the electric–magnetic coupled oscillator (e–m CO) mechanism. For example, diamino ligands such as ethylenediamine (en) and propylenediamine (pn) have intense, electric-dipole allowed transitions which only appear in the vacuum ultraviolet region of the spectrum, far away from the visible ligand-field transitions. The e–m CO contributions to the ligand-field rotatory strengths should be weak in this case. On the other hand, conjugated ligands such as the acetylacetonate ion (acac), orthophenanthroline (*o*-phen),

(1) I. Tinoco, *Advan. Chem. Phys.*, **4**, 113 (1962).
(2) J. A. Schellman, *J. Chem. Phys.*, **44**, 55 (1966).

and 2,2′-bipyridyl (bipy) exhibit very intense, electric-dipole allowed transitions ($\pi \rightarrow \pi^*$) in the near-ultraviolet region. Furthermore, in the tris complexes of these ligands with transition metal ions, these large transition dipoles are properly oriented to dissymmetrically couple with the magnetic dipole transitions on the metal. In these complexes, the e–m CO mechanism should make large contributions to the ligand-field rotatory strengths. The oxalate ligand represents an intermediate case since its low energy, electric-dipole allowed transitions occur in the far-ultraviolet region (210–180 nm).

For the tris complexes of conjugated ligands the greatest practical interest lies in the CD bands of the ligand transitions rather than in the d → d type metal transitions. These bands can be theoretically understood or analyzed in terms of the electric dipole–electric dipole coupled oscillator mechanism.[3] Dipole–dipole interactions between the large transition densities on the three ligands account for nearly all the sign and intensity properties of the observed CD bands. Formally this mechanism is relatively easy to treat and the use of absorption frequency and intensity data can provide the necessary data input for making semiempirical computations. The absorption frequencies give the necessary energy denominators in the perturbation expressions and the observed intensities give some measure of the magnitude of the interacting transition dipoles. The geometrical factors in the interaction potential can then be deduced and the desired structural and stereochemical information obtained. It is not so straightforward, formally or computationally, to extract structural information from CD which arises from one-electron or e–m CO mechanisms. In these cases, the accompanying absorption intensities are weak and usually arise from vibronic rather than static perturbations. Furthermore, neither the exact nor the approximate nature of the interaction potential functions are as clearly understood in these mechanisms as they are in the dipole–dipole coupling case.

In a previous paper,[4] both the one-electron and the e–m CO mechanisms were considered in deriving sector rules for the CD of optically active complexes of the pseudotetragonal class. Sector rules relate the "relative" signs and magnitudes of rotatory strengths (and, therefore, CD bands) to the spatial configuration of perturber groups about the chromophoric center of interest. Since they are based strictly on group theoretical arguments they can tell nothing about "absolute" signs and magnitudes. It was shown in ref 4 that the sector rules for the "net" rotatory strength associated with the ligand-field transitions of pseudotetragonal complexes were identical for the one-electron and the e–m CO mechanisms. This result implies that the CD spectral properties predicted on the basis of only a one-electron treatment should not be qualitatively altered if e–m CO effects were subsequently introduced. In the present treatment of trigonal dihedral complexes only the one-electron mechanism will be considered. Our reasons for this choice are threefold: (a) all of the essential, symmetry-controlled, qualitative aspects of the problem are displayed by this model; (b) the one-electron model permits a straightforward use of the crystal-field and simple ligand-field formalism; and, (c) vibronic effects can be easily represented (if not solved) on the one-electron model, whereas these effects introduce considerable complications on the e–m CO model.

II. Previous Theories

Moffitt[5] treated the problem of optical rotatory power in trigonal dihedral metal complexes by: (1) assuming that to zeroth order the relevant electronic wave functions of the complex could be constructed from a cubic (O_h) basis set composed of 3d metal orbitals; (2) applying an ungerade ligand-field potential of D_3 symmetry to the zeroth-order electronic states; (3) permitting the 4p metal orbitals to mix with the 3d orbitals under the influence of the D_3 ungerade potential. Perturbation of the zeroth-order states was carried out to first order in this model. Moffitt applied the model to the $^1A_{1g} \rightarrow {}^1T_{1g}$ transition in trigonal dihedral Co(III) complexes and to the $^4A_{2g} \rightarrow {}^4T_{2g}$ transition of Cr(III) trigonal dihedral complexes. Sugano,[6] working within the framework of Moffitt's physical model, gave an elegant treatment of the problem in which he deduced, contrary to Moffitt's conclusions, that an ungerade trigonal field of T_{2u} octahedral parentage acting on an octahedral complex cannot give rise to a *net* rotatory strength for the degenerate d → d transitions. Sugano's conclusions were based on the uniquely deduced arguments of group theory and therefore depended on the physical model only insofar as the zeroth-order states were assumed to be cubic and the ligand-field perturbation was of D_3 symmetry with T_{2u} octahedral parentage. Sugano further showed that, to first order, only a ligand field of A_{1u} symmetry can induce a *net* rotatory strength in the d → d transitions of octahedral complexes. If the perturbing ligand field potential is expressed as a multipole expansion, the first term which transforms as A_{1u} in O_h is of the ninth order with respect to electronic coordinates. Even if the 3d metal orbitals were mixed with 4f metal orbitals the direct product of the two sets spans no representation of the rotation group of order higher than five. Hamer has generalized Sugano's conclusions to show that, for any transition metal complex whose symmetry includes an inversion

(3) B. Bosnich, *Accounts Chem. Res.*, 2, 266 (1969).
(4) F. S. Richardson, *J. Chem. Phys.*, in press.
(5) W. Moffitt, *ibid.*, 25, 1189 (1956).
(6) S. Sugano, *ibid.*, 33, 1883 (1960).

center, only a ligand field potential which transforms as a pseudoscalar or A_{1u} irreducible representation can give rise to a *net* rotatory strength to first order.[7]

Poulet modified Moffitt's model to allow some trigonal splitting to occur within the degenerate octahedral electronic states.[8] In other words, it was postulated that a component of the D_3 ligand field transforming gerade in O_h lifted the degeneracy of the zeroth-order octahedral states. Of course the "net" rotatory strength of a given d → d transition was still computed to be zero (Sugano's result), but in Poulet's model the two components of the transition could be observed as separate Cotton effects in the ORD spectrum. The Cotton effects would be of equal magnitude, opposite in sign, and separated by an energy interval equal to the trigonal splitting. The experimental circular dichroism data obtained for $[Co(en)_3]^{3+}$ show two bands, one negative and one positive.[9-11] Furthermore, by measuring the CD of the crystal, 2(±)D-$[Co(en)_3]Cl_3 \cdot NaCl \cdot 6H_2O$, perpendicular to the trigonal axis of $[Co(en)_3]^{3+}$, the CD band associated with the $^1A_1 \rightarrow {}^1E$ component of the $^1A_{1g} \rightarrow {}^1T_{1g}$ transition was identified.[11] These experimental results confirmed the presence of trigonal splitting in the degenerate transition; however, it was found that the CD of the trigonal component ($^1A_1 \rightarrow {}^1E$) was quite a bit more intense than that of the $^1A_1 \rightarrow {}^1A_2$ component. The net rotatory strength of the degenerate transition is not zero. These results do not negate the correctness of Sugano's formal treatment, but point up the inadequacies of Moffitt's and Poulet's physical models.

Piper and Karipides have developed both a crystal field model[12] and a molecular orbital model[13] for optical activity in trigonal dihedral metal complexes. Their crystal field treatment is an extension of Moffitt's model to include trigonal splitting of the excited degenerate states and the mixing of 4f metal orbitals with the 3d orbitals. In their molecular orbital model the electric-dipole forbidden transitions between σ antibonding orbitals borrow electric-dipole intensity from the metal-to-ligand charge transfer transitions. In calculating the rotatory strength for $[Co(en)_3]^{3+}$, they assume that the ligating nitrogen atoms have been angularly displaced from their octahedral reference positions by 4° in a plane defined by a presumedly planar chelate ring. This physical model results in a net rotatory strength for the $^1A_{1g} \rightarrow {}^1T_{1g}$ transition, although the relative magnitudes of the component $^1A_1 \rightarrow {}^1E$ and $^1A_1 \rightarrow {}^1A_2$ rotatory strengths are not in agreement with experimental data. Furthermore, the sign of the net rotatory strength depends upon whether the N–Co–N angles in the chelate rings are >90° or <90°. If this sign dependence on the N–Co–N angle actually exists, it would be necessary to know beforehand whether N–Co–N is >90° or <90° in making absolute configuration assignments based on CD data. According to this model, a Λ configuration (*i.e.*, one having a left-handed screw sense with respect to the C_3 axis) in which the N–Co–N angles in the chelate rings were <90° would have a net rotatory strength of the same sign as a Δ configuration (*i.e.*, one having a right-handed screw sense with respect to the C_3 axis) in which the chelate N–Co–N angles were >90°. The influence of the nonligating atoms on the optical activity of trigonal complexes was not considered in this model.

Liehr[14] has developed a model in which the optical activity of trigonal dihedral complexes is understood in terms of a significant angle of "mis-match" existing between the directions of maximum charge density of the metal and ligand orbitals. In an optically active complex the real molecular orbitals, between which the chromophoric electrons are excited, are inherently dissymmetric. Liehr proposes that these dissymmetric molecular orbitals be built up from a set of hybridized orbitals constructed from the octahedral σ-type and π-type orbitals localized on the ligating atom and from the 3d and 4p metal orbitals. The hybridization parameters would, of course, be sensitive to the local environment of the ligating atoms (*e.g.*, the bridging atoms in the chelate rings) and would build the necessary dissymmetry into the molecular orbitals. In short, Liehr attempts to treat the overall complex as one, large, inherently dissymmetric chromophore. Presently, such an approach poses extremely difficult computational and economic problems. As the electronic structure calculations of large molecules improve (more accurate and complete wave functions) Liehr's model should become of predominant importance. However, perturbational models can be more easily adapted to semiempirical methods of calculation and prediction at present. More recently, Schaffer has discussed the optical rotatory properties of trigonal dihedral metal complexes in terms of the angular overlap model of bonding in coordination compounds.[15]

In each of the theoretical models discussed above, the optical rotatory properties exhibited by the visible absorption bands of trigonal dihedral transition metal complexes, such as $[Co(en)_3]^{3+}$ and $[Co(ox)_3]^{3-}$, are ascribed solely to the distortion of the ligating atoms (the ligand atoms bonded directly to the central metal ion), their orbitals, or their charge distributions from the apices of a regular octahedron. The ligand atoms

(7) N. K. Hamer, *Mol. Phys.*, **5**, 339 (1962).

(8) H. Poulet, *J. Chem. Phys.*, **59**, 584 (1962).

(9) R. Ballard, A. McCaffery, and S. F. Mason, *Proc. Chem. Soc.*, 331 (1962).

(10) A. J. McCaffery and S. F. Mason, *Mol. Phys.*, **6**, 359 (1963).

(11) A. J. McCaffery, S. F. Mason, and R. F. Ballard, *J. Chem. Soc.*, 2883 (1965).

(12) T. S. Piper and A. Karipides, *Mol. Phys.*, **5**, 475 (1962).

(13) A. Karipides and T. S. Piper, *J. Chem. Phys.*, **40**, 674 (1964).

(14) A. D. Liehr, *J. Phys. Chem.*, **68**, 665 (1964).

(15) C. E. Schaffer, *Proc. Roy. Soc., Ser. A*, **297**, 96 (1968).

not directly bonded to the central metal ion, such as the carbon and hydrogen atoms of the diamine complexes, are assumed to be passive toward the chromophoric electrons localized on the metal ion or in the metal-to-ligand σ bonds. They serve only to produce, mechanically or electrically (polarization of charge on the ligating atom), the required distortions of the ligating atoms or charges. According to these models there is not necessarily a connection between chelate ring conformation and the optical properties of the electronic transitions centered on the metal ion, except as the ring conformation would influence the distortions of the ligating atoms or thermodynamically stabilize a particular configuration of chelate rings about the metal ion. The results of X-ray diffraction studies on crystals containing the complex ion $[Co(en)_3]^{3+}$ show that the displacements of the nitrogen atoms from the octahedral positions are very small and uncertain in direction. Moreover, Mason[16] recently reported an observed correlation between the sign of the CD in the charge-transfer region of the spectrum and the conformation of the chelate ring, irrespective of the absolute configuration of the chelate rings about the metal ion. Circular dichroism studies on deuterated samples of $[Co(en)_3]^{3+}$ further suggest that the ligand atoms not bonded to the metal ion may play a more than passive role in altering the properties of electronic processes localized on the metal ion.[17] Furthermore, the effects due to vibronic interactions have not been explicitly treated in any of the current models although the possibility of their existence and importance has been acknowledged.

III. Description of Model

We represent the complex ions of the trigonal dihedral class by $[M(L_2\ell)_3]$, where $(L_2\ell)$ is a bidentate ligand with ligating atoms, L, ℓ = all nonligating atoms in the ligand, and M = metal ion. The full molecular symmetry of the $[M(L_2\ell)_3]$ system is presumed to be D_3. We specify a reference geometry for the ML_6 cluster which has octahedral (O_h) symmetry. It is assumed that the O_h reference geometry also represents the equilibrium configuration of the isolated ML_6 cluster in the absence of strong vibronic interactions. In zeroth order we represent the complex as composed of two independent subsystems, the ML_6 cluster and the nonligating parts of the complex. Interactions between the subsystems are then treated by perturbation methods. Since neither subsystem is inherently dissymmetric, the optical activity exhibited by the complex arises entirely from the interaction terms.

As stated in section I, we shall consider only "one-electron" type contributions to the optical activity associated with the ligand-field d $\rightarrow$ d transitions. For this reason, the only properties we need to know about the nonligating parts of the complex (which are, in this model, the perturbers) are their positions with respect to the metal ion and their ground-state charge distributions. The chromophoric electrons localized in the ML_6 cluster are perturbed by the "average" Coulomb field of the nonligating perturber groups. Before the effects of these perturbations on any optical property can be evaluated, an accurate and complete description of the electronic states of an isolated ML_6 chromophore must be available. This requirement presents extreme difficulties for treating any coordinated metal ion in which the electronic states of interest are degenerate or nearly degenerate. In these cases vibronic interactions can effectively compete with, or act in concert with, the low-symmetry ligand fields in altering the ML_6 electronic states and distorting its nuclear geometry. If we choose as our zeroth-order electronic states the eigenstates of an isolated ML_6 cluster clamped in a rigid octahedral geometry, the following interactions must be introduced as perturbation terms: (a) vibronic coupling within an orbitally degenerate electronic manifold *via* gerade vibrational modes (Jahn–Teller effect); (b) vibronic coupling between nearly degenerate electronic states (pseudo-Jahn–Teller effect); (c) vibronic coupling between electronic states of different energies and of opposite parity *via* ungerade vibrational modes (Herzberg–Teller coupling); (d) small, static distortions of the ML_6 cluster away from a true octahedral geometry; (e) static, Coulombic field of the nonligating parts of the ligand environment.

In this study we examine in some detail how the static perturbations (the interactions listed as d and e above) influence the CD of the trigonal dihedral complexes, and only discuss vibronic effects in a general way. A detailed study of vibronic effects and their influence on the CD spectra of metal complexes will be presented in a separate paper. Only possible vibronic modifications of the results obtained on our static model will be discussed here. Since the previous theories dealing with the optical activity of metal complexes have been based on "static" models, it is useful to present the effects originating with the static and the vibronic interactions separately. Furthermore, this is possible since the vibronic effects primarily influence the detailed structure of the CD bands and only weakly influence the net rotatory strength of the CD spectra, whereas the static effects primarily determine the net rotatory strengths but, of course, do not influence band structure except with respect to breaking electronic orbital degeneracies.

The Hamiltonian for the $M(L_2\ell)_3$ system is partitioned as follows

$$\mathcal{H} = H + h + P \qquad (2)$$

(16) A. J. McCaffery, S. F. Mason, and B. J. Norman, *Chem. Commun.*, 49 (1965).

(17) S. F. Mason and B. J. Norman, *ibid.*, 48 (1965).

where H is the Hamiltonian operator for the ML_6 cluster, h is the Hamiltonian for the nonligating parts of the chelate ring system, and P is an interaction potential between the ML_6 cluster and the nonligating atoms of the complex. Since we are principally concerned with the optical properties associated with electronic states "localized" in the ML_6 cluster, the operator h will not be of further interest here. Neglecting spin dependence, we write the Hamiltonian H as

$$H(r,Q) = T_\nu + T_\epsilon + V(r,Q) \tag{3}$$

where $\{r\}$ denotes the electron position coordinates, $\{Q\}$ represents a set of nuclear displacement coordinates for the octahedral ML_6 cluster, $V(r,Q)$ is the total potential energy of the ML_6 system, and T_ν and T_ϵ are the kinetic energy operators for the nuclei and electrons, respectively.

In the adiabatic approximation, the potential energy function $V(r,Q)$ is expanded as a Taylor's series in nuclear displacement coordinates about the octahedral reference configuration, $\{Q\} = 0$. We have

$$\begin{aligned} V(r,Q) &= V^0(r) + \sum_a Q_a\left(\frac{\partial V}{\partial Q_a}\right)_0 + \\ &\qquad \sum_a \sum_b Q_a Q_b\left(\frac{\partial^2 V}{\partial Q_a \partial Q_b}\right)_0 + \cdots \\ &= V^0(r) + \sum_a Q_a V_a' + \\ &\qquad \sum_a \sum_b Q_a Q_b V_{a,b}'' + \cdots \end{aligned} \tag{4}$$

where the normal coordinates Q_a, Q_b, ... Q of the octahedral ML_6 cluster are chosen as the expansion basis. The functions V_a' and $V_{a,b}''$ are evaluated at the reference configuration $\{Q\} = 0$, and $V^0(r)$ is the total potential energy of the ML_6 system when the nuclei are clamped in their octahedral reference positions.

The interaction operator P can be separated into two parts

$$P = P_\epsilon + P_\nu \tag{5}$$

where P_ϵ represents the direct influence of the nonligating subsystem on the electronic structure of the ML_6 cluster and P_ν represents the tendency of the nonligators to distort the nuclear framework of ML_6 from an octahedral configuration. The function P_ν may be expressed as

$$P_\nu = \sum_d f_d q_d \tag{6}$$

where q_d is a distortion coordinate and the force functions f_d depend upon the details of the interactions between the ligating and nonligating atoms of the complex.

We now define the "effective" Hamiltonian of the perturbed ML_6 cluster by

$$\begin{aligned} H_E = H_\epsilon^0(r) + H_\nu^0(Q) + \\ H_{\epsilon\nu}(r,Q) + P_\epsilon(r) + P_\nu(q) \end{aligned} \tag{7}$$

The operator $H_\epsilon^0(r)$ is the zeroth-order electronic Hamiltonian defined by

$$H_\epsilon^0(r) = T_\epsilon + V^0(r) \tag{8}$$

and $H_\nu^0(Q)$ consists of 15 harmonic oscillator Hamiltonians, one for each normal vibrational mode of the octahedral ML_6 cluster. The vibronic interaction operator $H_{\epsilon\nu}(r,Q)$ is given by

$$H_{\epsilon\nu}(r,Q) = \sum_a Q_a V_a' + \sum_a \sum_b Q_a Q_b V_{a,b}'' + \cdots \tag{9}$$

The operator $P_\nu(q)$ represents a static distortion of the ML_6 cluster from its octahedral reference configuration to its equilibrium configuration. If we express the distortion coordinates q in terms of normal coordinates Q, the "effective" Hamiltonian may then be rewritten in terms of the equilibrium nuclear displacement coordinates Q'

$$\begin{aligned} H_E(r,Q') = H_\epsilon^0(r) + H_\nu(Q') + \\ H_{\epsilon\nu}(Q') + P_\epsilon(r) + \sum_a V_a' \Delta Q_a \end{aligned} \tag{10}$$

where $Q_a' = Q_a - \Delta Q_a$, and $\Delta Q_a = f_a/M_a\omega_a^2$.

The molecular vibronic states are constructed from eigenfunctions of the operator $H_E(r,Q')$. In the Born–Oppenheimer approximation these functions reduce to single terms of the type

$$\Psi_{n\upsilon}(r,Q') = F_n(r,Q')f_{n\upsilon}(Q') \tag{11}$$

The functions $F_n(r,Q')$ are eigenfunctions of the total electronic Hamiltonian, H_ϵ, according to the eigenvalue equation

$$H_\epsilon F_n(r,Q') = E_n(Q')F_n(r,Q') \tag{12}$$

where

$$H_\epsilon = H_\epsilon^0(r) + H_{\epsilon\nu}(r,Q') + P_\epsilon(r) + \sum_a V_a' \Delta Q_a \tag{13}$$

The vibrational wave functions of the perturbed ML_6 cluster in the nth electronic state are obtained (in the B–O approximation) from

$$[T_\nu + E_n(Q')]f_{n\upsilon}(Q') = W_{n\upsilon}f_{n\upsilon}(Q') \tag{14}$$

It is assumed that the functions $F_n(r,Q')$ can be approximated by a perturbation expansion in terms of the eigenfunctions F_n^0 obtained from

$$H_\epsilon^0 F_n^0(r) = E_n^0 F_n^0(r) \tag{15}$$

Similarly, the vibrational wave functions $f_{n\upsilon}(Q')$ are expanded in terms of the functions $f_{n\upsilon}^0(Q)$, which are eigenfunctions of the harmonic oscillator Hamiltonians for an isolated and unperturbed ML_6 cluster of octahedral symmetry. The zeroth-order electronic states constructed from the functions F_n^0 will transform as irreducible representations (IR) of the O_h point group and will, of course, have a definite parity.

The perturbation operators P_ν and P_ϵ have trigonal dihedral (D_3) symmetry. Under their influence, elec-

tronic states of opposite parities can mix and the triply degenerate electronic states of octahedral parentage are each split into a doubly degenerate component and a nondegenerate component. The only nontotally symmetric normal modes in the octahedral ML_6 cluster which have components that transform as A_1 in the D_3 point group are the triply degenerate t_{2g} and t_{2u} modes. We designate the corresponding normal coordinates as $Q(t_{2g}^0)$ and $Q(t_{2u}^0)$, and the distortion coordinates as q_+ and q_-, respectively. Now P_ν can be written as

$$P_\nu = f_+q_+ + f_-q_- \tag{16}$$

In writing eq 6 and 16, we have assumed that only linear terms need be included. There would be twelve additional terms in eq 16 if distortions which are quadratic in normal coordinates were included.

IV. Static Trigonal Distortions

In this section we consider the influence of the static trigonal perturbations, P_ν and P_ϵ, on the electronic states of the ML_6 cluster and examine their contributions to the optical rotatory properties in the absence of vibronic interactions. The electronic Hamiltonian in this static-field approximation is written as $H_\epsilon^s = H_\epsilon^0(r) + P_\epsilon + f_+q_+ + f_-q_- = H_\epsilon^0(r) + P$. The eigenstates of $H_\epsilon^0(r)$ are classified and denoted as follows.

$|A_g\rangle^0$ = nondegenerate ground state with gerade parity

$|T_g^+\rangle^0$, $|T_g^0\rangle^0$, $|T_g^-\rangle^0$ = trigonal components of the first excited state (an orbital triplet) with gerade parity

$|M_g^\gamma\rangle^0$ = higher excited states with gerade parity

$|N_u^\gamma\rangle^0$ = higher excited states with ungerade parity

These state functions are expressed in a complex trigonal basis so that they transform as irreducible representations in both the D_3 and O_h point groups. The trigonal component $\gamma = 0$ belongs to either the A_1 or A_2 IR of D_3, and the components $\gamma = +$ and $\gamma = -$ transform as the E IR in D_3. For a given complex ion, the states, A_g, T_g, M_g, and N_u, are chosen to have the same spin-multiplicity since only spin-allowed transitions are considered on our model. Furthermore, if we choose to speak in terms of crystal-field theory, the combining states must not have configurational representations which differ by more than one in their d orbital occupation numbers, since only one-electron operators are used.

Using the eigenstates of $H_\epsilon^0(r)$ as an expansion basis, and treating P as a small perturbation on these states, we can write down the perturbed eigenstates, correct to second order in perturbation theory as follows

Ground state

$$\begin{aligned}|A_g\rangle = |A_g\rangle^0 &+ \sum_{N_u^0} P_{AN}^0|N_u^0\rangle^0/\Delta E_{AN} + \\ &\sum_{M_g^0} P_{AM}^0|M_g^0\rangle^0/\Delta E_{AM} + P_{AT}^0|T_g^0\rangle^0/\Delta E_{AT} + \\ &\Big[\sum_{M_g^0}(P_{TM}^0P_{MA}^0/\Delta E_{AT}\Delta E_{AM}) + \sum_{N_u^0}(P_{TN}^0P_{NA}^0/ \\ &\Delta E_{AT}\Delta E_{AN}) + (P_{TT}^0P_{TA}^0 - P_{AA}^0P_{TA}^0)/ \\ &\Delta E_{AT}^2\Big]|T_g^0\rangle^0 + \Big[\sum_{M_g^0}\sum_{N_u^0}(P_{MN}^0P_{NA}^0/\Delta E_{AM}\Delta E_{AN}) + \\ &\sum_{M_g^0}(P_{MT}^0P_{TA}^0/\Delta E_{AM}\Delta E_{AT}) + \sum_{M_g^0}(P_{MM}^0P_{MA}^0 - \\ &P_{AA}^0P_{MA}^0)/\Delta E_{AM}^2\Big]|M_g^0\rangle^0 + \Big[\sum_{M_g^0}\sum_{N_u^0}(P_{NM}^0P_{MA}^0/ \\ &\Delta E_{AN}\Delta E_{AM}) + \sum_{N_u^0}(P_{NT}^0P_{TA}^0/\Delta E_{AN}\Delta E_{AT}) + \\ &\sum_{N_u^0}(P_{NN}^0P_{NA}^0 - P_{AA}^0P_{NA}^0)/\Delta E_{AN}^2\Big]|N_u^0\rangle^0 \end{aligned} \tag{17}$$

Excited state

$$\begin{aligned}|T_g^\gamma\rangle = |T_g^\gamma\rangle^0 &+ \sum_{N_u^\gamma} P_{TN}^\gamma|N_u^\gamma\rangle^0/\Delta E_{TN} + \\ &\sum_{M_g^\gamma} P_{TM}^\gamma|M_g^\gamma\rangle^0/\Delta E_{TM} - P_{TA}^\gamma|A_g\rangle^0/\Delta E_{AT} + \\ &\Big[-\sum_{M_g^\gamma}(P_{AM}^\gamma P_{MT}^\gamma/\Delta E_{AT}\Delta E_{TM}) - \sum_{N_u^\gamma}(P_{AN}^\gamma P_{NT}^\gamma/ \\ &\Delta E_{AT}\Delta E_{TN}) + (P_{AA}^\gamma P_{AT}^\gamma - P_{TT}^\gamma P_{TA}^\gamma)/ \\ &\Delta E_{AT}^2\Big]|A_g\rangle^0 + \Big[\sum_{M_g^0}\sum_{N_u^0}(P_{MN}^\gamma P_{NT}^\gamma/\Delta E_{TM}\Delta E_{TN}) - \\ &\sum_{M_g^0}(P_{MA}^\gamma P_{AT}^\gamma/\Delta E_{TM}\Delta E_{AT}) + \sum_{M_g^0}(P_{MM}^\gamma P_{MT}^\gamma - \\ &P_{TT}^\gamma P_{TM}^\gamma)/\Delta E_{TM}^2\Big]|M_g^\gamma\rangle^0 + \Big[\sum_{M_g^0}\sum_{N_u^0}(P_{NM}^\gamma P_{MT}^\gamma/ \\ &\Delta E_{TN}\Delta E_{TM}) - \sum_{N_u^0}(P_{NA}^\gamma P_{AT}^\gamma/\Delta E_{TC}\Delta E_{AT}) + \\ &\sum_{N_u^0}(P_{NN}^\gamma P_{NT}^\gamma - P_{TT}^\gamma P_{TN}^\gamma)/\Delta E_{TN}^2\Big]|N_u^\gamma\rangle^0 \end{aligned} \tag{18}$$

Matrix elements of the type P_{NM}^γ are defined by

$$P_{NM}^\gamma = \langle N_u^\gamma|P|M_g^\gamma\rangle \tag{19}$$

and the energy differences appearing in the denominators of the terms in eq 17 and 18 are given by

$$\begin{aligned}\Delta E_{AM} &= (E_A^0 - E_M^0) \\ &= \langle A_g|H_\epsilon^0|A_g\rangle^0 - \langle M_g|H_\epsilon^0|M_g\rangle^0\end{aligned} \tag{20}$$

Note that all the energy differences appearing in eq 17 and 18 are negative since $E_A^0 < E_T^0 < E_M^0$ and E_N^0. The excited state, T_g, has three components corresponding to $\gamma = 0$, $\gamma = +$, and $\gamma = -$.

The rotatory strength associated with the γ component of the electronic transition, $A_g \rightarrow T_g$, is given by

$$R_{AT}^\gamma = \mathrm{Im}\,\langle A_g|\vec{\mu}|T_g^\gamma\rangle\cdot\langle T_g^\gamma|\vec{m}|A_g\rangle \tag{21}$$

where $\vec{\mu}$ = the electric-dipole moment operator and $\vec{m}$ = the magnetic dipole operator. Using the second-

order wave functions given in eq 17 and 18, the rotatory strength R_{AT}^{γ} can be expressed as

$$R_{AT}^{\gamma} = \mathrm{Im} \sum_{N_u^{\gamma}} \{ \vec{\mu}_{AN}^{\gamma} \cdot \vec{m}_{TA}^{\gamma} (P_{TN}^{\gamma}/\Delta E_{TN}) + \vec{\mu}_{NT}^{\gamma} \cdot \vec{m}_{TA}^{\gamma} (P_{AN}^{\gamma}/\Delta E_{AN}) + \vec{\mu}_{AN}^{\gamma} \cdot [\vec{m}_{TA}^{\gamma} P_{NT}^{\gamma} \times (P_{NN}^{\gamma} - P_{TT}^{\gamma})/\Delta E_{TN}^{2} - \vec{m}_{TA}^{\gamma} (P_{NA}^{\gamma} P_{AT}^{\gamma}/\Delta E_{TN}\Delta E_{AT}) + \vec{m}_{TT}^{\gamma} (P_{TN}^{\gamma} P_{AT}^{\gamma}/\Delta E_{AT}\Delta E_{TN}) - m_{AA}^{\gamma} (P_{TN}^{\gamma} P_{TA}^{\gamma}/\Delta E_{AT}\Delta E_{TN}) - \vec{m}_{TA}^{\gamma} (P_{AN}^{\gamma} P_{TA}^{\gamma}/\Delta E_{AN}\Delta E_{AT})] + \vec{\mu}_{NT}^{\gamma} \cdot [\vec{m}_{TA}^{\gamma} (P_{NT}^{\gamma} P_{TA}^{\gamma}/\Delta E_{AN}\Delta E_{AT}) + \vec{m}_{TA}^{\gamma} (P_{NN}^{\gamma} - P_{AA}^{\gamma}) P_{NA}^{\gamma}/\Delta E_{AN}^{2} + \vec{m}_{TT}^{\gamma} (P_{AT}^{\gamma} P_{AN}^{\gamma}/\Delta E_{AT}\Delta E_{AN}) - \vec{m}_{AA}^{\gamma} (P_{TA}^{\gamma} P_{AN}^{\gamma}/\Delta E_{AT}\Delta E_{AN}) + \vec{m}_{TA}^{\gamma} (P_{AT}^{\gamma} P_{TN}^{\gamma}/\Delta E_{AT}\Delta E_{TN})] + \sum_{M_0^{\gamma}} \vec{\mu}_{AN}^{\gamma} \cdot [\vec{m}_{TA}^{\gamma} (P_{NM}^{\gamma} P_{MT}^{\gamma}/\Delta E_{TN}\Delta E_{TM}) + \vec{m}_{TM}^{\gamma} (P_{AM}^{\gamma} P_{TN}^{\gamma}/\Delta E_{AM}\Delta E_{TM}) + \vec{m}_{MA}^{\gamma} (P_{TM}^{\gamma} P_{TN}^{\gamma}/\Delta E_{TN}\Delta E_{TM})] + \sum_{M_0^{\gamma}} \vec{\mu}_{NT}^{\gamma} \cdot [\vec{m}_{TA}^{\gamma} (P_{NM}^{\gamma} P_{MA}^{\gamma}/\Delta E_{AN}\Delta E_{AM}) + \vec{m}_{TM}^{\gamma} (P_{AM}^{\gamma} P_{AN}^{\gamma}/\Delta E_{AM}\Delta E_{AN}) + \vec{m}_{MA}^{\gamma} (P_{TM}^{\gamma} P_{AN}^{\gamma}/\Delta E_{TM}\Delta E_{AN})] + \sum_{M_0^{0}} \vec{\mu}_{MN}^{\gamma} \cdot \vec{m}_{TA}^{\gamma} [(P_{AM}^{\gamma} P_{TN}^{\gamma}/\Delta E_{AM}\Delta E_{TN}) + (P_{AN}^{\gamma} P_{TM}^{\gamma}/\Delta E_{AN}\Delta E_{TM})] \} \quad (22)$$

Only terms which are first or second order in the perturbation coefficients are retained in eq 22. All terms which have triple or quartic products of perturbation matrix elements are neglected since the inclusion of these would require that the wave functions also be developed to fourth order. Since $\vec{\mu}_{AT}^{\gamma} = 0$ for all components γ, there are no zeroth-order contributions to the rotatory strength. If we consider only one intermediate M_g state and one intermediate N_u state in the perturbation expansion, then two first-order terms appear in eq 22. These are: $\vec{\mu}_{AN}^{\gamma} \cdot \vec{m}_{TA}^{\gamma} P_{TN}^{\gamma}/\Delta E_{TN}$ and $\vec{\mu}_{NT}^{\gamma} \cdot \vec{m}_{TA}^{\gamma} P_{AN}^{\gamma}/\Delta E_{AN}$.

A. Results Deduced from Symmetry Arguments. The zeroth-order electronic state functions have been chosen to transform as IR's in both the O_h and D_3 point groups. The vector operators $\vec{\mu}$ and $\vec{m}$ can also be constructed from trigonal basis functions which transform as IR's in O_h and in D_3. The perturbation potential energy function P must transform as A_1 in D_3 and can be expressed as a linear combination of two components, say P_g and P_u, which transform gerade and ungerade, respectively, under the inversion operation of the O_h point group. Since only the A_{1g}, A_{1u}, T_{2g}, and T_{2u} IR's of O_h correlate with (or have components which correlate with) A_1 of D_3, P_g must transform as either A_{1g} or T_{2g} of O_h and P_u must transform as either A_{1u} or T_{2u} of O_h.

1. First-Order Terms. The total first-order rotatory strength associated with the $A_g \rightarrow T_g$ transition is

$$R_{AT}' = \mathrm{Im} \sum_{\gamma} \sum_{N_u^{\gamma}} [\vec{\mu}_{AN}^{\gamma} \cdot \vec{m}_{TA}^{\gamma} P_{TN}^{\gamma}/\Delta E_{TN} + \vec{\mu}_{NT}^{\gamma} \cdot \vec{m}_{NT}^{\gamma} P_{AN}^{\gamma}/\Delta E_{AN}] \quad (23)$$

Making use of the Wigner–Eckart theorem and the irreducible tensor formalism, this expression can be rewritten in terms of the reduced matrix elements and V coefficients as defined by Griffith.[18] We have

$$R_{AT}' = \mathrm{Im} \sum_{\gamma} \sum_{N_u^{\gamma}} \Big[(\langle A_g||\mu||N_u\rangle \times \langle T_g||m||A_g\rangle \langle T_g||P||N_u\rangle/\Delta E_{TN}) \times V\begin{pmatrix}\Gamma_A\Gamma_\mu\Gamma_N\\ \gamma_A\gamma_\mu\gamma_N\end{pmatrix} V\begin{pmatrix}\Gamma_T\Gamma_m\Gamma_A\\ \gamma_T\gamma_m\gamma_A\end{pmatrix} V\begin{pmatrix}\Gamma_T\Gamma_P\Gamma_N\\ \gamma_T\gamma_P\gamma_N\end{pmatrix} + (\langle N_u||\mu||T_g\rangle \langle T_g||m||A_g\rangle \langle A_g||P||N_u\rangle/\Delta E_{AN}) \times V\begin{pmatrix}\Gamma_T\Gamma_m\Gamma_A\\ \gamma_T\gamma_m\gamma_A\end{pmatrix} V\begin{pmatrix}\Gamma_N\Gamma_\mu\Gamma_T\\ \gamma_N\gamma_\mu\gamma_T\end{pmatrix} V\begin{pmatrix}\Gamma_A\Gamma_P\Gamma_N\\ \gamma_A\gamma_P\gamma_N\end{pmatrix} \Big] \quad (24)$$

where Γ denotes the appropriate IR's of the O_h point group and γ denotes the trigonal components of these IR's. The summation $\sum_{\gamma}$ is taken separately over the γ components of all Γ's in eq 24. From the orthonormality relationships between the coupling coefficients V, eq 24 can be further reduced to

$$R_{AT}' = \mathrm{Im} \sum_{\gamma_R,\gamma_N,\gamma_T} \sum_{N_u^{\gamma}} \Big[(\langle A_g||\mu||N_u\rangle \langle T_g||m||A_g\rangle \times \langle T_g||P||N_u\rangle/\Delta E_{TN}) \delta(\Gamma_N,\Gamma_T) \delta(\gamma_N,\gamma_T) \times V\begin{pmatrix}\Gamma_T\Gamma_P\Gamma_N\\ \gamma_T\gamma_P\gamma_N\end{pmatrix} + (\langle N_u||\mu||T_g\rangle \langle T_g||m||A_g\rangle \times \langle A_g||P||N\rangle/\Delta E_{AN}) \delta(\Gamma_A,\Gamma_N) \delta(\gamma_A,\gamma_N) \times V\begin{pmatrix}\Gamma_A\Gamma_P\Gamma_N\\ \gamma_A\gamma_P\gamma_N\end{pmatrix} \Big] \quad (25)$$

The necessary condition for the terms in eq 25 not to vanish is: $\Gamma_P = A_{1u}$. This result follows from the requirements that $\Gamma_N \equiv \Gamma_T$, $\gamma_N \equiv \gamma_T$, $\Gamma_N \equiv \Gamma_A$, and $\gamma_N \equiv \gamma_A$, and that the direct product, $\Gamma_A \cdot \Gamma_P \cdot \Gamma_N$, include the A_{1g} representation. If the potential energy function P is expanded in terms of spherical harmonic functions about an origin located at the metal ion, the first term in this expansion that transforms as A_{1u} in O_h is of degree nine ($\ell = 9$); that is, the first term has angular dependence Y_9^m, and radial dependence $1/R^{10}$, on the positions of the perturber sites. If the zeroth-order states, A_g and T_g, are constructed from d orbitals, then only orbitals with $\ell \geq 7$ can be mixed-in by the A_{1u} term of the perturbation P. The net first-order

(18) J. S. Griffith, "The Irreducible Tensor Method for Molecular Symmetry Groups," Prentice-Hall, Englewood Cliffs, N. J., 1962.

rotatory strength of the transition, $A_g \rightarrow T_g$, is negligibly small.

Equation 25 refers only to the net or total first-order rotatory strength. In terms of the three trigonal components of the excited state T_g, we have

$$R_{AT}' = R_{AT^0}' + R_{AT^+}' + R_{AT^-}' \quad (26)$$

The condition that P transforms as A_{1u} does not have to be satisfied to ensure the nonvanishing of the component rotatory strengths in eq 26. It is only necessary that P transform as A_1 in D_3 and as either A_{1u} or T_{2u} in O_h. The first term in the expansion of P that transforms as T_{2u} is of degree three ($\ell = 3$). This term can mix the d orbitals with p and f orbitals, and has $1/R^4$ dependence on the radial distances of the perturber sites with respect to the metal ion. It might be expected that the rotatory strengths arising from this type of term will be large. The sum of these rotatory strengths must, however, be zero.

Consider the individual terms of eq 26 for the case when $N_u = T_{1u}$, $T_g = T_{1g}$, and $A_g = A_{1g}$. The three component rotatory strengths for the $A_{1g} \rightarrow T_{1g}$ transition are

$$R_{AT^0} = \mathrm{Im}\left[K_1 V\begin{pmatrix} A_{1g} & T_{1u} & T_{1u} \\ 0 & 0 & 0 \end{pmatrix} \times V\begin{pmatrix} T_{1g} & T_{1g} & A_{1g} \\ 0 & 0 & 0 \end{pmatrix} V\begin{pmatrix} T_{1g} & T_{2u} & T_{1u} \\ 0 & 0 & 0 \end{pmatrix} + K_2 V\begin{pmatrix} T_{1u} & T_{1u} & T_{1g} \\ 0 & 0 & 0 \end{pmatrix} V\begin{pmatrix} T_{1g} & T_{1g} & A_{1g} \\ 0 & 0 & 0 \end{pmatrix} \times V\begin{pmatrix} A_{1g} & T_{2u} & T_{1u} \\ 0 & 0 & 0 \end{pmatrix}\right] = -(2/81)^{1/2} K_1 \quad (27)$$

and, by a similar procedure

$$R_{AT^+}' = R_{AT^-}' = 1/2(2/81)^{1/2} K_1 \quad (28)$$

In eq 27, K_1 and K_2 are factors which include the necessary reduced matrix elements, phase factors, and energy denominators. The V coefficients were obtained from Tables C2.1 and C2.4 in Griffith. We see that

$$R_{AT^0} = -(R_{AT^+} + R_{AT^-})$$

The gerade term in P will split the $T_{1g}{}^0$ and ($T_{1g}{}^+$, $T_{1g}{}^-$) states in energy. Therefore, considering only the first-order rotatory strength of the $A_{1g} \rightarrow T_{1g}$ transition, the CD spectrum should exhibit two bands which are equal in magnitude but which have opposite signs. The maxima of these bands will be separated by an energy difference

$$\Delta E = \langle T_{1g}{}^+ | P_g | T_{1g}{}^+ \rangle - \langle T_{1g}{}^0 | P_g | T_{1g}{}^0 \rangle \quad (29)$$

and the ellipticities of the bands will be proportional to R_{AT^0}' and ($R_{AT^+}' + R_{AT^-}'$). This result is general for all cases in which the excited state is an orbital triplet, the ground state is nondegenerate, and $\Gamma_P = T_{2u}{}^0$.

2. Second-Order Terms. It is not nearly so straightforward to derive a set of results, based on symmetry arguments, which has general applicability to a second-order terms of eq 22. From detailed treatments of several excitations involving various state symmetries, it can be shown that for those second-order terms which have nonvanishing trigonal components, the rotatory strengths of the individual trigonal components have identical signs and that the net second-order rotatory strength is, therefore, nonvanishing. These results for the second-order rotatory strengths can be displayed most clearly by adopting a pure crystal-field representation for the ligand-field transitions of the metal complex. Accurate quantitative calculations cannot be obtained with such a representation, but the essential symmetry rules and qualitative aspects of the CD spectra can be easily and clearly deduced. Furthermore, it will be convenient to express the rotatory strengths in terms of matrix elements of one-electron wave functions rather than the state functions of eq 22, since these matrix elements can then be used to obtain the rotatory strength of any state excitation.

B. Crystal-Field Model. We choose as our one-electron basis set, 3d, 4p, and 4f orbitals located on the central metal ion. For the 3d orbitals, we use the trigonal orbitals defined by Moffitt[5] and by Piper and Karipides[12]

$$t_+ = -(1/3)^{1/2} d_{+1} - i(2/3)^{1/2} d_{-2}$$
$$t_- = +(1/3)^{1/2} d_{-1} + i(2/3)^{1/2} d_{+2}$$
$$t_0 = d_0$$
$$e_+ = -(2/3)^{1/2} d_{+1} + i(1/3)^{1/2} d_{-2}$$
$$e_- = +(2/3)^{1/2} d_{-1} - i(1/3)^{1/2} d_{+2}$$

where the orbitals d_m are those prescribed by Condon and Shortley.[19] These orbitals form both trigonal (D_3) and octahedral (O_h) bases. In the O_h point group, the orbital set (t_0, t_+, t_-) transforms as T_{2g}, and the orbital set (e_+, e_-) transforms as E_g. In the D_3 point group, t_0 transforms as A_1 and the orbitals, e_+, e_-, t_+, and t_- transform as E. The trigonal coordinate system is defined in Figure 1. The static perturbation potential is expressed as

$$P = P_g + P_u = eA_2{}^0 r^2 Y_2{}^0 + eA_3{}^3 r^3 (1/2)^{1/2} (Y_3{}^{-3} - Y_3{}^3) \quad (30)$$

where only the leading gerade and ungerade terms in the multipolar expansion of P have been retained. The functions Y^m are spherical harmonics normalized to unity and are dependent upon electron angular

(19) E. U. Condon and G. H. Shortley, "The Theory of Atomic Spectra," 2nd ed, Cambridge University Press, London and New York, N. Y., 1963.

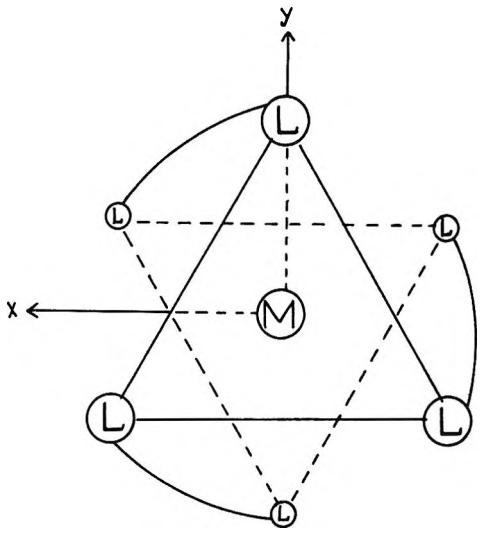

Figure 1. Trigonal coordinate system for [M(L2l)3] complex. The principal threefold (C_3) axis is taken as the Z axis and one of the twofold (C_2) axes is the X axis. The solid-line triangle is above the plane of the drawing; the dotted-line triangle is below this plane. The X and Y, axes are in this plane as is the metal atom. The solid curved lines connecting the ligating atoms depict the ligand part of the chelate rings.

coordinates; r is the electron radial coordinate and e is the electron charge. The factors A_2^0 and A_3^3 represent sums over all perturbing sites i and are dependent upon the positional coordinates of these sites with respect to the central metal ion, and the charge parameters chosen to represent these sites in the crystal field model. Note that in the crystal field model no distinction is made between the P_ϵ and P_ν terms of eq 5 and that both the ligating atoms L and the nonligating atoms ℓ are treated as perturbers. The first term in (30) transforms as A_1 in D_3 and as T_{2g} in O_h. It corresponds to a compression or an expansion of the zeroth-order octahedral complex along the $C_3(Z)$ axis. The second term in (30) transforms as A_1 in D_3 and as T_{2u} in O_h. This term corresponds to an azimuthal twist of the triangles shown in Figure 1 about the $C_3(Z)$ axis [the two triangles are rotated by equal amounts but in opposite directions about $C_3(Z)$]. If we assume that the perturber sites can be represented as point charges, the coefficients A_2^0 and A_3^3 can then be expressed as follows

$$A_2^0 = \left(\frac{\pi}{5}\right)^{1/2} \sum_i q_i(3\cos^2\theta_i - 1)/R_i^3 \qquad (31)$$

$$A_3^3 = \left(\frac{35\pi}{14}\right)^{1/2} \sum_i q_i \sin^3\theta_i \cos 3\phi_i/R_i^4 \qquad (32)$$

where (θ_i, ϕ_i, R_i) are the spherical coordinates for perturber site i, and q_i is the classical charge associated with the site. The angle θ is measured from the Z axis of the trigonal system and ϕ is measured from the X axis.

The matrix elements for d–p and d–f mixing under the influence of the perturbation P_u are given in Tables I and II, respectively. The d–d interaction

Table I: d–p Interaction Matrix[a]

$(P_u)_{pd}$	e_+	e_-	t_0	t_+	t_-
p_{+1}	$-i$	0	0	$+i(2)^{1/2}$	0
p_0	0	0	0	0	0
p_{-1}	0	$-i$	0	0	$+i(2)^{1/2}$

[a] In units of $\left(\frac{3}{56\pi}\right)^{1/2} eA_3^3 \langle R_p|r^3|R_d\rangle = P$.

Table II: d–f Interaction Matrix[a]

$(P_u)_{fd}$	e_+	e_-	t_0	t_+	t_-
f_{+3}	0	0	$+(75)^{1/2}$	0	0
f_{+2}	0	$+(50)^{1/2}$	0	0	+5
f_{+1}	$+i(10)^{1/2}$	0	0	$-i(20)^{1/2}$	0
f_0	0	0	0	0	0
f_{-1}	0	$+i(10)^{1/2}$	0	0	$-i(20)^{1/2}$
f_{-2}	$+(50)^{1/2}$	0	0	+5	0
f_{-3}	0	0	$-(75)^{1/2}$	0	0

[a] In units of $\frac{1}{6}\left(\frac{1}{21\pi}\right)^{1/2} eA_3^3 \langle R_f|r^3|R_d\rangle = F$.

Table III: d–d Interaction Matrix[a]

$(P_g)_{dd}$	e_+	e_-	t_0	t_+	t_-
t_0	0	0	+2	0	0
t_+	$(2)^{1/2}$	0	0	−1	0
t_-	0	$(2)^{1/2}$	0	0	−1

[a] In units of $\frac{1}{14}\left(\frac{5}{\pi}\right)^{1/2} eA_2^0 \langle R_d|r^2|R_d\rangle = D'$.

matrix elements due to P_g are displayed in Table III. The nonvanishing p–p, f–f, and p–f interaction matrix elements are listed as follows

$$\langle p_{\pm1}|P_g|p_{\pm1}\rangle = -P'$$
$$\langle p_0|P_g|p_0\rangle = +P'$$
$$\langle f_{\pm3}|P_g|f_{\pm3}\rangle = -5F'$$
$$\langle f_{\pm1}|P_g|f_{\pm1}\rangle = +3F'$$
$$\langle f_0|P_g|f_0\rangle = +4F'$$
$$\langle p_{\pm1}|P_g|f_{\pm1}\rangle = +(2)^{1/2}G'$$
$$\langle p_0|P_g|f_0\rangle = +(3)^{1/2}G'$$

where

$$P' = (1/20\pi)^{1/2} eA_2^0 \langle R_p|r^2|R_p\rangle$$
$$F' = (1/180\pi)^{1/2} eA_2^0 \langle R_f|r^2|R_f\rangle$$
$$G' = (9/140\pi)^{1/2} eA_2^0 \langle R_p|r^2|R_f\rangle$$

and R_p and R_f are the 4p and 4f radial functions, respectively.

We shall assume that the energy differences between the 3d orbitals and the 4p orbitals and between the 3d and 4f orbitals are much larger than the octahedral crystal-field splitting energies within the 3d, 4p, and 4f orbital manifolds. Making this assumption, we define the following energy parameters: E_p = average energy difference between the 4p and 3d orbital manifolds in an octahedral field; E_f = average energy difference between the 4f and 3d orbital manifolds in an octahedral field; E_d = crystal-field splitting energy within the 3*d*-orbital manifold = $E_e^0 - E_t^0 = 10D_q$. The second-order perturbed d orbitals can now be expressed in terms of the zeroth-order 3d, 4p, and 4f orbital sets, the three energy differences E_p, E_f, and E_d, and the six quantities D', P', F', G', P, and F. The latter six quantities depend upon the positions of the perturber sites, the charge assigned to each perturber site, and the radial integrals of the perturbation matrix elements. To calculate the one-electron rotatory strengths from these second-order wave functions, we further require the magnetic dipole transition moments for d → d transitions and the electric dipole transition for d → p and d → f transitions. These transition moments are given in Tables IV, V, and VI for the unperturbed one-electron wave functions.

The first-order rotatory strengths that arise from d–p mixing are given in Table VII and those due to d–f mixing are given in Table VIII. The second-order contributions to the rotatory strength in the case of d–p mixing are presented in Table IX and those arising from d–f mixing are given in Table X. With the use of these four tables, we can now obtain expressions for the rotatory strengths of the ligand-field transitions of trigonal dihedral transition metal complexes within the approximations of the crystal field theory of coordination compounds and the one-electron model of optical activity. These rotatory strengths are expressed in terms of the energy differences E_d, E_p, E_f, the perturbation parameters D', P', F', G', P, and F, and the transition integrals Q_{pd} and Q_{fd}. The expressions are complete to second-order in perturbation theory for a basis set restricted to 3d, 4p, and 4f orbitals. Since the trigonal dihedral d^3 and d^6 transition metal complexes have received the most attention in experimental studies, we shall consider the Cr(III) and Co(III) cases in more detail.

The ground state and the first two excited states of Cr(III) can be written in determinantal form as follows.

Ground state (t^3)

$$|A_{2g}\rangle = |t_0 t_+ t_-|, A_2$$

Excited states (t^2e)

$$|T_{2g}{}^0\rangle = (1/2)^{1/2}\{|t_0 e_+ t_-| - |t_0 t_+ e_-|\}, A_1$$

Table IV: Zeroth-Order Magnetic Dipole Transition Matrix[a]

$\vec{M}_{dd}$	t_0	t_+	t_-
e_+	$-\vec{\imath}_-$	$+\vec{k}$	$-i\vec{\imath}_+$
e_-	$+\vec{\imath}_+$	$-i\vec{\imath}_-$	$-\vec{k}$

[a] In units of $(2)^{1/2}(he/4\pi mc)$; $\vec{\imath}_+ = (\vec{i} + i\vec{j})$, $\vec{\imath}_- = (\vec{i} - i\vec{j})$, $\vec{k} = \vec{k}$; $\vec{i}$, $\vec{j}$, $\vec{k}$ = unit vectors in x, y, z directions.

Table V: Zeroth-Order d–p Electric Dipole Transition Matrix[a]

$\vec{Q}_{pd}$	e_+	e_-	t_0	t_+	t_-
p_+	$-(2)^{1/2}i\vec{k}$	$+(2)^{1/2}i\vec{\imath}_-$	$+\vec{\imath}_+$	$-\vec{k}$	$-2i\vec{\imath}_-$
p_0	$+(2)^{1/2}\vec{\imath}_-$	$+(2)^{1/2}\vec{\imath}_+$	$+2\vec{k}$	$+\vec{\imath}_-$	$+\vec{\imath}_+$
p_-	$+(2)^{1/2}i\vec{\imath}_+$	$+(2)^{1/2}\vec{k}$	$-\vec{\imath}_-$	$-2i\vec{\imath}_+$	$+\vec{k}$

[a] In units of $(1/15)^{1/2}eQ_{pd}$; $Q_{pd} = \langle R_p|r|R_d\rangle$.

Table VI: Zeroth-Order d–f Electric Dipole Transition Matrix[a]

$\vec{Q}_{fd}$	e_+	e_-	t_0	t_+	t_-
f_{+3}	0	$+i(5)^{1/2}\vec{\imath}_+$	0	0	$-i(10)^{1/2}\vec{\imath}_+$
f_{+2}	$+2\left(\frac{5}{3}\right)^{1/2}\vec{\imath}_+$	$-i\left(\frac{5}{3}\right)^{1/2}\vec{k}$	0	$+\left(\frac{10}{3}\right)^{1/2}\vec{\imath}_+$	$+i\left(\frac{10}{3}\right)^{1/2}\vec{k}$
f_{+1}	$-4\left(\frac{1}{3}\right)^{1/2}k$	$-i\left(\frac{1}{3}\right)^{1/2}\vec{\imath}_-$	$-(6)^{1/2}\vec{\imath}_+$	$-2\left(\frac{2}{3}\right)^{1/2}\vec{k}$	$+i\left(\frac{2}{3}\right)^{1/2}\vec{\imath}_-$
f_0	$-(2)^{1/2}\vec{\imath}_-$	$-(2)^{1/2}\vec{\imath}_+$	$+3k$	$-\vec{\imath}_-$	$-\vec{\imath}_+$
f_{-1}	$-i\left(\frac{1}{3}\right)^{1/2}\vec{\imath}_+$	$+4\left(\frac{1}{3}\right)^{1/2}\vec{k}$	$+(6)^{1/2}\vec{\imath}_-$	$+i\left(\frac{2}{3}\right)^{1/2}\vec{\imath}_+$	$+2\left(\frac{2}{3}\right)^{1/2}\vec{k}$
f_{-2}	$+i\left(\frac{5}{3}\right)^{1/2}\vec{k}$	$+2\left(\frac{5}{3}\right)^{1/2}\vec{\imath}_-$	0	$-i\left(\frac{10}{3}\right)^{1/2}\vec{k}_-$	$+\left(\frac{10}{3}\right)^{1/2}\vec{\imath}_-$
f_{-3}	$+i(5)^{1/2}\vec{\imath}_-$	0	0	$-i(10)^{1/2}\vec{\imath}_-$	0

[a] In units of $\left(\frac{1}{35}\right)^{1/2}eQ_{fd}$; $Q_{fd} = \langle R_f|r|R_d\rangle$.

Table VII: First-Order Rotatory Strength; d–p Mixing[a]

R_p'	e_+	e_-
t_0	−1	−1
t_+	−3	+4
t_-	+4	−3

[a] In the units $\left(\frac{2}{15}\right)^{1/2}\left(\frac{e^2\hbar}{2mc}\right)PE_p^{-1}Q_{pd}$.

Table VIII: First-Order Rotatory Strength; d–f Mixing[a]

R_f'	e_+	e_-
t_0	−7	−7
t_+	−1	+8
t_-	+8	−1

[a] In the units $\left(\frac{6}{7}\right)^{1/2}\left(\frac{e^2\hbar}{2mc}\right)FE_f^{-1}Q_{fd}$.

to each of the excited states are listed in Tables XI and XII. As has been previously demonstrated by Piper and Karipides,[12] the net rotatory strength calculated for the octahedral $^4A_{2g} \rightarrow {}^4T_{2g}$ transition is zero on the crystal field model carried to first-order in a d, p, and f basis and with the perturbation potential P_u (eq 30). The first-order rotatory strength of the $^4A_{2g} \rightarrow {}^4T_{1g}$ is likewise computed to be zero. However, when the crystal field model is carried to second order, there is a nonvanishing rotatory strength computed for both the $^4A_{2g} \rightarrow {}^4T_{2g}$ and the $^4A_{2g} \rightarrow {}^4T_{1g}$ transitions. The results presented in Tables XI and XII also apply to the $^1A_{1g} \rightarrow {}^1T_{1g}$ and $^1A_{1g} \rightarrow {}^1T_{2g}$ transitions of the d^6, Co(III) complexes, except that each entry in the tables must be multiplied by a factor of 2 in this case.

In analyzing how the formal results of our model are related to the physical details of the trigonal complexes, we shall consider only the largest approximate second-order terms in Table XII. The rotatory

Table IX: Second-Order Contributions to the Rotatory Strength; d–p Mixing[a]

R_p''	e_+	e_-
t_+	$+6PD'E_d^{-1} - 6(5)^{1/2}FG'E_f^{-1} - 3PP'E_p^{-1} + 2PD'E_p^{-1}$	$+2PD'E_d^{-1} + 8(5)^{1/2}FG'E_f^{-1} + 4PP'E_p^{-1} - 2PD'E_p^{-1}$
t_0	$-3PD'E_d^{-1} - 2(5)^{1/2}FG'E_f^{-1} - PP'E_p^{-1}$	$-3PD'E_d^{-1} - 2(5)^{1/2}FG'E_f^{-1} - PP'E_p^{-1}$
t_-	$+2PD'E_d^{-1} + 8(5)^{1/2}FG'E_f^{-1} + 4PP'E_p^{-1} - 2PD'E_p^{-1}$	$+6PD'E_d^{-1} - 6(5)^{1/2}FG'E_f^{-1} - 3PP'E_f^{-1} + 2PD'E_p^{-1}$

[a] In units of $\left(\frac{2}{15}\right)^{1/2}\left(\frac{e^2\hbar}{2mc}\right)E_p^{-1}Q_{pd}$.

Table X: Second-Order Contributions to the Rotatory Strength; d–f Mixing

R_f''	e_+	e_-
t_+	$+6(5)^{1/2}FD'E_d^{-1} + 12PG'E_p^{-1} - 28(5)^{1/2}FF'E_f^{-1} - 3(5)^{1/2}FD'E_f^{-1}$	$+12(5)^{1/2}FD'E_d^{-1} + 4PG'E_p^{-1} - 12(5)^{1/2}FF'E_f^{-1} - 12(5)^{1/2}FD'E_f^{-1}$
t_0	$-12(5)^{1/2}FD'E_d^{-1} - 6PG'E_p^{-1} + 18(5)^{1/2}FF'E_f^{-1}$	$-12(5)^{1/2}FD'E_d^{-1} - 6PG'E_p^{-1} + 18(5)^{1/2}FF'E_f^{-1}$
t_-	$+12(5)^{1/2}FD'E_d^{-1} + 4PG'E_p^{-1} - 12(5)^{1/2}FF'E_f^{-1} - 12(5)^{1/2}FD'E_f^{-1}$	$+6(5)^{1/2}FD'E_d^{-1} + 12PG'E_p^{-1} - 28(5)^{1/2}FF'E_f^{-1} - 3(5)^{1/2}FD'E_f^{-1}$

[a] In the units $\left(\frac{2}{105}\right)^{1/2}\left(\frac{\hbar e^2}{2mc}\right)E_f^{-1}Q_{fd}$.

$$|T_{2g}^+\rangle = (1/2)^{1/2}\{|e_+t_+t_-| - i|t_0e_-t_-|\},\ E_a$$
$$|T_{2g}^-\rangle = -(1/2)^{1/2}\{|e_-t_+t_-| - i|t_0t_+e_+|\},\ E_a$$
$$|T_{1g}^0\rangle = (1/2)^{1/2}\{|t_0e_+t_-| + |t_0t_+e_-|\},\ A_2$$
$$|T_{1g}^+\rangle = (1/2)^{1/2}\{|e_+t_+t_-| - i|t_0e_-t_-|\},\ E_b$$
$$|T_{1g}^-\rangle = -(1/2)^{1/2}\{|e_-t_+t_-| + i|t_0t_+e_+|\},\ E_b$$

where the symbols on the extreme right refer to the irreducible reps under which each state function transforms in the D_3 point group. The first- and second-order rotatory strengths for the transitions from $|A_{2g}\rangle$

Table XI: First-Order Rotatory Strength; Cr(III)

R'	d–p mixing[a]	d–f mixing[b]
T_{2g}^0	−6	−2
(T_{2g}^+, T_{2g}^-)	+6	+2
T_{1g}^0	0	0
(T_{1g}^+, T_{1g}^-)	0	0

[a] In the units: $\left(\frac{2}{15}\right)^{1/2}\left(\frac{e^2\hbar}{2mc}\right)PE_p^{-1}Q_{pd}$. [b] In the units: $\left(\frac{6}{7}\right)^{1/2}\left(\frac{e^2\hbar}{2mc}\right)FE_f^{-1}Q_{fd}$.

Table XII: Second-Order Rotatory Strengths; Cr(III)

R''	d–p mixing[a]	d–f mixing[b]
T_{2g}^0	$+12PD'E_d^{-1} - 12(5)^{1/2}FG'E_f^{-1} - 6PP'E_p^{-1} + 4PD'E_p^{-1}$	$+12(5)^{1/2}FD'E_d^{-1} + 24PG'E_p^{-1} - 56(5)^{1/2}FF'E_f^{-1} - 6(5)^{1/2}FD'E_f^{-1}$
(T_{2g}^+, T_{2g}^-)	$-2PD'E_d^{-1} + 12(5)^{1/2}FG'E_f^{-1} + 6PP'E_p^{-1} - 4PD'E_p^{-1}$	$-4PG'E_p^{-1} + 12(5)^{1/2}FF'E_f^{-1} - 24(5)^{1/2}FD'E_f^{-1}$
T_{1g}^0	0	0
(T_{1g}^+, T_{1g}^-)	$+10PD'E_d^{-1} + 20(5)^{1/2}FG'E_f^{-1} + 10PP'E_p^{-1} - 4PD'E_p^{-1}$	$+48(5)^{1/2}FD'E_d^{-1} + 20PG'E_p^{-1} - 60(5)^{1/2}FF'E_f^{-1} - 24(5)^{1/2}FD'E_f^{-1}$

[a] In the units: $\left(\frac{2}{15}\right)^{1/2}\left(\frac{e^2\hbar}{2mc}\right)E_p^{-1}Q_{pd}$. [b] In the units: $\left(\frac{2}{105}\right)^{1/2}\left(\frac{e^2\hbar}{2mc}\right)E_f^{-1}Q_{fd}$.

strengths are now written as

$$A_{2g} \longrightarrow T_{2g}^0$$

$$R''(A_1) \cong -(^2/_{15})^{1/2}(6 - 12D'E_d^{-1})PQ_{pd}E_p^{-1} - (^6/_7)^{1/2}(2\text{–}180D'E_d^{-1})FQ_{fd}E_f^{-1} \quad (33a)$$

$$A_{2g} \longrightarrow (T_{2g}^+, T_{2g}^-)$$

$$R''(E_a) \cong (^2/_{15})^{1/2}(6 - 2D'E_d^{-1})PQ_{pd}E_p^{-1} + 2(^6/_7)^{1/2}FQ_{fd}E_f^{-1} \quad (33b)$$

$$A_{2g} \longrightarrow T_{1g}^0$$

$$R''(A_2) = 0 \quad (33c)$$

$$A_{2g} \longrightarrow (T_{1g}^+, T_{1g}^-)$$

$$R''(E_b) \cong +10(^2/_{15})^{1/2}PD^1Q_{pd}E_d^{-1}E_p^{-1} + 720(^6/_7)^{1/2}FD'Q_{fd}E_d^{-1}E_f^{-1} \quad (33d)$$

where the units are $(e^2\hbar/2mc)$. The "net" rotatory strength of the $A_{2g} \rightarrow T_{2g}$ transition is approximated by

$$R_{net}(T_{2g}) \cong +(^2/_{15})^{1/2}10PD'Q_{pd}E_p^{-1}E_d^{-1} + 180\,(^6/_7)^{1/2}FD'Q_{fd}E_f^{-1}E_d^{-1} \quad (34)$$

and the "net" rotatory strength of the $A_{2g} \rightarrow T_{1g}$ transition is, of course, just $R''(E_b)$, given in eq 33d. The energy differences, E_p, E_f, and E_d have all been defined to be >0, and the products of radial integrals in $PD'Q_{pd}$ and in $FD'Q_{fd}$ are >0. The signs of the two terms in (34) are, therefore, identical and are determined by the sign of the product function

$$A_2^0A_3^3 = (^1/_{28})^{1/2}\pi\sum_i^N\sum_j^N q_iq_j(3\cos^2\theta_i - 1) \times \sin^3\theta_j \cos 3\phi_j/R_i^3R_j^4 \quad (35)$$

where (θ_i, ϕ_i, R_i) and (θ_j, ϕ_j, R_j) are the position coordinates of perturber sites i and j, q_i and q_j are the charges assigned to these sites, and each summation is taken over all perturber sites.

The cross terms (i, j) in eq 35 have their physical origin in situations where one perturber site provides a gerade distortion [compression or elongation along the $C_3(Z)$ axis] of the zeroth-order octahedral complex and a second perturber simultaneously provides an ungerade distortion [right- or left-handed azimuthal twist about $C_3(Z)$] of the octahedral structure. The terms (i, i) and (j, j) arise when single perturber groups provide both types of distortions at the same time. The function, $(3\cos^2\theta - 1)\sin^3\theta$, has nodes at $\theta = 0, \pi$, 54.7°, and 125.3°. The nodes of the function, $\cos 3\phi$, occur at $\phi = \pm(2n + 1)\pi/6$, $n = 0, 1, 2$.

C. Applications of Static, Crystal-Field Model. Now we can examine how the various structural features of trigonal dihedral complexes might be expected to influence the magnitude and sign of the electronic rotatory strength on the static crystal-field model. First we shall consider the case in which the ligating atoms are located at the vertices of a regular octahedron, the chelate rings are planar, and each chelate ring has two bridging atoms. As an example of this case, we consider $Cr(en)_3^{3+}$ in which the en ligands are assumed to be planar. This serves as our idealized case. We then examine how the rotatory strength might be influenced by the following deviations from

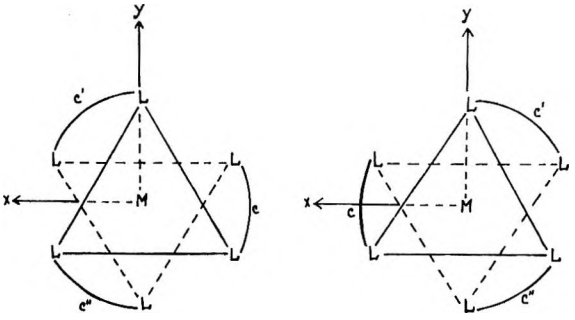

Figure 2. Configurational isomers of $[M(L_2l)_3]$. The individual chelate rings in each complex are labeled c, c', and c''. Nomenclature for the configuration of the three chelate rings about the metal atom is as follows: Λ ≡ a spiral about the C_3 axis with a left-handed screw sense; Δ ≡ a spiral about the C_3 axis with a right-handed screw sense. The correlations between these conventions and others in common usage are: Λ ≡ D ≡ (+); Δ ≡ L ≡ (−).

this idealized case: (1) chelate ring puckering (ob or lel); (2) distortion of the CrL_6 cluster from an octahedral configuration; (3) chelate ring substitutions [*e.g.*, propylenediamine (pn) in place of en]; and, (4) increasing ring size [*e.g.*, trimethylenediamine (tm) in place of en].

1. Idealized Case. In Figure 2 the two optical isomers of a trigonal dihedral complex are shown. In the idealized case the ligator atoms are assumed to be located at the regular octahedral sites and we consider only the perturbing influence of the nonligating chelate ring atoms. The polar angles θ_i of these nonligating atoms are within the limits, $125.3° > \theta_i > 54.7°$. Therefore, the function $(3\cos\theta_i - 1)\sin^3\theta_i$ is <0 for these perturbers. The closer these atoms are to the plane defined by the three dihedral axes of the trigonal system ($\theta = 90°$), the larger will be the function $(3\cos^2\theta - 1)\sin^3\theta$. The azimuthal angles ϕ_i of the nonligating perturbers will depend upon the configuration of the chelate rings about the metal ion. If we consider the optical isomers shown in Figures 2a and 2b, the following results are obtained

	Λ	Δ
C	$210° > \phi_i > 150°$	$30° > \phi_i > 330°$
C'	$90° > \phi_i > 30°$	$150° > \phi_i > 90°$
C''	$330° > \phi_i > 270°$	$270° > \phi_i > 210°$
C	$\cos 3\phi_i < 0$	$\cos 3\phi_i > 0$
C'	$\cos 3\phi_i < 0$	$\cos 3\phi_i > 0$
C''	$\cos 3\phi_i < 0$	$\cos 3\phi_i > 0$

If we further assume that the signs of both q_i and q_j are identical for all pairs of perturbers (i, j), then $A_2^0A_3^3 > 0$ for the Λ isomer and $A_2^0A_3^3 < 0$ for the Δ isomer. Therefore, Λ-$R_{net}(T_{2g}) > 0$, Δ-$R_{net}(T_{2g}) < 0$, Λ-$R_{net}(T_{1g}) > 0$, and Δ-$R_{net}(T_{1g}) < 0$. Note that the signs of the net rotatory strengths are independent of the absolute signs of the group charges, q_i and q_j, so long as they (the group-charge signs) are identical.

The "net" rotatory strength of the $A_{2g} \rightarrow T_{2g}$ transition is determined by second-order terms. However, if the trigonal components of this transition are split sufficiently then the CD spectrum will exhibit two bands, one due to the $A_2 \rightarrow A_1$, component and the other arising from the $A_2 \rightarrow E_a$ component. Since the first-order rotatory strengths are considerably larger than the second-order contributions, the signs of these individual CD bands will be determined by the signs of the first-order results given in Table XI. Since the products of radial integrals in PQ_{pd} and in FQ_{fd} are >0 and the energy differences, E_d and E_f, are > 0, the signs of the first-order terms are determined by the sign of the function eA_3^3 (eq 32). Furthermore, $\sin^3\theta_i > 0$ for all nonligating perturbers and $\cos 3\phi_i > 0$ for the Δ isomer and $\cos 3\phi_i < 0$ for the Λ isomer. If we assign a "net" positive charge to each of the nonligating perturber sites, then $eq_i < 0$ for all sites i and the signs of the component first-order rotatory strengths of the $A_{2g} \rightarrow T_{2g}$ transition are as follows

$$\Lambda \text{ isomer } R'(A_1) < 0; \quad R'(E_a) > 0$$

$$\Delta \text{ isomer } R'(A_1) > 0; \quad R'(E_a) < 0$$

For both the Λ and Δ isomers, the second-order rotatory strengths R'' will augment the first-order rotatory strengths of the doubly degenerate E_a trigonal component, but will diminish the first-order strengths of the nondegenerate A_1 trigonal component. R_{net} will have the same sign as $R'(E_a)$ in both isomers.

The trigonal splitting parameters, K and K', are defined here as

$$K = \langle t_+|P_g|t_+\rangle = -D' \tag{36}$$

$$K' = -(1/2)^{1/2}\langle t_+|P_g|e_+\rangle = -D' \tag{37}$$

where $D' = +1/14 e\langle r^2\rangle_{dd}\sum_i q_i(3\cos^2\theta_i - 1)/R_i^3$. For the nonligating perturbing sites, the geometrical factor is <0 and $eq_i < 0$, so that $K = K' < 0$. Note that when $K < 0$, the nondegenerate A_1 component lies higher in energy than the degenerate E_a component; that is, $K < 0$ if $(\nu_E - \nu_A) < 0$, where ν_E and ν_A are the transition frequencies from the ground state. Assuming, therefore, that the nonligating perturber sites have residual positive charges associated with them (giving rise to attractive interactions with the chromophoric d electrons), the trigonal splitting parameter, K, is predicted to be of negative sign and the degenerate state, E_a, is expected to lie lower in energy than does the nondegenerate A_1 state.

So far in our idealized case we have assumed that the interaction potentials, P_g and P_u, are predominantly attractive ($q_i > 0$ for all perturber sites i), since the most important perturbing centers are at the positive poles of polar bonds. In other words, in the C–N bonds of en the carbon bridging atoms would be assigned a residual positive charge and the ligating nitrogen atoms would possess a net negative charge. The repulsive interactions between the chromophoric electrons and the nitrogen atoms can only influence the octahedral ligand-field splitting, since, in our idealized case, the N atoms are octahedrally disposed about the metal ion. If we preferred the incomplete screening representations of P_g and P_u, again the perturbing potential would be attractive.

2. Ring Puckering. We shall consider the influence of ring puckering only insofar as it will lead to the ob or lel arrangement of the bonds between the bridging atoms in each chelate ring of the tris complex. Again we assume a five-membered chelate ring and an octahedral arrangement of the six ligating atoms.

The X-ray diffraction data on the structures of several $[M(en)_3]$-type complexes show that there is significant puckering in the five-membered chelate

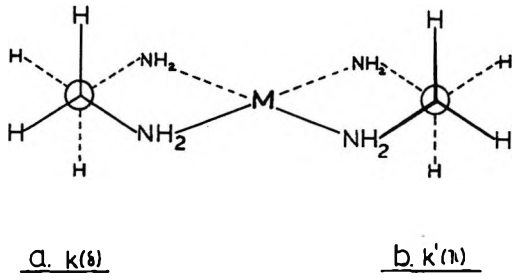

Figure 3. Conformational isomers of coordinated ethylenediamine.

rings.[20,21] In 1959 Corey and Bailar carried out a conformational analysis of $[Co(en)_3]^{3+}$ ion by applying the techniques used in the stereochemical analysis of carbocyclic rings.[22] They concluded that the $Co(en)^{3+}$ chelate ring should be most stable in either of two conformations which are mirror images and nonsuperimposable. They called these conformers k and k' (see Figures 3a and 3b). The bond distances and angles calculated by Corey and Bailer for these two $Co(en)^{3+}$ strain-free chelate ring systems agreed almost exactly with those obtained from the crystal structure of D-$[Co(en)_3]\cdot Cl_3\cdot NaCl\cdot 6H_2O$.[20] In their model the cobalt ion, two nitrogen atoms and one carbon atom are almost coplanar; the other carbon atom is out of this plane. The hydrogens on both the nitrogen atoms and the carbon atoms adopt axial or equatorial positions. In the transformation, $k \leftrightarrow k'$, the axial H atoms become equatorial and *vice versa*. When three en molecules coordinate with a metal ion to form a tris complex, four different combinations of the k and/or k' chelate ring conformations are possible for each of the diastereoisomers, Λ and Δ. In the Δ isomer these combinations are: $\Delta(kkk)$, $\Delta(k'kk)$, $\Delta(k'k'k)$, and $\Delta(k'k'k')$. Since the three chelate rings are in relatively close proximity in the tris complex, it might be expected that interactions between the substituents (H atoms in en) would tend to make one of the four possible arrangements energetically favored. By considering the various possible nonbonded interactions between the chelate ring atoms in the tris complex of Λ-$[Co(en)_3]^{3+}$, Corey and Bailar determined the $\Lambda(kkk)$ isomer to be the most stable and the $\Lambda(k'k'k')$ isomer the least stable of the four. The energy difference between these isomers was assessed as 1.8 kcal/mol. This structural prediction was in agreement with the crystal structure determination. In the $\Lambda(kkk)$ isomer the axes of the C–C bonds of the en ligands are parallel (lel) to the C_3 axis of the complex, while in the $\Lambda(k'k'k')$ isomer these bonds are oblique (ob) to this axis (see Figures 4a and 4b). In the $\Delta(kkk)$ complex the ob arrangement is present, and in the $\Delta(k'k'k')$ complex the lel arrangement. The $\Delta(k'k'k')$ isomer is the more stable, again by 1.8 kcal/mol. Since only nonbonded interactions were included in the Corey and Bailar study and since hydration energies might be significantly different for the four isomeric forms in solution, it is unclear whether one finds only the $\Lambda(kkk)$ or $\Delta(k'k'k')$ $[Co(en)_3]^{3+}$ isomers present in solution. There is some experimental evidence to suggest that Λ-$[Co(en)_3]^{3+}$ exists at least partly in the $\Lambda(kkk')$ form in solution.

In the ob form of tris complexes the bridging atoms in the chelate rings (carbon atoms in en) are forced toward the xy plane of the trigonal coordinate system. This causes the functions $(3\cos^2\theta_i - 1)$ to approach their maximum value of -1 (at $\theta_i = 90°$) resulting in an increased trigonal splitting. The sign of the splitting remains, of course, unchanged from that for the idealized case. The A component is pushed up and the E component is pushed down in energy. A larger value of $(3\cos^3\theta_i - 1)$ would also tend to increase the magnitude of the second-order electronic rotatory strength. However, in the ob form the atoms are moved closer to the nodal planes defined by the function $\cos 3\theta_i$. This would tend to decrease the rotatory strength of the ob complexes relative to that of the idealized complexes.

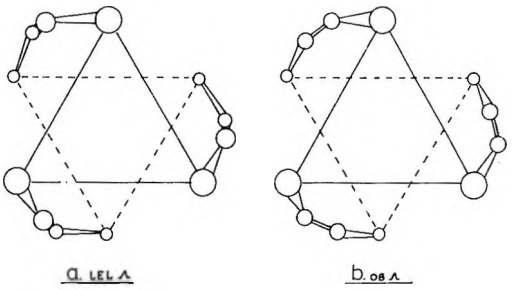

Figure 4. Lel and Ob Forms of Λ-$[M(L_21)_3]$.

In the lel form of tris complexes the bridging atoms are pulled away from the xy plane and the θ_i approach the octahedral values of 125.3 or 54.7°. This results in a diminished trigonal splitting compared to that predicted for the idealized case and for the ob complexes. However, in the lel complexes the bridging atoms approach the optimum values of ϕ_i necessary to attain maximum rotatory strength ($\phi = \pm n(\pi/3)$, $n = 0, 1, 2, 3\ldots$). The smaller K has the effect of decreasing the second-order rotatory strengths.

Altering the tris complexes from the idealized form to the ob form should increase the trigonal splitting, while changing to the lel form should decrease the splitting. The sign of the splitting should remain unchanged. In diagrammatic form we have, for example

(20) N. Nakatsu, M. Shiro, V. Saito, and H. Kuroya, *Bull. Chem. Soc. Jap.*, **30**, 795 (1957).

(21) N. Nakatsu, *ibid.*, **35**, 832 (1962).

(22) E. J. Corey and J. C. Bailar, *J. Amer. Chem. Soc.*, **81**, 2620 (1959).

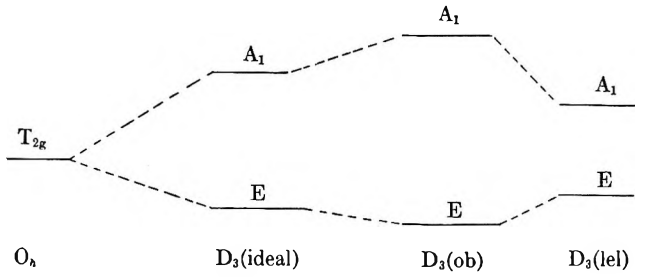

The relative magnitudes of the rotatory strength for the idealized, ob, and lel forms can only be assessed by carrying out a calculation in which the values of R_i, q_i, θ_i and ϕ_i are specified. In the lel form the ungerade perturbation is enhanced while the gerade perturbation is diminished, and in the ob form the opposite occurs.

3. Trigonal Distortion of the ML_6 Cluster. Contracting the L–M–L (where L = ligating atoms) angle in each chelate ring and simultaneously compressing the complex along the $C_3(Z)$ axis, would give the functions $(3\cos^2\theta_L - 1)$ and $\cos 3\phi_L$ the same signs as $(3\cos^2\theta_i - 1)$ and $\cos 3\phi_i$ for a given Λ or Δ isomer. The magnitudes of the former, however, would be significantly smaller since the deviation of θ_L and of ϕ_L from the octahedral values would be very small. (If they were not very small our concept of treating $M(L_2\ell)_3$ as a pseudooctahedral complex would break down.) The sign of q_L would be negative, opposite that of q_i. If we ignored the i atoms, the trigonal splitting due to the distorted ML_6 cluster would be positive. Now we have the result that the sign as well as the magnitude of K depends upon the relative magnitudes of the perturbations arising from the ligating atoms and from the nonligating atoms. More generally, the sign of K depends upon whether q is negative or positive. Since the ungerade perturbation has the same sign dependence as K, the sign of the second-order rotatory strength remains unchanged. It is uniquely determined by the arrangement, Λ or Δ, of the three chelate rings about the metal ion. Although the geometrical factors for the L atoms are relatively small to assess the relative importance of the i and L atoms as effective perturbing sites for inducing optical activity and trigonal splitting, one must compare q_L with q_i, and R_L with R_i.

Expanding the L–M–L azimuthal angles in the chelate rings to >60° and simultaneously elongating the complex along the $C_3(Z)$ axis would give the functions $(3\cos^2\theta_L - 1)$ and $\cos 3\,\theta_L$ signs opposite to those for $(3\cos^2\theta_i - 1)$ and $\cos 3\,\phi_i$ for a given Λ or Δ isomer. In this case, if q_L is negative and q_i is positive, then the splitting induced by the distorted L atoms is of the same sign as that caused by the i atoms. Again, the sign of the second-order rotatory strength is uniquely determined by the arrangement Λ or Δ of the chelate rings. (See Figure 5 for definitions of distortion operations on the ML_6 cluster.)

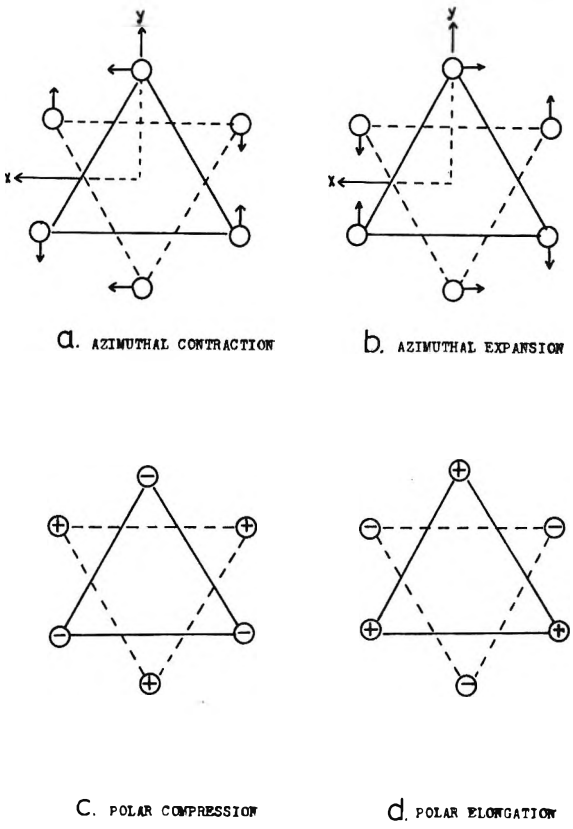

Figure 5. Distortion operations on ML_6 cluster.

Only two types of trigonal distortion involving the ligating atoms can effectively scramble the signs of the second-order rotatory strengths associated with the Λ and Δ isomers. If, in a Λ isomer, the azimuthal angles were expanded and the complex was simultaneously compressed along the $C_3(Z)$ axis, the sign of $\cos\phi_L$ would be positive and the sign of $(3\cos^2\theta_L - 1)$ would be negative. These signs are identical with those obtained by elongating a Δ isomer along the $C_3(Z)$ axis while simultaneously expanding the azimuthal chelate ring angles to >60°. Likewise, if both isomers were compressed and one has its L–M–L azimuthal ring angles expanded while in the other these angles are contracted, the two isomers would have second-order rotatory strengths of the same sign.

In Table XIII we have summarized the effects expected to occur if the ligating atoms are distorted from their octahedral positions and if the influences of the nonligating atoms are neglected. We refer to changes in the L–M–L chelate ring azimuthal angles as expansion or contraction from 60°, and to changes in the size of the ML_6 cluster as elongation or compression of the complex along the $C_3(Z)$ axis. The isomers Λ(a), Λ(d), Δ(a), and Δ(d) are those most likely to occur in real systems. If a complex were compressed and its L–M–L angles were greater than 60° the geometry of the ML_6 cluster would deviate significantly from that of a regular octahedron. Likewise if a complex were expanded and the L–M–L chelate ring angles were

Table XIII: Distortions of ML_6 Cluster

Isomer	Distortion operations	K	$R_{net}(T_{1g})$
Λa	Expansion + elongation	<0	>0
Λb	Expansion + compression	>0	<0
Λc	Contraction + elongation	<0	<0
Λd	Contraction + compression	>0	>0
Δa	Expansion + elongation	<0	<0
Δb	Expansion + compression	>0	>0
Δc	Contraction + elongation	<0	>0
Δd	Contraction + compression	>0	<0

less than 60°, the ML_6 geometry would differ significantly from O_h. Each of these situations would be highly unfavorable to the formation of tris complexes of transition metal ions and, consequently, the isomers Λb, Λc, Δb, and Δc of Table XIII are of little physical interest here. The signs of the second-order rotatory strengths are uniquely determined by the configurational arrangement, Λ or Δ, of the three chelate rings about the metal ion. This is true since the signs of both the ungerade and gerade perturbations change when trigonal distortions occur in the Λa, Λd, Δa, and Δd isomers.

4. Substitutions on the Chelate Rings. In general, substitutions on the chelate ring for the hydrogen atoms should tend to increase the rotatory strength. Alkyl substitution would increase the number of perturbing sites, aryl substitution would both increase the number of i sites and provide a stronger perturbing force, and halide substitution would also increase the strength of the perturbation. It would be misleading, however, to project these or other generalizations concerning the influence of substitution on the magnitude of the rotatory strength into a set of rules. Substitution on the chelate rings is usually accompanied by small changes in ring conformation and distortion of the ligating atoms. Therefore, the principal influence of substitution may very well be an indirect one. Our model is explicit, however, concerning the influence of substitution on the sign of the net rotatory strength. It should remain unaffected by the number and the nature of the substituent groups. The sign of the trigonal splitting is, of course, sensitive to the repulsive or attractive nature of the new perturbing sites. If they are repulsive, $K_i > 0$; if they are attractive, $K_i < 0$.

5. Increased Ring Size. If we assume that the ML_6 cluster retains its O_h geometry and that the chelate rings are planar, six-membered rings should induce a larger rotatory strength than do five-membered rings so long as the radial distances, R_i are not significantly increased. This is simply because the number of perturbing sites is increased. Assuming ring pucker and the lel form for tris complexes, the rotatory strength should still be higher than for the five-membered ring analogs. Now if we introduce the likely condition that the bridging structure will distort the O_h geometry of ML_6 such as to make the L–M–L chelate ring angles greater than 90°, we find that the trigonal splitting should be increased significantly. This follows from the fact that now the ligating atoms and the nonligating atoms both contribute negative splitting factors.

In general, the distance between the nonligating atoms and the metal ion in six-membered chelate systems will be slightly greater. This will tend to decrease the trigonal splitting and the rotatory strength.

6. The Sign and Magnitude of the Trigonal Splitting. At present there is considerable controversy concerning the sign and magnitude of the trigonal splitting in the first excited singlet ($^1T_{1g}$) state of $[Co(en)_3]^{3+}$. From the polarized crystal spectra of $(\pm)$-$[Rh(en)_3Cl_3]_2 \cdot NaCl \cdot 6H_2O$ doped with ~1 mol % of (+)-$[Co(en)_3]^{3+}$, Denning determined K to be +3.5 cm^{-1}.[23] Dingle analyzed the polarized crystal spectrum of (+)-$[Co(en)_3Cl_3]_2 \cdot NaCl \cdot 6H_2O$ and reported the splitting to be approximately zero ($K = 0 \pm 2$ cm^{-1}).[24] The CD spectrum of (+)-$[Co(en)_3]^{3+}$ in solution exhibits two bands in the region of the $^1A_{1g} \rightarrow {}^1T_{1g}$ absorption.[10] These bands are of unequal intensity and opposite in sign. The lower energy CD band (493 nm) is positive and somewhat more intense than the higher energy CD band (428 nm) of negative sign. The band maxima are separated by about 3100 cm^{-1}. McCaffery and Mason also measured the CD of the uniaxial crystal, (+)-$[Co(en)_3Cl_3]_2 \cdot NaCl \cdot 6H_2O$, with the radiation propagated along the C_3 rotation axis of the $[Co(en)_3]^{3+}$ complex ion.[10] In this case only the CD of the $^1A_1 \rightarrow {}^1E$ component of the $^1A_{1g} \rightarrow {}^1T_{1g}$ transition is observed; the measurements show a single positive band centered at 475 nm which is much more intense than the analogous band found in solution. These results have been cited as evidence that the positive band in the solution CD spectrum of (+)-$[Co(en)_3]^{3+}$ is due to the $^1A_1 \rightarrow {}^1E$ component of the $^1A_{1g} \rightarrow {}^1T_{1g}$ transition and that the less intense negative band arises from the $^1A_1 \rightarrow {}^1A_2$ component. If this interpretation is correct, then the sign of the trigonal splitting is negative; that is, the ^1E component of the $^1T_{1g}$ state lies lower in energy than the $^1A_2$ component in the presence of the trigonal environment. It is difficult to assess the magnitude of the splitting from the CD spectrum since there is probably considerable overlap of the two CD bands.

The results of Denning and Dingle, mentioned above, indicate that the trigonal splitting is very small in the crystal. The CD results indicate that the trigonal splitting is of finite magnitude in solution and is consistent with the possibility that it is small. A negative value of K is consistent with the CD results in solution. According to our model the vicinal effects originating with the ligating atoms and with the non-

(23) R. G. Denning, *Chem. Commun.*, 120 (1967).
(24) R. Dingle, *ibid.*, 304 (1965).

ligating members of the chelate rings are additive. If the CoN_6 cluster is distorted from an octahedral configuration so that $125.3° > \theta_L > 54.7°$, then the individual contributions of each ligating atom L to K will be positive. This corresponds to compression of the complex along the C_3 axis. The contributions of the nonligating atoms to K will, in general, be of negative sign. The net value of the splitting parameter K is given by a sum of terms. The individual terms originate with the various perturbing sites which constitute the trigonal environment. If the effective charge q on the perturbing site is negative its contribution to K will be positive (when $125.3° > \theta_p > 54.7°$); if q is positive then the contribution to K is negative. If the nonligating as well as the ligating atoms are presumed to be effective in perturbing the electronic distribution at the metal ion, then the net value of K could be quite small due to cancellation of the oppositely signed terms in the expression for K. This could possibly account for the small magnitude of K determined from the polarized crystal spectra studies.

According to our model, a very small net value of K does not necessarily lead to a vanishing second-order rotatory strength or to a small net rotatory strength within the $^1A_{1g} \rightarrow {}^1T_{1g}$ transition. The net rotatory strength is obtained from the sum of contributions made by the individual perturbing sites in the trigonal environment. The sign of each term is determined by the sign of $q_p^2 \cos 3\phi_p \sin^3 \theta_p(3 \cos^2 \theta_p - 1)$, where p labels the perturbing sites. If the complex is compressed along the trigonal axis and if the N–M–N chelate ring angles are contracted from 90°, the terms arising from the ligating atoms and those arising from the nonligating atoms are of the same sign in the expression for the second-order rotatory strength. The signs and magnitudes of the individual contributions to K are gaged by $q_p(3 \cos^2 \theta_p - 1)$. The sign of this function depends upon the sign of q_p, as has been explained previously. Although the individual contributions to K may sum to zero or to a very small net value, the sum over the individual contributions to the second-order rotatory strength will not vanish so long as there are perturbing sites not situated on the nodal surfaces of the function $\cos 3\phi_p \sin^2 \theta_p(3 \cos^2 \theta_p - 1)$. All the terms in the sum that determines the rotatory strengths are of the same sign so long as both the ligating and nonligating atoms are in the same sector.

In order, then, to rationalize the observed CD spectra of $[Co(en)_3]^{3+}$ in solution and in a crystal, it is necessary that in solution K be of finite magnitude and negative in sign. According to the static crystal-field model, a small trigonal splitting does not preclude a large net rotatory strength within the $^1A_{1g} \rightarrow {}^1T_{1g}$ transition, if the nonligating atoms are effective perturbing sources.

V. Vibronic Effects

In section IV we dealt only with the static part of the more general model discussed in section III. More specifically, we assumed that the behavior of the electrons responsible for the optical rotatory properties could be described in terms of the eigenfunctions of the wave equation

$$(H_\epsilon - H_{\epsilon\nu})\psi = E\psi \tag{38}$$

where H_ϵ is defined by eq 13 and $H_{\epsilon\nu}$ is defined in eq 9. All the nuclei in the complex ion are clamped in their equilibrium positions and each electron is assumed to move in the electrostatic field created by the stationary nuclei and the rest of the electrons. To obtain a more complete description of any electronic property of the complex, it is necessary to treat explicitly the couplings between the electrons and the vibrational motions of the nuclei. As stated earlier, a detailed treatment of the vibronic effects on the optical activity of metal complexes will not be given here. However, it is of some interest to consider in a very qualitative way how vibronic interactions of the Jahn–Teller type might influence the trigonal splitting parameter K, and our interpretation of the two CD bands observed in the region of the $^1A_{1g} \rightarrow {}^1T_{1g}$ transition of Λ-$Co(en)_3^{3+}$.

If vibronic effects are to be included, an immediate problem is to determine at what stage in the perturbation sequence they should be introduced. For example, in the systems of interest here, the low-lying electronic excited states are orbital triplets in an octahedral field. There is strong experimental evidence that in these cases the most important Jahn–Teller (J–T) interaction is between an e_g vibrational mode and the orbital triplet. This interaction leads to a tetragonally distorted excited state of ML_6 whose lowest energy level is triply degenerate. The wave functions associated with this energy level are eigenfunctions of the vibronic Hamiltonian. Although degenerate in energy, they are spatially nondegenerate and individually correspond to distortions along the three tetragonal axes of the cubic system.

In complexes with true trigonal dihedral symmetry, the static perturbations on ML_6 will tend to cause trigonal distortions. If, to zeroth order, the triply degenerate electronic states are expressed in terms of a cubic basis, the perturbation matrix due to the trigonal field has only off-diagonal elements (*i.e.*, the orbital components of the electronic triplet state mix). In the absence of vibronic interactions, the component electron-vibrational wave functions of the electronic triplet state can be written as, $\psi_\xi\phi_v$, $\psi_\eta\phi_v$, $\psi_\zeta\phi_v$, where the vibrational functions ϕ_v are identical for each electronic orbital function ξ, η, and ζ. The trigonal perturbation matrix elements depend, therefore, only on electron coordinates since, $\langle\psi_\xi\phi_v|V_{trig}|\psi_\eta\phi_v\rangle = \langle\psi_\xi|V_{trig}|\psi_\eta\rangle\langle\phi_v|\phi_v\rangle = \langle\psi_\xi|V_{trig}|\psi_\eta\rangle$ for each vibrational level v. However, if the electronic state can effectively couple to an e_g mode resulting in a tetragonal J–T distortion, then the vibronic wave functions must be written as

$\psi_\xi\phi_\xi$, $\psi_\eta\phi_\eta$, $\psi_\zeta\phi_\zeta$, where ϕ_ξ, ϕ_η, and ϕ_ζ are displaced oscillator functions located at the three minima on the J–T distorted potential energy surface. Now the perturbation matrix elements due to the trigonal field must be written, for example, as $\langle\psi_\xi\phi_\xi|V_{trig}|\psi_\eta\phi_\eta\rangle = \langle\psi_\xi|V_{trig}|\psi_\eta\rangle\langle\phi_\xi|\phi_\eta\rangle$, where the overlap factor $\langle\phi_\xi|\phi_\eta\rangle$ is not equal to unity. When the J–T effect is very strong then $\langle\phi_\xi|\phi_\eta\rangle$ approaches zero and the trigonal perturbation is completely quenched. In any case, the presence of e_g–T_g coupling will quench the effects of any operator which is off-diagonal in the cubic bases. This quenching (partial or complete) of an electronic trigonal perturbation on the orbital triplet states of cubic systems by dynamical J–T coupling is just a specific example of the Ham effect. It was pointed out by Ham[25] that profound changes in such observables as spin–orbit splittings, trigonal field splittings, and g factors in orbital triplet states can occur as a result of the dynamic J–T effect. These changes are collectively known as the Ham effect.

It is also possible for a triply degenerate electronic state in a regular octahedral system to suffer a J–T distortion by coupling with the t_{2g} vibrational mode. In this case, however, the vibronic Hamiltonian is diagonal only in a trigonal (D_{3d}) basis. Consequently, the matrix elements for electronic operators which are also diagonal in a trigonal basis remain finite in the extreme J–T coupling limit. The Jahn–Teller effect due to T–t_{2g} coupling leads to a distorted potential energy surface for the ground vibronic level which has four minima, one along each trigonal axis.

In addition to altering the potential energy surface (e_g and t_{2g} modes) or mixing the orbital components (t_{2g} mode) of a particular orbital triplet state, vibronic coupling *via* the e_g and t_{2g} modes can also induce mixing between two different triply degenerate electronic states [*e.g.*, the $^1T_{1g}$ and $^1T_{2g}$ in Co(III) and the $^4T_{1g}$ and $^4T_{2g}$ in Cr(III)]. These "interstate" interactions will, of course, be much weaker than the "intrastate" interactions since, in most systems of interest, the adjacent triplets are separated by 5000–8000 cm^{-1}. Another type of "interstate" interaction whose consideration is essential for understanding the optical absorption spectra of cubic or nearly cubic metal complexes originates with the coupling of the ungerade t_{1u} and t_{2u} vibrational modes with the electronic states. This coupling through the ungerade modes induces mixing between the gerade and ungerade electronic states and accounts for nearly all of the observed intensity in the ligand-field bands of cubic and nearly-cubic transition metal complexes. This coupling (commonly called the Herzberg–Teller intensity mechanism) has little effect on the energies of the electronic states involved, but produces the electric transition dipoles essential for observable light absorption.

The matrix elements for any operator whose orbital part is exclusively off-diagonal in the real representation forced on the triply degenerate electronic term by vibronic coupling with the e_g vibrational mode are reduced by the factor $\gamma = \langle\phi_\xi|\phi_\eta\rangle = \langle\phi_\xi|\phi_\zeta\rangle = \langle\phi_\eta|\phi_\zeta\rangle$. This applies to the orbital angular momentum operator $\vec{\ell}$ whose nonvanishing matrix elements within the T_{1g} vibronic state are

$$\langle\psi_\xi\phi_\xi|\ell_y|\psi_\zeta\phi_\zeta\rangle = \langle\psi_\eta\phi_\eta|\ell_z|\psi_\xi\psi_\xi\rangle = \langle\psi_\zeta\phi_\zeta|\ell_x|\psi_\eta\phi_\eta\rangle = i\ell\hbar\gamma \quad (39)$$

where it has been assumed that the electronic functions can be taken as pure metal 3d orbitals. This will result in a quenching of spin–orbit coupling and in a reduction of the magnetic moment of the $^1T_{1g}$ state. Evidence that the $^1T_{1g}$ excited state of $[Co(en)_3]^{3+}$ undergoes a strong Jahn–Teller distortion has recently been reported by Denning.[23] Using magnetic circular dichroism, Denning determined the magnetic moment of the excited $^1T_{1g}$ state and subsequently deduced a reduction factor <0.05. The extraordinarily small value observed for the trigonal splitting in $[Co(en)_3]^{3+}$ could also be attributed to a strong tetragonal distortion of the complex (a manifestation of the static J–T effect). Denning has further suggested that the two CD bands observed in the $^1A_{1g} \rightarrow {}^1T_{1g}$ region arise from two different J–T vibronic states which are derived from the $^1T_{1g}$ electronic state rather than from the two trigonal components $^1A_1$ and ^1E.

If we assume that the T_{1g} electronic state is strongly coupled to an e_g vibrational mode, the lowest vibronic level resulting from this coupling is an orbital triplet whose component wave functions may be written as: $\psi_\xi\phi_{\xi,00}$, $\psi_\eta\phi_{\eta,00}$, and $\psi_\zeta\phi_{\zeta,00}$, where the subscripts 00 on the vibrational wave functions ϕ indicate that both components of the e_g mode are in their ground vibrational levels. The next lowest vibronic level is sixfold degenerate and is composed of two orbital triplets, one transforming as T_{1g} in O_h and the other as T_{2g}. The basis functions for these vibronic states are: $\psi_\xi\phi_{\xi,01}$, $\psi_\xi\phi_{\xi,10}$, $\psi_\eta\phi_{\eta,01}$, $\psi_\eta\phi_{\eta,10}$, $\psi_\zeta\phi_{\zeta,01}$, and $\psi_\zeta\phi_{\zeta,10}$, where the subscripts 01 and 10 on ϕ specify that one of the components of the e_g vibrational mode is singly excited. The energy level scheme for the three lowest vibronic states that result from T_{1g}–e_g coupling is

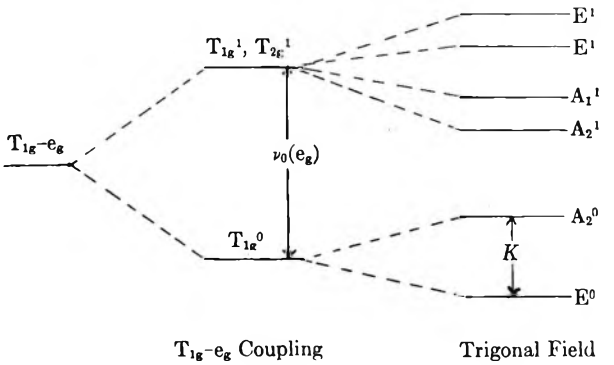

(25) F. S. Ham, *Phys. Rev.*, **138**, A1727 (1965).

where T_{1g}^1 and T_{2g}^1 represent vibronic states in which the e_g mode is singly excited, and T_{1g}^0 represents the vibronic state in which the e_g mode is unexcited. $\nu_0(e_g)$ is the fundamental frequency of the e_g mode and K is the trigonal splitting parameter.

Expanding on Denning's suggestion, it might be supposed that the two CD bands associated with the $^1A_{1g} \rightarrow {}^1T_{2g}$ electronic transition in $[Co(en)_3]^{3+}$ arise from separate transitions from the ground state A_{1g} to the two vibronic levels, T_{1g}^0 and (T_{1g}^1, T_{2g}^1). If this were the case, then the band maxima should be separated by the fundamental frequency of the e_g mode, $\nu_0(e_g) \approx 410$ cm^{-1}. Furthermore, both bands should have components which are polarized $\perp$ to the C_3 axis of the trigonal system. Additionally, the signs of the net rotatory strengths associated with the two vibronic transitions should be the same. The CD data reported by McCaffery and Mason[10] on the uniaxial crystal, (+)-$[Co(en)_3Cl_3]\cdot NaCl\cdot 6H_2O$, show that only the low-frequency CD band apparently has a component polarized $\perp$ to the C_3 axis. Furthermore, a simple analysis does not reveal how the two CD bands observed in the solution spectra can have opposite signs if they are assumed to arise from transitions to the two vibronic levels, T_{1g}^0 and (T_{1g}^1, T_{2g}^1).

At this point we must reject the suggestion put forth by Denning concerning the CD spectra of $[Co(en)_3]^{3+}$. The interpretation of the CD data based on the static model presented in section IV appears to be qualitatively correct, and a small trigonal splitting is not inconsistent with this interpretation. The reduced magnetic moment of the excited T_{1g} state reported by Denning does, however, indicate the presence of a strong J–T coupling between the e_g vibrational mode and the T_{1g} electronic state. The influence of this coupling on the optical rotatory properties should be studied in greater detail than has been done here.

VI. Summary

The primary purpose of this study was to examine the optical rotatory properties of trigonal dihedral transition metal complexes on a one-electron model in which the chromophoric electrons localized on an octahedral ML_6 cluster are subjected to a static trigonal field provided by the ligands. The trigonal field originating with the ligand environment was assumed to be small compared to the essentially octahedral (O_h) field exerted by the ML_6 cluster. The wave functions of the chromophoric electrons responsible for the ligand-field transitions were developed to second order in a perturbation expansion in which the static trigonal field potential was treated as the perturbation operator. In order to avoid complications introduced by exchange effects and yet retain the essential symmetry-determined aspects of the optical rotatory properties, the trigonal field potential was represented by a single-center multipolar expansion (crystal-field expansion) about the metal atom. In this expansion of the perturbation potential, the ligand environment is represented as a constellation of classical point charges whose overall symmetry is D_3. In such a representation, overlaps between the charge distributions centered on the ML_6 cluster and those centered on other sites in the ligand environment are completely neglected. This procedure of representing the ligand environment by a constellation of point charges is an acceptable approximation so long as each atomic site is included and the expansion of the perturbation potential is carried to a sufficiently high order.

It was shown that the net rotatory strength associated with the complete manifold of ligand-field transitions vanishes to first order on the one-electron model but is nonvanishing if second-order contributions are considered. The second-order contributions to the rotatory strength arise from the simultaneous actions of a trigonal perturbation (P_g) with gerade octahedral percentage and a trigonal perturbation (P_u) with ungerade octahedral percentage. The contributions due to d–p and d–f orbital mixing under the influence of P_u, and d–d mixing under the influence of P_g, were considered in detail. The influences exerted on the optical rotatory properties by chelate ring conformation, ring size, ring substituents, and distortions of the octahedral ML_6 cluster, were also examined and predictions were made.

The results obtained to first order in perturbation theory are similar to those previously obtained by Moffitt,[5] Piper and Karipedes,[12] and Poulet[8] on a static, one-electron model. In carrying the static, one-electron model to second order in perturbation theory, we obtained results which are in close agreement with the experimental CD data and which easily interpreted in terms of specific structural features of trigonal dihedral metal complexes. Reduction of the general model to a crystal-field representation of the electronic states of the complex ion further aids in elucidating the essential symmetry-determined aspects of the optical rotatory properties. Although the static, one-electron model is not appropriate for making accurate quantitative calculations of the rotatory strength, it provides a simple and correct representation of the nodal structure in the electronic states of the ML_6 chromophore and in the interaction potential between the ML_6 chromophore and the ligand environment. The simplicity of this representation and the facility with which it can be used in making correlations between CD data and molecular structure make it particularly attractive.

Ab initio quantum mechanical calculations on the class of complex ions considered in this paper are, at present, out of the question. Even minimum basis set SCF wave functions for these systems cannot be obtained with sufficient economy to justify the effort. On the other hand, semiempirical molecular orbital models are not yet sufficiently accurate or reliable for making useful calculations of the electronic spectral properties of transition metal complexes except when

extensive calibration calculations can be performed. If the parameters of the molecular orbital model are calibrated for one or two spectral properties of a few systems belonging to a specific class of complex ions, then it is possible in some cases to compute the same properties for other members of this class. This procedure has been used with some success in determining the relative transition energies in certain complexes. However, its application to the calculation of the rotatory strengths associated with d → d transitions appears to have little promise at this time. Optical activity can be classified as a second-order optical property and its extreme sensitivity to the details of the electronic structure of the overall system requires that very accurate wave functions be used in calculating the rotatory strengths. In the absence of accurate electronic wave functions, a theoretical analysis of the optical rotatory properties is best accomplished by determining the symmetry-controlled aspects of the problem. This type of analysis has been of enormous importance in correlating the stereochemical properties of optically active systems with experimental ORD and CD spectra. Theoretically, the success of such an analysis depends upon the correctness with which the nodal surfaces of the molecular electronic states are represented. If a one-electron perturbation model is adopted (as was done in this study), then the nodal surfaces of the predominant perturbation potential functions must also be correctly represented.

So long as quantitative calculations of rotatory strengths are not our goal, it would appear that the optical rotatory properties of metal complexes can be most clearly analyzed and understood in terms of an independent systems model in which the metal atom and the ligands are treated as nonoverlapping subsystems. For the d → d transitions, the crystal-field model becomes appropriate if the ligands have no strong electric-dipole allowed transitions in the visible part of the spectrum.

Acknowledgments. I wish to express my gratitude to Professor W. J. Kauzmann for his discussions and helpful suggestions concerning this work. I also gratefully acknowledge the support provided by the National Science Foundation through a grant to W. Kauzmann, Princeton University, and a grant to F. R. administered through the Center for Advanced Studies, University of Virginia.

NOTES

Electron Spin Resonance Spectroscopy of the Fluorosulfate Radical ($SO_3F\cdot$) in Solution. Line Width and Its Temperature Dependence[1]

by Paul M. Nutkowitz and Gershon Vincow*,[2]

Department of Chemistry, University of Washington, Seattle, Washington 98105 *(Received August 10, 1970)*

Publication costs assisted by the U.S. Army Research Office, Durham

There has been considerable recent experimental and theoretical interest in the esr line width of small inorganic free radicals and ions in liquid solution, and in the variation of these widths with temperature and solvent viscosity.[3] The experimental results have been explained on the basis of a variety of relaxation mechanisms such as motional modulation of the anisotropic electronic Zeeman interaction, the electron-nuclear hyperfine interaction, the spin-rotational interaction, and the Ohrbach process. The possibility of a chemically shortened lifetime as the dominant line-broadening mechanism has also been invoked.[4]

In this note we report measurements of the temperature-dependent line width of the fluorosulfate radical, $SO_3F\cdot$, in peroxydisulfuryl difluoride, $S_2O_6F_2$, and in a fluorocarbon solvent. The contributions of a variety of mechanisms to the line width are discussed in order to establish which is the principal line-broadening effect.

Results

Our results for the line width of $SO_3F\cdot$ in its neat liquid dimer $S_2O_6F_2$ are given in Figure 1. The width

(1) This work was supported by the U. S. Army Research Office, Durham.

(2) Alfred P. Sloan Foundation Research Fellow; to whom inquiries should be addressed.

(3) (a) P. W. Atkins, N. Keen, and M. C. R. Symons, *J. Chem. Soc.*, 2873 (1962); (b) S. Fujiwara and H. Hayashu, *J. Chem. Phys.*, **43**, 23 (1965); (c) R. Wilson and D. Kivelson, *ibid.*, **44**, 154 (1966); (d) P. W. Atkins and D. Kivelson, *ibid.*, **44**, 169 (1966); (e) W. B. Lewis, M. Alei, and L. O. Morgan, *ibid.*, **44**, 2409 (1966); (f) D. Kivelson, *ibid.*, **45**, 1324 (1966); (g) J. Q. Adams, *ibid.*, **45**, 4167 (1966); (h) N. Vanderkooi, Jr., and R. T. Poole, *Inorg. Chem.*, **5**, 1351 (1966); (i) J. R. Thomas, *J. Amer. Chem. Soc.*, **88**, 2064 (1966); (j) P. W. Atkins, *Mol. Phys.*, **12**, 201 (1967); (k) P. W. Atkins and M. T. Crofts, *ibid.*, **12**, 211 (1967); (l) R. E. D. McClung and D. Kivelson, *J. Chem. Phys.*, **49**, 3380 (1968); (m) L. Burlamacchi, *Mol. Phys.*, **16**, 369 (1969).

(4) D. M. Gardner and G. K. Fraenkel, *J. Amer. Chem. Soc.*, **78**, 3279 (1956).

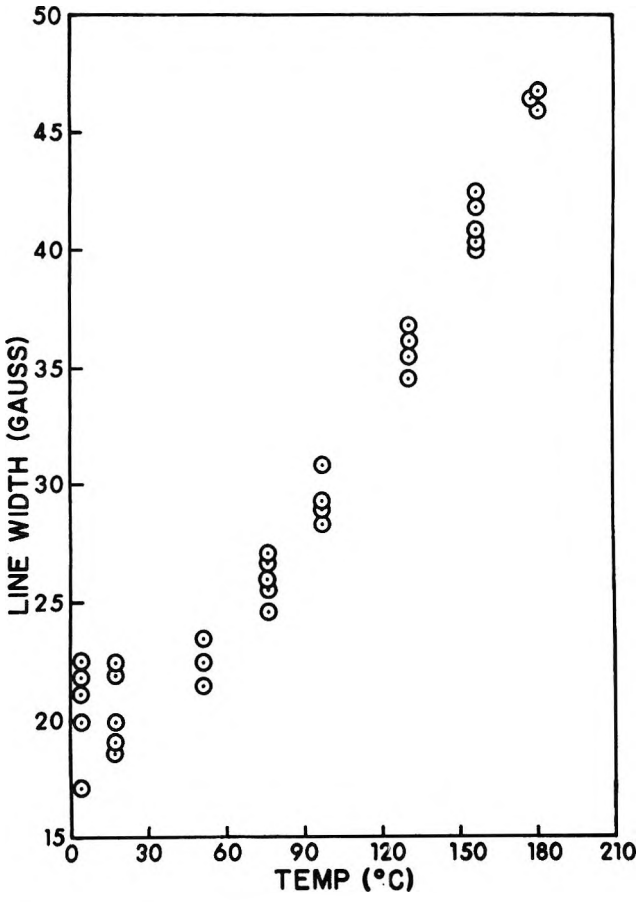

Figure 1. Temperature dependence of the line width of a component of the esr spectrum of $SO_3F\cdot$ in neat liquid $S_2O_6F_2$.

increases nonlinearly from *ca.* 20 G at 4° to *ca.* 46 G at 180°. These values are peak-to-peak widths of the first derivative of a *component* of the spectrum. The observed spectrum consists of a single approximately Lorentzian line composed of two *unresolved* fluorine hyperfine components separated by 9.5 G. Computer simulations have been employed to relate the measured width to that of a single component.[5] For example, at 125°, the spectrum width between points of maximum slope is 35 G (±2 G), and the width of a component is 32 G.

The effect of dilution on line width has been studied to test the hypothesis that the width is principally due to shortening of the spin-state lifetime by a chemical reaction. The component width of $SO_3F\cdot$ in *ca.* 0.2 and 0.1 mole fraction solutions of $S_2O_6F_2$ in perfluorodimethylcyclohexane has been measured.[6] At 75° these widths are 27.5 ± 1.4 and 28.8 ± 0.4 G, respectively. Corresponding values at 98° are 34.8 ± 0.7 and 34 G. The line widths at each temperature are thus independent of the concentration of $S_2O_6F_2$.

Discussion

We have considered a variety of possible mechanisms for the observed line width of the fluorosulfate radical. All but a few can be readily eliminated from consideration as having the principal effect. For example, the contributions of spin relaxation due to motional modulation of the g and hyperfine tensors are estimated to be negligible compared with the observed widths[5b] and further are expected to *decrease* with increasing temperature. The contribution of the intermolecular dipolar effect is also small since the radical concentration is small (*ca.* 10^{-3} M at 100°), and the solution is free of paramagnetic impurities such as O_2. Intermolecular exchange effects may likewise be eliminated because the line width is at least a factor of 2 larger than the hyperfine splitting and increases with increasing temperature.[7]

Another mechanism which can lead to line broadening is spin relaxation through chemical reaction.[8] The $SO_3F\cdot$ radical in liquid $S_2O_6F_2$ can react through two mechanisms, either a radical recombination reaction

$$2SO_3F\cdot \xrightarrow{k_1} S_2O_6F_2$$

or a radical displacement reaction

$$SO_3F\cdot + S_2O_6F_2 \xrightarrow{k_2} S_2O_6F_2 + SO_3F\cdot$$

Although radical recombination reactions are usually considered to require approximately zero energy of activation and should therefore be favored energetically, the velocity of the recombination reaction is probably much less than the displacement reaction because $[SO_3F\cdot] \ll [S_2O_6F_2]$. Perhaps the most cogent reason for dismissing the recombination reaction as a significant line-broadening mechanism is that, from an analysis of the kinetic equations, the energy of activation is predicted to be large and *negative*.

Analysis of the kinetic equations for the recombination reaction[4,5b] leads to the equation

$$\mathrm{d} \ln \tau/\mathrm{d}T = -[(E_a/RT^2) + (\Delta H^\circ/2RT^2)]$$

where τ is the radical lifetime, E_a is the Arrhenius activation energy, and ΔH^c is the enthalpy of homolytic cleavage of $S_2O_6F_2$. If we equate our chemical lifetime with spin-state lifetime and further note that, from the Van Vleck–Weisskopf theory of pressure broadening,[4] spin-state lifetime is inversely proportional to line width, then τ may be replaced by line width in the above equation. We have fit our experimental line width

(5) (a) P. M. Nutkowitz and G. Vincow, *J. Amer. Chem. Soc.*, 91, 5956 (1969); (b) for further details see P. M. Nutkowitz, Ph.D. Thesis, University of Washington, Seattle, Wash., 1967; copies of this thesis are available from University Microfilms, Inc., Ann Arbor, Mich., Order No. 68-9316.

(6) Maximum limits of error in the individual mole fractions are ±10%. Relative concentrations at each temperature are considerably more accurate due to cancellation of errors.

(7) J. D. Currin, *Phys. Rev.*, 126, 1995 (1962).

(8) S. I. Weissman, *Z. Elektrochem.*, 64, 47 (1960).

data to the form $\ln w = A/T + B$ and find $A = 615 \pm 30$ and $B = 5.10 \pm 0.8$. Using these constants and $\Delta H^\circ = 22.4$ kcal/mol,[5a] we compute $E_a = -9.6$ kcal/mol, a value which is unreasonable.

For the radical displacement reaction

$$\tau = \frac{1}{k_2[S_2O_6F_2]}$$

and hence the line width should be proportional to the concentration of $S_2O_6F_2$. We prepared two dilute solutions of $S_2O_6F_2$ in $C_6F_{10}(CF_3)_2$ with the concentrations of $S_2O_6F_2$ in the ratio 2:1. The use of dilute solutions minimizes any solvent effect on k_2. If the radical displacement mechanism dominates the line width, then the widths of the radicals in these two solutions should be in the ratio 2:1. Since they have been found to be equal, the chemical mechanism has been eliminated.[9]

By the process of elimination we are led to propose that the most likely mechanism to explain the line width is spin relaxation due to motional modulation of the spin-rotational interaction. Line widths of comparable magnitude to those reported in this paper and similar variations with temperature have been found for ClO_2 and have been ascribed to the spin-rotational interaction.[3g,h,1] A quantitative analysis of the results for SO_3F awaits the availability of additional data in a variety of solvents of *known* viscosity.

One other mechanism deserves mention, namely the Ohrbach process[3f] which is important for species with nearly degenerate ground states ($\Delta E/kT \leq 6$). Because of the probable symmetry of SO_3F, C_{3v}, one might expect the possibility of a ^2E ground state. The results of recent spectroscopic measurements and a CNDO calculation[10] suggest however that the ground state of $SO_3F\cdot$ is probably $^2A_2$ and that the lowest-lying excited states of ^2E symmetry are too far removed from the ground state to make a significant contribution *via* the Ohrbach mechanism.

Finally, we should comment on a discrepancy between our work and that of Stewart, who reported that the line width of $SO_3F\cdot$ in a mixture of $S_2O_6F_2$ and $S_2O_5F_2$ is independent of temperature.[11] We believe that Stewart's samples were partially decomposed, as evidenced by his observation of boiling of the samples in *sealed* tubes above 100°. We have observed such bubbling (probably O_2) in some samples; the line widths measured were not reproducible under thermal cycling, and we discarded these results.

(9) The fact that the line width is independent of $[S_2O_6F_2]$ is additional evidence for eliminating the recombination mechanism. For this mechanism the line width should vary as $[SO_3F\cdot]^{-1}$ or approximately as $[S_2O_6F_2]^{-1/2}$.

(10) G. W. King, D. P. Santry, and C. H. Warren, *J. Chem. Phys.*, **50**, 4565 (1969).

(11) R. A. Stewart, *ibid.*, **51**, 3406 (1969).

Interpretation of Electron Spin Resonance Evidence for the Mechanism of Free-Radical-Induced Reactions of Methylenecyclobutane and Methylenecyclopentane[1]

by David H. Volman

Department of Chemistry, University of California, Davis, California 95616 *(Received October 8, 1970)*

Publication costs assisted by the National Science Foundation

From esr studies in the frozen state at 77°K, Takeda, *et al.*,[2] have concluded that methylenecyclobutane yields a substituted vinyl radical by reaction with

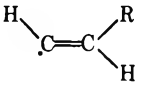

I

hydroxyl radicals produced by photolysis of hydrogen peroxide but not by reaction with methyl radicals produced by photolysis of methyl iodide; and that methylenecyclopentane yields a cyclic substituted allylic radical by reaction with either radical. Ring

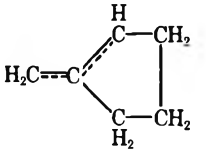

II

opening for the four-carbon ring and a stable cyclic radical for the five-carbon ring were attributed to the larger strain energy for the ring with fewer carbon atoms. It will be shown here that the esr spectrum for methylenecyclobutane has definitely been interpreted incorrectly. In consequence, radical I is not a a product but allenyl radical is formed, and radical II is probably not a product but a noncyclic substituted radical may be formed.

Substituted Vinyl vs. Allenyl. Takeda, *et al.*,[2] interpreted their results with methylenecyclobutane on the basis of radical I locked in the position of unpaired electron orbital cis to the β proton. Using the coupling constant reported by Cochran, Adrian, and Bowers,[3] $a_{H(\alpha)} = 16$ *G* and $a_{H(\beta,cis)} = 34$ G, the theoretical spectrum yields line-to-line spacings of 16, 18, and 16 G and intensity ratios of 1:1:1:1:1. Although the spacings are in some conformity with the experimental values, the intensities clearly are not. Moreover, in-

(1) This investigation was supported by a grant from the National Science Foundation.

(2) K. Takeda, H. Yoshida, K. Hayashi, and S. Okamura, *Bull. Inst. Chem. Res. Kyoto Univ.*, **45**, 55 (1967).

(3) E. L. Cochran, F. J. Adrian, and V. A. Bowers, *J. Chem., Phys.* **40**, 213 (1964).

version of the α hydrogen, with a frequency of at least 10^8 sec^{-1} in vinyl radical at 90°K,[4] makes it unlikely that the radical is locked in the cis position. As $a_{H(\beta,trans)} = 68$ G,[3] the trans radical I should yield a four-line spectrum of equal intensities and with spacings of 16, 52, and 16 G. A mixture of the cis and trans forms or inversion between the forms would yield a spectrum which would deviate even more widely from that reported. There is, therefore, no evidence that the radical is substituted vinyl.

The spectrum obtained by Takeda, *et al.*, is virtually identical with that attributed to allenyl by Morgan and White[5] from the reaction of hydrogen atoms with propyne at 77°K and by us[6] from the photolysis of allene and of propargyl alcohol at 77°K. The first derivative spectrum obtained in the latter two laboratories consists of four lines with peak-to-peak separations of 18, 14, and 18 G and approximate intensity ratios of 1:2:2:1. We have shown that such a spectrum results from incomplete resolution with coupling constants of 18 and 14 G assigned to the CH_2 and CH protons.[6] From the absorption spectrum constructed on this basis, the theoretical peak intensities are 1:2.3:2.3:1. (It may be noted that well resolved spectra of allenyl radical have been obtained in fluid media by Fessenden and Schuler,[4] $a_{CH_2} = 18.9$ G and $a_{CH} = 12.6$ G, and by Kochi and Krusic[7] $a_{CH_2} = 18.9$ G and $a_{CH} = 12.7$ G). The spacings reported by Takeda, *et al.*, are 18, 15, and 18 G and from an examination of their published spectrum an approximate intensity ratio of 1:2:2:1 is obtained. Therefore, both from appearance and analysis the spectrum is undoubtedly that of allenyl free radicals.

Cyclic Allyl vs. Noncyclic Allyl. The esr spectrum[1] from methylenecyclopentane attributed to radical II consists of five lines with an average separation of 15 G and intensity ratios somewhat less than theoretical for four equivalent protons. The interpretation of this spectrum was that of the five protons which might be expected to couple, the three allyl system protons and the CH_2 ring protons adjacent, β, to the CH group, one of the β protons does not interact. As the allyl radical system is certainly planar, if it is assumed that the ring system is planar the two β hydrogen protons would undergo equivalent interaction with the delocalized electron. Although the ring may not be completely planar, it is probably nearly so. In any case the four-carbon system leading to the spectrum would tend to be planar since the primary cause of puckering in the five-carbon ring, hydrogen–hydrogen repulsion, is eliminated by having the CH hydrogen atom staggered with respect to the β hydrogen atoms.

The spectrum shown is very similar to that reported by a number of workers for free allyl radical in frozen systems at 77°K.[8] The small splitting expected from the proton on the central carbon atom is not resolvable in the low-temperature glassy systems and consequently the spectrum approximates that expected from interaction of four equivalent protons with the delocalized unpaired electron. Thus substitution for the central hydrogen atom would not be expected to affect the spectrum significantly. The spectrum obtained from methylenecyclopentane is, therefore, explicable on the basis of either free allyl or a noncyclic substituted allyl but not by a cyclic substituted allyl.

Discussion

The mechanism suggested for the decomposition of methylenecyclobutane[2] was

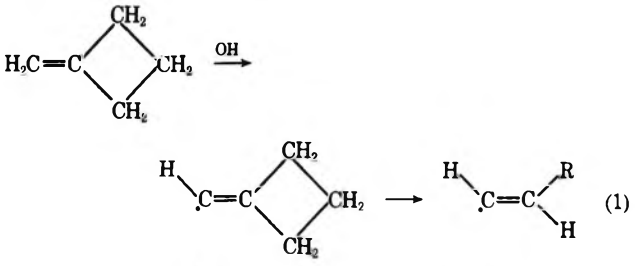

(1)

the abstraction of a methylenic hydrogen followed by ring opening and the shift of two hydrogen atoms if R is $-CH_2-CH=CH_2$; if R is cyclopropyl, only one hydrogen atom needs to shift. As there is no evidence for the vinyl radical and as abstraction of an allylic hydrogen, of which there are four, is much more favorable than abstraction of a methylenic hydrogen, and as the radical is allenyl, a plausible mechanism is

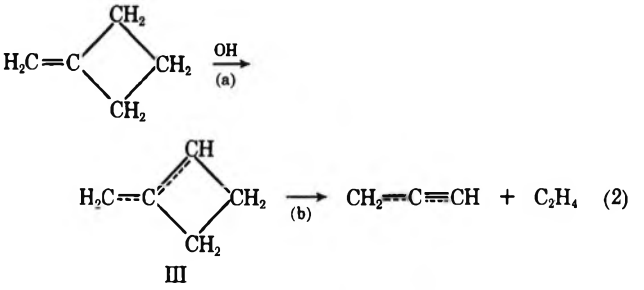

(2)

III

The enthalpy change for reaction 2 may be calculated from the tabulated enthalpies of formation of the hydrocarbons[9] and free radicals[10] and from the value for allenyl,[11] $\Delta Hf°_{298} = 75.0$ kcal. For the reaction with OH in which case water is an abstraction product, $\Delta H°_{298}$ (g) $= -10$ kcal, while for the reaction with CH_3

(4) R. W. Fessenden and R. H. Schuler, *J. Chem. Phys.*, 39, 2147 (1963).

(5) C. V. Morgan and K. J. White, *J. Amer. Chem. Soc.*, 92, 3309 (1970).

(6) D. H. Volman, K. A. Maas, and J. Wolstenholme, *ibid.*, 87, 3041 (1965).

(7) J. K. Kochi and P. J. Krusic, *ibid.*, 92, 4110 (1970).

(8) K. A. Maas and D. H. Volman, *Trans. Faraday Soc.*, 60, 1202 (1964).

(9) S. W. Benson, F. R. Cruikshank, D. M. Golden, G. R. Haugen, H. E. O'Neal, A. S. Rodgers, R. Shaw, and R. Walsh, *Chem. Rev.*, 69, 279 (1969).

(10) J. A. Kerr, *ibid.*, 66, 465 (1966).

(11) J. Collin and F. P. Lossing, *J. Amer. Chem. Soc.*, 79, 5848 (1957).

yielding methane, $\Delta H°_{298}$ (g) = +5 kcal. This difference in enthalpies can explain the formation of allenyl by reaction with OH but not with CH_3. The enthalpy of formation of III may be estimated by assuming that the resonance stabilization energy of III is approximately equal to that of the allyl radical and that the ring strain energy in III is intermediate between that for cyclobutane, 26.5 kcal, and that for cyclobutene, 30.0 kcal.[12] ΔHf(III) then should exceed ΔHf(methylenecyclobutane) by the difference in strain energies, 1.8 kcal, plus the difference between the enthalpies of formation of propene and allyl radical, 33.1 kcal. These values yield $\Delta Hf°_{298}$ (III) $\cong$ 65 kcal and for reaction 2b, $\Delta H°_{298}$(g) $\cong$ 26 kcal. Despite the approximations, this value is not likely to be in error by more than $\pm$5 kcal. Therefore, unless III receives energy liberated in step 2a it is not likely to be the precursor of the products, allenyl and ethene. It is not, however, necessary that III be formed as the reaction may occur by a concerted mechanism accompanying free-radical abstraction of an allylic hydrogen atom

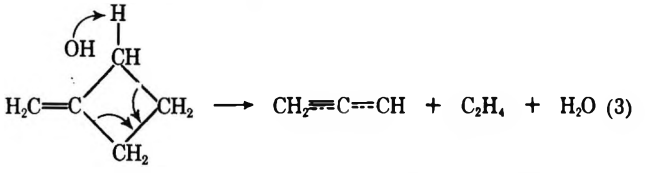

For methylenecyclopentane an analogous mechanism yielding allyl radical and allene seems attractive, but the calculated enthalpy changes yield 14 and 29 kcal endothermicity for the reactions with hydroxyl and methyl. However, as observed earlier, any centrally substituted allyl radical should yield the same esr spectrum as allyl. It is not possible to choose between several alternatives but a possible one is

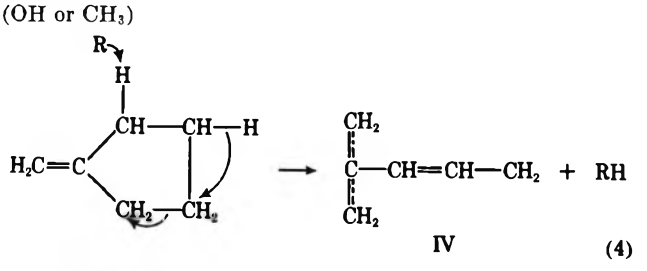

$\Delta Hf°_{298}$(IV) may be estimated in the same way as for III. By group-contribution methods for the parent hydrocarbon of IV, $\Delta Hf°_{298}$(2-methyl-1,3-pentadiene) = 11 $\pm$ 2 kcal yielding $\Delta Hf°_{298}$ (IV) $\cong$ 44 kcal. With OH, $\Delta H°_{298}$(g) = $-$25 kcal and with CH_3, $\Delta H°_{298}$(g) = $-$10 kcal, and formation of IV from the reaction with either radical is exothermic. As for methylenecyclobutane, thermochemical calculations indicate that a concerted process rather than the formation of an intermediate is favored.

(12) J. D. Cox and G. Pilcher, "Thermochemistry of Organic and Organometallic Compounds," Academic Press, New York, N. Y., 1970, pp 571 and 580.

Measurement of the Isothermal Piezooptic Coefficient with the Ultracentrifuge

by Robert Josephs* and Allen P. Minton

Polymer Department, Weizmann Institute of Science, Rehovoth, Israel *(Received October 13, 1970)*

Publication costs borne completely by The Journal of Physical Chemistry

The isothermal piezooptic coefficient, $(\partial n/\partial P)_T|_{\rho,\lambda}$ [hereafter abbreviated as $(\partial n/\partial P)_T$], is a physical quantity of interest in the theory of light scattering of pure liquids[1] and, in conjunction with PVT data, as a measure of intermolecular interaction in a pure liquid.[2] The only reported measurements of this quantity for liquids other than water and methanol are those of Coumou, *et al.*,[3] who have determined $(\partial n/\partial P)_T$ at 23°, 5460 Å, and 1 atm for a number of organic liquids using a specially adapted Rayleigh interferometer. Waxler, *et al.*,[4,5] have measured the refractive index of water, benzene, and carbon tetrachloride as a function of pressure at several temperatures and wavelengths, but only at pressure intervals of several hundred atmospheres, necessarily rendering imprecise any evaluation of the differential quantity from their reported data.

In view of the lack of corroborating data for organic liquids it was felt that another set of measurements by a different method entirely would prove useful. Furthermore, the method presented here is of interest as a novel application of the ultracentrifuge. Finally, this method, in distinction to that of Coumou, *et al.*,[3] will be shown to provide information on the pressure dependence of $(\partial n/\partial P)_T$.

Basis of the Method. In a liquid-filled rotating centrifuge cell there exists a radially directed pressure gradient $(\partial P/\partial r)_T$ in the liquid, from 1 atm at the meniscus to up to several hundred atmospheres at the centrifugal edge of the cell, depending on the quantity of the liquid, its density and compressibility, and the rotor speed. Since the refractive index of the liquid is a function of the pressure, a radially directed refractive index gradient $(\partial n/\partial r)_T$ also exists which may be measured using the schlieren optical system built into the ultracentrifuge. The isothermal piezooptic coefficient $(\partial n/\partial P)_T$ is readily obtained from $(\partial n/\partial r)_T$ and $(\partial P/\partial r)_T$ as shown below.

(1) M. Kerker, "The Scattering of Light and Other Electromagnetic Radiation," Academic Press, New York, N. Y., 1969, Chapter 9.

(2) H. Eisenberg, *J. Chem. Phys.*, **43**, 3887 (1965).

(3) D. J. Coumou, E. L. Mackor, and J. Hijmans, *Trans. Faraday Soc.*, **60**, 1539 (1964).

(4) R. M. Waxler and C. E. Weir, *J. Res. Nat. Bur. Stand., Sect. A*, **67**, 163 (1963).

(5) R. M. Waxler, C. E. Weir, and H. W. Schamp, *ibid.*, **68**, 489 (1964).

The increment of pressure dP at radius r in the centrifuge cell is

$$dP = 4\pi^2\omega^2\rho r dr \quad (1)$$

where ω is the rotor velocity in revolutions per second and ρ is the density of the liquid.

Since the liquid in the cell is compressible, ρ is a function of P. We assume that the compressibility is independent of pressure at the pressures encountered in this experiment. Test calculations show that this assumption introduces an error of less than 0.2% in the density at 350 atm and negligible error at pressures of less than 100 atm. The isothermal compressibility β_T is defined as

$$\beta_T \equiv \left(\frac{\partial \ln \rho}{\partial P}\right)_T \quad (2)$$

Converting pressure units to $P^* \equiv P - 1$ atm, eq 2 may be integrated to obtain

$$\rho = \rho_T e^{\beta_T P^*} \quad (3)$$

where ρ_T is the density of the liquid at temperature T and 1 atm. Substituting (3) into (1) and observing that $dP^* = dP$, we obtain

$$dP^* = 4\pi^2\omega^2\rho_T e^{\beta_T P^*} r dr \quad (4)$$

At the meniscus $P^* = 0$ and $r = r_m$. With these boundary conditions, eq 4 may be integrated to obtain

$$P^* = \frac{1}{\beta_T} \ln\left(\frac{1}{1 - 2\pi^2\omega^2\rho_T\beta_T[r^2 - r_m^2]}\right) \quad (5)$$

the radial derivative of which is

$$\left(\frac{\partial P^*}{\partial r}\right)_T = \left(\frac{\partial P}{\partial r}\right)_T = \frac{4\pi^2\omega^2\rho_T r}{1 - 2\pi^2\omega^2\rho_T\beta_T[r^2 - r_m^2]} \quad (6)$$

The schlieren optical system of an ultracentrifuge provides the required link between this relation and the isothermal piezooptic coefficient in a particularly simple fashion; an image of a line is produced whose height h at radius r is proportional to the value of the radial gradient of the refractive index $(dn/dr)_T$ at r.

$$\left(\frac{\partial n}{\partial r}\right)_T = Kh \quad (7)$$

The value of the constant of proportionality K may be precisely determined by the calibration method recommended by the manufacturer.[6] Then

$$\left(\frac{\partial n}{\partial P}\right)_T = \left(\frac{\partial n}{\partial r}\right)_T \Big/ \left(\frac{\partial P}{\partial r}\right)_T = \frac{Kh(1 - 2\pi^2\omega^2\rho_T\beta_T[r^2 - r_m^2])}{4\pi^2\omega^2\rho_T r} \quad (8)$$

At atmospheric pressure eq 8 reduces to

$$\left(\frac{\partial n}{\partial P}\right)_{T,1\text{ atm}} = \frac{Kh}{4\pi^2\omega^2\rho_T r} \quad (9)$$

Equations 5, 8, and 9 will be used in the analysis of experimental results.

Technique of Measurement. The experiments were carried out on a Spinco Model E centrifuge equipped with an electronic speed control and multiplex unit permitting measurement of the rotor velocity to one part in 10^4. Two sets of photographs were taken on each variable speed run, with increasing and decreasing rotor speeds. The two photographs so obtained at a given speed were found to be experimentally indistinguishable.

Experiments were performed with 30-mm single sector aluminum cells and 12-mm double sector aluminum cells having only one sector filled with liquid. These latter experiments were carried out to assay the effects of cell distortion. Even at the highest speeds encountered (40,000 rpm) the base line in the empty sector (*i.e.*, air filled) of the double sector cell and the base line in the region centripetal to the meniscus in the liquid filled sector formed a single continuous line, indicating distortion in the region of the meniscus was negligible. Distortion did however become evident towards the bottom (~2 mm) of the cell as indicated by an upward slope of the base line in both sectors. The upward slope was also observed in experiments with single sector cells, and for this reason measurements of base line height (for dn/dP determinations) were not carried out closer than 4 mm from the cell bottom.

In order to determine the value of h required in eq 8 and 9 the height of the schlieren line at radius r was measured (relative to that of the air base line immediately above the meniscus) to a precision of ±0.01 mm using a Nikon Shadowgraph microcomparator. The schlieren optical constant K (eq 7) at 55° phase plate angle used in these experiments was found by calibration to be 2.375×10^{-5} mm^{-2}.

The application of eq 5 and 8 requires knowledge of the value of β_T, the isothermal compressibility at 1 atm, and the experimental temperature. For carbon tetrachloride at 21.2° this was found to be 104.1×10^{-12} cm^2/dyne by interpolation of the data of Tyrer.[7]

Results and Discussion

The results of a series of determinations of $(\partial n/\partial P)_T$ for benzene, toluene, and carbon tetrachloride at 21.2° are presented in Table I. The first three sets give $(\partial n/\partial P)_T$ at 1 atm pressure, calculated at the indicated rotor velocities using eq 9. The fourth set of data gives $(\partial n/\partial P)_T$ as a function of pressure for carbon tetrachloride; these values were determined by measurement of h at several values of r in a single photograph and calculated using eq 5 and 8. This procedure

(6) Technical Bulletin E-TB-003C, Spinco Division, Beckman Instruments, Palo Alto, Calif., 1963.

(7) D. Tyrer, *J. Chem. Soc.*, 103, 1675 (1913).

Table I

Liquid	Speed	r_m, mm	r, mm	P, atm	h, mm	$\left(\frac{\partial n}{\partial P}\right)_T \times 10^{12}$, cm²/dyne: Single measurement	Run average
Benzene	39,941	63.70	63.70	1.00	21.38	51.95	
ρ, g/cm³ = 0.877	30,039				12.19	52.37	52.1
	19,977				5.35	51.97	
Toluene	39,767	63.20	63.20	1.00	19.53	48.98	
ρ = 0.864	29,892				11.00	48.82	48.7
	20,083				4.91	48.28	
Carbon tetrachloride	36,010	61.90	61.90	1.00	31.03	52.55	
ρ = 1.543	33,971				27.84	52.98	
	29,501				20.87	52.66	52.7
	19,931				9.51	52.58	
Carbon tetrachloride	33,971	61.95	61.95	1.00	27.85	52.96	
			62.51	8.01	27.88	52.54	
			63.43	19.47	27.98	51.97	
			64.34	31.11	28.11	51.47	
			65.25	42.92	28.23	50.96	
			66.16	54.92	28.35	50.47	
			67.07	67.11	28.45	49.96	
			67.99	79.47	28.62	49.59	
			68.90	92.02	28.73	49.12	

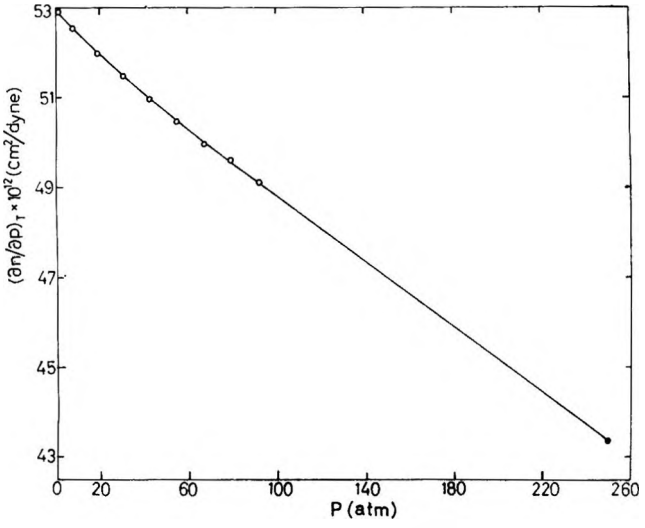

Figure 1. The pressure dependence of the isothermal peizooptic coefficient of CCl_4 at 21.2° and 5460 Å. Points below 100 atm are from the present work. Point at 250 atm interpolated from results given in ref 5.

was repeated on plates photographed at two other rotor velocities and the results obtained were in agreement with those reported here to well within the estimated accuracy of the method (1–2%).

The values here reported for $(\partial n/\partial P)_T$ at 21.2° and 1 atm pressure agree to within 0.2×10^{-12} cm²/dyne (0.4%) with those reported by Coumou, *et al.*,[3] at 23°. There are no quantitative data on the effect of temperature upon $(\partial n/\partial P)_T$ in these liquids but Eisenberg[2] has given the following empirical relation which seems to be generally valid in pure liquids

$$\frac{1}{\beta_T}\left[\frac{\partial \ln \dfrac{n^2-1}{n^2+2}}{\partial P}\right]_T = \text{constant} \qquad (10)$$

With this relation and the temperature dependent compressibility data of Tyrer[7] one can estimate the temperature dependence of $(\partial n/\partial P)_T$, and it is found that the isothermal piezooptic coefficient would be expected to decrease by about 1% on heating from 21.2 to 23°. While this increases the discrepancy between the results presented here and those of Coumou, *et al.*,[3] they still agree within the estimated error of the present method.

In Figure 1 $(\partial n/\partial P)_T$ for carbon tetrachloride at 5460 Å and 21.2° is plotted as a function of pressure. The value plotted at P = 250 atm is interpolated from the results of Waxler, *et al.*[5] While the uncertainty of this value is certain to be greater than that of the data obtained in this study (P < 100 atm) and whereas the validity of a linear exptrapolation from under 100 to 250 atm may be questioned, nevertheless it can be clearly seen that the results of the two studies are not obviously contradictory.

Acknowledgment. The authors are indebted to Dr. Martin Hirschfeld for his calibration of the schlieren optical system. R. J. and A. P. M. express their thanks to the Helen Hay Whitney Foundation and the Weizmann Institute, respectively, for postdoctoral fellowships.

Absorption Coefficients and Ionization Yields of Some Small Molecules at 58.4 nm

by S. W. Bennett, J. B. Tellinghuisen, and L. F. Phillips*

Chemistry Department, University of Canterbury, Christchurch, New Zealand *(Received October 26, 1970)*

Publication costs borne completely by The Journal of Physical Chemistry

Several studies have been reported on the photolysis of small hydrocarbon molecules by 58.4-nm helium resonance radiation.[1-3] It has been shown that the use of a thin aluminum window between the lamp and absorption cell in such work avoids errors that can arise from the presence of unwanted radiation (notably Lyman-α at 121.6 nm) in the output from the lamp.[2] As a preliminary to some studies of photolysis by He radiation we have measured ionization yields and absorption coefficients for a number of small molecules. For many of these substances absorption coefficients and/or ionization yields have been measured previously in the range 50–100 nm by workers using line or continuum sources in conjunction with differentially-pumped monochromators. Results obtained by different groups with this type of system are not always in satisfactory agreement.[4] Therefore, we feel that the values measured using our photolysis cell arrangement are of some interest.

Experimental Section

A diagram of the lamp and photolysis cell is given in Figure 1. The Pyrex photolysis vessel A is separated from the microwave-powered quartz lamp D by the thin-film Al window B (Sigmatron type TF101, film thickness 110 ± 10 nm). Vacuum wax is used to fasten the window to the Pyrex insert C, and to hold the insert in the cell. Gases are admitted to the cell and lamp through tubes E and F, and pressures are measured with a Texas Instruments quartz spiral gauge. The lamp is operated at a helium pressure of 1.0–1.2 Torr, with the closed end immersed in liquid air. Ionization currents in the cell were determined with an electrometer connected to a straight central copper-wire cathode H terminating in a glass bead, and to a copper spiral anode G which makes electrical contact with the Al window. (Tying the anode electrically to the window proved to be the key to obtaining proper plateau characteristics in the ion current *vs.* applied voltage curves.)

The lamp was capable of outputs of ~5 μA, but to obtain good plateaus in the ion current curves, it was necessary to work with fluxes below $\sim 3 \times 10^{11}$ quanta/sec (50 nA), which required operating the discharge in the horizontal section of the quartz tube. Higher

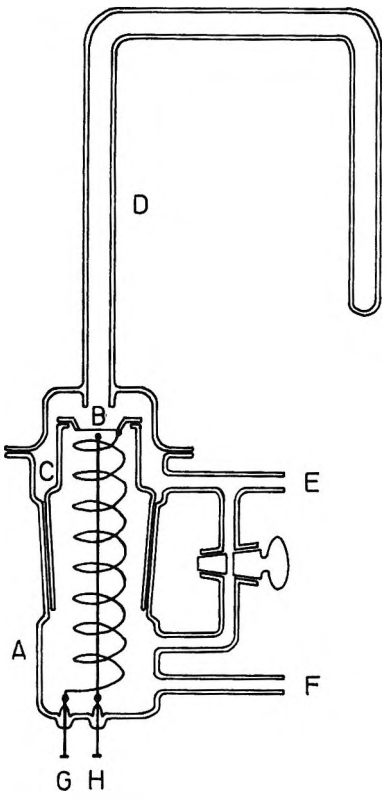

Figure 1. Lamp and photolysis cell (key in text).

fluxes could be determined by reducing the pressure so as to obtain plateaus at a known fractional absorption, or preferably by using H_2 as a calibrating gas.[5] Short-term fluctuations in lamp intensity were generally less than 1%; long-term drifts were typically 10% per hr.

All of the gases achieved essentially total absorption at pressures of 2–3 Torr, and saturation currents were obtained near 150 V for these pressures. At lower pressures the plateau region shifted to lower voltages, so that in the region of 0–80% absorption, where the absorption coefficient data were recorded, measurements at 50 V gave true saturation currents. The typical current–voltage characteristics shown for CO_2 in Figure 2 illustrate these points.

He, Ar, N_2, O_2, H_2, and CO were Matheson prepurified, high-purity grade or equivalent, Xe was spectroscopic grade, and the other materials were spectroscopic grade (alcohols), analytical reagent grade (ether), or were purified by trap-to-trap distillation.

Results and Discussion

Ionization efficiencies ϕ were determined by comparing saturation currents with those for Ar, for which the

(1) D. C. Walker and R. A. Back, *J. Chem. Phys.*, **38**, 1526 (1963).

(2) C. A. Jensen and W. F. Libby, *Phys. Rev.*, **135**, A1247 (1964); *J. Chem. Phys.*, **49**, 2831 (1968).

(3) R. E. Rebbert and P. Ausloos, *J. Amer. Chem. Soc.*, **90**, 7370 (1968).

(4) R. I. Schoen, *Can. J. Chem.*, **47**, 1879 (1969).

(5) R. Gordon, Jr., R. E. Rebbert, and P. Ausloos, *Nat. Bur. Std. (U. S.) Tech. Note*, 496 (1969).

yield was taken to be 1.00. Absorption coefficients k were calculated in the usual way from the equation

$$I/I_0 = \exp(-knx/n_0)$$

where I/I_0 is the fraction transmitted (determined from the difference between the measured current at concentration n and the current obtained for total absorption), n_0 is the particle concentration of a gas at STP, and x ($=12.0 \pm 0.3$ cm) is the length of the light path in the cell. The logarithmic plots in Figure 3 are typical of the good adherence to Beer's law observed for all the gases investigated.

The measured ionization efficiencies and absorption coefficients are summarized in Table I together with

Table I: Ionization Yields, ϕ, and Absorption Coefficients, k, at 58.4 nm. (References are for literature values that are given in parentheses.)

Gas	ϕ	k, cm^{-1}	Ref
Ar	1.00 (standard)	785 (980)	*a*
Xe	1.00 (1.00)	830 (750)	*a*
H_2	1.00 (1.00)	175 (155)	*b*
	(1.00)	(170)	*c*
N_2	1.00 (1.00)	510 (620)	*d*
O_2	1.00 (1.00)	520 (620)	*d*
CO	0.97 (0.97)	490 (609)	*e*
NO	0.98 (0.94)	570 (620)	*f*
N_2O	0.98	820	
H_2O	1.00 (0.70)	500 (400)	*g*
NH_3	1.00 (0.50)	650 (600)	*g*
CO_2	1.00 (0.99)	790 (919)	*e*
CH_4	1.00 (0.75)	660 (760)	*g*
C_2H_6	0.98 (0.80)	1420 (1450)	*g*
	(0.90)	(1400)	*h*
CH_3OH	0.98	1200	
C_2H_5OH	0.98	1830	
i-C_3H_7OH	0.99	2540	
$(C_2H_5)_2O$	1.00	3000	

[a] J. A. R. Samson in "Advances in Atomic and Molecular Physics," Vol. 2, Academic Press, New York, N. Y., 1966, p 177. [b] R. W. Ditchburn and U. Opik in "Atomic and Molecular Processes," D. R. Bates, Ed., Academic Press, New York, N. Y., Chapter 3, 1962. [c] G. R. Cook and P. H. Metzger, *J. Opt. Soc. Amer.*, **54**, 968 (1964). [d] R. E. Huffman, *Can. J. Chem.*, **47**, 1823 (1969). [e] R. B. Cairns and J. A. R. Samson, *J. Geophys. Res.*, **70**, 99 (1965). [f] K. Watanabe, F. M. Matsunaga, and H. Sakai, *Appl. Opt.*, **6**, 391 (1967). [g] P. H. Metzger and G. R. Cook, *J. Chem. Phys.*, **41**, 642 (1964). [h] R. I. Schoen, *ibid.*, **37**, 2032 (1962).

available literature values. It is worth noting that our ionization yields are all very close to unity. From the simplicity of our experiment we believe these values to be accurate within 2%, although our measurements could be slightly high if the quanta which are absorbed in nonionizing processes are re-emitted at energies above the ionization potential of the molecule in question. The logarithmic transmission plots give no indication of such anomalies, and we consider the low

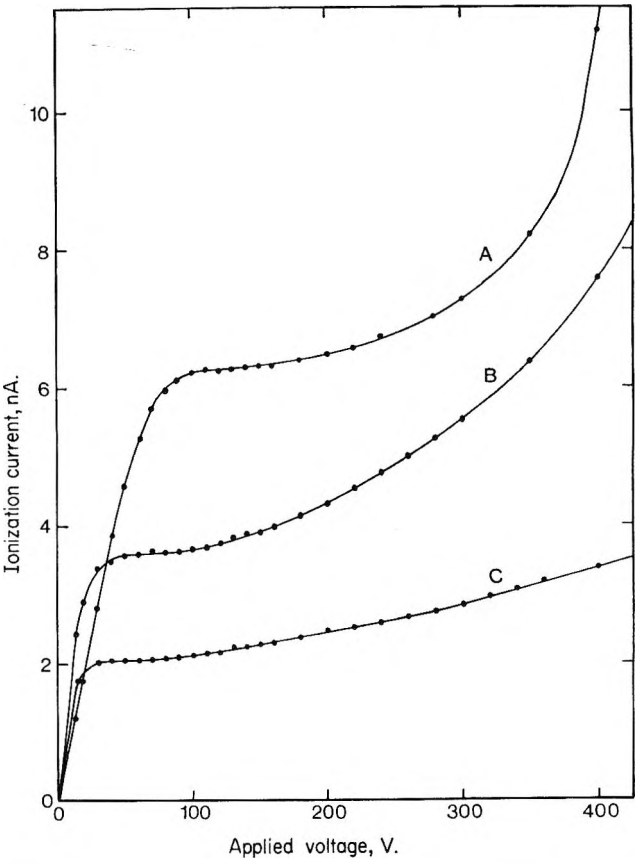

Figure 2. Typical current–voltage characteristics for CO_2. Gas pressures: (A) 2.130; (B) 0.080; and (C) 0.033 Torr.

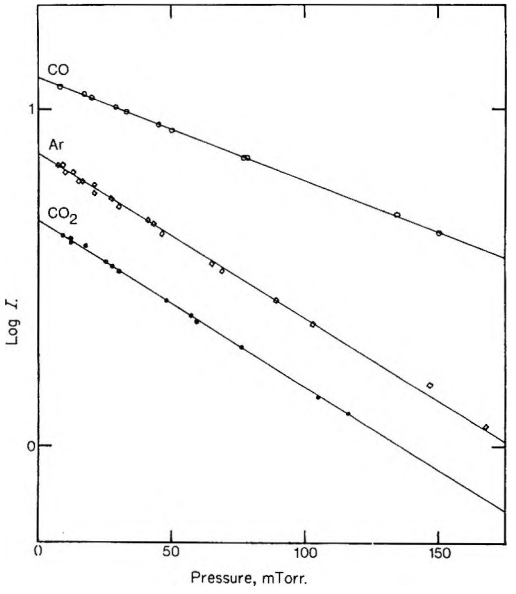

Figure 3. Typical Beer's law plots for CO, Ar, and CO_2.

results in ref *g* to be very doubtful. Our absorption coefficients were generally determined from 15–20 points in two or three sets of measurements, and the internal consistency of the data indicated a reliability of about ±5%, with the cell length the major source of uncertainty.[6] However, these values differ by as

much as 20% from previously published results. There are a number of possible causes for these discrepancies. (a) Impurity lines in our source could lead to errors. We were not equipped to examine the extreme uv output of the source spectrally; however, Gordon and coworkers[5] have examined sources similar to ours and found them free from contamination. In addition, the observed compliance with Beer's law is a good indication that, for the 0–80% absorption range where the measurements were recorded, impurity lines are insignificant. (b) Although the 58.4-nm line in our source is undoubtedly broad and totally reversed, the bandpass of the radiation is still probably much smaller than that employed in the work involving continuum sources with differentially-pumped monochromators. Again, the good Beer's law behavior of the data implies that our source line is much narrower than any fine structure in the spectra of the absorbing molecules. It is conceivable that fine structure of the order of the band widths used in the monochromator work (0.01–0.1 nm) exists, in which case the present results might be either higher or lower than previous findings, depending on whether our sharp source line hits or misses absorption features. (c) Path lengths in the windowless, differentially-pumped systems may be ill-defined, as the absorbing gas is continually streaming through the slits. Under these circumstances the measured absorption coefficients will be consistently too large. Although it would be desirable to confirm the present measurements using a double-cell arrangements such as that described by Gordon, *et al.*,[5] we feel that our k values are reliable enough to suggest that (c) can be a significant source of error in the work with windowless systems.

Acknowledgments. This work was supported by the New Zealand Universities Research Committee and by Grant AF-AFOSR-1265-67 from the United States Air Force Office of Scientific Research.

(6) Some of the 58.4-nm radiation entering the cell from the lamp will arrive *via* multiple absorption–emission processes (radiation diffusion) and will not be as well collimated as that (mostly in the weakly absorbed wings of the line) which traverses the length of the lamp tube from the first bend. For the small fraction of quanta emitted near the lower end of the tube, the path length in our system is poorly defined.

Comments on the Dynamic Method for Measuring Decomposition Pressures of Salts

by Kurt H. Stern

Electrochemistry Branch, Naval Research Laboratory, Washington, D. C. 20390 *(Received July 17, 1970)*

Publication costs assisted by the Naval Research Laboratory

Lorenz and Janz[1] have described a dynamic method for measuring dissociation pressures which is much more rapid than the well-established static method. In applying the dynamic method to the measurement of the dissociation pressure of carbonates, a stream of an N_2–CO_2 gas mixture at a fixed and known partial pressure of CO_2 was passed over the sample. The temperature of the salt was changed until it showed neither gain nor loss in weight. This temperature was taken to be the equilibrium temperature. The method was applied to solid $CaCO_3$, and good agreement with previously published values was obtained. The method was then applied to molten Li_2CO_3,[2] but the pressures were not compared to calculated ones.

It is the purpose of this note to point out that, although the dynamic method may give correct results when the salt is solid, it is very unlikely to do so when the salt is liquid. Consider the reaction

$$Li_2CO_3(l) = Li_2O(l) + CO_2(g)$$

The carbonate and oxide are miscible, and therefore their activities in the expression for the equilibrium constant

$$K_p = \frac{a_{Li_2O}}{a_{Li_2CO_3}} p_{CO_2} \quad (1)$$

will not be unity. Thus K_p has a unique value at every temperature, but p_{CO_2} depends on the composition of the melt. Recently K_p for the above reaction has been calculated from thermal data of the components.[3] A comparison of these values with the pressures measured by Lorenz and Janz is given in Table I. The last column is the activity ratio calculated from eq 1. The activity ratio is thus consistent with almost pure Li_2CO_3.

Table I

t, °C	p_{CO_2}, atm	K_p, atm	$a_{Li_2O}/a_{Li_2CO_3}$
750	0.0215	2.65×10^{-6}	1.2×10^{-4}
800	0.162	9.9×10^{-6}	6.1×10^{-5}
840	0.600	2.2×10^{-5}	3.7×10^{-5}

It then remains only to account for the significance of the constant weight which was taken as evidence for equilibrium. When Li_2O is nearly absent from the melt any further conversion of it to Li_2CO_3 will produce only such a very small change in weight that it may go undetected. For example, if a 1-g sample of Li_2CO_3 is used and the mole fraction of Li_2O in the melt is 10^{-4}, the complete conversion into Li_2CO_3 would corre-

(1) M. R. Lorenz and G. J. Janz, *J. Chem. Educ.*, **40**, 611 (1963).

(2) G. J. Janz and M. R. Lorenz, *J. Chem. Eng. Data*, **9**, 94 (1964).

(3) K. H. Stern and E. L. Weise, "High Temperature Properties and Decomposition of Inorganic Salts. Part 2. Carbonates," National Standard Reference Data System, NBS-30, 1969.

spond to a weight change of 60 μg. However, just because the melt is so dilute in oxide, very small and undetected changes in weight will correspond to very large changes in the partial pressure of CO_2.

It follows from the above argument that the dynamic method is not suitable for the measurement of liquid salt decomposition pressures if the salt and oxide are miscible—a condition which usually applies.

For the decomposition of solid salts which do not form solid solutions with their oxides the dynamic method may have the advantage of speed over the static method. Moreover the good agreement between the observed dissociation pressures of calcium carbonate[1] and those calculated from thermal data[3] indicates that the assumption of thermodynamic equilibrium holds even if the fraction of condensed phase present as oxide is extremely small. The hazard in the dynamic method is that one depends on kinetic factors to prevent the complete conversion of the salt into the oxide. In the static method, on the other hand, the ratio of the two solid phases is controlled by the experimenter who can prove that equilibrium has been attained by showing that the gas pressure is independent of that ratio. For this case the meaning of the term "decomposition pressure" is unambiguous since the activities in eq 1 are unity. If the salt and oxide do form a solid solution—a question to be investigated experimentally in each case—the equilibrium pressure will depend on the solid phase composition, and there is no longer a unique value of the "decomposition pressure" at each temperature.

Decomposition pressures measured above one-phase liquid mixtures by the static method are also not unique. However, this method permits the experimenter to determine the composition of the melt in equilibrium with gas of known pressure. From this information and a knowledge of activity coefficients (or the assumption of ideal behavior) K_p and the thermodynamic variables derived from its temperature dependence can be calculated. (For an example of such a study see ref 4.) However, the term "decomposition pressure" should not be used for these systems, since it conveys the impression that it is a unique function of temperature only. A meaningful description of the equilibrium state requires the statement of the equilibrium pressure above a melt of specified composition and temperature.

In summary, the dynamic method cannot give meaningful results for single-phase liquid mixtures, and its use for measuring the decomposition pressure above a two-phase solid system is hazardous if the relative amount of one of these phases is very small and cannot be controlled.

Finally, the generality of the above arguments makes them applicable to any reversible process of the type condensed phase 1 = condensed phase 2 + gas(es).

(4) R. F. Bartholemew, *J. Phys. Chem.*, **70**, 3442 (1966).

Mass Spectrometric Study of the Reaction of Hydrogen Atoms with Nitrosyl Chloride

by M. R. Dunn, M. M. Sutton, C. G. Freeman, M. J. McEwan, and L. F. Phillips*

Chemistry Department, University of Canterbury, Christchurch, New Zealand *(Received October 26, 1970)*

Publication costs borne completely by The Journal of Physical Chemistry

The reaction of H atoms with ONCl has been studied previously by Clyne and Stedman,[1] who found that the products were HCl and NO and that the stoichiometry of the reaction was close to 1:1 in a flow system in which the walls were coated with phosphoric acid. They also showed that the primary reaction

$$H + ONCl \longrightarrow HCl + NO \qquad (1)$$

was very fast ($k_1 > 1.5 \times 10^{-12}$ cm^3 molecule^{-1} sec^{-1}) and suggested that the reaction could be used as a gas-phase titration for the measurement of H atom concentrations.

We have investigated the reaction mass spectrometrically in a fast-flow system at pressures near 0.1 Torr. We used sufficiently small reagent concentrations to allow the progress of the primary reaction to be followed over a range of several milliseconds and thus to allow measurement of the primary reaction rate. In addition, for reaction times of 100 msec or more, we have confirmed the results of Clyne and Stedman regarding the nature of the reaction products and overall stoichiometry in a system in which the walls are poisoned against recombination of chlorine atoms. However, when the walls are not freshly poisoned, we find that the number of hydrogen atoms removed by each ONCl molecule typically rises to a value of about 2, and varies in a nonreproducible manner as the wall coating ages. This behavior we attribute to the presence of a chain reaction, involving chlorine atoms, which is initiated by the reaction of H with vibrationally excited HCl produced in the primary reaction. Provided chlorine atoms are removed only by reacting with ONCl, and not by recombination on the wall, the chain does not affect the overall stoichiometry. Hence, if the reaction is to be used to estimate hydrogen atom concentration on the basis of an assumed 1:1 stoichiometry, care must be taken to ensure that an effective wall coating is present.

Experimental Section

The apparatus was similar to that used in our previous studies of reactions of atoms with Cl_2O.[2] The flow

(1) M. A. A. Clyne and D. H. Stedman, *Trans. Faraday Soc.*, **62**, 2164 (1966).

(2) C. G. Freeman and L. F. Phillips, *J. Phys. Chem.*, **72**, 3025 (1968).

speed in the 17-mm i.d. reaction tube was in the range 8.5–10.5 m sec^{-1}, except when the gas flow was throttled to allow measurements to be made at long reaction times. For most of the experiments, including all of the primary rate measurements, the walls of the flow tube were poisoned with phosphoric acid.[3] Hydrogen atoms were generated by passing a stream of argon containing 1–10% of H_2 through a microwave discharge; their concentration was calculated from the decrease in peak height at mass 46 which resulted from the titration reaction with an excess of NO_2.[4] Typically 80% of the H_2 was dissociated to atoms, so that vibrationally excited H_2[5] should have been relatively unimportant in this system. Matheson nitrosyl chloride was purified by condensation onto P_2O_5 followed by repeated fractionation with a LeRoy still. Other materials were as used previously.[2] All measurements were made at room temperature (*ca.* 23°).

Results and Discussion

The electron-impact mass spectrum of ONCl appears not to have been reported previously, so we present it in Table I. The main feature of this spectrum is the very low contribution from the parent $ONCl^+$ peak. The parent peak is also very small or absent in the mass spectrum obtained by photon impact.[6] Because of the lack of a significant parent peak we have been obliged to monitor the ONCl concentration using the NCl^+ peak at mass 49; unfortunately the larger NO^+ peak could not be used because NO is a product of the reaction and the sensitivity of the instrument at mass 30 is almost the same for NO and ONCl.

The low sensitivity of the mass spectrometer for ONCl at mass 49 was a major source of difficulty during the measurements of the primary rate, and in fact these measurements could not be attempted at all except when the instrument was behaving exceptionally well. The mean of 28 determinations of k_1, calculated on the assumption of 1:1 stoichiometry at short reaction times, was 3.0×10^{-11} cm^3 $molecule^{-1}$, with a standard deviation of 1.0×10^{-11}. Of these results, two sets of six determinations each were made under what appeared to be optimum conditions and were considered particularly reliable. The mean of these 12 values gave $k_1 = 2.7 \times 10^{-11}$ cm^3 $molecule^{-1}$ sec^{-1}, with a standard deviation of 0.5×10^{-11}. We give this as our preferred final value for k_1, with an estimated error of 1.5 times the standard deviation. One of the two sets of six measurements was obtained with excess ONCl, the other with excess H atoms. The partial pressure of the reagent which was in excess was typically 3×10^{-4} Torr.

Recently, Niki, *et al.*,[7] reported the results of a mass spectrometric study which gave $k_1 = 4.5 \times 10^{-11}$ cm^3 $molecule^{-1}$ sec^{-1}, in fair agreement with our value. (According to a referee of this paper the value quoted at the 160th National Meeting of the American Chemical Society was $(3.2 \pm 1.6) \times 10^{-11}$, in which case the agreement is very satisfactory indeed.)

The stoichiometry of the reaction was determined by measuring the number of ONCl molecules removed by a known concentration of atomic hydrogen, at reaction times greater than 100 msec, with excess ONCl present. Measurements were made with both old and fresh coatings of phosphoric acid, and with uncoated Pyrex walls. In the freshly-coated system the number of H atoms removed per ONCl molecule consumed was found to be 1.02, with a standard deviation of 0.08, in good agreement with Clyne and Stedman's figure of 0.94 (standard deviation 0.06) for the same quantity. However, when the walls were not freshly coated the number of H atoms removed per ONCl molecule destroyed ranged from 1.2 to 2.3, with a tendency for higher values to be obtained as the age of the coating increased. This implies that the observed stoichiometry is dependent upon secondary reactions involving atomic chlorine, since the different results were obtained under conditions where different numbers of chlorine atoms could be lost by wall recombination. (Wall recombination of hydrogen atoms is a slow process in both coated and uncoated Pyrex systems.)

The HCl molecule produced by reaction 1 is vibrationally excited, molecules in levels up to $v = 9$ having

Table I: Mass Spectrum of Nitrosyl Chloride[a,b]

Mass no.	Species	Relative abundance
14	N^+	3.00
16	O^+	0.85
30	NO^+	100.0
31	$^{15}NO^+$	0.38
35	Cl^+	18.7
37	Cl^+	5.9
46	NO_2^+	0.23
49	$N^{35}Cl^+$	1.33
51	$N^{37}Cl^+$, $O^{35}Cl^+$	0.59
53	$O^{37}Cl^+$	0.05
65	$ON^{35}Cl^+$	0.03
67	$ON^{37}Cl^+$	0.01
70	$^{35,35}Cl_2^+$	1.00
72	$^{35,37}Cl_2^+$	0.62
74	$^{37,37}Cl_2^+$	0.10

[a] Source pressure: 9×10^{-6} Torr; electron energy: 50 V. [b] The peak at mass 46 can be attributed to the presence of *ca.* 0.5% NO_2; those at masses 70, 72, and 74, arise from a similar concentration of chlorine impurity.

(3) E. A. Ogryzlo, *Can. J. Chem.*, **39**, 2556 (1961).
(4) L. F. Phillips and H. I. Schiff, *J. Chem. Phys.*, **37**, 1233 (1962).
(5) R. F. Heidner and J. V. V. Kasper, *ibid.*, **51**, 4163 (1969).
(6) A. J. Nicholson, C.S.I.R.O. Melbourne, private communication.
(7) H. Niki, D. H. Stedman, and D. Steffenson, Abstracts, 160th National Meeting of the American Chemical Society, Chicago, Ill., Sept 1970, p 116.

been detected from their infrared emission.[8] Hence the secondary reaction

$$H + HCl \longrightarrow H_2 + Cl \qquad (2)$$

would be expected to occur up to 100 times faster for the newly-formed HCl molecules than in the thermally-activated case. The factor of 100 is derived on the assumption that all of the necessary 3 kcal mol^{-1} of activation energy[1] can be accepted in the form of vibrational excitation of the HCl. With this assumption the effective value of k_2 is about 1.5×10^{-12} cm^3 $molecule^{-1}$ sec^{-1}. In the freshly coated system the chlorine atom produced by reaction 2 would react with ONCl according to

$$Cl + ONCl \longrightarrow Cl_2 + NO \qquad (3)$$

Thus preserving the 1:1 stoichiometry. The fast reaction

$$H + Cl_2 \longrightarrow HCl + Cl \qquad (4)$$

($k_4 = 3.5 \times 10^{-11}$ cm^3 $molecule^{-1}$ sec^{-1} [1,7]) would then be expected to compete effectively with reaction 1, except in the presence of a large excess of ONCl. This view is supported by the observation that less than 0.1% of the ONCl appeared in the form of Cl_2 in the products. Reactions 3 and 4 constitute a chain which would continue until all of either the ONCl or the atomic hydrogen had been used up, and which would give rise to the observed 1:1 stoichiometry. The presence of this chain does not affect our measurement of the primary rate because our value of k_1 is ten times as large as the effective value of k_2, so that reaction 2 would not be significant at short reaction times with very low reagent pressures.

In a clean Pyrex system, or with an ineffective wall poison, reaction 3 would experience competition from the process

$$Cl + \text{wall} \longrightarrow {}^1/_2Cl_2 \qquad (5)$$

which, together with reaction 4, would bring about a rapid catalyzed removal of H atoms. In the limit of $k_5 \gg k_3[ONCl]$ the result would be to remove three H atoms per ONCl molecule destroyed. Thus this mechanism can account satisfactorily for the observed stoichiometry in both the poisoned and unpoisoned systems. In view of the small amount of undissociated H_2 emerging from our microwave discharge, the reaction

$$Cl + H_2(v \gg 0) \longrightarrow HCl + H \qquad (6)$$

which Niki, *et al.*, found to be important in the $H + Cl_2$ system is not likely to have been significant except perhaps when H atoms were in very large excess. This reaction could not affect our primary rate measurements because it requires the prior occurrence of reaction 2.

Acknowledgments. This work was supported by the New Zealand Universities Research Committee and by Grant AF-AFOSR-1265-67 from the United States Air Force Office of Scientific Research.

(8) J. K. Cashion and J. C. Polanyi, *J. Chem. Phys.*, **35**, 600 (1961).

COMMUNICATIONS TO THE EDITOR

Q-Switched Laser-Induced Reactions of Thiacyclobutane and Thiacyclopentane with Oxygen

Publication costs assisted by the U.S. Department of the Interior, Bureau of Mines

Sir: The phenomenon of laser-induced gas breakdown has been a subject of considerable interest in the field of plasma physics.[1] Except for the work of Adelman,[2] Verdieck and Mau,[3] and Wiley and Reich[4] practically all of the research to date has been concerned with the physics of the problem, and very little effort has been made toward an understanding of the chemical reactions that occur during laser-induced gas breakdown of molecular gases. We report here the results of some of our investigations of the chemical reactions occurring during laser-induced gas breakdown of sulfur compounds in the presence of oxygen. Thiacyclobutane and thiacyclopentane were chosen because they are sulfur compounds found in shale oil, a possible source of fuel for future use. While the reactions occurring during gas breakdown are chemically interesting in themselves, they are important practically in the sense that the products formed during the combustion of fuels containing sulfur compounds present a serious air pollution problem. Since the mechanisms of the oxidation of sulfur compounds are not well understood,[5] chemical reactions initiated by laser-induced gas breakdown provide a technique for the study of reactions initiated at a high temperature.

A Q-switched ruby laser was used for these experiments. Each pulse had a peak power of over 100 MW and a duration of about 20 nsec. About 80 μl of a cyclic sulfide was added to a 50-cc spherical Pyrex bulb to ensure that the same concentration of sulfide was present in the gas phase for each partial pressure of added oxygen. Each gaseous mixture was exposed to one shot which was sufficient to initiate the reaction. The resultant plasma formation and subsequent radiation completely filled the reaction vessel. Extensive degradation was noted from the change in color of the liquid at the bottom of the bulb and from the condensate on the sides of the bulb. Gas analyses of the products formed were performed by gas chromatography[6] and mass spectroscopy.

From the nature of the reaction products, it appeared that a very high-temperature reaction occurred. The gaseous products identified were: CO_2, SO_2, H_2S, H_2O, COS, CS_2, and C_2H_2. Not all of these products were observed for each pressure of added oxygen, nor were all the products observed for both sulfides. For instance, no reaction was observed in thiacyclobutane or thiacyclopentane in the absence of oxygen, or with oxygen at a partial pressure of 50 Torr. At an oxygen pressure of 100 Torr CO_2, SO_2, and H_2O were detected as reaction products of both sulfides. At a pressure of 150 Torr of added oxygen H_2S, COS, CS_2, and C_2H_2 were also detected as reaction products of thiacyclobutane, whereas H_2S was the only additional product formed from the reaction of thiacyclopentane. The same product distribution was obtained at oxygen pressures of 200 and 250 Torr, with the reaction at 200 Torr producing the maximum yield. For the range 300–500 Torr of oxygen, COS, H_2S, and CS_2 were not detected for the thiacyclobutane reaction. However, at pressures of 600 and 800 Torr of oxygen, COS, H_2S, and CS_2 reappeared as reaction products. At a pressure of about 1200 Torr of oxygen, quenching effects due to the large excess of oxygen were noted. At a pressure of about 1,500 Torr of oxygen, the reaction was thoroughly quenched, therefore no reaction occurred. For both sulfides and at all pressures in which reaction occurred CO_2, SO_2, and H_2O were the major products. The variation in product distribution as a function of oxygen pressure suggests that products such as CS_2, COS, and H_2S are dependent upon the concentration of cyclic sulfide present in the mixture.[7]

The appearance and disappearance of H_2S, COS, and CS_2, as well as the formation of CS_2 itself, are suggestive of a complex process involving several mechanisms. It is difficult to propose such mechanisms at this time because laser-induced gas breakdown occurs in a complicated fashion.[1] Initial ionization is caused by multiphoton absorption by the gas, resulting in a plasma of ions at a very high temperature ($>10^4$ °K). The expansion of the plasma also generates a shock wave. At which point in time or temperature of the expanding plasma stable product formation occurs is

(1) C. DeMichelis, *IEEE J. Quan. Electron.*, QE-5, 188 (1969).

(2) A. H. Adelman, *J. Chem. Phys.*, 45, 3152 (1966).

(3) J. F. Verdieck and A. W. H. Mau, *Chem. Commun.*, 1969, 226.

(4) R. H. Wiley and E. Reich, *Ann. N. Y. Acad. Sci.*, 168, 610 (1970).

(5) A. Levy, E. L. Merryman, and W. T. Reid, *Environ. Sci. Technol.*, 4, 653 (1970).

(6) A 10-ft Porapak Q, 150–200 mesh column was used. After 2 min of isothermal operation at 50°, the column temperature was programmed to 210° at 10°/min. Detection was by thermal conductivity.

(7) The product distribution is probably also affected by the plasma temperature. Similar related experiments in our laboratory have shown that the chemical reactions occurring during gas breakdown are dependent upon the laser output power which in turn can be related to the plasma temperature.

impossible to determine without the use of time-resolved spectroscopy. Furthermore, whether or not the products are formed from ion–molecule reactions, or radical–radical, radical–atom combinations cannot be established on the basis of product formation. Adelman[2] observed emission from C_2 as the only polyatomic emission in the laser-induced gas breakdown of carbon tetrachloride, chloroform, acetone, methanol, and hexane. Other emissions observed were from ionized atomic species including C^{2+}. We suspect that in our reactions, due to the extremely high temperatures attained, thiacyclobutane and thiacyclopentane become nonentities and only highly energetic ions, atoms, and radicals are formed which react along the shock front producing stable products.

Only small amounts of acetylene were produced in our reactions, although this is usually the major compound formed by degradation of solids[3,8–10] and gases.[4] Except for the work of Verdieck,[3] all the other experiments used conventional mode lasing. In the conventional mode, the degradation process probably results from a rapid thermal heating of the sample. A Q-switched laser is needed to achieve the threshold for multiphoton ionization. In our experiments, combustion did not occur when operating the laser in the conventional mode.

Acknowledgment. The authors wish to thank Mr. Robert Ellefson of the spectroscopy group of the Laramie Energy Research Center for providing the mass spectral data. Reference to a company or product name does not imply approval or recommendation of the product by the U. S. Bureau of Mines to the exclusion of others that may be suitable.

(8) R. H. Wiley and P. Veeravaga, *J. Phys. Chem.*, **72**, 2417 (1968).
(9) J. L. Schultz and A. G. Sharkey, *Carbon (Oxford)*, **5**, 57 (1967).
(10) F. S. Karn, R. A. Friedel, and A. G. Sharkey, Jr., *ibid.*, **5**, 25 (1967).

LARAMIE ENERGY RESEARCH CENTER
BUREAU OF MINES
U. S. DEPARTMENT OF THE INTERIOR
LARAMIE, WYOMING 82070
F. P. MIKNIS*

DEPARTMENT OF PHYSICS
UNIVERSITY OF WYOMING
LARAMIE, WYOMING 82070
J. P. BISCAR

RECEIVED DECEMBER 7, 1970

Cleaning Our Environment The Chemical Basis For Action

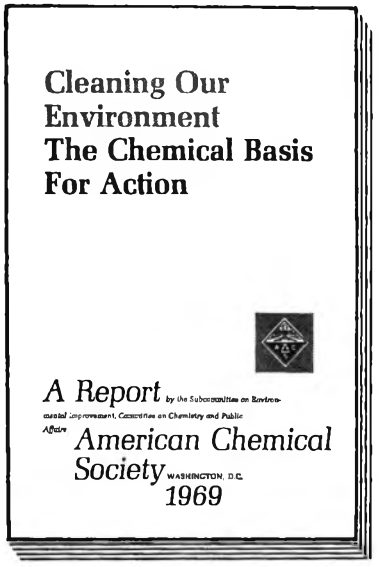

Cleaning Our Environment—The Chemical Basis for Action is the highly acclaimed 249-page report based on a three-year study by the Subcommittee on Environmental Improvement of the ACS Committee on Chemistry and Public Affairs. Leading experts from the fields of chemistry, biochemistry, chemical engineering, biology, entomology, and other disciplines comprised the Task Force on Environmental Improvement which conducted the study, one of the most comprehensive of its kind.

The report divides the problem of environmental improvement into four parts: air environment, water environment, solid wastes, and pesticides. It clearly shows where extensive fundamental research is required to provide a better working understanding of the environmental system. Focusing strongly on chemistry, chemical engineering, and related disciplines, the report concludes that the U.S. possesses enough technical know-how to take enormous strides now toward a cleaner environment.

Included in the report are 73 recommendations for action on such topics as:

- *flow, dispersion, and degradation of water and air pollutants*
- *short- and long-range effects of water and air pollutants*
- *municipal and industrial waste water treatment*
- *advanced treatment processes*
- *eutrophication*
- *air quality criteria*
- *air monitoring systems*
- *emission control on motor vehicles*
- *abatement of pollutants from power plants*
- *municipal and industrial solid wastes*
- *mining and processing wastes*
- *pesticides and human health*
- *pesticides and wildlife*
- *methods of pest control*

Although the ACS report is directed primarily at technical and nontechnical administrators in the environmental field, research managers, legislators and others working in this area, the nature of the subject makes it required reading for all scientists interested in environmental problems and their solutions.

The report is available from the ACS Special Issues Sales. Price: $2.75.

American Chemical Society
Special Issues Sales
1155 Sixteenth Street, N.W.
Washington, D.C. 20036

Please send me the ACS Report "Cleaning Our Environment—The Chemical Basis for Action."

*Name*_____

*Address*_____

*City*_____ *State*_____ *Zip*_____

Number of copies _____

I enclose _____. *(Payable to the American Chemical Society.)*

Please bill me _____. *$2.75 a copy.*